EXPLORATION OF THE MITOCHONDRIA AS A POTENTIAL THERAPEUTIC TARGET IN DUCHENNE MUSCULAR DYSTROPHY

MEGHAN C HUGHES

A DISSERTATION SUBMITTED TO THE FACULTY OF GRADUATE STUDIES IN PARTIAL FULFILLMENT OF THE REQUIREMENTS FOR THE DEGREE OF DOCTOR OF PHILOSOPHY

GRADUATE PROGRAM IN Kinesiology and Health Sciences
YORK UNIVERSITY
TORONTO, ONTARIO

April 2019

Abstract

Duchenne muscular dystrophy (DMD) is a progressive muscle wasting disease resulting from a mutation in the X-linked gene encoding the protein dystrophin. DMD is characterized by profound muscle weakness as degenerating muscle is replaced by fat and connective tissue. Early loss of ambulation followed by premature death due to cardiac and/or respiratory failure characterize the most debilitating aspects of DMD, a disease for which there is currently no cure. Limited success has been reported when treating DMD with gene based therapies. Current standard of care involves glucocorticoids, which target a secondary cellular myopathy; inflammation. While this line of treatment has provided promising benefits, these drugs present a variety of negative side effects for patients. As such, extensive research has been focused on identifying both therapeutic targets and corresponding novel therapies for the treatment of the DMD myopathy.

The focus of this dissertation was to first determine the degree and precise mechanism of mitochondrial dysfunction in DMD followed by the evaluation of SBT-20, a mitochondrial-targeted peptide, as a therapeutic candidate for the treatment and prevention of DMD pathophysiology. In order to address these questions, we first comprehensively evaluated mitochondrial bioenergetics across a spectrum of oxidative and glycolytic muscles in the D2.B10-DMD^{mdx}/2J mouse (D2.*mdx*) in early and late stages of disease progression. We then tested the efficacy of SBT-20 in improving both DMD myopathy in respiratory and skeletal muscles, as well as the underlying mechanism of mitochondrial dysfunction in dystrophic muscle.

Our findings reveal that the mitochondrial H_2O_2 emission is elevated during impaired oxidative phosphorylation in cardiac, respiratory, oxidative and glycolytic muscle in young (4-week) and aged (52-week) D2.*mdx* mice and furthermore, that there is a specific defect in mtCK functionality in oxidative muscle. SBT-20 was effective in improving mitochondrial bioenergetics following

short (4 weeks) and long (12 weeks) term treatment. This was associated with improved pathophysiology following short-term treatment. Taken together, this thesis identifies impairments in mitochondrial bioenergetics as a contributing factor to the pathophysiology in dystrophic muscle and further highlights SBT-20 as a promising therapy for the improvement of myopathy in DMD.

Acknowledgements

This thesis would not have been possible without the help and support from a variety of important individuals. First and foremost, I would like to thank my supervisor Dr. Chris Perry. May 2013 feels like a very long time ago at this point but it is enjoyable to look back and think about all that we have accomplished since that time. Thank you for your constant support, mentorship and guidance. Under your leadership, not only have I developed as an independent scientist, but my bad joke repertoire and fluid sense of time have been expanded immensely. While most of our meetings involved a series of eye rolls more often than not, I truly am grateful for everything you have helped me accomplish over the last 6 years. While a thank-you to express my gratitude doesn't seem to suffice, a "Chris Sized" stein of beer and a framed copy of the quote board might start to cover it.

Second, I would like to thank the Perry lab members, past and present. While things were certainly never dull (or quiet), I enjoyed coming to the lab each day and working with each of you. In particular, to Sofhia Ramos, we have spent enough hours together over the past 5 years to last a life time but I am incredibly grateful that it was you I spent those marathon experiment days with. While I can't say I will miss spending holidays in the lab, our Easter feast following the Farquharson Flood of 2016 stands out as a favourite memory from the past 5 years with you. Looking forward to comparing our latest TV favourites out in the real world. To Patrick Turnbull (the Statler to my Waldorf?) thank you for always being my science sound board and my favourite person to debate sports with. While others may not have appreciated it as much as we did, our "hilarious" banter made day to day lab life much more enjoyable. My only regret from the past 5 years is how late in the game we discovered those $10 pitchers.

I would also like to thank the amazing collaborators I have had the chance to work with during my time at York. Specifically, to Dr. Tom Hawke and the Hawke lab, working with and learning from you has been a true highlight of my PhD. To Tom in particular, thank you for your advice, support and contributions throughout my thesis. I really enjoyed hearing your perspectives, interpretations and insight on my data and your involvement in this thesis was pivotal, for which I am truly grateful.

Finally, I would like to thank my parents, Bob and Louise Hughes. While you couldn't really picture what day to day life was like in the Perry lab, you were always incredibly supportive and at least faked interest when I tried to talk science over dinner. Your unconditional love and support has meant the world during this long haul as a graduate student. I don't think any of us will ever forget the Micky and Minnie Farewell Tour ☺.

Table of Contents

List of Tables

Chapter 2

Chapter 4

Chapter 5

List of Figures

Chapter 2

Chapter 4

Chapter 5

Chapter 6

Chapter 7

Chapter 8

List of Supplemental Figures

Chapter 4

Chapter 5

Chapter 6

Chapter 7

List of Abbreviations

b-DG	Beta-dystroglycan
ADP	Adenosine diphosphate
ATP	Adenosine Triphosphate
Ca^{2+}	Calcium
cCK	Cytosolic creatine kinase
cDMD	Canine Duchenne muscular dystrophy
Cr	Creatine
CyPD	Cyclophilin D
D2.*mdx*	D2.B10-DMD^{mdx}/2J mouse model
dko	Utrophin-Dystrophin$^{-/-}$ mouse model
DMD	Duchenne muscular dystrophy
Δp	Proton motive force
EBD	Evan's Blue Dye
ERV	Expiratory reserve volume
ETC	Electron transport chain
FDB	Flexor digitorum bravis
FVC	Forced vital capacity
GPX	Glutathione peroxidase
GR	Glutathione reductase
GRX	Glutaredoxin
GSH	Reduced Glutathione
GSSG	Oxidized Glutathione
H^+	Proton
H_2O_2	Hydrogen peroxide
IMM	Inner mitochondrial membrane
MAO	Monoamine oxidase
MCU	Mitochondrial calcium uniporter
MEP	Maximal expiratory pressure
mH_2O_2	Mitochondrial hydrogen peroxide
mtCK	Mitochondrial creatine kinase
NAC	N-acetylcysteine
NCLX	Sodium-Calcium exchanger
NO	Nitric oxide
NOX	NADPH Oxidase
$O_2^{\cdot -}$	Superoxide
OMM	Outer mitochondrial membrane
OXPHOS	Oxidative phosporylation
PCr	Phosphocreatine

Pi	Inorganic phosphate
PTP	Permeability transition pore
RNS	Reactive nitrogen species
ROS	Reactive oxygen species
RV	Residual volume
SERCA	Sarco/endoplasmic Ca^{2+} ATPase
SOD	Superoxide dismutase
SR	Sarcoplasmic reticulum
TCA	Tricarboxylic Acid cycle
TLC	Total lung capacity
WT	Wildtype

1 Introduction

Duchenne muscular dystrophy (DMD) is a progressive muscle wasting disease affecting 1 in 3500 boys. Resulting from a mutation in the X-linked gene encoding the protein dystrophin, DMD is characterized by profound muscle weakness and exercise intolerance as degenerating muscle is gradually replaced by fat and connective tissue [1-3]. This debilitating disease results in boys being wheelchair bound by the age of 10-12 and eventual death due to cardiac and/or respiratory failure in their early 20s [4, 5]. There is currently no cure for DMD.

A lack of dystrophin presents a myriad of problems within the muscle as this protein is the anchor between the cell membrane and the cytoskeleton [1, 2]. Dystrophin, a 427 KDa rod-shaped protein, establishes structural integrity and cytoskeletal organization within muscle fibres. Without this anchor, muscle fibres become more susceptible to damage, particularly through tearing of cell membranes, leading to impairments in a variety of cell functions and the subsequent activation of cell death pathways [6, 2]. Current therapies are glucocorticoid based and have successfully extended lifespan while helping to maintain some muscle function. However, given the long-term requirement for treatment, these drugs present a variety of negative side effects for patients and ultimately do not provide a cure [7]. As such, extensive research to date has focused on gene-based therapies, given the genetic origin of this disease. Unfortunately, limited success has been reported [8]. This highlights the importance of the search for other therapeutic targets to alleviate the multitude of cellular impairments associated with DMD.

Formulated several years prior to the discovery of the genetic defect underlying this disease [9], the calcium (Ca^{2+}) hypothesis of DMD identified increases in cytosolic Ca^{2+} as the link between increased sarcolemmal tearing and muscle fibre degeneration in dystrophic muscle [10]. Since such time, the cellular implications of elevated cytosolic Ca^{2+} in DMD have been studied

extensively, yet the exact mechanisms that render the muscle more susceptible to elevated cell death are not well understood [11]. Cellular oxidative stress has long been considered a contributing factor to the pathogenesis of DMD, dating back to a time before dystrophin had been discovered. Early researchers established similarities between muscle pathology in DMD and the pathology associated with Vitamin E deficiency as well as ischemia reperfusion, two conditions in which oxidative damage is an established contributor to the pathogenesis [12, 13]. Later work revealed that cellular oxidative stress is indeed altered in patients with DMD as indicated through elevated lipid peroxidation [14-16] and protein carbonylation [17, 18], as well as increased activity of glutathione peroxidase [14, 19, 20] and increased levels of total glutathione [17, 20, 21]. While it is generally accepted that elevated oxidative stress is present within DMD, the source of oxidative stress remains controversial.

The mitochondria are a key source of reactive oxygen species production (ROS) and have often been hypothesized to play a role in DMD pathology given the well-documented reduction in ATP content in both human and animal models of DMD [20, 22-24]. This energy-producing organelle also acts as a "sink" for Ca^{2+} during times of cytosolic Ca^{2+} overload [25, 26] and has the ability to induce mitochondrial derived apoptosis and necrosis [27]. Seemingly, it is possible that dystrophic muscle contain dysfunctional mitochondria that buffer cytosolic Ca^{2+}, have limited ATP supply and produce elevated levels of ROS, consequentially activating cell death, the primary pathologic process in DMD [6]. This concept, while theoretically plausible, remains controversial as studies investigating mitochondrial oxidative phosphorylation reveal divergent findings [23, 28-34] and to our knowledge, only one study to date has measured mitochondrial ROS production, revealing decreased mitochondria H_2O_2 (mH_2O_2) release but increased rates of mH_2O_2 scavenging, indicative of compensation [33]. Furthermore, measurement of mitochondrial calcium retention

capacity (CRC), an index of susceptibility to permeability transition pore (PTP) opening and subsequent cell death, has also provided conflicting results. While some studies demonstrate a decrease in time to PTP opening [33, 35], studies quantifying the concentration of calcium required to induce PTP opening have found no differences between DMD and WT animals [33, 36]. Given mitochondrial oxidative phosphorylation, ROS generation and Ca^{2+}-induced PTP opening form a triad whereby each bioenergetic pillar concurrently influences, and is influenced, by the other two parameters, the evaluation of all three components of mitochondrial bioenergetics in tandem is necessary to comprehensively evaluate mitochondrial function. Therefore, the purpose of this thesis is to 1. Determine the degree and specific source of altered mitochondrial bioenergetics in DMD and 2. Determine the contribution of the mitochondria to DMD disease pathology through the use of a mitochondrial-targeted therapeutic.

2 Literature Review

2.1 Overview and Introduction to Duchenne muscular dystrophy

2.1.1 Overview of Duchenne muscular dystrophy

Duchenne muscular dystrophy (DMD) is the most common form of childhood muscular dystrophy and results from a mutation in the gene encoding for the protein dystrophin; a sub-sarcolemmal protein that plays a role in cell membrane integrity and in linking the extracellular matrix to the cytoskeleton (**Figure 2.1)** [37]. This condition is genetic in nature due to its X-linked pattern of inheritance, although about 25% of cases are due to *de novo* gene mutations [38]. Approximately 1 in 3500 boys are affected and there is currently no cure.

Dystrophin is associated with the cell membranes of skeletal, cardiac and smooth muscle cells yet individual muscles are affected in a heterogenic manner. Disease progression can be divided into stages and are summarized in **Table 2.1**.

2.1.2 Genetic Nature of DMD

The full-length dystrophin gene is predominately expressed in skeletal and cardiac muscle with smaller proportions found in the smooth muscle of the brain. This gene is located at Xp21.2 and contains 79 exons [39] with mutations occurring as deletions in ~60% of patients, duplications in ~10% of patients and small mutations in ~30% of patients, including small insertions or deletions within an exon (~7%) and nonsense mutations (~15%) [40-42]. Within patients in Canada between 2000 and 2009, 43% of mutations involved exons 45 to 53. The top ten deletions, which encompassed 26% of occurrences, were exons 45-47, 45-48, 45, 45-50, 45-55, 51, 45-49, 45-52, 49-50, and 46-47. 29% of mutations involved exons 2 to 20. In cases involving duplications, exons 2, 2-7, 2-17, 3-7, 8-11, 10, 10-11, and 12 are most commonly duplicated [41]. It is the size of the gene and the wide range of specific mutations that make gene based therapy so difficult to implement as a treatment option for patients with DMD.

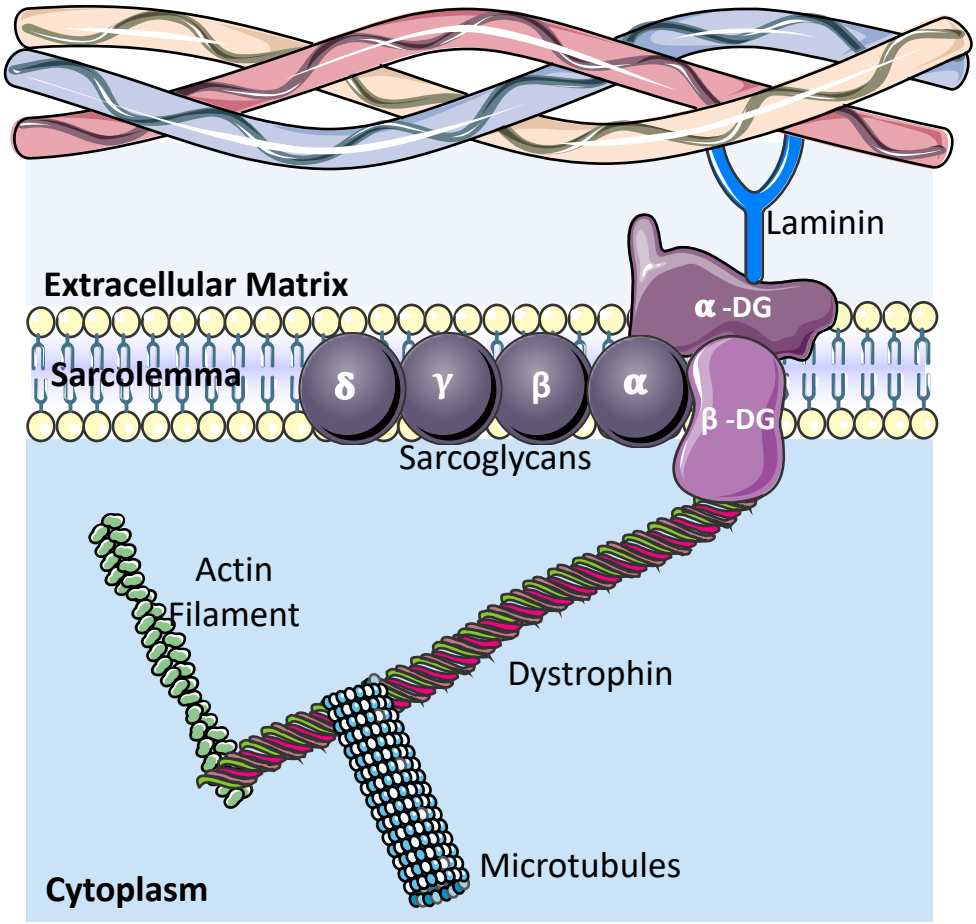

Figure 2-1: Schematic representation of the integral components of the dystroglycan complex. The dystroglycan complex is comprised of β-dystroglycan (β-DG), α-dystroglycan (α-DG) and the sarcoglycan complex including subunits α, β, γ and δ which together with functional dystrophin provides structural support by anchoring actin in the cytoplasm and laminin in the extracellular matrix.

Table 2-1: Disease progression in DMD. Adapted from [43-45].

Stage of Disease	Key Characteristics
Early Ambulatory (0-7 years)	**Skeletal:** - Delays in developmental milestones such as sitting and walking - Move slower than peers - Balance Issues **Cardiac/Respiratory:** N/A **Cognitive:** - Delays in talking
Late Ambulatory (7-10 years)	**Skeletal:** - Severe difficulty walking; may require braces - Use of Gower's maneuver to stand from sitting - Early onset of fatigue when walking - Difficulty lifting and carrying items despite full use of hands and fingers **Cardiac/Respiratory:** ECG abnormalities begin to appear **Cognitive:** - Evident delays in cognitive development
Early Non-Ambulatory (10-14 years)	**Skeletal:** - Become wheelchair dependent - Weakness in arms make daily activities difficult - Development of scoliosis due to weak back muscles and chronic sitting **Cardiac/Respiratory:** - Cardiomyopathy onset – early stages of heart failure **Cognitive:** - Evident delays in cognitive development
Late Non-Ambulatory (15+)	**Skeletal:** - Function is similar to Early Non-Ambulatory phase **Cardiac/Respiratory:** - Heart and respiratory issues become more prevalent and life-threatening - Ultimate cause of death is due to cardiac and pulmonary complications **Cognitive:** - Function is similar to Early Non-Ambulatory phase

2.1.3 Current Therapeutic Strategies

Current therapeutic strategies for DMD can be categorized into two groups: 1. Strategies targeting the primary defect – a lack of dystrophin and 2. approaches to mitigate secondary and downstream pathological mechanisms – the cellular defects that result from a lack of dystrophin. Therapies

designed to restore dystrophin expression are complex in nature and involve either the read-through of the premature termination codon, exon skipping or vector mediated gene therapy. In recent years, great advancements in gene based therapies have been made such that there are currently twelve different compounds in various stages of clinical trials (for comprehensive reviews see [8, 46]). Of these approaches, read-through and exon skipping therapies have been in the forefront of development in recent years. Specifically, Ataluren, involving read-through technology is involved in four separate phase 3 clinical trials and has conditional approval in Europe while Eteplirsen, which skips exon 51, is in phase 2/3 clinical trials and has conditional approval for use in the United States [8]. In general, despite promising results in rodents, most compounds targeting the lack of dystrophin have demonstrated non-significant improvements in functional parameters when administered to patients in clinical trials [46, 8]. Furthermore, given the wide range of sites and types of mutations that exist amongst patients, each compound targets a very limited population of patients in terms of the genetic defect it addresses. Indeed, while Eteplirsen has provided positive results, it's therapeutic target is only beneficial in approximately 13% of patients [47]. As such, while targeting the primary defect will ultimately be the cure for DMD, current administered therapies target the downstream cellular defects that result from a lack of dystrophin.

The current standard of care for patients with DMD is the chronic administration of glucocorticoids, which target inflammation, a secondary pathology in DMD [48]. The first noted benefits of short-term glucocorticoid administration dates back to 1989 where a randomized clinical trial demonstrated improved strength, timed functional tests (time to stand, time to walk 9m, time to climb 4 stairs) and forced vital capacity following treatment with prednisone [49]. A more recent Cochrane Review concluded that there is evidence to support improvements in muscle

strength or function, or both, through the use of glucocorticoids for up to two years [7]. Furthermore, chronic administration of glucocorticoids (1 year or longer) resulted in an increased median age of loss of mobility as well as extended life span relative to those who were treated for one month of less [48]. Despite these positive results, use of glucocorticoids in treatment plans remain variable amongst physicians, likely due to the myriad of negative side effects that occur, particularly as a result of long term administration [50]. Indeed, clinically adverse effects include weight gain, cushingoid symptoms, insulin resistance or diabetes, osteopenia and risk of bone fractures, cataracts as well as behavioral side effects [48, 7]. Despite these negative side effects, to date, glucocorticoid treatment is the best option as limited success has been found when targeting the primary defect.

2.1.4 Animal Models of DMD

Both naturally occurring and laboratory-generated animal models exist to study the pathophysiology of DMD. Please see **Table 2.2** for a comparison of the most commonly used rodent models.

2.1.4.1 Rodent Models of DMD

As of 2015, there were over 60 animal models of DMD available for study yet the most commonly used remains the *mdx* mouse. Discovered in 1984, when a colony of C57BL/10ScSn mice showed severely elevated levels of serum creatine kinase, a hallmark phenotype of DMD, these animals were found to have a nonsense point mutation in exon 23 resulting in full deletion of the dystrophin gene [51]. Despite being dystrophin deficient, this rodent model displays minimal clinical symptoms and lifespan is only reduced by about 25%, contrary to the 75% reduction experienced in patients with DMD (**Table 2.2**) [52]. Disease progression in *mdx* mice occurs in several distinct phases; in the first 2 weeks, muscle is undistinguishable from that of healthy mice yet from weeks 2-4, muscle undergoes a high degree of necrosis, triggering the start of a highly active regenerative

phase. During this regenerative phase, *mdx* limb muscles often become hypertrophic and muscle function actually improves, while the diaphragm shows progressive degeneration as seen in patients with DMD [53]. The severe dystrophic phenotype does not present until mice are 15 months or older [52, 54, 55]. As such, the *mdx* mouse has been crossed with several different genetic backgrounds in an attempt to eliminate the compensatory mechanisms that prevent this model from developing clinical symptoms of DMD. While there are countless models being reported (for a complete review see [52], Supplementary Table 1), the majority arise from the crossing of the *mdx* mouse with another model designed to worsen the DMD myopathy, with two models of note in recent years, the Utrophin-Dystrophin double knockout (*dko*) and the DBA/2-*mdx* (D2.*mdx*).

The *dko* mouse lacks utrophin, which is shown to be upregulated in *mdx* mice as a compensatory response to a lack of dystrophin. Indeed, within the *mdx* model, muscles with the greatest upregulation of utrophin demonstrate the least pathological changes [56]. *Dko* mice have a markedly reduced life span (4-20 weeks), pronounced muscle weakness and impaired growth beginning at weaning. Muscle damage is similar to that of the *mdx* mouse from 2-6 weeks but remains severe throughout lifespan in contrast to the improvements seen in the *mdx* model [57]. This rodent model resembles disease progression and phenotype of patients with DMD and offers an alternative model to the *mdx* mouse. However, these animals often die prematurely and importantly, unlike in patients with DMD, carry an extra mutation that is not affected in humans. In fact, utrophin overexpression is currently being explored as a potential therapeutic target in DMD and as such, makes findings from this model difficult to interpret in the context of human disease [58].

The D2.*mdx* mouse model is a relatively new strain of mouse used to study DMD. These animals are a cross between the classic *mdx* mouse and the DBA/2J background, which, due to the deletion of latent TGF-B-binding protein 4 gene, demonstrates increased proteolysis, fibrosis, and inflammation as well as decreased self-renewal efficacy of satellite cells, preventing the robust regeneration seen in the classic *mdx* model [59]. D2.*mdx* mice demonstrate significantly decreased body mass and individual muscle mass relative to both wildtype and *mdx* counterparts. These animals also display elevated fibrosis, fat accumulation and loss of individual myofibers relative to *mdx* mice. Finally, this model exhibits impaired muscle function relative to WT controls at a time point where *mdx* mice show no decrements to function [60, 59]. Despite mimicking human disease progression more accurately, to date, there are limited studies published using this new model of DMD.

2.1.4.2 Canine Models of DMD

Dystrophin deficiency has been reported in approximately 20 different dog breeds and generally, the clinical phenotype of canine DMD (cDMD) is considered the best match to human disease. Additionally, given the size of this species, cDMD models are viewed as a way to bridge the gap between rodent research and application of therapies in humans particularly in the context of gene therapy [52]. Golden retriever muscular dystrophy dogs, which have a point mutation at intron 6 resulting in the skipping of exon 7, are the most commonly used model with colonies existing across the USA, France, Brazil and Australia. These dogs share a very similar time course of disease progression to that of boys with DMD including muscle weakness and exercise intolerance occurring around 2-3 months of age (equivalent to three years in humans) as well as muscle atrophy, limb fibrosis, abnormal gait and cardiomyopathy by six months of age [61]. However, despite the early onset of clinical symptoms, cDMD animals never fully lose ambulation, unlike boys with DMD but do on average, also see a 75% reduction in life span. It should be noted that

disease manifestation is not heterogenic amongst dogs, though this is similar to disease in boys wherein there is variation in clinical symptoms despite all patients lacking dystrophin [61, 57].

Table 2-2: Comparison of commonly used animal models of DMD. Adapted from [52, 57, 59, 60, 62].

	Rodent Models				
	mdx	**utr/mdx$^{-/-}$**	**D2.*mdx***	**cDMD**	**Human**
General					
Genetic Defect	Nonsense point mutation in exon 23	Nonsense point mutation in exon 23	Nonsense point mutation in exon 23	Point mutation at exon 7	See section 2.1.2
Lifespan	Reduced by 20-25%	Reduced by 95%	No Data	Reduced by 75%	Reduced by 75%
Body Weight	Increases after 8 weeks; reduced by 25% after 6 months	Reduced at time points ≥ 4 weeks of age	Reduced at time points ≥ 4 weeks of age	Reduced at all ages	Reduced at all ages past birth
Manifestation of Clinical Symptoms	2-4 weeks; followed by a stable phase due to robust regeneration; severe muscle wasting and loss of function become evident at ≥ 15 months	At birth	4 weeks (no data prior to this time point)	Birth-3 months	2-4 years
Loss of Ambulation	Rarely occurs	Rarely occurs	Rarely occurs	Rarely occurs	Common by early teens
First evidence of cardiomyopathy	10 - 20 months. 10 months = abnormalities in echocardiography 15-20 months = cardiac fibrosis	8 weeks	28 weeks	6 months	Mid-teens
Creatine Kinase Levels	Elevated	Elevated	Elevated	Elevated	Elevated
Histopathology					
Acute Necrosis	3-4 weeks	As early as 2 weeks	No Data	none	none
Limb Muscle Fibrosis	Minimal in adult mice	Extensive throughout lifespan	Extensive in adult mice, earlier time points unknown	Extensive throughout lifespan	Extensive throughout lifespan
Muscle Regeneration	Robust	Robust	Poor	Poor	Poor

2.2 Primary Pathologic Outcomes in DMD

2.2.1 Skeletal Muscle Wasting

Duchenne muscular dystrophy is characterized by severe muscle wasting with limb skeletal muscle being the earliest target of the disease. In patients with DMD, muscle biopsies reveal necrotic muscle fibres, often in clusters, surrounded by macrophages and lymphocytes, indicative of muscle degeneration and an inflammatory response. At the early stages of this disease, necrotic fibres are accompanied by centrally located nuclei, indicative of regeneration that matches the degree of degeneration [54]. However, the stem cell pool in humans is limited and within a short period of time, regenerative capabilities within the muscle become exhausted, resulting in the infiltration of fibrotic and adipose tissue.

Despite a homogenous absence of dystrophin within patients with DMD, disease progression is heterogeneous across skeletal muscles. Firstly, it has been demonstrated that fast twitch fibres, particularly IIB, are the earliest target of muscle degeneration with type I fibres being affected at later stages of the disease [63]. Indeed, by 5 years of age, IIB fibres are virtually absent in biopsy samples from patients with DMD [64].While the exact reason for this preferential degradation of fast twitch fibres is unknown, it has been hypothesized that the faster contraction of IIB fibres results in greater mechanical stress. Furthermore, as muscle wasting occurs, the remaining muscle fibres must compensate and as such, the shift to a greater proportion of type I fibres could be viewed as an adaptation to the increased load, similar to the adaptions that occur in response to endurance training in healthy individuals [63, 64]. Secondly, and perhaps most interesting, specific muscles within the body are completely spared of muscle wasting. Extraocular muscles, which are responsible for the most rapid eye movements known as saccades, are believed to closely mimic fibre type and function of type IIB fibres in the extremities, yet are found to function within 95% of the range of healthy individuals, even in the late stages of DMD disease progression [65]. This

suggests that extraocular muscles possess features that allow these fibres to resist degeneration. Karpati and colleagues proposed the small diameter of these fibres protects against mechanical stress due to the high surface to volume ratio that exists in these muscles [66]. While the exact mechanism of this protection remains to be elucidated, understanding how these fibres are spared could provide a potential treatment option for patients with DMD.

Patients with DMD also undergo selective muscle hypertrophy, which is somewhat counterintuitive given the severity of muscle wasting that occurs in the disease. Indeed, calf hypertrophy is seen as a hallmark phenotype of patients with DMD. Additionally, at early stages of this disease, multiple reports of quadriceps hypertrophy exist within the literature yet this increase in fibre diameter occurs at a young age only, as atrophy of the vastus lateralis develops by the age of 7 or 8 [67, 68]. At this same young age, calf hypertrophy is at its peak with diameter values reaching twice the normal range, however the degree of hypertrophy decreases with age, despite values always exceeding normal. It has been proposed that this calf hypertrophy is due to postural abnormalities while patients with DMD are ambulatory. Patients with DMD are known to walk on their toes, which increases the power required from the calf. This increase in workload is likely the cause of fibre hypertrophy which explains the plateau of fibre diameter increases as patients age and become wheelchair bound [68, 67]. True hypertrophy is defined as an increase in the number/or size of individual muscle fibres within a given muscle, without the concomitant increase of connective tissue. Alternatively, psuedohypertrophy is defined as the infiltration of a muscle with collagen, fat, tumour, inflammatory cells and/or amyloidosis [67]. Early work by Cros and colleagues revealed that while the gastrocnemius-soleus complex appears to be unanimously hypertrophied in patients with DMD, this is a case of psuedohypertrophy. Indeed, despite increased fibre diameter relative to normal values, 18-38% of the gastrocnemius contained fat and connective

tissue, a significantly higher contribution compared to the 8% average found in healthy muscle [67]. Therefore, while compensatory hypertrophy within the calf is occurring, there is also a significant degree of muscle wasting exhibited as well.

Ultimately, skeletal muscle wasting results in the loss of ambulation by the mid teenage years. This includes an inability to walk or lift/carry items. While quality of life is significantly impacted by the loss of skeletal muscle function the ultimate cause of death for patients with DMD is due to cardiac and/or respiratory failure.

2.2.2 Respiratory Failure

In patients with DMD, respiratory weakness does not manifest until the second decade of life [69] despite the early onset of degeneration of the diaphragm [53]. However, once this weakness manifests, a progressive loss in respiratory capacity is evident. In the *mdx* mouse, diaphragm strength is reduced to 13.5% and the proportion of type I fibres has doubled in relation to age matched controls by the late stages of disease [53]. Within patients with DMD, as pulmonary function declines, the risk for bronchopulmonary illness as well as hypoventilation and dependence on ventilatory support increases. The greatest decline in respiratory function occurs between the ages of 10 and 18 (**Figure 2.2**), beginning with increases in residual volume (RV) and decreases in expiratory reserve volume (ERV), the amount of air that remains in the lungs after fully exhaling and the additional amount of air that can be expired from the lungs by determined effort after normal expiration respectively. This ultimately leads to a decline in total lung capacity (TLC) by the age of 17 [70, 69, 5].

While respiratory failure remains a leading cause of death in patients with DMD, recent advances in treatment options including nocturnal noninvasive home ventilation have improved survival rates of patients with DMD. A meta-analysis from the UK revealed 53% of patients survive past

the age of 25 when provided with home ventilation options whereas this number drops to 12% when patients were non-ventilated with a mean age of survival of just 19.3 years [71]. Despite these clear benefits, home nocturnal ventilation is not routinely offered given the remaining ethical uncertainties surrounding this treatment, particularly in the context of quality of life.

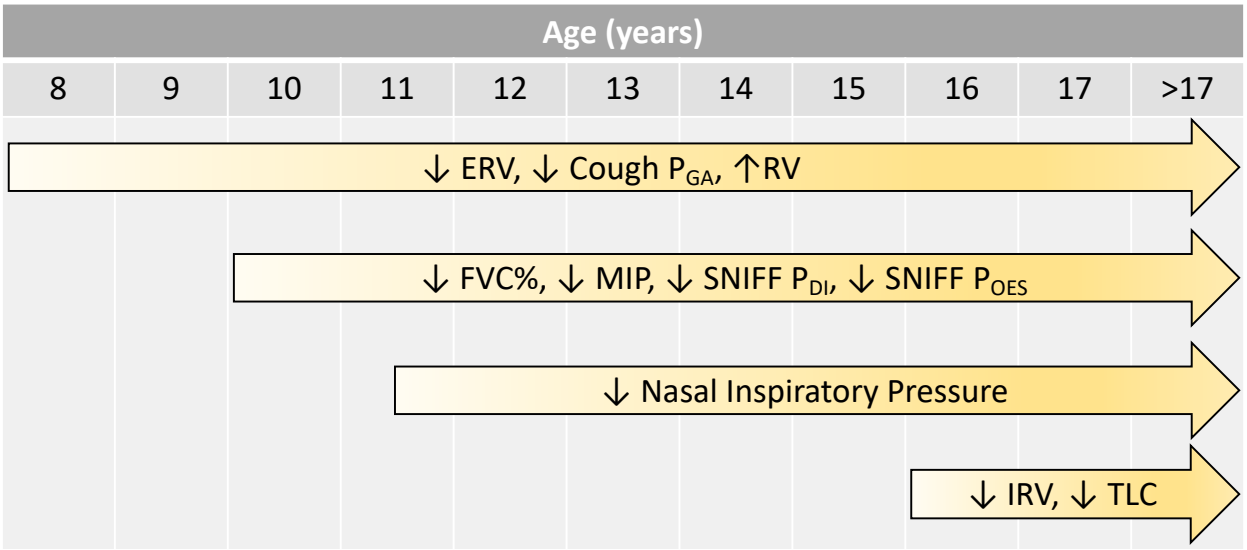

Figure 2-2: Time course of decline in respiratory capacity in patients with DMD. Schematic representation summarizing the decline in respiratory capacity based on numerous pulmonary functional measurements. ↑represents an increase in measurement, ↓ represents a decrease in measurement. **ERV:** expiratory reserve volume; **Cough P_{GA}:** abdominal gastric pressure during cough; **RV:** residual volume; **FVC%;** forced vital capacity; **MIP;** maximal static inspiratory pressure; **SNIFF P_{DI}:** trans diaphragmatic pressure during a sniff; **SNIFF P_{OES}:** esophageal pressure during a sniff; **IRV:** inspiratory reserve volume; **TLC:** total lung capacity. Adapted from [70].

Given that respiratory muscles are considered skeletal muscles, muscle training in an attempt to improve strength and endurance is also considered as a form of therapy. Specifically, inspiratory muscle training though resistive breathing targets the diaphragm and improves endurance and strength within this muscle which coincides with improvements in Sniff P_{DI} and Sniff P_{OES}. However, once patients with DMD reach a certain threshold of disease progression, muscle training no longer becomes effective and may in fact exacerbate the muscle wasting process [70]. At the pharmacological level, there is currently no form of treatment aimed specifically at

preserving respiratory function. The previously mentioned glucocorticoids (see section *2.1.3 Current Therapeutic Strategies*), whose predominant role is to slow down skeletal muscle weakness by targeting inflammation, have been suggested to also affect respiratory function. In recent years, treatment with glucocorticoids has continued in patients past the point of loss of ambulation although results have been divergent. Some studies have reported no benefit of steroid use on respiratory function [72, 73] while others have reported improvements in parameters such as forced vital capacity (FVC) [74], maximal expiratory pressure (MEP) and spirometry [75, 76]. Given the myriad of negative side effects associated with long term administration of glucocorticoids, current clinical standard of care does not involve the use of these steroids past loss of ambulation. As such, respiratory function remains a primary concern for patients with DMD.

2.2.3 Cardiomyopathy

While cardiomyopathy develops in 98% of patients with DMD, the age of onset varies considerably. As such, clinical guidelines recommend ECG evaluations every two years up to the age of ten followed by yearly assessments as boys age with the goal of preventing the onset of fatal heart failure [77]. During the preclinical stage (0-10 years) patients present with no classic signs of heart failure, yet cardiomyocyte hypertrophy as well as ECG abnormalities (diastolic dysfunction, sinus tachycardia) can be identified. During the clinical stage of the disease (10-18 years) while heart failure will still not be present in the majority of patients, cardiomyocyte atrophy, endocardial fibrosis and the progressive dilation of heart chambers is evident. Finally, during late stages of life (18+ years), 60% of patients will exhibit symptoms of heart failure while almost all patients will demonstrate diastolic dysfunction, dilated cardiomyopathy and arrhythmic complications [4, 78, 77]. This heart failure will be the ultimate cause of death in 40% of patients [37, 43]. Unfortunately, the mechanisms underlying heart failure in DMD remain poorly

understood and as such, current therapeutic approaches aim to treat the cardiomyopathy itself, rather than the cause of the myopathy within these patients [4].

2.3 Secondary Pathophysiologic Responses in DMD

2.3.1 Impaired Calcium Handling

Dating back to 1978, the calcium (Ca^{2+}) hypothesis of DMD suggests that chronic Ca^{2+} overload may play a role in muscle fibre degeneration as a result of the disruption to the cytoskeletal network that occurs in the absence of dystrophin [10]. Specifically, a lack of dystrophin results in the destabilization of the linkage between actin of the cytoskeleton and laminin of the extracellular matrix (**Figure 2.1**) resulting in a loss of integrity of the sarcolemma [11]. During stretch contraction, dystrophic fibres undergo micro tearing of the sarcolemma, requiring a Ca^{2+} dependent resealing process at the site of the tears. The influx of extracellular Ca^{2+} initiates a cytotoxic event that produces patches to seal the leaky cell membrane. These newly formed patches contain Ca^{2+} channels, which promote the influx of Ca^{2+} into the cytoplasm of the fibre [79].

There are several pathological consequences resulting from the increase in [Ca^{2+}] within the cytoplasm. Firstly, Ca^{2+}-dependent proteases, known as calpains are activated which promote the degradation of proteins within the muscle fibre, leading to necrosis (**Figure 2.4**) [80, 81]. Additionally, this proteolytic activity further activates Ca^{2+} leak channels, which promotes more protease activity, thereby forming a damaging cycle of continuous protein degradation [79]. Indeed, increased calpain activity in *mdx* mice has been reported during both periods of muscle degeneration and regeneration and furthermore, the use of a calpain inhibitor reduced degeneration and necrosis by up to 50% [82].

Secondly, cytosolic Ca^{2+} overload requires redistribution into other organelles, mainly the sarcoplasmic reticulum (SR) and the mitochondria [83]. Unfortunately, issues with Ca^{2+} buffering

by the SR have consistently been reported [84-86]. SR Ca^{2+} ATPase (SERCA) is responsible for the uptake of Ca^{2+} during relaxation as well as the release of Ca^{2+} for muscle contraction and is believed to account for about 70% of Ca^{2+} removal from the cytoplasm [87]. Decreased SERCA activity [84-86, 88] as well as a decrease in the binding capacity of calsequestrin [89], the protein responsible for Ca^{2+} sequestering within the lumen of the SR, have been reported in DMD. Furthermore, overexpression of SERCA or the stabilization of SERCA activity [90-92] have improved the DMD pathology, further indicating impairments in the function of SERCA as a Ca^{2+} buffer within dystrophic muscle. This leaves the mitochondria to act as the predominant Ca^{2+} sink (see *2.4.3.1 Mitochondrial* Ca^{2+} *Handling*) which can result in further decrements to cell function (see *2.4.3 Mitochondrial Induced Cell Death*). Finally, this increase in cytosolic Ca^{2+} can stimulate the production of ROS from both mitochondrial and non-mitochondrial sources which results in whole cell oxidative stress, another potential trigger of cell death (**Figure 2.4)** [93, 82, 94].

2.3.2 Oxidative Stress

2.3.2.1 Oxidative Stress Overview

Oxidative stress occurs when the production of oxidants results in either macromolecular damage (protein carbonylation, lipid peroxidation, DNA oxidation) or the disruption of thiol redox circuits leading to dysfunctional cell signaling [95]. Oxidants are produced in the form of free radicals and non-radical oxidants, namely reactive oxygen species (ROS) and reactive nitrogen species (RNS) with the predominant initial forms being superoxide ($O_2\bullet$-) and nitric oxide (NO) respectively [96]. Superoxide is generated through either the incomplete reduction of oxygen in the electron transport chain (see *2.4.2 mitochondrial reactive oxygen species production*) or as a specific product of enzymatic systems (NADPH Oxidase, Xanthine Oxidase), whereas NO is generated through enzymatic reactions. Both $O_2\bullet$- and NO can react to form a series of other ROS and RNS which act as the primary signaling molecules within the cell [97]. While NO is an important signaling

molecule in skeletal muscle, for simplicity sake, this literature review will focus solely on ROS signaling in DMD given the specific relevance to the presented data.

Catalyzed by superoxide dismutase, $O_2\bullet$- reacts with itself and two protons (H^+) to form hydrogen peroxide (H_2O_2) and oxygen (**Figure 2.3**). H_2O_2 is a nonradical oxidant that plays an important role in redox signaling [95]. While the fate of most $O_2\bullet$- is the dismutation into H_2O_2, $O_2\bullet$- itself an also act as a redox signal and is the primary driver of the aforementioned macromolecular damage [98]. $O_2\bullet$- is highly reactive with iron containing proteins and is known to partake in chain reactions whereby the initiation of a reaction with a single $O_2\bullet$- molecule can cause a chain reaction resulting in damage to multiple molecules [95]. This is the case in lipid peroxidation, a well characterized component of disease pathology in the late stages of DMD [14], wherein polyunsaturated fatty acids found in the cell membrane are oxidized through $O_2\bullet$- chain reactions in the presence of O_2 and trace metal ions [95]. This results in further damage to an already fragile cell membrane in DMD. However, the network of intercellular antioxidant enzymes, including superoxide dismutase (SOD), catalase (CAT), glutathione (GSH), glutathione peroxidase (GPX), glutathione reductase (GR) and thioredoxin reductase (TRX) (**Figure 2.3**) are in high abundance in biological systems and can largely prevent these chain reactions from occurring. As such, any macromolecular damage is usually a result of single initiation events by $O_2\bullet$- and even then, free radical intermediates quantitatively play a very small role in overall cellular oxidative stress given their high reactivity and short half-life [95, 98]. As such, nonradical oxidants are the predominant contributors to oxidative stress through their ability to alter redox signaling.

H_2O_2 is believed to be produced at 1-4% of the rate of O_2 consumption and therefore represents a major source of oxidants within the cell [95]. This nonradical oxidant signals through the reversible modification of proteins, predominately thiols on exposed cysteines, thereby altering their function

[98]. Furthermore, H_2O_2 can act as a redox signal indirectly through redox couples within the antioxidant system including glutathione and thioredoxin. H_2O_2, like free radicals, is toxic to cells and therefore it's concentration is tightly regulated *in vivo* (**Figure 2.3**) [98]. In the context of DMD, macromolecular damage is well quantified while the influence of non-radical oxidants on redox signaling within dystrophic tissue has garnered far less attention. Given the need for identifying novel therapeutic targets, understanding the sources of oxidants and their cellular targets is of great necessity.

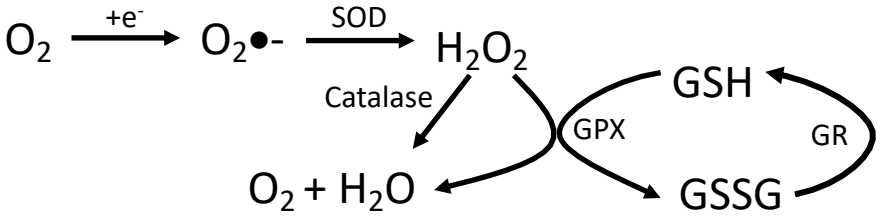

Figure 2-3: Schematic of the glutathione antioxidant defense system. When oxygen combines with a free electron, a superoxide radical is formed. Superoxide is then dismutated by superoxide dismutase into hydrogen peroxide (H_2O_2). H_2O_2 can be degraded to water and oxygen by the enzyme catalase or through the coupled oxidation of glutathione (GSH->GSSG) catalyzed by glutathione peroxidase (GPX). The oxidized glutathione (GSSG) must then be reduced by glutathione reductase to reform GSH.

2.3.2.2 Evidence of ROS-induced Damage in DMD

Throughout decades of research, excessive ROS production has been proposed as a possible mediator of muscle damage in dystrophic tissue. DMD was actually recognized as a disease of elevated oxidative stress before the cause of this condition (dystrophin, or lack thereof) was even discovered. Indeed, early researchers established similarities between muscle pathology in DMD and the pathology associated with Vitamin E deficiency as well as ischemia reperfusion, two conditions in which oxidative damage is an established contributor to the pathogenesis [12, 13]. Analysis of biopsies from patients with DMD show evidence of oxidative stress through the presence of a two-fold increase in protein carbonylation [18] as well as lipid peroxidation [99] two

previously mentioned forms of irreversible oxidative damage. These findings have been replicated in rodent models of DMD [14-17] along with reports of increased glutathione peroxidase activity [14, 19, 20] and increased levels of total glutathione [17, 20, 21]. At a functional level, work by Rando et al. revealed that dystrophic muscle is more susceptible to ROS-induced damage, in that myotubes from *mdx* mice underwent cell death in the presence of much lower concentrations of ROS relative to WT myotubes [100]. A second separate study showed that *mdx* mice were more susceptible to oxidative stress-induced cell death than myotubes expressing a truncated version of dystrophin (mimicking Becker's MD), which in turn, were more susceptible to cell death than myotubes expressing full length dystrophin [16]. These findings collectively demonstrate that the susceptibility to ROS-induced cell death is positively correlated with dystrophic severity and furthermore, that there is a direct link between dystrophin and sensitivity to oxidative damage. In addition, evidence of increased ROS production causing lipid peroxidation and a compensatory increase in antioxidant enzymes was found in young *mdx* mice (19 days of age) prior to the presence of any necrosis, indicating that ROS may be a primary cause of muscle degeneration as opposed to a secondary response to muscle breakdown [16]. This is further supported by the notion that muscles that are spared in DMD (see section 2.2.1 *Skeletal Muscle Wastin*g*)* have higher concentrations of antioxidant enzymes than the most susceptible muscles (type IIB fibres) [101] and that type IIB fibres have lower levels of glutathione peroxidase than all other fibre types [20] rendering them more susceptible to ROS-induced damage given their less robust antioxidant defense system.

2.3.2.3 Antioxidant Clinical Trials in DMD

A myriad of antioxidants have been tested in rodent models of DMD. Early work in an avian model of DMD tested both Penicillamine, a sulfhydryl compound with antioxidant properties and vitamin E, reporting modest benefits including the slowing of degeneration in avian skeletal muscle [102,

103]. Additionally, a low-iron diet, which reduces the production of hydroxyl radicals resulted in a decrease in necrosis in the *mdx* mouse [104]. More recently, several membrane permeable antioxidants have been tested in young *mdx* mice with varied success. While most antioxidants provided benefit at the histopathologic level, in most cases, minimal changes in muscle function were reported [105-110]. For example, the most widely used and potentially most promising antioxidant to date, n-acetylcysteine (NAC), has been shown to improve the dystrophic pathology in terms of markers of necrosis, muscle degeneration and inflammation following oral administration [111-114]. Only one study to date has assessed muscle strength following the oral administration of NAC and found that while force production was increased in *mdx* mice, NAC significantly reduced body weight gain and muscle weight gain in both healthy and dystrophic animals and therefore should be used with caution in the context of patients with DMD [115].

Based on the early findings of elevated oxidative stress, several clinical trials using various antioxidants were also carried but ended with overall disappointing results. The use of superoxide dismutase, Vitamin E, penicillamine, and ascorbate (vitamin C) all resulted in minimal clinical benefits [116-119, 96, 120]. In retrospect, these early clinical studies (1954-1988) involved patients with advanced muscle degeneration (average age ≥ 10 years). Based on the theory that oxidative stress is a primary cause of cell death and the use of antioxidants would prevent this cell death from occurring, clinical trials need to be initiated early in disease progression with the ultimate goal of this therapeutic target being to slow the progression of muscle degeneration not reverse the loss of muscle [96, 82, 121]. Additionally, all antioxidants tested to date are classified as non-specific scavengers, meaning they are 1. untargeted within the cell and 2. their mechanism of action involves scavenging already produced ROS as opposed to targeting the source of the elevated ROS production. In recent years it has been proposed that the specificity of ROS, the

spatial source of the oxidants and the timing of treatment should all be controlled when assessing the efficacy of antioxidants in the prevention of disease progression in DMD and more specifically, antioxidant treatments should be targeted to a specific source and initiated very early in disease progression [122].

2.3.2.4 Mechanisms of elevated ROS in DMD

While there is extensive evidence supporting the presence of elevated oxidative stress in DMD in both human and animal models as well as an established contribution of oxidative stress to disease pathology in animals, the specific source(s) of the elevated oxidative stress remain somewhat controversial.

As previously mentioned, DMD is a disease of membrane fragility and impaired Ca^{2+} handling, two distinct pathological features that can both be caused by, and result in, elevated ROS production (**Figure 2-4**). Firstly, ROS have been shown to play an important role in the increased membrane permeability in DMD. Following eccentric contractions in the EDL of *mdx* mice, Evan's Blue Dye (EBD) uptake, which signifies membrane damage, was significantly increased relative to WT controls while treatment with the antioxidant NAC prevented this dye uptake [111]. Similarly, treatment with ascorbic acid, another free radical scavenger, reduced EBD uptake and serum creatine kinase levels [123]. Additionally, ROS have been shown to directly stimulate Ca^{2+} entry into the cell both basally and following a stretch contraction [124]. Taken together, these results suggest that elevated ROS production plays a role in increased membrane permeability which subsequently leads to Ca^{2+} overload within the cell. In turn, Ca^{2+} overload within the cell can lead to ROS production, further amplifying the production of ROS, thus establishing another intracellular positive feedback loop for damaging Ca^{2+} and ROS signals [93]. Work by Shrykl et al., demonstrated this reciprocal amplification of ROS and Ca^{2+} signals and interestingly,

identified divergent sources of ROS responsible for different oxidative events. Specifically, in flexor digitorium brevis (FDB) fibres from *mdx* mice, basal levels of ROS were higher relative to WT, and following osmotic shock, which simulates mechanical stress, Ca^{2+} influx was significantly increased, along with an increase in ROS production in *mdx* muscle [121]. Basal levels of ROS appeared to be NOX specific, while post osmotic stress, mitochondrial accumulation of Ca^{2+} was significantly increased and was accompanied by an increase in mitochondrial ROS production. This signifies the potential of source specific increases in ROS production, dependent upon the activity level of the muscle [125].

NADPH Oxidase, and specifically the isoform NOX2, has garnered particular interest in recent years as being a predominant source of ROS in DMD. NOX was first identified in inflammatory cells and more recently, subunits were found in close proximity to the sarcolemma of muscle fibres [126]. In dystrophic tissue, increased NOX activity as well as increased expression of NOX subunits has been reported [127-129]. Furthermore, blocking NOX2 activity using various NOX inhibitors results in a decrease in Ca^{2+} influx and improved force production in *mdx* muscle following a stretch contraction [121, 130]. Therefore, it is believed that elevated NOX activity results in an increase in ROS production that increases membrane permeability causing Ca^{2+} influx. However, the source of the subsequent burst of ROS that occurs in response to this Ca^{2+} influx remains unknown.

It is well established that abnormal uptake of Ca^{2+} by the mitochondria results in an increase in ROS production via the electron transport chain. Therefore, it is plausible to believe that the mitochondria are a source of elevated ROS in DMD given the known impairments in Ca^{2+} associated with this disease. The mitochondria as a source of ROS will be discussed in greater detail in section *2.5.2 Mitochondrial ROS Production*.

2.3.3 Inflammation

Completing the triad of cellular pathologies contributing to muscle wasting in DMD is inflammation. In fact, inflammation is the therapeutic target of corticosteroids, the current standard of care for patients with DMD (see *2.1.3 Current Therapeutic Strategies*). Inflammation is an early event in the pathological process of DMD with the first signs of inflammation and cell death occurring at 3-4 weeks of age in *mdx* mice and is believed to a be a key contributor to muscle cell death in dystrophic tissue [131]. The inflammatory process in dystrophic muscle involves the invasion of innate immune cells into sites of muscle damage, characteristic of chronic damage and repair cycles [122]. However, due to the chronic nature of muscle damage in DMD, repair cycles inevitably become exhausted, resulting in the infiltration of fibrotic tissue. Identified through histological observations, the predominant immune cells infiltrating dystrophic muscle include macrophages, t-cells and eosinophils and are believed to play an important role in the accumulation of fibrotic tissue in dystrophic muscle through their role in degeneration, necrosis and apoptosis [131]. Specifically, when knocking out T-cells from *mdx* mice, the degree of apoptosis and necrosis was decreased [132] while the onset of fibrosis was significantly delayed [133]. Furthermore, the depletion of macrophages, $CD4^+$ and $CD8^+$ cells ameliorated muscle histopathology and increased regeneration in young (3-4 week) *mdx* mice [132, 134, 135].

While the exact mechanisms remain unknown, it is proposed that these immune cells mediate the progression of DMD through the stimulation of the translocation of NF-κB to the nucleus, which regulates the expression of pro-inflammatory cytokines including TNFα and Il-1β [136]. In 15-day old *mdx* mice, there is evidence of elevated NF-κB DNA binding activity as well as elevated expression of TNFα and Il-1β at a time point that precedes the onset of muscle wasting [137]. Furthermore, genetic manipulation or pharmacological blockade of NF-κB improves the

dystrophic phenotype in *mdx* skeletal muscle [107, 138, 139]. Finally, glucocorticoids, which are known to improve muscle strength and function, also decrease the expression of NF-κB.

NF-κB acting as the master regulator of inflammatory-mediated disease progression is an intriguing possibility, particularly given the finding that ROS are implicated in the activation of NF-κB in *mdx* muscle, as evidenced by the fact that NF-κB activation could be prevented by NAC [137]. As previously mentioned, NF-κB activation increases the expression of pro-inflammatory cytokines including TNFα, which is known to stimulate the production of mitochondrial ROS in a calcium-independent manner [140]. This could, once again, create a positive feedback loop whereby the increased ROS production via TNFα causes further activation of NF-κB with the end result being a chronic state of inflammation and subsequent muscle degeneration [82]. This idea is supported by reports of improvements in muscle necrosis and reduced inflammation in *mdx* mice injected with Remicade, an anti-TNFα antibody, although ROS levels were not evaluated in that work [141].

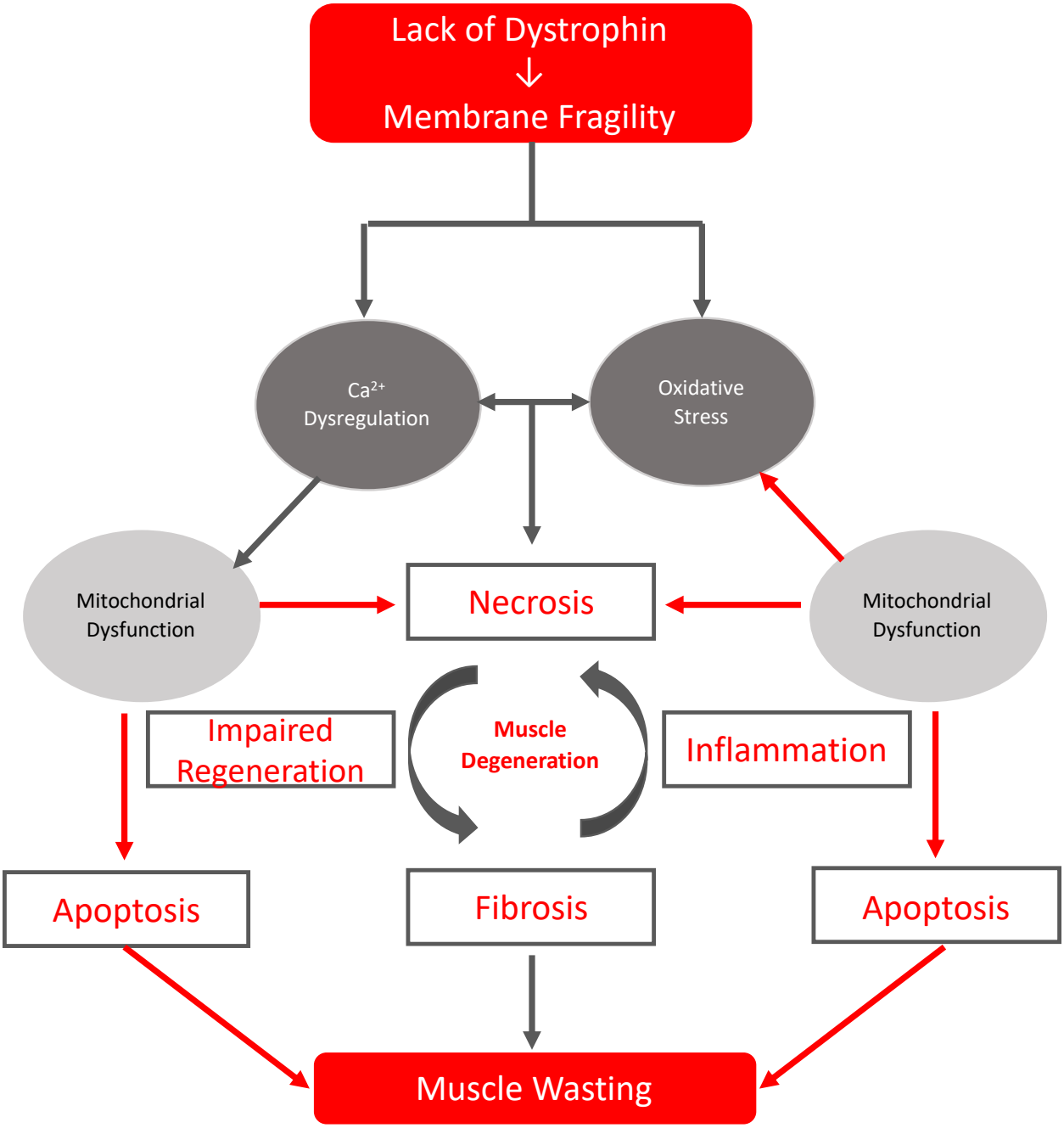

Figure 2-4: Overview of the pathophysiological consequences of dystrophin deficiency. A loss of dystrophin results in membrane fragility and subsequent tearing. Sarcolemmal tearing causes an influx of Ca^{2+} into the cytosol of dystrophic muscle fibres. This Ca^{2+} overload triggers oxidative stress via cytosolic sources as well as the uptake of Ca^{2+} by the mitochondria. Excessive Ca^{2+} uptake by the mitochondria can trigger both ROS production as well as the activation of cell death pathways which contribute to muscle wasting. Adapted from [46].

2.4 Introduction to Mitochondrial Bioenergetics

2.4.1 Oxidative Phosphorylation

Mitochondria are a double membrane structure, consisting of an ion permeant outer membrane (OMM), an intermembrane space rich with key physiological proteins and an inner mitochondrial membrane (IMM) that separates the mitochondrial matrix from the intermembrane space. Embedded within this IMM are proteins comprising the electron transport chain (ETC), a key component in mitochondrial energy transduction (**Figure 2.5a**). The ETC is made up of five protein complexes (I-V) and two mobile electron carriers, which together catalyze the 'downhill' transfer of electrons through a series of redox reactions that produce free energy [142]. The use of free energy in the production of ATP is based on a hypothesis proposed by eventual Nobel Prize winner Peter Mitchell in 1961 [143]. Known as the chemiosmotic theory of oxidative phosphorylation, it is used to explain how the energy produced from redox reactions can be coupled to ATP synthesis through the use of proton pumps in an energy transducing membrane, such as the IMM. Within the mitochondria, this energy is used to generate an electrochemical gradient by pumping protons from the negative side (matrix) to the positive side (intermembrane space), producing Δp (proton motive force). This Δp is sufficient to force the secondary pump, known as the ATP synthase, to reverse and synthesize ATP from ADP and P_i, powered by the flow of protons against the chemical gradient back into the matrix through complex V [144]. The coupling of the energy produced through oxidation of reducing equivalents and phosphorylation of ADP is known as oxidative phosphorylation (OXPHOS) and contributes 95% of the ATP produced within the cell under normal conditions [142].

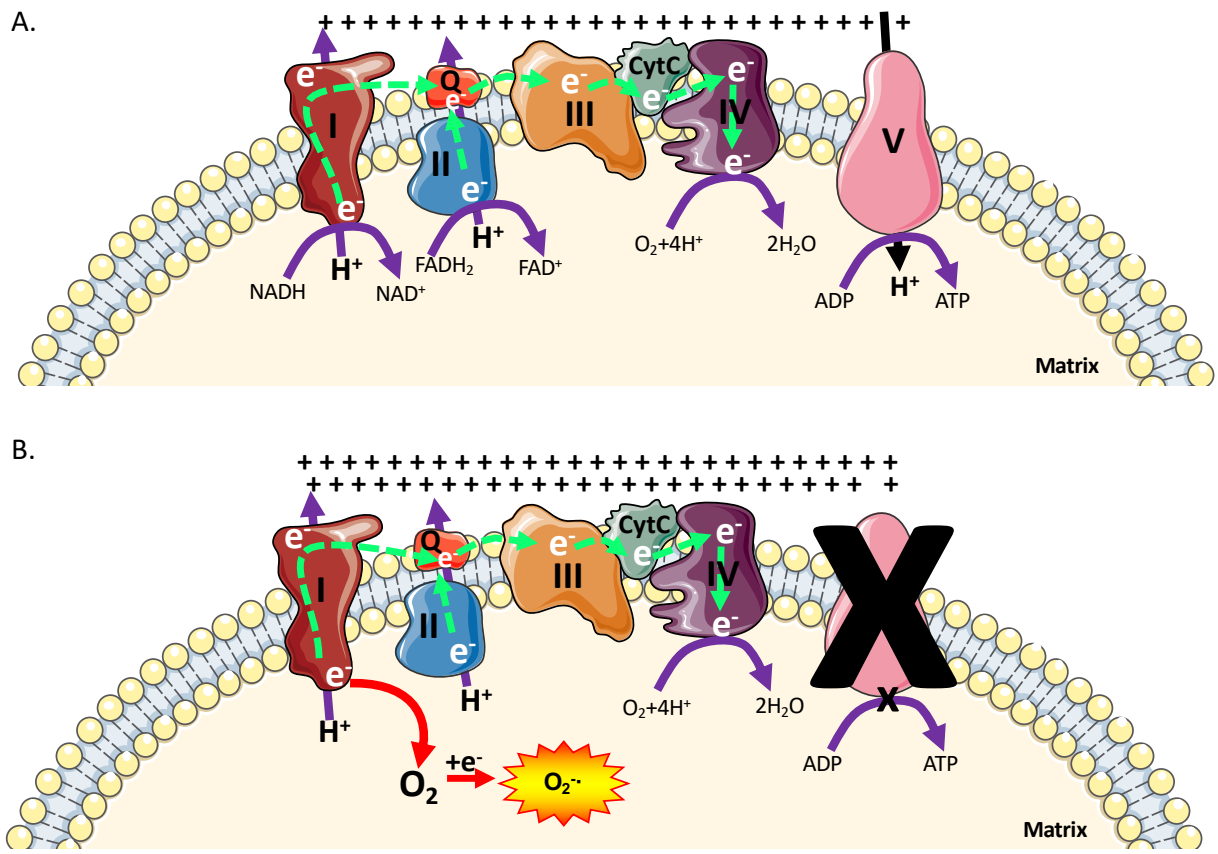

Figure 2-5: Schematic of the pillars of mitochondrial bioenergetics. The primary function of the mitochondria is to produce ATP through **A.** Oxidative phosphorylation. Embedded within the IMM, the ETC consists of five protein complexes (I-V) and two mobile electron carriers which catalyze the transfer of electrons downhill through redox reactions that release free energy. This free energy is used to pump protons from the mitochondrial matrix to intermembrane space, establishing an electrochemical gradient that can be used to power the phosphorylation of ADP to produce ATP at complex V. A natural by-product of oxidative phosphorylation is **B.** Reactive Oxygen Species Production. When the electrochemical gradient is established in the absence of ATP production, membrane potential rises. A high membrane potential promotes the slipping of electrons prior to complex IV where they combine with oxygen to form free radicals.

2.4.2 Mitochondrial Creatine Kinase

Creatine kinase (CK), an important enzyme in cellular energetics, is comprised of a system of isoenzymes strategically located at sites of oxidative phosphorylation (mitochondria, mtCK) and utilization (cytosolic, cCK) within the cell [145, 146]. CK catalyzes the reversible transfer of the phosphoryl group between PCr and ATP through the reaction: $MgADP^- + PCr^{2-} + H^+ \leftrightarrow$

$MgATP^{2-}$ + Cr. The most common and well accepted function of the CK system is to act as a "temporal energy buffer" maintaining high intracellular ATP/ADP ratios at the expense of PCr **[147].** cCK has been found to be bound to myofibrils and functionally coupled to myosin ATPase as well as Sarcoendoplasmic Ca^{2+} ATPase and Na,K-ATPase where it's main role is to maintain a high ATP/ADP ratio during periods of elevated activity [148]. More recently, the importance of mtCK in the movement of ADP and ATP between the cytosol and matrix has been establishe**d** [149, 150, 146]. mtCK has a strong affinity for acidic phospholipids, much like those comprising the IMM and OMM. In fact, mtCK directly binds to VDAC on the OMM and to cardiolipin of the IMM. Given the high abundance of ANT on the IMM, this affinity for cardiolipin results in contact sites between mtCK and ANT and a direct binding to VDAC [151-153]. These three proteins create a functional substrate channel within the mitochondria that allows for the efficient transport of energy into and out of the mitochondria (**Figure 2-6**). This channel is the key component in what is known as the creatine-dependent model of energy exchange. Specifically, as ATP is produced through OXPHOS, ANT shuttles this ATP into the intermembrane space. mtCK can trans-phosphorylate the phosphate group on ATP to Cr, producing ADP and PCr. This ADP can be shuttled back into the matrix through ANT to be used, once again, for the production of ATP through OXPHOS while PCr is shuttled out of the intermembrane space through VDAC until it comes in contact with cCK. cCK phosphorylates cytosolic ADP to produce ATP for the working muscle [147, 152, 154]. The high reliance on CK to facilitate the transfer of these high energy phosphates makes this model creatine-dependent and it is estimated that 80% of energy transfer occurs through this model of phosphate shuttling in cardiac muscle [146, 150]. Indeed, using spermatozoa, a species with a vast distance between the site of oxidative phosphorylation and site of energy utilization, it was established that PCr/Cr can overcome diffusion limitations

experienced by ATP/ADP, better meeting the demands of the working muscle [155, 147]. Specifically, PCr can diffuse at a rate seven times faster than ATP and Cr can diffuse at a rate 2000 times faster than ADP, further demonstrating the improved capability of energy transfer when mtCK plays an active role [147]. While this is the main pathway for energy exchange, it is important to note, ADP and ATP can also freely diffuse through ANT and VDAC (**Figure 2-6**), a model of energy exchange, which is creatine-independent in nature as mtCK is not involved in this transfer of energy.

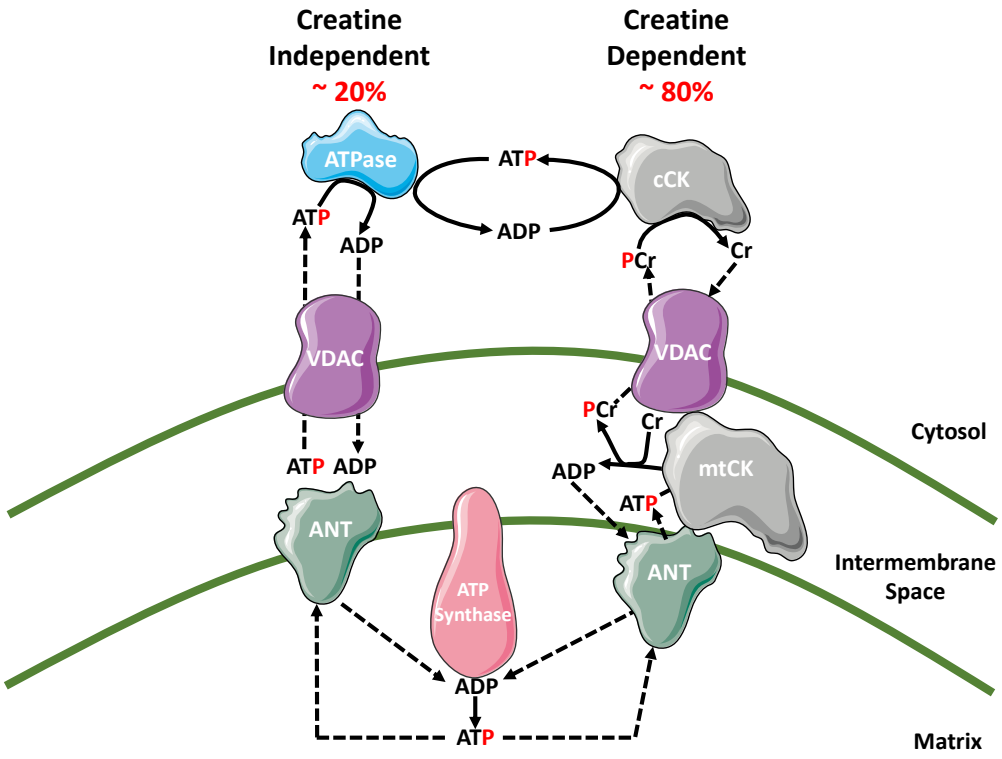

Figure 2-6: Schematic representation of energy transfer between mitochondria and cytosol. The leading model for energy exchange involves a creatine-independent (-Cr) and creatine-dependent (+Cr) pathway. The left side depicts the –Cr pathway whereby ADP/ATP transfer occurs solely through diffusion across voltage dependent anion carrier (VDAC) on the outer mitochondrial membrane and adenosine nucleotide translocase (ANT) on the inner mitochondrial membrane. The right side depicts the +Cr pathway where, in the presence of Cr, energy transfer is facilitated by mitochondrial creatine kinase (mtCK) through the transfer of the phosphate group from ATP to Cr, producing phosphocreatine (PCr) and ADP in the inner membrane space. The PCr is exported via VDAC into the cytosol while the ADP is directly recycled back via ANT into the mitochondrial matrix. This schematic is published as part of **Chapter 4 – Early myopathy in Duchenne muscular dystrophy is associated with elevated mitochondrial H_2O_2 emission**

during impaired oxidative phosphorylation [156]. Figure adapted from Aliev et al., 2011, Guzun et al., 2012, Myer et al., 1984 and Wallimann et al., 2011 [146, 150, 147, 157]**.**

2.4.3 Mitochondrial Reactive Oxygen Species Production

A natural by-product of OXPHOS is the production of reactive oxygen species (ROS), specifically in the form of superoxide (O_2•-). When electrons are transferred in groups of four, they harmlessly form water at complex IV, which drives OXPHOS. If electrons leak prior to complex IV they form O_2•- through the one-electron reduction of O_2 (**Figure 2.5b**) [158]. As previously mentioned, the energy released when electrons flow through the electron transport chain is converted into a proton gradient, Δp, which powers the phosphorylation of ADP into ATP. During this process, known as state III respiration, the concentration of O_2•- produced is minimal as the majority of electrons effectively get transferred at complex IV (CIV) to produce water with a small amount of O_2•- being concomitantly produced. However, in the absence of ADP and inorganic phosphate (Pi), ATP synthesis does not occur. Yet, if reducing equivalents are present, their oxidation without subsequent ATP production results in a buildup of Δp, causing electron flow to slow and coenzyme Q to become highly reduced. This results in the favoring of premature electron slip and a subsequent increase in the concentration of O_2•- produced [159, 160]. To date, there are eleven identified sites of mitochondrial O_2•- production in mammalian mitochondria that are located within the mitochondrial matrix and IMM (**Table 2.3 and associated Figure 2.7**). In addition, there are a class of enzymes termed monoamine oxidases (MAO) which are located in the OMM that are known to produce ROS [161].

Table 2-3: Sites of Mitochondrial Superoxide Production. Adapted from [158, 162]. See Figure 2.6 for schematic representation. The maximal capacity for ROS production is ranked from 1-11 with the site ranked 1 producing the most ROS.

Site	Localization of ROS	Method of ROS production	Maximal Capacity for ROS production
Sites 1-4: 2-Oxoacid Dehydrogenase Complex			
2-oxoglutarate (O_F)	Matrix	The dihydrolipoamide dehydrogenase component of all sites catalyzes the transfer of reducing equivalents and can generate ROS at the Flavin.	4
Branched Chain 2-oxoacid (B_F)	Matrix		7
2-oxoadipate (A_F)	Matrix		8
Pyruvate Dehydrogenase (P_F)	Matrix		5
Sites 5 and 6: Complex I			
I_F	Matrix	Oxidizes NADH to NAD^+ and reduces Q to QH_2. Produces ROS when electrons leak from the fully reduced Flavin.	10
I_Q	Matrix	When QH_2/Q is highly reduced and Δp is high, QH_2 is oxidized to drive the reduction of NAD^+ during reverse electron transport. ROS is produced during this process	2
Site 7: Complex II			
II_F	Matrix	Q is reduced to QH_2 by complex II through the oxidation of succinate to fumarate. ROS can be produced in both the forward (succinate) and reverse (QH_2) direction.	3
Site 8: Glycerol-3-Phosphate Dehydrogenase			
G_Q	Matrix and Inner Membrane Space	Reducing equivalents from carbohydrate and fat metabolism are transferred to Q with ROS as a by-product of this reaction.	6
Site 9: Electron-transferring Flavoprotein-ubiquinone oxidoreductase			
E_F	Matrix	This system transfers reducing equivalents from β-oxidation to the Q	9

		pool with ROS as a by-product of this reaction.	
Site 10: Dihydroorotate Dehydrogenase			
D_Q	Matrix	This enzyme supports *de novo* pyrimidine biosynthesis and through the oxidation of dihydroorotate to orotate to reduce Q, ROS is produced.	11
Site 11: Complex III			
III_{Qo}	Matrix and Inner Membrane Space	In the presence of Q site inhibitors that block the oxidation of cytochrome b *heme,* reduced cytochrome b *heme* accumulates which limits the oxidation of the semiquinone at Q and allows for the interaction with O_2 to form ROS	1

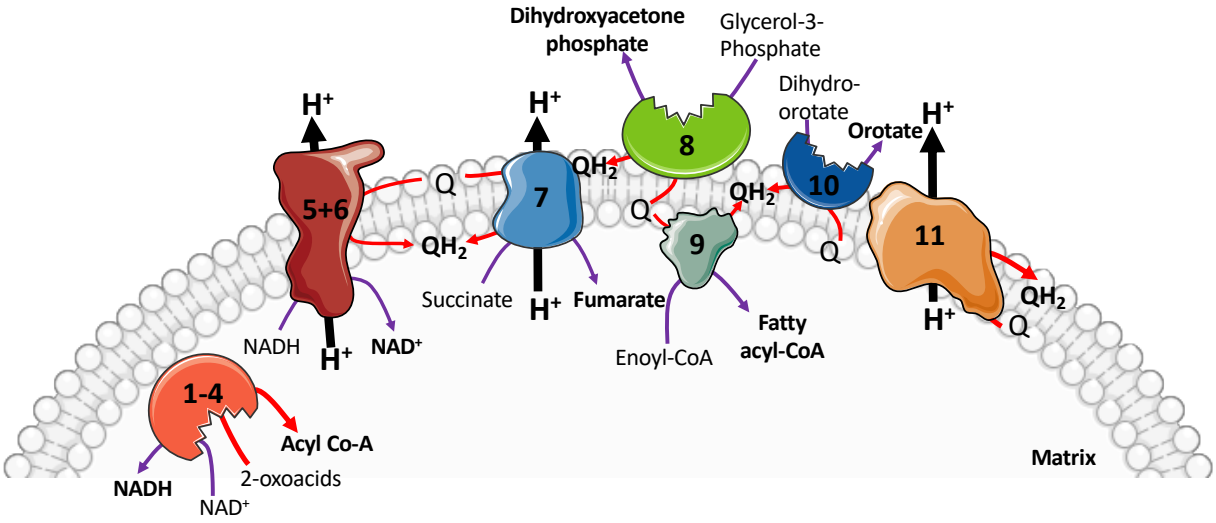

Figure 2-7: Mitochondrial Sites of ROS Production. Adapted from Wong et al. [162]. Eleven sites within the mitochondria that leak electrons to oxygen to produce ROS have been identified to date. All sites of ROS production are associated with substrate oxidation and the ETC. Electrons are passed from metabolites to the main ETC by dehydrogenases and all sites have the ability to produce ROS at either flavin groups (Sites 1-4: O_F, B_F, A_F, P_F; Site 5: I_F; Site 7: II_F and Site 9: E_F) or quinone binding sites (Site 6: I_Q; Site 8: G_Q; Site 10: D_Q and Site 11: III_{Qo}).

A central theme of this thesis surrounds ADP's governance of mitochondrial bioenergetics (see section *2.5.2.1 ADP as a Central Governor of Bioenergetics)*. As such, the remaining work focuses on sites of ROS production that are membrane potential dependent (specifically complex I and II) wherein the role of ADP in the attenuation of ROS production can be evaluated.

Regular levels of ROS production that occur during state III respiration are necessary for cellular signaling and for the maintenance of homeostasis. However, an increase in $O_2\bullet$- production can become pathological in nature due to an increase in oxidative stress and subsequent pathology (see *2.3.2.1 Overview of Oxidative Stress*). Indeed, the discovery that mitochondria have their own source of superoxide dismutase (MnSOD) confirmed the importance of mitochondrial $O_2\bullet$- contribution to cellular oxidative stress [163]. $O_2\bullet$- is a highly reactive form of ROS that not only has an incredibly short half-life but is impermeable to lipid membranes [164, 165]. High concentrations of MnSOD within the mitochondrial matrix catalyze the dismutation of $O_2\bullet$- to H_2O_2. As previously discussed, the production of H_2O_2 is tightly coupled with its removal through endogenous cellular antioxidant systems including glutathione (**Figure 2.3**) and thioredoxin systems [166]. During healthy conditions, the majority of H_2O_2 is scavenged before being emitted from the mitochondria. However, under pathological conditions, if H_2O_2 emission is excessive, it will either act as a redox stressor within the mitochondria or be emitted from the mitochondria at elevated rates that disrupts cellular homeostatic mechanisms through excessive redox pressure on a variety of regulatory pathways, thereby creating a functional oxidative stress. Indeed, there are several signaling pathways in which mitochondrial ROS production has been implicated including apoptosis, autophagy, endoplasmic reticulum stress and hypoxia [158]. Additionally, and perhaps most importantly, elevated levels of mitochondrial ROS production can contribute to the activation

of cell death pathways from within the mitochondria itself through the sensitization of the mitochondrial permeability transition pore (PTP) [167].

2.4.4 Mitochondrial Induced Cell Death

2.4.4.1 Mitochondrial Ca^{2+} Handling

Ca^{2+} is an ion required for most physiological processes within a cell. Changes in [Ca^{2+}] within the cytosol is a tightly regulated process used to modify the activity of target molecules. This control over cytosolic [Ca^{2+}] is achieved predominately through the sarcoplasmic reticulum, the main intracellular storage site of Ca^{2+}. However, during times of cytosolic Ca^{2+} overload, the mitochondria has been identified as a key regulator of Ca^{2+} homeostasis within the muscle due to their capacity to uptake high concentrations of the ion at rapid rates [26]. In respiring mitochondria, the Δp (which results in a negatively charged matrix) drives the uptake of Ca^{2+} into the mitochondrial matrix through the mitochondrial calcium uniporter (MCU) [25]. Under healthy conditions, the Na^{+}- Ca^{2+} exchanger (NCLX) acts as an efflux pathway to counteract this uptake and prevent the build-up of matrix Ca^{2+} [168]. However, when cytosolic [Ca^{2+}] is increased, the mitochondria become a sink for Ca^{2+} as there is a kinetic imbalance between Ca^{2+} import and efflux. The MCU can facilitate Ca^{2+} accumulation at a rate of 1400 nmol Ca^{2+} •mg mitochondrial $proteion^{-1}$•min^{-1} while the combined rate of efflux from all pathways is approximately 20 nmol Ca^{2+} •mg mitochondrial $proteion^{-1}$•min^{-1} which can quickly result in Ca^{2+} overload within the mitochondria [168]. Ca^{2+} overload can trigger the opening of the PTP and the subsequent activation of mitochondrial derived cell death pathways which are described in detail below.

2.4.4.2 Mitochondrial Permeability Transition Pore

While the predominant role of the mitochondria is to produce ATP to meet the energetic demands of the cell, the mitochondria also maintain an intrinsic ability to induce cell death through apoptosis and necrosis. This switch in roles from life support of the cell to programmed cell death is mediated

by the opening of a pore located on the IMM known as the mitochondrial permeability transition pore (PTP) [169-171]. Under normal physiological conditions, the IMM is relatively impermeable, save for a few select metabolites and ions. Under conditions of cellular stress, the PTP can open and allow the free passage of any molecule less than 1.5 kDA in size [172, 173]. The primary factor responsible for triggering PTP opening is mitochondrial calcium (Ca^{2+}) overload, which occurs when the [Ca^{2+}] within the mitochondrial matrix is excessively high [174]. Ca^{2+} is known as a "permissive" factor in PTP formation yet the threshold concentration required varies depending on *in vivo* conditions as Mg^{2+} and other divalent cations appear to compete for the same binding sites as Ca^{2+}[26, 175].

While the role of Ca^{2+} in PTP formation has been well established within the literature, much debate has remained over the structural components of the PTP and the mechanism by which Ca^{2+} can force the opening of this channel [169-171]. Indeed, Cyclophilin-D (CyPD), a peptidyl-prolil *cis-trans* isomerase, remains the best characterized protein involved in PTP opening yet acts as a modulator as opposed to a structural component of the pore. ATP synthase has recently been identified as a channel matching the properties of the PTP. The β-subunit of ATP synthase contains a catalytic binding site for Mg^{2+}-ATP which can be replaced with Ca^{2+}-ATP, resulting in a conformational change of the enzyme [176]. Furthermore, CyPD was found to bind to oligomycin-sensitivity conferring protein (OSCP), a component of the F_1 subunit of ATP Synthase responsible for coupling H^+ flux to ATP synthesis [26]. This left the working hypothesis that PTP opening occurs when Ca^{2+} replaces Mg^{2+} at the catalytic site, causing a conformational change that is transmitted through OSCP resulting in an opening of the pore through the IMM; a concept that has since been proven correct in multiple laboratories [176-178].

In addition to Ca^{2+} overload, there are several other cellular effectors that, while not required, increase the probability of PTP formation. Firstly, as previously mentioned in section 2.4.2, PTP opening is very sensitive to oxidative stress. Specifically, pore opening is promoted by the oxidation of matrix pyridine nucleotides (NADH/NADPH) and dithiols and can be prevented through the use of reducing agents and the reduction of glutathione [167]. Furthermore, ROS production at complex I is a key modulator of PTP opening and can be prevented through the use of rotenone, a complex I inhibitor [179]. In addition to elevated levels of oxidative stress, the PTP is also modulated through matrix pH, with 7.4 being optimal for opening and values above and below this acting as inhibitory conditions for opening. Finally, despite the fact that inorganic phosphate can decrease matrix [Ca^{2+}], this metabolite acts as an inducer of PTP opening in mammalian mitochondria [175].

The opening of the PTP results in two major consequences for the cell. Firstly, the increase in permeability of the IMM causes a rise in osmotic pressure and subsequent swelling of the mitochondria. The unfolding of the cristae allows the matrix to expand and prevents the IMM from rupturing but the OMM will break leading to the release of proteins in the intermembrane space, including cytochrome c, which plays an important role in the activation of apoptosis (see section 2.4.3.3). Secondly, the IMM becomes completely permeable to protons which results in the uncoupling of OXPHOS and the hydrolyzation, as opposed to synthesis, of ATP [172]. The swelling of the mitochondria and OMM rupture are sufficient to activate the apoptotic cascade and unless pore closure occurs, irreversible damage to the cell will be caused, resulting in necrotic cell death.

2.4.4.3 Mitochondrial-Derived Apoptosis

Apoptosis, known as "programmed" cell death, is a tightly regulated pathway that occurs in during both normal development as well as in response to cell damage or stress [180]. Indeed, apoptosis is used to remove unwanted and harmful cells during both embryonic development, and for the maintenance of tissue homeostasis and immune regulation [181]. This process can be triggered by external stimuli through cell surface death receptors or through intrinsic stimuli that activate the mitochondrial signaling pathway. For the purpose of this review, only mitochondrial derived apoptosis will be discussed.

Apoptosis is predominately regulated by a group of cysteine proteases, called caspases, that cleave cellular substrates and dismantle cellular components [182]. Briefly, Bcl-2, an anti-apoptotic protein situated on the OMM is inactivated by BH3-only proteins which are activated in response to certain cellular stressors. The inactivation of Bcl-2 results in the activation of pro-apoptotic proteins BAX and BAK which promote the permeabilization of the OMM. This permeabilization promotes the release of cytochrome c, which binds with APAf-1 forming an apoptotosome. This apoptotosome then cleaves initiator caspase-9 which further cleaves executioner caspase-3, thereby inducing apoptosis [27, 183]. Apoptosis requires ATP as both the binding of cytochrome c to APAf-1 and the enzymatic activation of caspase 9 are ATP-dependent processes [183, 184]. Therefore, if PTP opening is prolonged and an energy crisis ensues, an ongoing apoptotic process can be converted into a less favourable necrotic process [184].

The resulting cellular outcomes of the activation apoptosis include the condensation of chromatin followed by cell shrinkage to revoke contact with neighbouring cells. The membrane then blebs and forms vacuoles which are removed from phagocytic cells (macrophages) [185]. Apoptosis, which occurs in single cells, is seen as an efficient way to remove cellular "debris" without evoking

a full inflammatory response and as such, is considered the preferential form of cell death over necrosis (**Table 2.4**).

2.4.4.4 Mitochondrial-Derived Necrosis

While apoptosis is identified as an active, programmed process that plays a role in normal muscle development, necrosis is viewed as a more pathological process involving passive, unordered cellular explosion in response to a stress or trauma [27]. While apoptosis has established activation pathways in response to extrinsic stimuli (death receptors; TNF-α) and intrinsic stimuli (mitochondria), less is known about the precise signaling pathway that occurs following the initiation of mitochondrial-derived necrosis although TNF-α, which is activated by mitochondrial ROS [186], is considered to be a key player [27]. Given TNF-α also induces apoptosis, two key steps in the signaling process distinguish the two processes from each other. The activation of necrosis includes the inhibition of caspases by a small peptide, zVAD as well as the activation of the poly(ADP-ribose)polymerase, PARP1, which reduces ATP levels – a hallmark feature of the necrotic process [27].

Necrosis in an energy-independent process and affects large fields of cells, evoking an inflammatory response (**Table 2.4**). Morphologically, necrosis results in cell swelling and loss of membrane integrity. This results in the release of cytoplasmic contents into the surrounding tissues and the subsequent recruitment of inflammatory cells (neutrophils, dendritic cells, macrophages [180, 187, 188]. In turn, the field of affected cells are degenerated and remain in a necrotic state until regeneration occurs. Given this large scale, pathological response, necrosis is viewed as the less favored cell death pathway relative to apoptosis.

Table 2-4: Comparison of Mitochondrial-Derived Apoptosis and Necrosis. Adapted from [189, 185, 27].

Apoptosis	Necrosis
Programmed cell death	Un-programmed cell death
Response to "physiologic" stimuli	Response to "pathologic" stimuli
Affects single cells	Affects neighbouring cells
Cells shrink in size	Cells and organelles swell
Membrane remains intact; blebbing occurs	Loss of cell membrane integrity
Caspase-dependent	Caspase-independent
Formation of Apoptotic Body → phagocytosis of apoptotic cells and fragments	Leakage of cellular components
No inflammatory response*	Evokes an inflammatory response
Requires ATP	Passive process – no ATP required

2.5 Mitochondrial Function in Duchenne Muscular Dystrophy

2.5.1 Mitochondrial Oxidative phosphorylation

DMD has long been considered a disease involving metabolic impairments with several reports of deficiencies in key systems and regulators. Specifically, decreases in enzymes comprising the glycolysis pathway [190-193] and Tricarboxylic Acid cycle (TCA) [193] as well as decreased protein content of the electron transport chain have consistently been reported [34, 30, 194, 195, 23]. The physiological consequence of these deficiencies is a reduction in ATP production, as evidenced by the severely reduced ATP content (~50% reduction) present in both animal models and patients with DMD [20, 22-24].

Research to date indicates that this reduction in ATP content is due to functional abnormalities within the mitochondria. Firstly, functional deficits in specific enzymes (succinic CoA synthetase, aconitase, malate dehydrogenase and IDH) of the TCA cycle have been reported which would result in a decrease in the quantity of reducing equivalents available for reduction by the ETC [21,

196, 197]. Secondly, decreased oxidation rates of substrates including glucose, pyruvate, malate and glutamate have been reported in both *mdx* muscle and muscle from patients with DMD [198, 29, 194, 34]. These combined findings suggest there should be concomitant decreases in the rate of oxidative phosphorylation in dystrophic muscle yet the results to date are divergent in nature [23, 28-34, 199]. It should be noted, albeit in limited sample sizes, the two evaluations of oxidative phosphorylation in human muscle to date both reveal impairments in respiration rates [29, 30] indicating there is likely an intrinsic impairment in oxidative phosphorylation within the mitochondria in DMD although this remains to be conclusively determined.

2.5.1.1 Creatine Impairments in DMD

MtCK plays a vital role in maintaining cellular energy homeostasis and as a result, diseases characterized by impairments in cell metabolism or oxidative phosphorylation are increasingly being identified with mtCK defects [152]. MtCK is extremely susceptible to the compensatory up-regulation of its expression in response to dysfunction as well as alterations by oxidative stress resulting in functional impairments [200, 152, 153]. Only one study to date has assessed mtCK functionality in dystrophic muscle. In oxidative muscle (soleus and left ventricle), an insensitivity to creatine was evident in dystrophic mice based on the inability of exogenous creatine to increase mitochondrial sensitivity to ADP [201]. Specifically, in WT muscle, the addition of creatine results in a greater rate of oxygen consumption for a given [ADP] because creatine activates mtCK, which promotes the transfer of energy through the efficient creatine-dependent pathway. On the contrary, the addition of creatine had no effect on ADP sensitivity, indicating an impairment in mtCK functionality in oxidative dystrophic muscle which was not due to alterations in mtCK activity levels [201]. These findings may account for some of the divergent data surrounding mitochondrial oxidative phosphorylation as no other study has assessed the two energy systems separately and as a result, may have masked dysfunctions that exist in specific pathways in dystrophic muscle.

2.5.2 Mitochondrial Reactive Oxygen Species Production

As previously discussed in section 2.3.2 *Oxidative Stress in DMD*, there is a plethora of evidence to suggest that mitochondrial ROS should be elevated and in turn, that mitochondrial ROS contributes to DMD disease pathology yet the literature to date remains is inconclusive. Work by Shkryl et al., found that in FDB single fibres from *mdx* mice aged 4-8 weeks of age, basal levels of mitochondrial ROS were not different from WT but following an osmotic shock, mimicking the conditions that occur in dystrophic muscle following stretch-induced contractions, mitochondrial ROS levels were significantly higher than WT controls [125]. While basal levels of mitochondrial ROS were not higher, this work implicates the mitochondria as a contributor to oxidative stress in response to Ca^{2+} overload within the fibre. Additionally, given the compensatory nature of the *mdx* mouse [52], a time frame of 4-8 weeks makes it difficult to draw conclusions on the bioenergetic status of the muscle. Indeed, the only study to date to directly measure mitochondrial ROS emission rates in skeletal muscle did so in the TA muscle of *mdx* mice at 6 weeks of age. This novel work by Godin et al., found no increases in H_2O_2 emission rates but found a significant increase in H_2O_2 scavenging capabilities in *mdx* muscle, indicative of compensation occurring at this early time point [33].

A second study by Ascah et al., found no increases in H_2O_2 emission in cardiac muscle from 12 week old *mdx* mice but did report decreased aconitase activity, indicative of a loss of function due to oxidative modifications [199]. Therefore, while basal levels of ROS production were not higher in cardiac or skeletal muscle, it does not rule out the possibility that this impairment is being masked by the high degree of compensation that occurs in the *mdx* mouse. Evidence to support this idea comes from an *mdx* mouse model with "humanized" telomere lengths. Recent work by Chang and colleagues suggests the hyper-regeneration that occurs in the *mdx* mouse [51, 52, 202] masks the ability to detect early attenuations in mitochondrial bioenergetics in dystrophic heart

[203, 204]. Indeed, shortening telomeres to a more "humanized" length, thereby lowering the stem cell pool, revealed an increase in mitochondrial superoxide production and impairments in respiration in cardiomyocytes relative to the classic *mdx* model [204]. Additionally, treatment with two antioxidants, butylated hydrooxyanisole (BHA), a global antioxidant and MnTBAP a mitochondrial targeted antioxidant, lowered oxidative stress and prolonged the onset of cardiomyopathy in dystrophic animals with shortened telomeres, with MnTBAP providing far more benefit than BHA [204]. To date, no study has confirmed whether mitochondrial ROS production is elevated in non-compensated, dystrophic tissue relative to healthy controls despite the evidence suggesting this may be the case and the potential implications of the identification of the mitochondria as a source of ROS in the context of DMD disease pathology.

2.5.2.1 ADP as a Central Governor of Bioenergetics

Defined impairments in creatine sensitivity in DMD [201] highlight the need for the careful design of *in vitro* assessments in order to capture the specific source and degree of bioenergetic dysfunction in a disease. Given the membrane potential dependency of superoxide production in the ETC, ADP plays an important role in not only stimulating OXPHOS, but lowering superoxide production and consequentially, the amount of H_2O_2 emitted from the mitochondria [230]. As such, it is possible that mitochondrial dysfunction could manifest as a loss of central control by ADP to govern both H_2O_2 emission and respiration during oxidative phosphorylation. Furthermore, mtCK is known to play an essential role in optimizing ADP-stimulation of oxidative phosphorylation and attenuation of H_2O_2 emission given its ability to accelerate mitochondrial matrix ADP cycling which ultimately reduces H_2O_2 emission and stimulates oxidative phosphorylation (**Figure 2-6**) [205, 157]. Overall, given the complexity of how bioenergetics are governed by ADP and creatine, it is plausible that re-designing *in vitro* protocols to mimic *in vivo*

conditions may uncover specific impairments in the governance of mitochondrial H_2O_2 emission during oxidative phosphorylation in DMD.

2.5.2.2 Targeting Mitochondrial ROS in DMD

Recent results from clinical trials (2011-2019) involving the compound Idebenone infer that mitochondria may be a source of oxidative stress in DMD. Idebenone, a synthetic analog to coenzyme Q_{10}, is known for its ability to improve mitochondrial oxidative phosphorylation and reduce oxidative stress through its role as an electron shuttler [206, 207]. In recent years, idebenone has been tested in both *mdx* mice and in clinical trials involving patients with DMD where the primary focus of these studies was idebenone's effect on cardiac and respiratory function. In *mdx* mice, long term treatment with Idebenone corrected cardiac diastolic dysfunction and prevented mortality from cardiac pump failure induced by dobutamine stress testing in vivo, significantly reduced inflammation and fibrosis in cardiac tissue, and significantly improved voluntary running performance [208]. Results from clinical trials were equally promising with reports of improved cardiac and respiratory function in patients with DMD [76, 209-211]. Specifically, in the clinical trial DELOS, which involved patients aged 10-18 not currently taking glucocorticoids, assessed peak expiratory flow as a percentage of expected as well as forced vital capacity and peak cough flow. All three parameters improved in the treatment group, yet there was no effect on arm strength or function [210, 211]. A separate clinical trial DELPHI assessed cardiac and respiratory function in boys with DMD aged 8-16 years comprised of both glucocorticoid users and glucocorticoid-naïve participants. Idebenone treatment resulted in a trend for increased peak systolic radial strain in the left ventricle and significantly improved peak expiratory flow [209]. Further post-hoc analysis revealed a greater improvement in peak expiratory flow following idebenone treatment in glucocorticoid-naïve patients, potentially indicative of a steroid-mediated suppression of idebenone or a maximal treatment effect reached by steroids [76].

Despite these beneficial effects, it remains unknown whether improvements following idebenone treatment are due to alterations in mitochondrial function. Firstly, idebenone is not a mitochondrial-targeted compound but a general antioxidant based on its structure. To date, the beneficial effects of idebenone on mitochondrial function in DMD have been inferred based on the structural similarity to coenzyme $Q_{10,}$ yet the specific mechanism of action remains to be elucidated Additionally, while promising at high doses, there are concerns over idebenone's limited bioavailability [212]. Overall, these promising results highlight the need to directly evaluate whether the mitochondria are a secondary mechanism contributing to DMD disease pathology as the identification of the mitochondria as a therapeutic target would provide several therapeutic candidates to evaluate in the development of a portfolio of compounds to be considered for clinical trials.

2.5.3 Mitochondrial Calcium Handling and Mitochondrial-Derived Cell Death

In addition to oxidative phosphorylation, the mitochondria play a key role in the regulation of cell death pathways, which, by nature, are Ca^{2+} dependent. Dating back to 1987, TEM analysis of mitochondria in muscle fibres from patients with DMD revealed no differences in mitochondrial content but vast ultrastructural abnormalities ranging from "small and dense" mitochondria, indicative of apoptosis to "large and dilated" mitochondria, indicative of necrosis [213]. This is associated with evidence of excess Ca^{2+} uptake by the mitochondria dystrophic tissue. In fact, work by Robert et al., revealed that dystrophic mitochondria will take up excess calcium in response to increased cell membrane permeability, even before cytosolic Ca^{2+} overload is evident [214]. Further work by Ascah et al., revealed that in unstressed mitochondria, Ca^{2+} uptake velocity is significantly higher in *mdx* muscle relative to WT controls [199]. Together these findings indicate that the mitochondria may actually be a direct cause of impaired Ca^{2+} homeostasis in dystrophic tissue as opposed to an organelle simply responding to perturbations in cytosolic [Ca^{2+}].

Surprisingly, direct assessment of mitochondrial susceptibility to Ca^{2+}-induced PTP opening has led to divergent results. In permeabilized muscle fibre systems, whereby the cell membrane is removed but the mitochondrial membrane remains intact, mitochondrial susceptibility to Ca^{2+}-induced PTP opening is assessed using membrane impermeant fluorophores which bind Ca^{2+} in the cytoplasm, but not in the mitochondria. Following the addition of exogenous Ca^{2+} mitochondrial uptake and subsequent release of Ca^{2+}, indicative of PTP opening can be assessed. When analyzing the time to PTP opening in response to a set [Ca^{2+}], dystrophic tissue consistently demonstrates an increased susceptibility to PTP opening relative to WT [199, 33, 35] which is likely related to the previously mentioned increase in mitochondrial Ca^{2+} uptake velocity in dystrophic tissue. Alternatively, when Ca^{2+} is titrated into the system in small amounts, the [Ca^{2+}] required to induce PTP opening is unchanged between *mdx* and WT animals [33, 215]. Perhaps, given the increased Ca^{2+} uptake velocity, a single large bolus of Ca^{2+} better reflects the *in vivo* Ca^{2+} influx experienced by dystrophic mitochondria while the small titrations allow the *in vitro* system to deal with the influx better. For example, when intact hearts from *mdx* mice are subjected to I/R injury, the number of mitochondria undergoing PTP opening is increased compared to normal hearts. However, this physiological stressor was required to unmask differences, as PTP opening was unchanged prior to the induction of I/R relative to WT controls [199, 32]. In essence, the mitochondria needed to be primed with Ca^{2+} in order to mimic *in vivo* conditions and to further unmask the increased susceptibility to PTP opening.

While functional data remains perplexing, the most compelling evidence for the contribution of mitochondrial derived cell death to the DMD disease pathology stems from the use of PTP inhibitors in DMD. Millay et al., genetically modified *mdx* mice to delete the gene encoding Cyclophilin D, resulting in resistance to mitochondrial Ca^{2+}overload-induced swelling and

decreased levels of necrosis in diaphragm and gastrocnemius muscle [36]. However, this was not associated with a recovery in muscle function [36]. A second study, conducted by Reutenauer et al., aimed to pharmacologically inhibit Cyclophillin D using a compound Debio 025. Treatment with this compound partially reduced necrosis in the diaphragm and soleus of *mdx* mice during the peak necrotic period as well as provided a greater resistance to fatigue in the triceps muscle, despite maximal tetanic force being unchanged [215]. Finally, the use of sildenafil, which inhibits PTP opening through the activation of cGMP signaling, resulted in improvements in diaphragm strength and enhanced respiratory muscle contractility [216]. In a second study, sildenafil decreased PTP opening and caspase 9 activity [199] as well as necrosis [217] in dystrophic cardiac muscle prior to the onset of cardiomyopathy. Perhaps most striking, sildenafil also demonstrated the capability to improve cardiac function in aged *mdx* mice, after the onset of cardiomyopathy [218]. Unfortunately, the subsequent clinical trial in patients with DMD was unsuccessful with the trial being terminated early due to several patients worsening on sildenafil [219].

While it is evident that mitochondrial-derived cell death is a contributing factor to DMD disease pathology, it appears that targeting the cell death itself provides minimal benefit at a clinical level. These findings highlight need to consider targeting the upstream causes of mitochondrial-derived cell death in order to prevent this pathological process from needing to occur.

2.6 Mitochondrial Targeted Antioxidants

It has been proposed that previously tested global antioxidants were ineffective at treating DMD because of their un-targeted nature and that targeting the specific source of ROS production may be more effective [82, 93, 208]. Over the past decade or so, extensive research has gone in to developing mitochondrial targeted antioxidants given the important role the mitochondria play in the control of cell life and death. There are three predominant ways that drugs can be targeted to

the mitochondria: 1. Targeting the biophysical properties of the mitochondria (ie. A negatively charged mitochondrial matrix), 2. Targeting based on the location of mitochondrial enzymes which catalyze the release of drugs from prodrugs and 3. Targeting based on transporter dependent prodrugs [220]. A wide range of general antioxidants have been targeted to the mitochondria through the conjugation with the lipophilic cation triphenylphosphonim (TPP). Lipophilic cations pass easily through lipid bilayers because their charge is dispersed over a large surface area and their positive charge allows the potential gradient to drive their accumulation into the mitochondrial matrix [221]. The most extensively used antioxidant, MitoQ (**Figure 2-8a**), sees Coenzyme Q conjugated to TPP and has been shown to scavenge superoxide and peroxynitrite as well as prevent lipid peroxidation [221, 220]. A second set of compounds, similar in structure and functionality to MitoQ are the Sk compounds with SKQ1 (**Figure 2-8b**) being most commonly used. SKQ1 is comprised of plastiquinone, a compound equivalent to ubiquinone found in chloroplasts which has been found to be a stronger antioxidant, conjugated to TPP [222]. Both MitoQ and SkQ1 act as antioxidants at low doses, yet are found to become pro-oxidants at high doses. Additionally, due to their dependence on membrane potential to accumulate within the mitochondria, diseases with dissipated mitochondrial membrane potential are likely not potential targets for this form of antioxidant.

The SS peptides, which represent another group of mitochondrial targeted antioxidants, are aromatic–cationic peptides that bear alternating aromatic and basic amino acid residues with some compounds (SS-31, SS-02) also containing a 2′,6′-dimethyltyrosine (Dmt) residue (**Figure 2-8c**). These cell permeable compounds bind to cardiolipin on the IMM and are shown to improve oxidative phosphorylation, decrease ROS, prevent oxidative damage and prevent the dissociation of cytochrome c from cardiolipin, thereby preventing the activation of cell death pathways [223].

SS-31 and SS-02 appear to have the strongest antioxidant capabilities which are attributed to the Dmt residue, which is a phenolic antioxidant [220]. While SS-20 does not act as a direct scavenger of ROS, it still has beneficial effects on mitochondrial function and the prevention of oxidative damage [224]. Unlike MitoQ and SKQ1, the uptake of SS peptides is only reduced by approximately 20% upon the depolarization of the mitochondria and therefore, may be an attractive alternative in diseases of dissipated membrane potential. The SS compounds have been shown to effectively protect against damage caused by ischemia-reperfusion injury and myocardial infarction in rats [224-226] while SS-31 (elamipretide) specifically is currently being used in clinical trials for Primary Mitochondrial Myopathy, Barth syndrome, Leber's Hereditary Optic Neuropathy and Age-Related Macular Degeneration, diseases that are all characterized by elevated oxidative stress [227, 228].

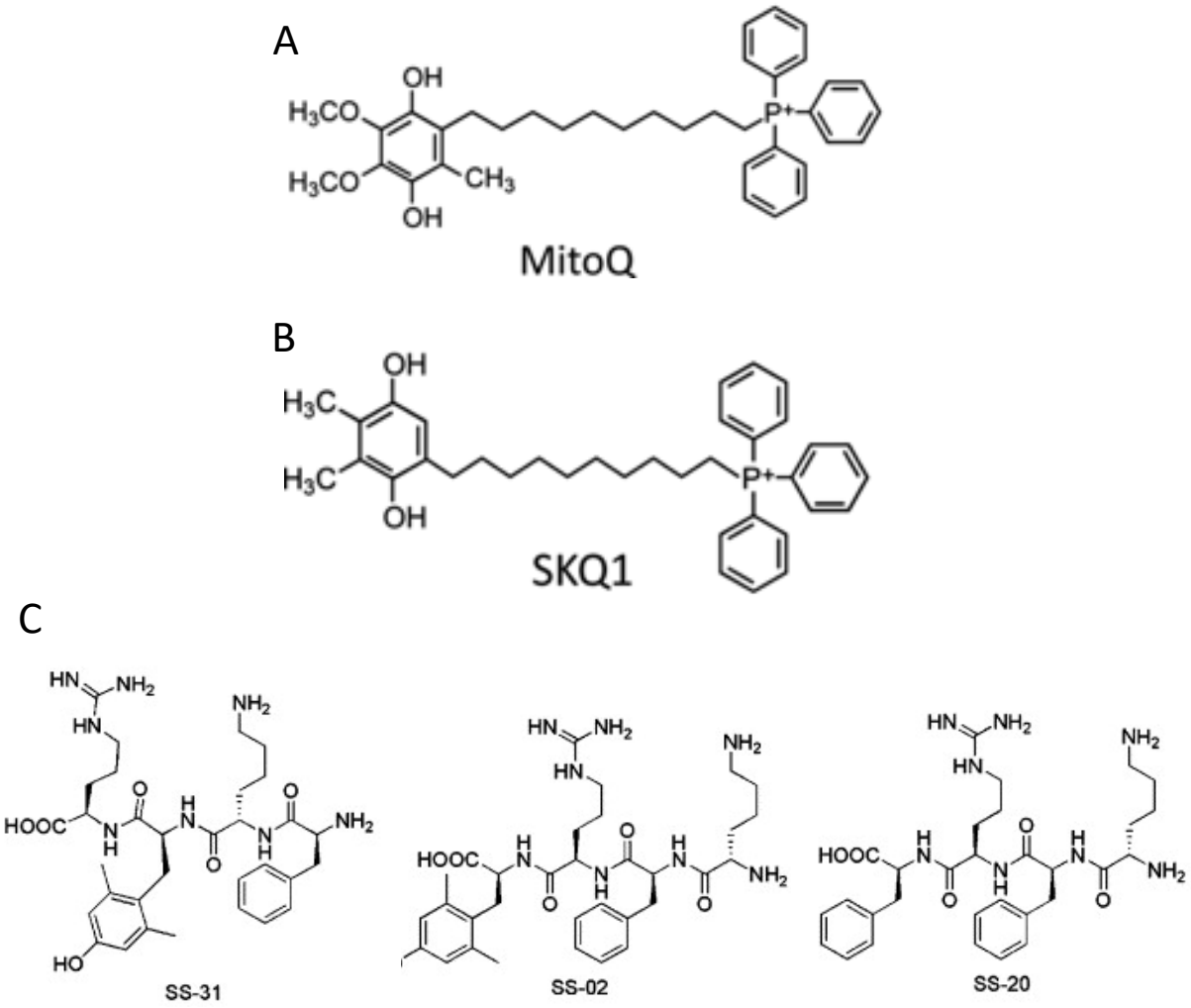

Figure 2-8: Structures of commonly used mitochondrial targeted antioxidants. MitoQ: 10-(6′-ubiquinolyl)decyltriphenylphosphonium bromide. **B.** SKQ1: 10-(6'-plastoquinolyl)decyltriphenylphosphonium. **C.** SS Peptides: **SS-31**, D-Arg–Dmt–Lys–Phe–NH_2; Dmt, 2′,6′-dimethyltyrosine; **SS-02**, Dmt–D-Arg–Phe–Lys–NH_2; **SS-20**, Phe–D–Arg–Phe–Lys–NH.

3 Objectives and Hypothesis

3.1 Overview of Thesis

The overall purpose of this thesis was to determine whether the mitochondria represent a viable therapeutic target for the treatment and prevention of disease progression in Duchenne muscular dystrophy (DMD). The specific objectives and hypotheses for each study are outlined below.

3.2 Objective and Hypotheses for Study 1 (CHAPTER 4)

While the mitochondria have always been proposed to contribute to DMD disease pathology, the literature evaluating the actual contribution of the mitochondria remains controversial. The objective of this study was to determine the specific source(s) and degree of altered mitochondrial bioenergetics in diaphragm and skeletal muscle in young D2.*mdx*, a new mouse model that more closely mimics human disease progression and furthermore, to determine if these potential alterations in mitochondrial bioenergetics were associated with muscle wasting and weakness.

Hypotheses:

1. By modelling *in vivo* conditions *in vitro*, altered mitochondrial bioenergetics (oxidative phosphorylation, H_2O_2 emission, susceptibility to calcium-induced permeability transition pore opening) will be evident in dystrophic muscles exhibiting cell membrane damage.
2. Corresponding muscle weakness as exhibited through muscle functional assessments will be present in dystrophic tissue displaying membrane damage.
3. These impairments in mitochondrial and muscle function will be associated with muscle wasting.

3.3 Objective and Hypotheses for Study 2 (CHAPTER 5)

The heart represents a unique muscle in DMD given the late onset of muscle degeneration and subsequent cardiomyopathy within this tissue despite a lack of dystrophin akin to all other muscles in the body. Cardiomyopathy occurs in 98% of patients and develops into heart failure in 40% of

patients yet the underlying mechanisms causing this myopathy remain unknown. Literature to date suggests the mitochondria should be a contributing factor yet the compensatory nature of the animal models used appear to mask any bioenergetic defects that may be present. The objective of this study was to evaluate mitochondrial function in dystrophic heart muscle prior to the onset of cardiomyopathy in the D2.*mdx* mouse, a mouse model with impaired regenerative capabilities and subsequently, less compensation than classical models.

Hypothesis:

1. Mitochondrial bioenergetics (oxidative phosphorylation, H_2O_2 emission, susceptibility to calcium-induced permeability transition pore opening) will be altered in dystrophin deficient heart muscle at a time point prior to the onset of cardiomyopathy.

3.4 Objective and Hypotheses for Study 3 (CHAPTER 6)

Based on the findings from study 1, we then sought to determine if a mitochondrial-targeted peptide (SBT-20) could improve altered bioenergetics and subsequently improve DMD disease pathology in diaphragm and skeletal muscle of young D2.*mdx* mice.

Hypotheses:

1. 28 days of treatment with SBT-20 will improve mitochondrial bioenergetics in dystrophic diaphragm and quadriceps muscle
2. Improved bioenergetics will be associated with improvements in mitochondrial quality (permeability transition pore induction, mitochondrial ultrastructure), muscle quality (specific force production, histopathology) and lean muscle volume relative to saline treated D2.*mdx* mice

3.5 Objective and Hypotheses for Study 4 (CHAPTER 7)

Study 4 can be divided into two parts and subsequently has two distinct objectives. While studies 1-2 demonstrated impaired mitochondrial bioenergetics in young D2.*mdx* mice, the first objective

of study 4 was to determine if these impairments were still evident in the late stages of disease progression using aged (52 week old) D2.*mdx* mice. Objective 2 of this study was to determine if the mitochondrial-targeted peptide SBT-20 could improve impaired mitochondrial bioenergetics by preventing oxidation of the pathways that were identified as dysfunctional in part 1.

Hypotheses:

1. Mitochondrial bioenergetics (oxidative phosphorylation, H_2O_2 emission, susceptibility to permeability transition pore opening) will be altered in heart, diaphragm and skeletal muscle of aged animals with DMD.
2. Longer term in *vivo* treatment with SBT-20 will prevent oxidative inhibition of mitochondrial bioenergetics
3. After revealing creatine-specific impairments in bioenergetics, we hypothesized that *In vitro* treatment with SBT-20 will improve creatine-dependent energy exchange and protect mtCK from oxidative modification-induced dysfunction

3.6 Additional Contributions

The following work encompasses the additional contributions made throughout my PhD that are not included in my dissertation. *Denotes equal contribution.

Co-First Author - Published

1. Monaco CMF*, **Hughes MC***, Ramos SV, Varah NE, Lamberz C, Rahman FA et al. Altered mitochondrial bioenergetics and ultrastructure in the skeletal muscle of young adults with type 1 diabetes. *Diabetologia*. 2018;61(6):1411-23. doi:10.1007/s00125-018-4602-6.

2. Ramos SV*, **Hughes MC***, Perry CGR. Altered skeletal muscle microtubule-mitochondrial VDAC2 binding is related to bioenergetic impairments after paclitaxel but not vinblastine chemotherapies. *American Journal of Physiology-Cell Physiology*. 2019. doi:10.1152/ajpcell.00384.2018.

Co-Author - Published

1. Edgett BA, **Hughes MC**, Matusiak JB, Perry CG, Simpson CA, Gurd BJ. SIRT3 gene expression but not SIRT3 subcellular localization is altered in response to fasting and exercise in human skeletal muscle. *Exp Physiol*. 2016;101(8):1101-13. doi:10.1113/EP085744.

2. Smith BK, Ford RJ, Desjardins EM, Green AE, **Hughes MC**, Houde VP et al. Salsalate (Salicylate) Uncouples Mitochondria, Improves Glucose Homeostasis, and Reduces Liver Lipids Independent of AMPK-β1. *Diabetes*. 2016;65(11):3352.

3. Bhattacharya D, Ydfors M, **Hughes MC**, Norrbom J, Perry CGR, Scimè A. Decreased transcriptional corepressor p107 is associated with exercise-induced mitochondrial biogenesis in human skeletal muscle. *Physiological Reports*. 2017;5(5).

4. Pinho RA, Sepa-Kishi DM, Bikopoulos G, Wu MV, Uthayakumar A, Mohasses A, **Hughes MC**, Perry CGR and Ceddia RB. High-fat diet induces skeletal muscle oxidative stress in a fiber type-dependent manner in rats. *Free Radical Biology and Medicine*. 2017;110 (Supplement C):381-9. doi:https://doi.org/10.1016/j.freeradbiomed.2017.07.005.

Co-First Author – In Progress

1. Ramos SV*, **Hughes MC***, Bellissimo CA and Perry CGR. Mitochondrial bioenergetic dysfunction in Duchenne muscular dystrophy is associated with microtubule disorganization in skeletal muscle. *Submitted to PLoS One*. March 2019.

2. Ramos SV*, **Hughes MC***and Perry CGR. The effects of microtubule-binding chemotherapies on cardiac mitochondrial bioenergetcs.

3. Ramos SV*, **Hughes MC***and Perry CGR. The role of mitochondrial function in chemotherapy induced muscle weakness.

Co- Author – In Progress

1. Al-Sajee D, Molt S, Gingrich M, Au M, Coleman SK, Filler T, Provias J, DeBeer J, **Hughes MC**, Perry CGR, Chambers P, Tupling RA, Tarnopolsky MA, Fürst D and Hawke TJ. The Absence of Xin Results in Triadopathy; Evidence of Xin as a Novel Player in Skeletal Muscle Calcium Handling.

2. Colon cancer specific cell death in response to palmitoylcarnitine is caused by elevated H_2O_2 and glutathione depletion. Turnbull PC, **Hughes MC** and Perry CGR.

3. Decreasing Mitochondrial H_2O_2 Emission and Increased Glutathione Levels mediate a unique fatty Acid-Induced HepG2 Growth. Turnbull PC, Dehghani AC, **Hughes MC**, Theriau C, Connor M and Perry CGR.

4. Auranofin coupled with serine and glycine depletion selectively targets p53-null cells for ROS induced cell death through antioxidant depletion. Turnbull PC, Dehghani AC, Deep B, Delfinis LJ, **Hughes** MC, Abdul-Sater A and Perry CGR.

5. The mitochondrial-enhancing drug Olesoxime improves quadriceps mitochondrial function and force recovery but not diaphragm function in a mouse model of Duchenne muscular dystrophy. Belissimo CA, Delfinis LJ, **Hughes** MC, Tadi P, Amaral C, Dehghani A and Perry CGR.

6. Collaboration with Dr. Robert Tsushima (York University) evaluating the alterations in mitochondrial bioenergetics in pancreatic β-cells following statin therapy.

7. Collaboration with Drs. David MacLennan and Anthony Gramolini (University of Toronto) evaluating mitochondrial bioenergetics in the left atria and ventricle from phospholamban-mutated (R9C) mice.

8. Collaboration with Dr. Keith Avin (Indiana University) evaluating the role of kidney dysfunction in mitochondrial-mediated cachexia

4 Early myopathy in Duchenne muscular dystrophy is associated with elevated mitochondrial H_2O_2 emission during impaired oxidative phosphorylation

This chapter is an original published article. It is presented in its published form.

Early myopathy in Duchenne muscular dystrophy is associated with elevated mitochondrial H_2O_2 emission during impaired oxidative phosphorylation. MC Hughes, SV Ramos*, PC Turnbull, IA Rebalka, A Cao, CMF Monaco, NE Varah, BA Edgett, JS Huber, P Tadi, LJ Delfinis, U Schlattner, JA Simpson, TJ Hawke and CGR Perry. The Journal of Cachexia, Sarcopenia and Muscle Wasting. DOI:10.1001/jcsm.12405.*

**Co-first authors*

Assay Development Prior to the start of Project 1:

1. Standardization of Whole Body *In Vivo* Muscle Function Measurements
2. Hindlimb Plantarflexor Force Production
3. Mouse μCT scanning and analysis SOP
4. Calcium Retention Capacity
5. Serum Creatine Kinase Evaluation
6. Caspase Activity Assay
7. Mitochondrial Membrane Potential
    a. The method I established to measure mitochondrial membrane potential was used to collect data for Chapters 4, 5 and 7. However, due to technical limitations related to signal artifacts specifically in permeabilized fibres, we deemed this data unusable and therefore it is not included in this thesis. However, the development of this method benefited the collaborative component of my PhD through my contribution to the publication by Smith et al., (2016) which employed this assay in isolated mitochondria, as classically performed. I also established a protocol to measure proton conductance for this publication.

Author Contributions: The majority of experiments for this project were carried about by Meghan Hughes. MH established and maintained the breeding colony required for this project as well as all subsequent studies (Chapter 5-7). MH ran all *in vivo* whole body functional testing as well as hindlimb plantarflexor force production measurements. MH completed μCT scans while PT completed the analysis following training from MH. MH and SV Ramos performed all tissue harvests and mitochondrial bioenergetic assays (respiration, mH_2O_2 emission, calcium retention capacity) together. Due to the nature of these experiments, two people are required in order to

efficiently complete all bioenergetic assays on fresh, viable tissue. As such, MH and SVR completed surgeries and bioenergetics experiments for all projects contributing to both theses (see Appendix B - additional contributions). MH ran all serum creatine kinase experiments, caspase assays and western blotting experiments. JAS performed the *in vivo* respiratory occlusion experiments. PCT completed glutathione measurements. CMFM and NEV analyzed TEM images. IAR, AC, BAE and JSH performed all immunohistochemistry staining and analysis. MH and CGRP wrote and revised the manuscript.

Early myopathy in Duchenne muscular dystrophy is associated with elevated mitochondrial H_2O_2 emission during impaired oxidative phosphorylation

Authors: MC Hughes[1*], SV Ramos[1*], PC Turnbull[1], IA Rebalka[2], A Cao[2], CMF Monaco[2], NE Varah[2], BA Edgett[3], JS Huber[3], P Tadi[1], LJ Delfinis[1], U Schlattner[4], JA Simpson[3], TJ Hawke[2] and CGR Perry[1†].

Affiliations:

[1]Muscle Health Research Centre, School of Kinesiology, York University, 4700 Keele Street, Toronto, ON, Canada, M6J 1P3.

[2]Department of Pathology and Molecular Medicine, McMaster University, 1280 Main St W, Hamilton, ON, Canada L8N 3Z5.

[3]Department of Human Health and Nutritional Sciences and Cardiovascular Research Group, University of Guelph, 50 Stone Rd E, Guelph, ON, Canada, N1G 2W1.

[4]Laboratory of Fundamental and Applied Bioenergetics (LBFA) and SFR Environmental and Systems Biology (BEeSy), University Grenoble Alpes, 621 Avenue Centrale, 38400 Saint-Martin-d'Hères, Grenoble, France

*Authors contributed equally to this work

Figure count: 9 + 5 supplemental

†Address for Correspondence:

Christopher Perry, PhD
School of Kinesiology and Health Science
Muscle Health Research Centre
344 Norman Bethune College
York University
4700 Keele Street
Toronto, Ontario M3J 1P3
(P) 416 736 2100 ext. 33232
cperry@yorku.ca

Abstract

Background: Muscle wasting and weakness in Duchenne muscular dystrophy (DMD) causes severe locomotor limitations and early death due in part to respiratory muscle failure. Given current clinical practice focuses on treating secondary complications in this genetic disease, there is a clear need to identify additional contributions in the etiology of this myopathy for knowledge-guided therapy development. Here we address the unresolved question of whether the complex impairments observed in DMD are linked to elevated mitochondrial H_2O_2 emission in conjunction with impaired oxidative phosphorylation. This study performed a systematic evaluation of the nature and degree of mitochondrial-derived H_2O_2 emission and mitochondrial oxidative dysfunction in DMD by designing *in vitro* models that attempt to mimic *in vivo* conditions known to be critical for the regulation of mitochondrial bioenergetics.

Methods: Mitochondrial bioenergetics were compared to functional and histopathological indices of myopathy early in DMD (4 weeks) in D2.B10-DMD^{mdx}/2J mice – a model that demonstrates severe muscle weakness. ADP's central effect of attenuating H_2O_2 emission while stimulating respiration was compared under two models of mitochondrial-cytoplasmic phosphate exchange (creatine-independent and dependent) in muscles that stained positive for membrane damage (diaphragm, quadriceps and white gastrocnemius).

Results: Pathway-specific analyses revealed complex I-supported maximal H_2O_2 emission was elevated concurrent with a reduced ability of ADP to attenuate emission during respiration in all three muscles (mH_2O_2: +17 to +197% in DMD vs WT). This was associated with an impaired ability of ADP to stimulate respiration at sub-maximal and maximal kinetics (-17 to -72% in DMD vs WT), as well as a loss of creatine-dependent mitochondrial phosphate shuttling in diaphragm and quadriceps. These changes largely occurred independent of mitochondrial density or

abundance of respiratory chain complexes, except for quadriceps. This muscle was also the only one exhibiting decreased calcium retention capacity which indicates increased sensitivity to calcium-induced permeability transition pore. Increased H_2O_2 emission was accompanied by a compensatory increase in total glutathione, while oxidative stress markers were unchanged. The mitochondrial bioenergetic dysfunctions were associated with induction of mitochondrial-linked caspase 9, necrosis, and markers of atrophy in some muscles as well as reduced hindlimb torque and reduced respiratory muscle function.

Conclusions: These results provide evidence that Complex I dysfunction and loss of central respiratory control by ADP and creatine cause elevated oxidant generation during impaired oxidative phosphorylation. These dysfunctions may contribute to early stage disease pathophysiology and support the growing notion that mitochondria are a potential therapeutic target in this disease.

Keywords: bioenergetics, Duchenne muscular dystrophy, mitochondria, reactive oxygen species, respiration, oxidative stress

Introduction

Duchenne muscular dystrophy (DMD) is a debilitating disease that causes progressive muscle atrophy and weakness. Immobility related to skeletal muscle weakness manifests in childhood while eventual respiratory muscle failure causes ~40% of deaths in early adulthood [45, 2]. Inherited mutations in the gene dystrophin causes a loss in the normal function of this sarcolemmal-cytoskeletal protein [229]. Subsequent disruptions to cell membrane stability and cytoskeletal organization are linked to increased cytosolic calcium, oxidative stress and cell death that are cellular hallmarks of this disease [93, 2]. Moreover, a highly pro-inflammatory environment worsens the myopathy [230]. In this light, it has been proposed that mitochondrial dysfunctions arise from these multiple cellular stressors and may even reciprocate as a direct influence on muscle fibre degeneration [34, 195, 33].

Given there is no cure for DMD, identifying secondary contributions has been a major focus for guiding therapy development [46]. Indeed, current clinical practice targets inflammation rather than the genetic mutation itself [46]. To this end, compounds that target mitochondria have attenuated the myopathy in mouse models of this disease. For example, the quinone-based idebenone - an electron shuttler [207] - improved cardiac function and exercise performance in mice [208] as well as cardiac and respiratory function in Patients with DMD [210, 211, 209]. These drugs were developed based in part on pre-clinical evidence of impaired mitochondrial respiratory function in skeletal muscle of mice with DMD [30, 33, 231] and humans [30, 29]. As such, identifying additional mitochondrial abnormalities could guide further therapy development.

As mitochondria naturally emit H_2O_2 during oxidative phosphorylation, impairments to efficient electron transport through the electron transport system could contribute to excessive H_2O_2 emission. To our knowledge, only one study to date has compared mitochondrial-specific H_2O_2

emission in DMD muscle to wildtype [33]. This well-designed investigation demonstrated the expected impairment in oxidative phosphorylation and calcium retention capacity (an index of permeability transition linked to apoptosis), but also reported a surprising decrease in mitochondrial H_2O_2 emission in C57bl/10-*mdx* mice. However, a concomitant increase in oxidant buffering capacity was noted and could represent a compensatory response in this mouse model, suggesting that mitochondrial H_2O_2 may indeed be elevated *in vivo*, particularly in relation to impaired oxidative phosphorylation [33]. Given these observations, it is uncertain if mitochondrial H_2O_2 is elevated in DMD.

The design of *in vitro* assessments of both mitochondrial H_2O_2 emission and respiration can be essential for capturing the degree of bioenergetic dysfunction in a disease. It is well-established that ADP lowers mitochondrial H_2O_2 emission while stimulating oxidative phosphorylation by virtue of reduced premature electron slip from the electron transport system [232]. As such, it is possible that mitochondrial dysfunction could manifest as a loss of central control by ADP to govern both H_2O_2 emission and respiration during oxidative phosphorylation. Furthermore, it has also been proposed that creatine is essential for optimizing ADP-stimulation of oxidative phosphorylation and attenuation of H_2O_2 emission. This is believed to occur through a process of 'high energy phosphate shuttling' facilitated by mitochondrial creatine kinase (mtCK) **(**Figure 2) [200, 146, 150, 147] whereby the rapidly diffusing phosphocreatine export ultimately accelerates mitochondrial matrix ADP cycling, reduces H_2O_2 emission and stimulates oxidative phosphorylation [205, 157]. Overall, given the complexity of how bioenergetics are governed by ADP and creatine, it follows that a re-design of *in vitro* protocols may reveal the extent to which DMD impairs the governance of mitochondrial H_2O_2 emission during oxidative phosphorylation.

In this investigation, we determined the precise mechanism and degree of mitochondrial dysfunction in dystrophic locomotor muscles as well as respiratory muscle. The ability of ADP to attenuate H_2O_2 emission during oxidative phosphorylation was determined in the D2.B10-DMD^{mdx}/2J (D2.*mdx)* mouse. This model demonstrates severe muscle atrophy and weakness that more closely mimics human disease progression compared to the classic C57bl/10-*mdx* mice due to attenuated muscle regeneration arising from a natural mutation in TGF-β4 binding protein 4 in the background D2A strain [60, 59]. By employing these methodological approaches, we provide new evidence that a central impairment in ADP and creatine's control of bioenergetics is linked specifically to increased Complex I-supported H_2O_2 concurrent with impaired respiration. This observation is ubiquitous across locomotor and respiratory muscles and may be related to muscle weakness, atrophy and cellular pathology in very early stages of DMD.

Material and Methods

Animal Care

The 4-week old D2.*mdx* animals originated from a colony maintained at York University (Toronto, Canada) and sourced from Jackson Laboratories (Bar Harbor, United States). Post-weaning (28 days) animals were housed with male littermates until they underwent functional testing, at which time they were singly housed. 4-week old DBA/2J wildtype (WT) mice were obtained directly from Jackson Laboratories due to breeding challenges with this strain. Upon arrival, DBA/2J mice were singly housed and given a minimum of 72 hours to acclimatize before experiments were performed. All animals were provided access to standard chow and water ad libitum. All experiments and procedures were approved by the Animal Care Committee at York University (AUP Approval Number 2016-18) in accordance with the Canadian Council on Animal Care.

Body Composition and Functional Assays

Timeline of measurements

A variety of tests were performed on mice before surgical removal of muscle for *in vitro* analyses. Specifically, 2 days prior to surgery, whole body functional testing (Cage Hang Time, Forelimb Grip Strength and Voluntary Wheel Running) were performed. On the day of surgery, prior to muscle harvest, animals underwent a μCT scan for muscle volume (see below). Due to tissue limitation, a separate set of animals were used for histochemistry and TEM analysis. Finally, in order to avoid confounding influences of force/pressure measurements on mitochondrial bioenergetic analysis, a separate set of animals were used to assess esophageal pressure transduction and *in vivo* force production.

In Vivo μCT Scans

In vivo body scans were performed using μCT (SkyScan 1278, Bruker-microCT, Kontick, Belgium). Mice were anaesthetized and maintained with isoflurane anesthetic during the scans.

Mice were laid supine with hind limbs extended and secured in place. Body scans were completed with a 100 μm resolution using a 0.5 mm aluminum filter at 50 kV and 996 μA, with a 30 ms exposure time and a 0.75° rotation step. Following scans, lower limb muscle volume was analyzed by first reconstructing the image using NRecon (software version 1.7.0.4, Bruker-microCT, Kontick, Belgium). Reconstructed images were then imported into CTAn (software version 1.15.4.0, Bruker-microCT, Kontick, Belgium) where the region of interest was selected and analyzed. The region of interest for hind-limb muscle volume was landmarked from the top of the patella to the ankle joint and was quantified by setting thresholds for fat free mass (76-102), expressed as volume (mm^3) of lean mass/g body weight.

Voluntary Wheel Running

Animals were placed in individual cages equipped with a locked 14 cm diameter running wheel and rotation counter (VDO m3 bike computer, Mountain Equipment Co-Op, Vancouver, Canada). After 24 hours of acclimatization, wheels were unlocked and distance run over 24 hours was recorded.

Cage Hang Time

Animals were placed on top of a metal cage lid approximately 30 cm above soft bedding and positioned so that all four limbs grasped the cage. The cage lid was inverted so that the mouse was hanging, and a timer was started. Cage hang time was recorded for a maximum of 180 seconds. Animals that fell off prior to 180 seconds were given three minutes to recover before a second trial and third trial. The maximum hanging time for each animal was recorded [233].

Forelimb Grip Strength

A metal grid was attached to a force transducer (Mark 10 Digital Force Gauge, Copiague, NY) set to peak tension mode. The force transducer was placed on the edge of a table top allowing the grid to extend past the table. Mice were removed from their cages by the tail and brought towards the

grid until such time that the mice grasped the grid with their forepaws. Upon grasping, animals were pulled away from the grid until their grasp was broken. Peak tension was recorded, and the trial was repeated twice more. If the animal did not show resistance to the experimenter, the trial was not recorded. Maximum peak tension from the best of 3 trials was used for analysis [233].

Esophageal Pressure Transduction

Esophageal pressure measurements were performed as previously described [234]. Briefly, mice were anesthetized with an isoflurane/oxygen mix (2%:100%) and body temperature was maintained at 37°C. Mice were intubated using a 20-gauge angiocatheter (Becton, Dickinson and Company) to maintain an open/unobstructed airway. Compressible tubing was attached to the angiocatheter to facilitate inducible airway occlusions. Esophageal pressure (P_{es}) was measured with a 1.2F catheter (Transonic) recorded on LabScribe2 software (iWorx) and analyzed with Spike2 software (Cambridge Electronic Design). Immediately after 2 min of baseline P_{es} recording, the trachea was occluded, and P_{es} was monitored for changes. Tracheal occlusions were initiated at end expiratory volume to ensure consistency of the Diaphragm length-tension relationship. Maximum inspiratory pressure (P_{Iocc}) was evaluated after 30s of occlusion when pressure generation reached a plateau.

In Vivo Hind-limb Force Production

In vivo force production of the hind-limb plantarflexor muscles was partially adapted from previous methods [235]. In brief, mice were anesthetized with isoflurane and placed on a platform maintained at 37° C. The left foot was secured to a footplate attached to an Aurora Scientific 305C muscle lever (Aurora, Ontario, Canada) so that the ankle's axis of rotation coincided with that of the servomotor shaft. The knee was clamped in place such that the knee and ankle angles were both 90°. Contraction of the plantarflexors was controlled through percutaneous stimulation of the

sciatic nerve. Peak isometric torque was determined by varying the voltage delivered to the sciatic nerve at a frequency of 60 Hz and 0.2-ms square wave pulse. Torque as a function of stimulation frequency was measured during 7 isometric contractions at varying stimulation frequencies (40, 60, 80, 100, 120, 140, 160 Hz). Maximum torque produced during the torque-frequency protocol was recorded and compared between groups.

Serum Creatine Kinase

Blood was collected through cardiac puncture and allowed to clot at room temperature for 30 minutes. Following clotting, blood was spun at 1000g for 10 minutes and serum was collected. Creatine kinase activity was measured spectrofluorometrically (QuantaMaster 80, HORIBA Scientific, Edison, NJ, USA) based on the autofluorescence of NADPH (excitation – 340 nm, emission – 450 nm) using the Pointe Scientific Serum Creatine Kinase kit (Pointe Scientific, Canton, MI, USA). Creatine kinase activity (U/L) was calculated from the rate of NADPH production (F/min) applied to a standard curve produced under the same conditions and normalized to volume dilution.

Selection of Muscles for Analyses

A subset of mice (n=2) were injected *i.p*. with 1% Evans Blue Dye (Sigma, St Louis, MO, USA) (w/v) in phosphate-buffered saline (PBS, pH 7.5) sterilized by passage through a Millex®-GP 0.22 μm filter (Millipore, Bedford, MA, USA). 16 hours post injection animals were sacrificed and muscles were harvested to allow for the visual inspection of dye uptake. We selected skeletal muscles that stained positive for Evans Blue Dye to ensure mitochondrial bioenergetics were assessed in muscle displaying a severe phenotype **(Supplemental Figure 1).** The vastus intermedius of the quadriceps (Quad), comprised of IIA, IIX and IIB fibres [236], and white gastrocnemius (WG), comprised of predominantly of IIB fibres [236] were selected in addition to Diaphragm which also showed substantial membrane damage.

Mitochondrial Bioenergetic Assessments

Preparation of Permeabilized Muscle Fibre Bundles (PmFB)

This technique is partially adapted from previous methods and has been described elsewhere [237-240]. Briefly, muscles were removed from mice during anaesthesia with isoflurane. We performed all tissue harvests in approximately half an hour to minimize the chance of negative effects of isoflurane on mitochondrial function as has been reported with longer 6 hour durations [241]. The Quad and WG from the non-stimulated leg as well as a strip of Diaphragm were removed and immediately placed in ice-cold BIOPS, containing (in mM): 50 MES Hydrate, 7.23 K_2EGTA, 2.77 CaK_2EGTA, 20 imidazole, 0.5 dithiothreitol, 20 taurine, 5.77 ATP, 15 PCr, and 6.56 $MgCl_2 \cdot 6\ H_2O$ (pH 7.1). Each muscle was trimmed of connective tissue and fat and divided into several small muscle bundles (~2–7 mm, 1.0–2.5 mg wet weight). Each bundle was gently separated along the longitudinal axis to form bundles that were treated with 40 μg/ml saponin in BIOPS on a rotor for 30 minutes at 4° C. Bundles destined for Complex I and pyruvate dehydrogenase complex mitochondrial H_2O_2 emission (mH_2O_2) measurements (described below) were also treated with 35 μM 2,4-dinitrochlorobenzene (CDNB) during the permeabilization step to deplete glutathione and allow for detectable rates of mH_2O_2 [242]. Following permeabilization, the PmFB were divided into three groups; 1) bundles intended for high resolution respirometry were placed in MiR05 containing (in mM): 0.5 EGTA, 10 KH_2PO_4, 3 $MgCl_2 \cdot 6\ H_2O$, 60 K-lactobionate, 20 Hepes, 20 Taurine, 110 sucrose and 1 mg/ml fatty acid free BSA (pH 7.1) while 2) bundles intended for mH_2O_2 were placed in Buffer Z containing (in mM): 105 K-MES, 30 KCl, 10 KH_2PO_4, 5 $MgCl_2 \cdot 6\ H_2O$, 1 EGTA and 5mg/ml BSA (pH 7.4). PmFB were washed on a rotor at 4°C in MiR05 or Buffer Z until the measurements were initiated. 3) bundles intended for calcium retention capacity were placed in Buffer Y + 1 mM EGTA containing (in mM): 250 sucrose, 10 tris-HCl, 20 tris-base, 10 KH_2PO_4 and 0.5mg/mL BSA and washed on a rotor at 4° C for 10 minutes. PmFB were

then transferred to a second wash of Buffer Y + 10 μM blebbistatin (BLEB, see below) and were washed on a rotor at 4°C until measurements were initiated. Following permeabilization and washing, all mitochondrial bioenergetic measurements were performed in the same order from one animal to another and between groups to ensure consistent durations of the wash step.

Mitochondrial Respiration

High-resolution O_2 consumption measurements were conducted in 2 ml of respiration medium (MiR05) using the Oroboros Oxygraph-2k (Oroboros Instruments, Corp., Innsbruck, Austria) with stirring at 750 rpm at 37 °C [239, 240, 243-245]. Respiration medium contained 20mM Cr to saturate mitochondrial creatine kinase or no creatine to prevent the activation of mtCK [243, 246]. A third condition of 13.9mM PCr and 9.1mM Cr was used to provide an equilibrium across mtCK as occurs in skeletal muscle at rest *in vivo* [247]. For ADP-stimulated respiratory kinetics, standard procedures to determine Complex I and II-supported respiration were employed [245]. 5 mM pyruvate, accompanied by 2 mM malate, were added as Complex I-specific substrates (via generation of NADH to saturate electron entry into Complex I) followed by a titration of submaximal ADP (25 μM and 500 μM) and maximal ADP (5 mM). Cytochrome *c* was added to test for mitochondrial membrane integrity, with all experiments demonstrating <10% increase in respiration. Finally, succinate (20 mM) was then added to saturate electron entry into Complex II. All experiments were conducted in the presence of 5μM BLEB in the assay media to prevent spontaneous contraction of PmFB which has been shown to occur in response to ADP at 37 °C which alters respiration rates [243, 248, 244]. Each protocol was initiated with a starting [O_2] of approximately 350 μM and was completed before the oxygraph chamber [O_2] reached 150 μM as done previously [239, 240, 243-245]. Polarographic oxygen measurements were acquired in 2 s intervals with the rate of respiration derived from 40 data points and expressed as pmol/s/mg wet

weight. PmFB were weighed in ~1.5 ml of tared BIOPS (ATP-containing relaxing media) to ensure PmFB remained relaxed.

Mitochondrial H_2O_2 Emission (mH_2O_2)

mH_2O_2 was determined fluorometrically (QuantaMaster 40, HORIBA Scientific, Edison, NJ, USA) in a quartz cuvette with continuous stirring at 37°C, in 1 mL of Buffer Z supplemented with 10 μM Amplex Ultra Red, 0.5 U/ml horseradish peroxidase, 1 mM EGTA, 40 U/ml Cu/Zn-SOD1,5 μM BLEB and 20mM Cr. Site specific induction of mH_2O_2 was measured through the addition of either 10 mM pyruvate and 2 mM malate (NADH, Complex I), 10 mM succinate ($FADH_2$, Complex I via reverse electron flux from Complex II) or 2.5 μM antimycin A (Complex III). Additionally, using 0.5 μM rotenone, a complex I inhibitor, plus 10 mM pyruvate, electron slip specific to pyruvate dehydrogenase complex was also measured in CDNB-treated fibres as noted above [242]. Following the induction of state II mH_2O_2 by Complex I and Complex II substrates, a titration of ADP was added to progressively attenuate mH_2O_2. Complexes I and II-supported mH_2O_2 were repeated with no creatine in the assay buffer to compare ADP's effects without mtCK-mediated phosphate shuttling. All measurements were made in the presence of 1 μM BLEB to prevent ADP-induced rigor as described above. The rate of H_2O_2 emission was calculated from the slope (F/min), from a standard curve established with the same reaction conditions and normalized to fibre bundle wet weight as described above, or citrate synthase content determined by western blot in muscle sampled from the same mouse as bioenergetics.

Mitochondrial Calcium Retention Capacity

This assay is partially adapted from methods previously described [249]. Mitochondrial calcium retention capacity measurements were completed spectrofluorometrically (QuantaMaster 80, HORIBA Scientific, Edison, NJ, USA) in a cuvette with continuous stirring at 37° C, in 300 μL

of Buffer Y containing 1 μM Calcium Green-5N (Invitrogen), 2 μM tharpsigargin, 5 mM 2-deoxyglucose, 2 U/mL hexokinase, 20mM creatine, 5 μM BLEB and 40 μM EGTA. Prior to the initiation of each experiment, the cuvette was placed on a stir plate with **500 μl water** and 10 mM EGTA. The water was then aspirated from the cuvette but not rinsed, leaving the EGTA coating on the cuvette walls to chelate any residual Ca^{2+} in the assay buffer. Minimum fluorescence was obtained following the addition of the PmFB and 5 mM glutamate + 2 mM malate to the assay buffer. Calcium uptake was then initiated by a single 8 nmol pulse of $CaCl_2$. Subsequent 4 nmol pulses of Ca^{2+} were added until mitochondrial permeability transition pore (PTP) opening was evident. Two 0.5 mM pulses of Ca^{2+} were then added to saturate the fluorophore and establish a fluorescent maximum. All experiments were conducted at 37 °C. Changes in free Ca^{2+} in the cuvette during mitochondrial Ca^{2+} uptake were then calculated using the known K_d for Calcium Green 5-N and the equations established for calculating free ion concentrations using ion-sensitive fluorophores [250]. After the experiments, the fibres were rinsed in double deionized H_2O, lyophilized in a freeze-dryer (Labconco, Kansas City, MO, USA) for >4 h and weighed on a microbalance (Sartorius Cubis Microbalance, Gottingen, Germany).

In Vitro Muscle and Blood Analyses

Caspase Activity

Enzymatic activities of caspase 3 and caspase 9 were measured fluorometrically using substrates Ac-DVED-AMC and Ac-LEHD-AMC (Enzo Life Sciences, Farmingdale, NY) as previously described [251, 252].

Transmission Electron Microscopy (TEM)

Fresh plantaris tissue was immediately fixed in 2% (v/v) glutaraldehyde in 0.1 mol/l sodium cacodylate buffer and processed as described previously [253]. Eight representative micrographs from a unique fiber containing a portion of the subsarcolemmal region adjacent to the nucleus with

most of the image containing the intermyofibrillar area were acquired at x15000 magnification. Quantification was achieved using the Nikon Elements software by manually outlining mitochondria and converting these to actual size using a calibration grid [254].

Glutathione

Glutathione was assessed as previously described [255]. GSH was assessed by UV-HPLC monitoring of NEM-GSH while GSSG was assessed by fluorescent-HPLC by tracking O-pthalymide (OPA, Sigma-Aldrich, Oakville, Canada) tagged GSH through a flow-through cuvette following GSSG conversion to GSH (FireflySci 8830, NY, USA) in a QuantaMaster 40 spectrofluorometer (HORIBA, NJ, USA). All values were referenced to protein concentration and reported in μmol/g protein. USA).

Western Blotting

An aliquot of frozen Quad, WG and Diaphragm (10–30 mg) from each animal was homogenized in a plastic microcentrifuge tube with a tapered teflon pestle in ice-cold buffer containing (mm): 40 Hepes, 120 NaCl, 1 EDTA, 10 $NaHP_2O_7 \cdot 10H_2O$ pyrophosphate, 10 β-glycerophosphate, 10 NaF and 0.3% CHAPS detergent (pH 7.1 adjusted using KOH). Protein concentrations were determined using a BCA assay (Life Technologies, Carlsbad, CA, USA). Fifty μg of denatured and reduced protein was subjected to 6–12% gradient SDS-PAGE followed by transfer to low-fluorescence polyvinylidene difluoride membrane. Membranes were blocked with LI-COR Odyssey Blocking Buffer (LI-COR, Lincoln NE, USA) and immunoblotted overnight (4°C) with antibodies specific for each protein. A commercially available monoclonal antibody was used to detect electron transport chain proteins (human OXPHOS Cocktail, ab110411; Abcam, Cambridge, UK, 1:250 dilution), including V-ATP5A (55 kDa), III-UQCRC2 (48 kDa), IV-MTCO1 (40 kDa), II-SDHB (30 kDa) and I-NDUFB8 (20 kDa). Commercially available

polyclonal antibodies were used to detect voltage dependent anion carrier 2 (VDAC 2) (32059, 32 kDa; Santa-Cruz, 1:1000), adenine nucleotide translocase 1 (ANT 1) (ab180715, 33 kDa; Abcam, 1:1000), citrate synthase (ab96600; Abcam, 1:3000), **MnSOD** (ab13534; Abcam, 1:2000), 4-hydroxynoneonal (4-HNE) (ab46545; Abcam, 1:1000) and sarcomeric s-mtCK (Dr Uwe Schlattner, Grenoble, France; 42 kDa, 1:1000). The mtCK antibody has been validated previously to confirm specificity[256]. Protein carbonylation was detected using the OxyBlot Protein Oxidation Detection Kit (Millipore Sigma, Burlington, MA, USA).

After overnight incubation in primary antibodies, membranes were washed three times, for 5 minutes each time, in TBST and incubated for 1 hour at room temperature with the corresponding infrared fluorescent secondary antibody (LI-COR). Immunoreactive proteins were detected by infrared imaging (LI-COR CLx; LI-COR) and quantified by densitometry (ImageJ, http://imagej.nih.gov/ij/). All images were normalized to a whole membrane Amido Black total protein stain (A8181, Sigma, St Louis, MO, USA). A double band was detected at 33 kDa for ANT 1 in skeletal muscle. Similar results were achieved when analyzing either band. As such, the bottom band closer to 33kDa has been reported.

Histochemistry

Immediately after removal from the animal, Quad and WG muscles were embedded in O.C.T compound (Tissue Tek), frozen in liquid nitrogen-cooled isopentane and stored at -80°C until analysis. Haematoxylin and eosin (H&E) staining was performed on hind-limb muscle sections (8 μm thickness) to determine average cross-sectional area (CSA) and the area of necrotic muscle fibres (i.e. fibres with fragmented sarcoplasm and/or areas of inflammatory cells). Three images spaced evenly throughout the muscle were used for analysis, and a total of 100 fibres per Quad and 100 fibres per WG were counted (n=3 per group). Necrotic area was expressed as a percentage

of the whole muscle section. To determine fibrotic area, skeletal muscle sections were stained with Masson's Trichrome (fibrotic regions stain blue for collagen), and expressed as a percentage of the whole muscle section. Quad and WG sections were imaged Nikon 90i-eclipse microscope (Nikon Inc.; Melville, NY) and analyzed with the NIS Elements AR software (v 4.6; Nikon).

For the Diaphragm, a piece attached to the rib cage was immediately placed in 10% neutral buffered formalin for 72 hours. After 72 hours, the Diaphragm was placed in 70% ethanol where it was preserved until processing using routine procedures. Processed Diaphragm was embedded in paraffin wax (Thermo Fisher Scientific, Burlington, Canada) prior to sectioning (5 μm thickness). Diaphragm sections were stained with H&E to measure CSA and necrotic area, and picrosirius red to measure fibrotic area (fibrotic regions stain red for collagen). Two to five images (4 on average) were used for Diaphragm analyses, and 200-250 fibres were used to determine CSA (n=7 per group). Diaphragm sections were imaged using an Olympus FSX100 light microscope (Olympus), Richmond Hill, Canada) and analyzed in cellSens software (Olympus) for necrosis and fibrosis analysis, or ImageJ (http://imagej.nih.gov/ij/) for CSA analysis.

Statistics

Results are expressed as means ± SEM. The level of significance was established as $p<0.05$ for all statistics. The D'Agostino – Pearson omnibus normality test was first performed to determine whether data resembled a Gaussian distribution. Given all data passed normality, parametric tests were then performed. For all data excluding state III respiration, state III mH_2O_2 emission and torque-frequency data, statistical differences were analyzed using unpaired t-tests between WT and DMD groups, within a given muscle where applicable. State III respiration, mH_2O_2 emission and torque-frequency curves were analysed within a given muscle (where applicable) using a 2-

way ANOVA with a main effect for group being reported (GraphPad Prism Software, La Jolla, CA, USA).

Results

Early onset of muscle wasting and weakness in D2.mdx mice

Body weight was 20% lower in D2.*mdx* mice ($p<0.05$, **Figure 1a**). Diaphragm fibre CSA was 30% lower in D2.*mdx* which demonstrates muscle atrophy at this young age. ($p<0.05$, **Figure 1c).** In contrast, D2.*mdx* Quad CSA was increased by 42% ($p<0.05$, **Figure 1c)** while WG CSA was not different between groups (**Figure 1c**) despite a 15% reduction in lower limb muscle volume ($p=0.07$, **Figure 1b**) suggesting other lower limb muscles may have been atrophied. Serum creatine kinase activity was evaluated as a marker of net muscle damage with activity elevated by 392% in D2.*mdx* mice ($p<0.05$, **Figure 1d).**

In conjunction with muscle wasting, muscle weakness was also evaluated through several approaches. Four week old D2.*mdx* mice demonstrated reduced 24-hour voluntary wheel running (-98%, $p<0.05$, **Figure 1e**), cage hang time (-53%, $p<0.05$**, Figure 1f**) and forelimb grip strength (-32%, $p<0.05$, **Figure 1g)**. Given the voluntary nature of these *in vivo* assays and the potential for neurological contributions to performance, muscle-specific measurements of force production were also performed. *In vivo* force production in the hind-limb plantarflexors revealed a main effect for decreases in D2.*mdx* torque production as a function of frequency ($p<0.05$, **Figure 1h)** as well as a 13% decrease in maximum isometric torque ($p<0.05$, **Figure 1i)** compared to WT. Diaphragm force production, measured through maximal inspiratory pressures produced during tracheal occlusion, revealed significant decreases in D2.*mdx* pressures from 15-30 seconds of tracheal occlusion ($p<0.05$) but there were no differences at the earlier time points (0-10 seconds) of the occlusion protocol (**Figure 1j**).

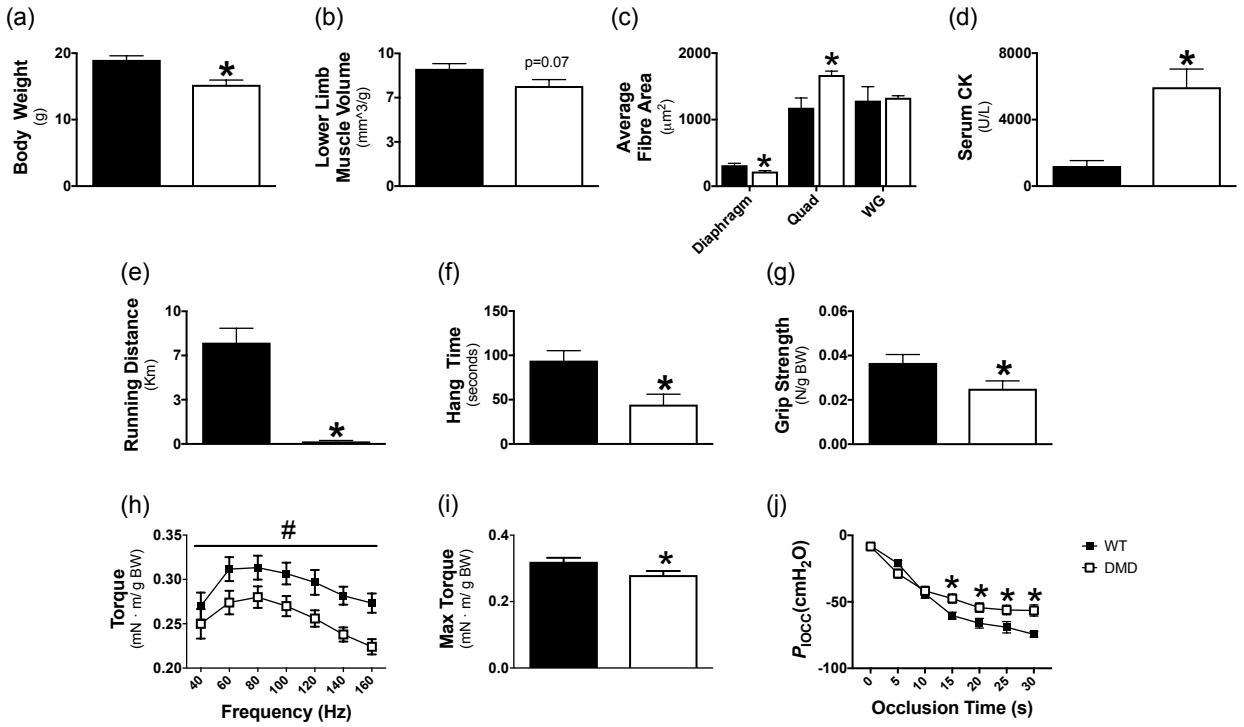

Figure 4-1: Evaluation of muscle wasting and weakness in DMD. Body weight (a, n=8-10), microCT analysis of lower limb muscle volume (b, n=6-7) and muscle-specific cross-sectional area (CSA) using wheat germ stain for Diaphragm (n=6) and H&E for Quad (n=3) and WG (n=3) (c). Whole body muscle damage was quantified by serum creatine kinase (CK) activity (d, n=5-7). Indices of muscle function were assessed by 24-hour voluntary wheel running (e, n=13-14), cage hang time (f, n=10-11) and forelimb grip strength (g, n=9-11). Lower hindlimb force production was assessed in vivo using through torque-frequency relationship (h) followed by a max-torque challenge (i, n=5-6). Respiratory function in vivo was assessed through esophageal pressure transduction to determine maximal inspiratory pressure (PIocc) (j, n=7). Results represent mean ± SEM; # $p<0.05$ main effect compared to WT; * $p<0.05$ compared to WT.

Elevated Complex I induced mH_2O_2 during oxidative phosphorylation in D2.mdx mice

We first determined whether the central role of ADP in stimulating respiration and attenuating H_2O_2 emission was altered. Complex I-supported respiration and H_2O_2 emission was stimulated with NADH generated by pyruvate (5mM) and malate (2mM) in the presence of low/physiological (25μM), high sub-maximal (500μM) and saturating concentrations (5mM) of ADP. This titration

was repeated with (+Cr) and without (-Cr) 20mM creatine to drive energy transfer dependent or independent of mtCK, respectively **(**as depicted in **Figure 2)**.

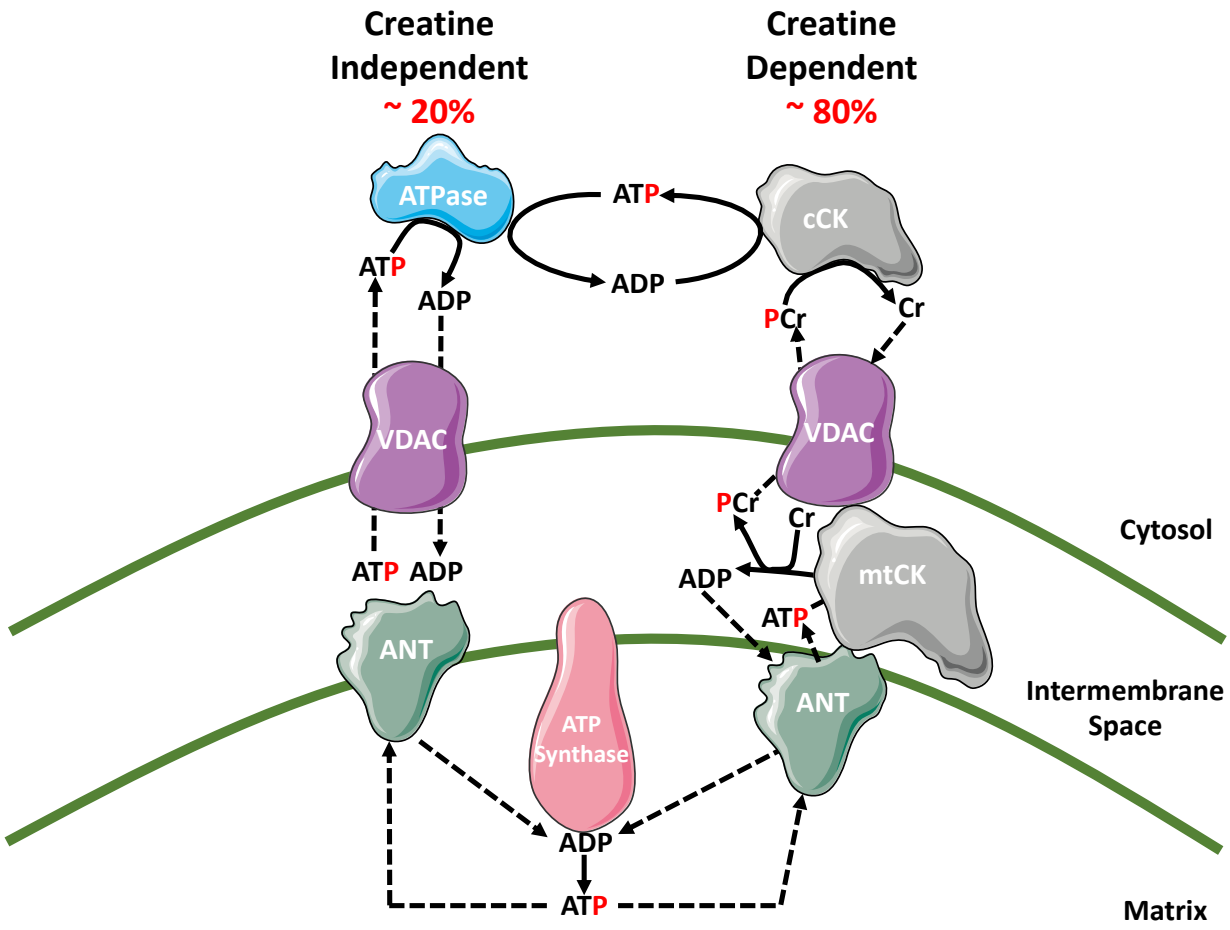

Figure 4-2: Schematic representation of energy transfer between mitochondria and cytosol. The leading model for energy exchange involves a creatine-independent (-Cr) and creatine-dependent (+Cr) pathway. The left side depicts the –Cr pathway whereby ADP/ATP transfer occurs solely through diffusion across voltage dependent anion carrier (VDAC) on the outer mitochondrial membrane and adenosine nucleotide translocase (ANT) on the inner mitochondrial membrane. The right side depicts the +Cr pathway where, in the presence of Cr, energy transfer is facilitated by mitochondrial creatine kinase (mtCK) through the transfer of the phosphate group from ATP to Cr, producing phosphocreatine (PCr) and ADP in the inner membrane space. The PCr is exported via VDAC into the cytosol while the ADP is directly recycled back via ANT into the mitochondrial matrix. Figure adapted from Aliev et al., 2011, Guzun et al., 2012, Myer et al., 1984 and Wallimann et al., 2011 *[146, 150, 147, 157]***.**

In both -Cr and +Cr, ADP-stimulated respiration was decreased at various ADP concentrations in Diaphragm (-12 to -46%), Quad (-47 to -72%) and WG (-27 to -53%) in DMD vs WT ($p<0.05$, **Figure 3**). Similar impairments in respiration were seen when mtCK flux was maintained by both PCr and Cr **(Supplemental Figure 2)**. mH_2O_2 was elevated during oxidative phosphorylation in both –Cr and +Cr across low and high [ADP] in DMD Diaphragm (+17 to 88%, $p<0.05$), Quad and (+19 to 197%, $p<0.05$) and WG (+18 to +74%, $p<0.05$) vs WT **(Figure 4).**

We also determined the capacity for Complex I-supported H_2O_2 emission in the absence of ADP. This test promotes maximal electron slip and oxidant generation at Complex I given ADP is not present to attenuate membrane potential and promote forward electron flux. As such, the test reveals the capacity of oxidant generation by Complex I independent of the influence of ADP (State II). Respiration is driven by proton leak through uncoupling pathways independent of ATP synthase. Proton leak-dependent respiration trended lower in D2.*mdx* Diaphragm (-31%, $p=0.06$), and was significantly lower in D2.*mdx* Quad (-58%, $p<0.05$) and WG (-39%, $p<0.05$) vs WT (**Supplemental Figure 3a**). Concurrent pyruvate/malate-supported H_2O_2 in the absence of ADP was unchanged in Diaphragm, elevated by 110% in Quad ($p<0.05$) and tended to be higher in WG (+47%, $p=0.09$) vs WT (**Supplemental Figure 3b).**

We then determined the degree to which other pathways support mH_2O_2. Complex III (2.5μM Antimycin A) and pyruvate dehydrogenase-supported mH_2O_2 (10mM pyruvate, 0.5μM Rotenone to inhibit Complex I) were decreased in the Quad (-53%, $p=0.05$) and WG (-60%, $p<0.05$), while the Diaphragm showed a trend for increased Complex III mH_2O_2 (+35%, $p=0.11$) and no differences in pyruvate dehydrogenase-supported mH_2O_2 between D2.*mdx* and WT (**Supplemental Figure 4a and 4b)**. Normalizing mH_2O_2 to Complex III subunit content

(**Supplemental Figure 4c)** or pyruvate dehydrogenase E1α content (**Supplemental Figure 4d)** altered rates such that no differences existed in mH_2O_2 in any muscle vs WT.

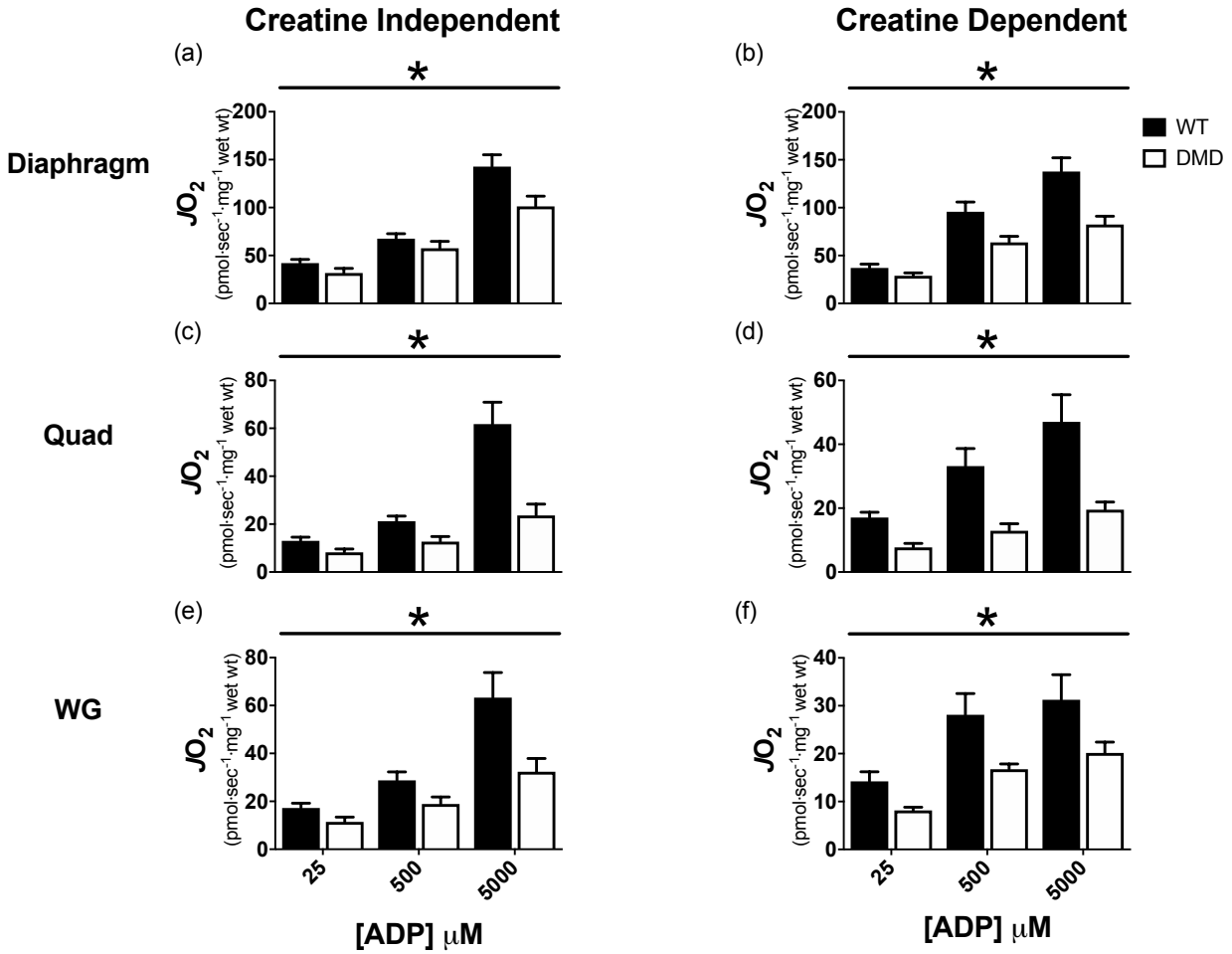

Figure 4-3: Complex I-supported respiration in DMD. State III respiration, supported by Complex-I substrates pyruvate (5mM) and malate (2mM), was assessed in the absence (Creatine Independent) and presence (Creatine Dependent) of 20mM creatine at physiological (25μM), sub-maximal (500μM) and maximal (5000μM) [ADP]. Assessments of bioenergetic function were completed in Diaphragm (a-b), Quad (c-d) and WG (e-f) muscles. Results represent means ± SEM; n=8-14; * $p<0.05$ compared to WT.

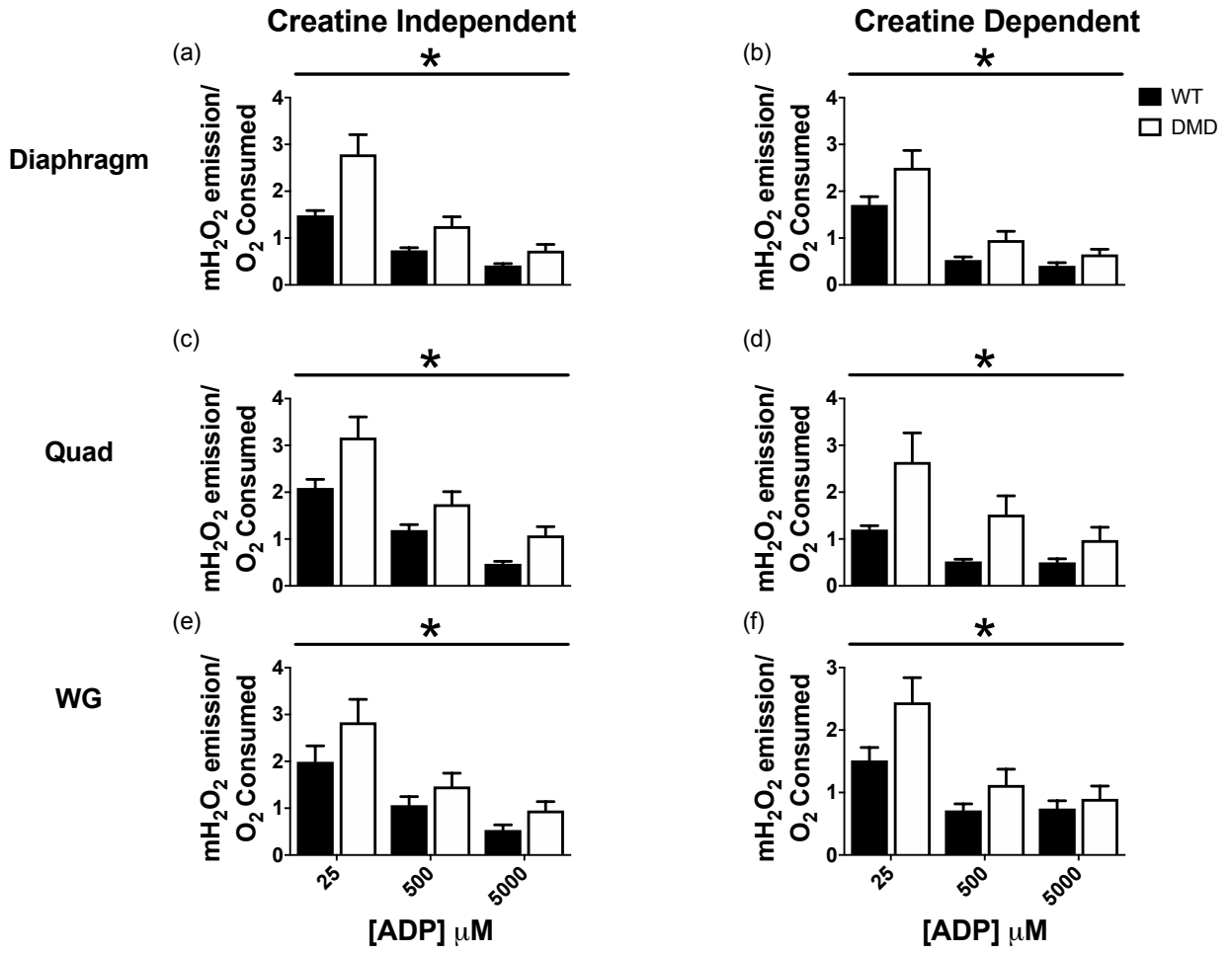

Figure 4-4: mH_2O_2 emission during oxidative phosphorylation in DMD. State III mH_2O_2, supported by Complex-I substrates pyruvate (5mM) and malate (2mM), was assessed in the absence (Creatine Independent) and presence (Creatine Dependent) of creatine at physiological (25μM), sub-maximal (500μM) and maximal (5000μM) [ADP]. Assessments of bioenergetic function were completed in Diaphragm (a-b), Quad (c-d) and WG (e-f) muscles. Results represent means ± SEM; n=8-14; * $p<0.05$ compared to WT.

Impaired creatine sensitivity in oxidative D2.mdx muscle

Given impaired bioenergetics were seen in both creatine-independent and creatine-dependent models of phosphate shuttling, we also compared whether creatine insensitivity existed in D2.*mdx* to gain insight on the role of mtCK in this disease. As seen in **Table 1**, at 500μM ADP, creatine tended to increase respiration in both Diaphragm (+43%, $p=0.06$) and Quad (+57%, $p=0.08$), and decreased mH_2O_2 (Diaphragm: -37%, $p<0.05$; Quad: -56%, $p<0.01$) in WT consistent with its proposed role in facilitating phosphate shuttling (**Figure 2**). In contrast, +Cr had no effect on

respiration at 500μM in any D2.*mdx* muscle vs -Cr or on mH_2O_2 in Quad or WG, although it lowered mH_2O_2 in D2.*mdx* Diaphragm (-42%, $p<0.05$; **Table 1**) suggesting mtCK and phosphate shuttling are impaired in DMD in addition to loss of control by ADP (**Figure 2**).

Table 4-1: Impairment in creatine sensitivity with 500μM ADP in DMD

	Wildtype			D2.*mdx*		
	-Cr	+Cr	P Value (-Cr vs +Cr)	-Cr	+Cr	P Value (-Cr vs +Cr)
JO_2 (pmol·sec^{-1}·mg^{-1} wet wt)						
Diaphragm	67.2 ± 5.2	95.8 ± 10.2	P<0.05	57.6 ± 7.2	63.7 ± 6.4	P=0.94
Quad	21.2 ± 2.2	33.2 ± 5.5	P=0.07	12.7 ± 2.1	12.9 ± 2.2	P=0.53
WG	28.7 ± 3.5	28.1 ± 4.4	P=0.94	18.9 ± 3.0	16.7 ± 1.1	P=0.53
mH_2O_2/O_2 Consumed						
Diaphragm	0.73 ± 0.06	0.53 ± 0.07	P<0.05	1.25 ± 0.21	0.72 ± 0.10	P<0.05
Quad	1.19 ± 0.11	0.52 ± 0.05	P<0.01	1.76 ± 0.26	1.54 ± 0.40	P=0.64
WG	1.09 ± 0.19	0.72 ± 0.10	P=0.16	1.46 ± 0.28	1.11 ± 0.25	P=0.37

Creatine Dependent (+Cr), Creatine Independent (-Cr), Quadriceps (Quad), White Gastrocnemius (WG). Values represent mean ± SEM, (n=8-14).

Increased susceptibility to PTP opening and elevations in mitochondria-derived apoptosis in D2.mdx Quad

Previous work has shown that calcium-overload leads to PTP opening more rapidly in DMD Diaphragm and Tibialis Anterior muscle from C57bl/10-*mdx* mice[35, 33]. We next determined whether reduced calcium retention capacity was related to the elevated mH_2O_2 during oxidative phosphorylation seen in the D2.*mdx* mice **(Figure 5a,b)**. D2.*mdx* Diaphragm and WG muscle showed no differences in the [Ca^{2+}] required to induce PTP opening vs WT (**Figure 5b)** whereas Quad required 62% less [Ca^{2+}] vs WT ($p<0.05$, **Figure 5b).** Caspase 9 activity was also elevated in Quad (+25%, $p<0.05$) suggesting the reduced calcium retention capacity is related to mitochondrial-induced apoptosis in this muscle unlike WG (**Figure 5c).** Interestingly, despite no differences in calcium retention capacity, caspase 9 activity tended to be elevated in D2.*mdx*

Diaphragm (+43%, p=0.08; **Figure 5c).** These elevations in caspase 9 did not result in activation of its downstream target, caspase 3, in any muscle (**Figure 5d).**

Given the decrease in D2.*mdx* Quad calcium retention capacity and subsequent increase in mitochondria-derived apoptotic signalling, further analysis of mitochondria structure and morphology was performed. Due to tissue limitations, the plantaris muscle, which displays a similar fibre type composition to the vastus intermedius component of the Quad used for calcium retention capacity [236], was used for TEM analysis. D2.*mdx* plantaris muscle was found to contain swollen mitochondria (**Figure 5e),** regardless of the mitochondrial location (subsarcolemmal vs intermyofibrillar). D2.*mdx* plantaris muscle also contained less mitochondria per unit area **(Figure 5f)** but due to their larger size, no differences in mitochondria density was evident (**Figure 5g).**

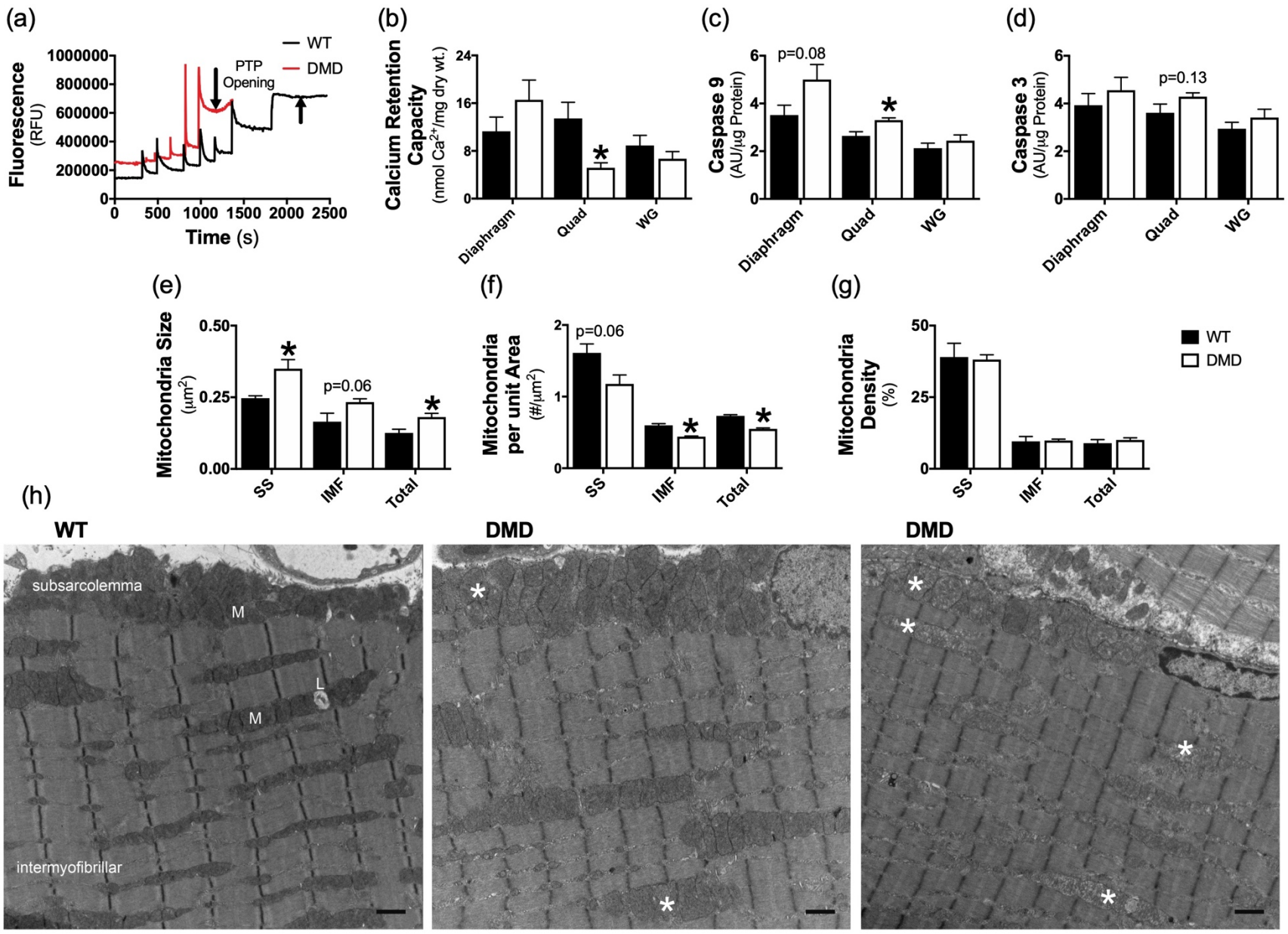
(a)
Fluorescence (RFU)
1000000
800000
600000
400000
200000
0
0 500 1000 1500 2000 2500
Time (s)
WT
DMD
PTP Opening
(b)
Calcium Retention Capacity
(nmol Ca2+/mg dry wt.)
24
16
8
0
Diaphragm
Quad
WG
(c)
Caspase 9
(AU/µg Protein)
p=0.08
6
4
2
0
Diaphragm
Quad
WG
(d)
Caspase 3
(AU/µg Protein)
p=0.13
6
4
2
0
Diaphragm
Quad
WG
(e)
Mitochondria Size
(µm2)
0.50
0.25
0.00
p=0.06
SS
IMF
Total
(f)
Mitochondria per unit Area
(#/µm2)
p=0.06
2
1
0
SS
IMF
Total
(g)
Mitochondria Density
(%)
50
25
0
SS
IMF
Total
WT
DMD
(h)
WT
DMD
DMD
subsarcolemma
M
L
M
intermyofibrillar

Figure 4-5: Evaluation of mitochondrial calcium retention capacity, content and disbursement. Calcium retention capacity, an index of susceptibility to permeability transition pore opening (a), was assessed in permeabilized fibres from Diaphragm, Quad and WG muscle (b); n=6-8. Mitochondrial-induction of apoptosis was evaluated through caspase 9 activity (c) followed by it's down-stream target caspase 3 (d); n=7. Transmission electron micrographs were acquired in the plantaris muscle and analyzed for mitochondrial size (e, mean area, μm^2), distribution (f, # per μm^2) and density (g, μm^2 x # per μm^2 x 100) within the subsarcolemmal (SS) area and intermyofibrillar (IMF) area of the muscle. Representative images (h) demonstrate the large accumulation of swollen mitochondria (*) in DMD animals relative to the normal conformation of WT mitochondria (M); scale bar = 1 μm, n=2-3. Results represent mean ± SEM; * $p<0.05$ compared to WT.

Increased redox buffering with no change in markers of cellular oxidative stress in D2.mdx mice

Content of the reduced form of glutathione (GSH) content was increased in D2.*mdx* Quad (+55%, $p<0.05$) and WG (+38%, $p<0.05$), and tended to be higher in Diaphragm (+8%, $p=0.09$), indicative of a compensatory increase in redox buffering (**Figure 6a)** consistent with increased mH_2O_2 noted earlier. WG muscle demonstrated elevated levels of oxidized glutathione (GSSG) content (+50%, $p<0.05$) relative to WT, while no differences were found in Quad or Diaphragm (**Figure 6b).** However, total glutathione (GSH + 2xGSSG) was elevated or tended to be elevated in all muscles (Diaphragm: +8%, $p=0.09$; Quad: +54%, $p<0.05$; WG: +38%, $p<0.05$; **Figure 6c)** predominately due to increases in reduced GSH content. Importantly, the ratio of GSH:GSSG was unchanged in all muscles, suggesting the elevated mH_2O_2 was buffered to prevent cellular oxidation at this early time point **(Figure 6d)**. Indeed, western blotting for lipid peroxidation **(Figure 6e)** and protein carbonylation **(Figure 6f),** indicators of whole cell oxidative stress, revealed no differences between D2.*mdx* and WT muscle. Mitochondrial matrix MnSOD was lower in Quad (-29%, $p<0.05$) and WG (-22%, $p<0.05$) with no change in diaphragm being observed (**Figure 6g**).

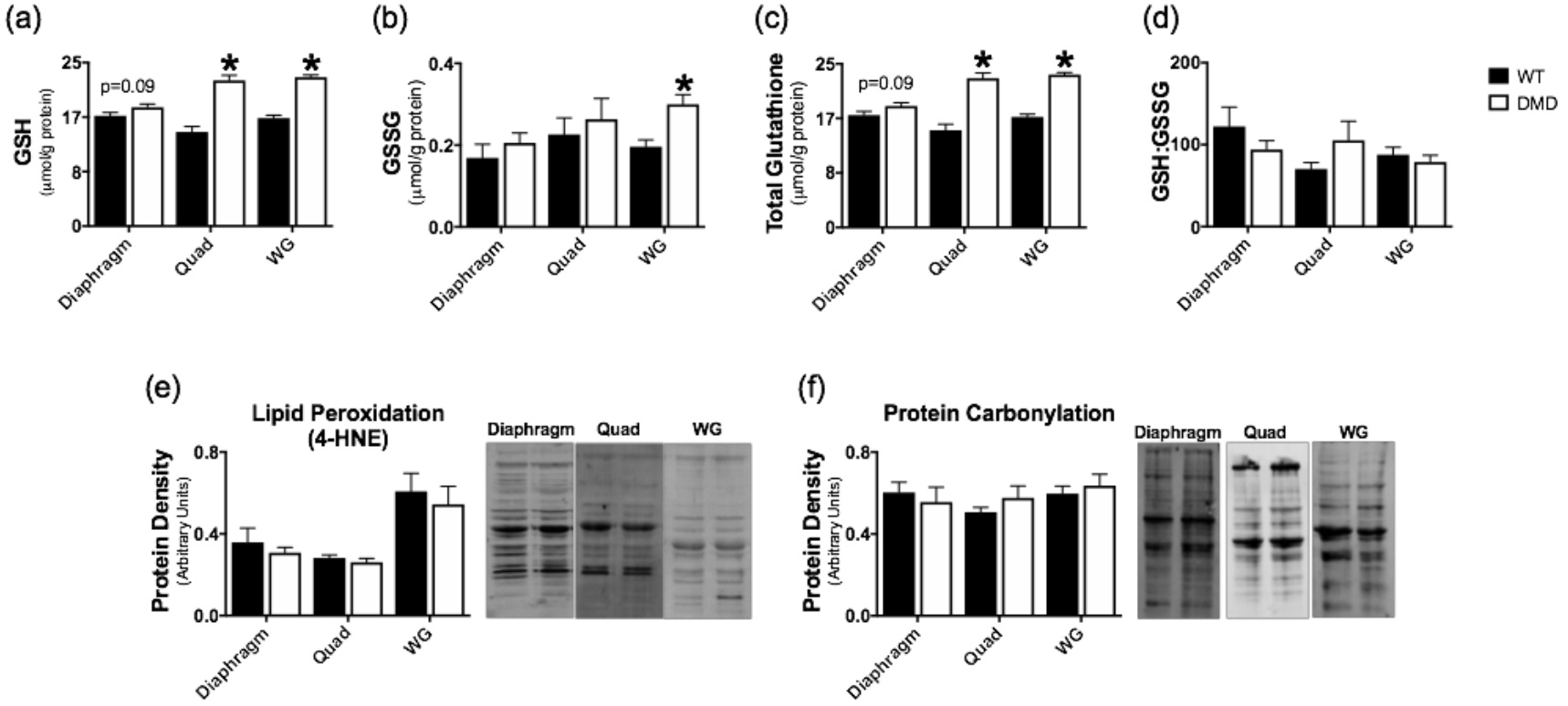

Figure 4-6: Evaluation of redox buffering capacity and whole cell oxidative status. Glutathione was measured in muscle homogenate using HPLC-UV for the detection of GSH (a) and HPLC-Fluorescence for the detection of GSSG (b). The GSH:GSSG ratio (c) and total glutathione (d) were calculated from GSH and GSSG measurements; n=6. Whole muscle lysate was used for the quantification of proteins modified through lipid peroxidation (e) and carbonylation (f) as well as the quantification of protein content of MnSOD (g); n=6-8. Results represent mean ± SEM; * $p<0.05$ compared to WT

Muscle-specific alterations in key regulators of energy shuttling

Given the alterations in state III respiration and mH_2O_2 in D2.*mdx* muscle, we next quantified key regulators of energy shuttling. ANT 1 and VDAC 2, situated in the inner and outer mitochondrial membranes respectively (**Figure 2)**, were unchanged in Diaphragm muscle but were significantly decreased in D2.*mdx* Quad (ANT 1: -48%, $p<0.05$; VDAC 2: -33%, $p<0.05$) and WG (ANT 1: -53%, $p<0.05$; VDAC 2: -36%, $p<0.05$) relative to WT **(Figure 7a and 7b).** Similarly, mtCK content was unchanged in Diaphragm but significantly lower in D2.*mdx* Quad (-45%, $p<0.05$) and WG (-38%, $p<0.05$; **Figure 7c).** Citrate synthase protein content was reduced in Quad only (-23%, $p<0.05$; **Figure 7d**). Normalizing respiration to citrate synthase content (Supplemental Figure 5) as validated previously [257] generally did not explain the changes in respiration observed when normalized per mg weight seen in **Figure 3**. Quantification of the complexes comprising the ETC was also completed to provide an index of ETC content. ETC subunit contents were unchanged relative to WT in both Diaphragm (**Figure 7e)** and WG (**Figure 7g)** muscle apart from a decrease in Complex II subunit content in D2.*mdx* Diaphragm (-15%, $p=0.06$, **Figure 7e).** However, Quad demonstrated decreases or trends for decreases in subunit content of Complex I (-38%, $p<0.05$), II (-36%, $p=0.08$), III (-34%, $p<0.05$), IV (-55%, $p<0.05$) and V (-19%, $p=0.09$) as well as the sum of all 5 complex subunits (-37%, $p<0.05$) (**Figure 7f**).

Bioenergetic impairments are associated with elevations in muscle damage in D2.mdx muscle

Muscle specific membrane damage was evaluated though Evans Blue Dye staining in a separate subset of animals. 16 hours post injection of 1% Evans Blue Dye, animals were sacrificed, and muscle was visually inspected for dye uptake. Dye uptake, which occurs in muscles with damaged cell membranes[55], was evident in the Quad, WG and tricep brachii muscles with minimal uptake occurring in the soleus, plantaris, extensor digitorum longus and the tibialis anterior. A striated pattern of dye uptake was evident in the Diaphragm muscle (**Supplemental Figure 1).**

Necrotic area was elevated in Diaphragm (5.5% vs 0% of total area vs WT, $p<0.05$; **Figure 8a)**, Quad (31.8% vs 0.6%, $p<0.05$; **Figure 8b)**, and WG (48.2% vs 0.2%, $p=0.06$; **Figure 8c).** Fibrotic area was also elevated in Diaphragm (12.7% vs 8.4% of total area vs WT, $p<0.05$; **Figure 8d)**, Quad: 17.0% vs 6.3%, $p<0.05$; **Figure 8e)** and WG: 22.0% vs 3.5%, $p<0.05$; **Figure 8f).**

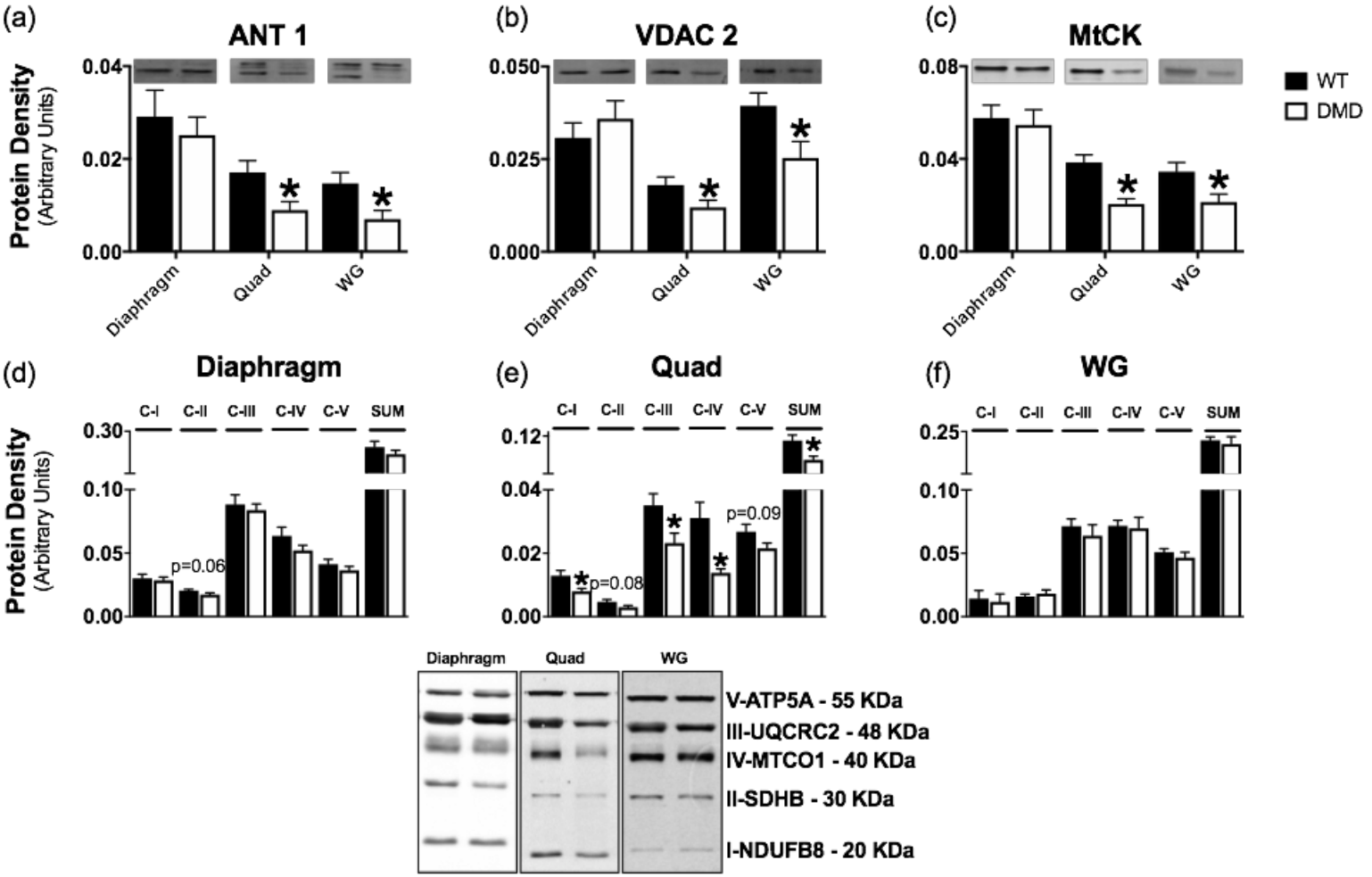

Figure 4-7: Muscle-specific changes in essential regulators of bioenergetics in DMD. Protein content of adenine nucleotide translocase 1 (ANT 1) on the inner mitochondrial membrane (a), voltage dependent anion carrier 2 (VDAC 2) on the outer mitochondrial membrane (b), mitochondrial creatine kinase (mtCK) found in the inner membrane space (c) and citrate synthase which catalyses the first reaction in the citric acid cycle (d). Protein content of electron transport chain components were also quantified in Diaphragm (e), Quad (f) and WG (g). Results represent mean ± SEM; n=8-12; * $p<0.05$ compared to WT

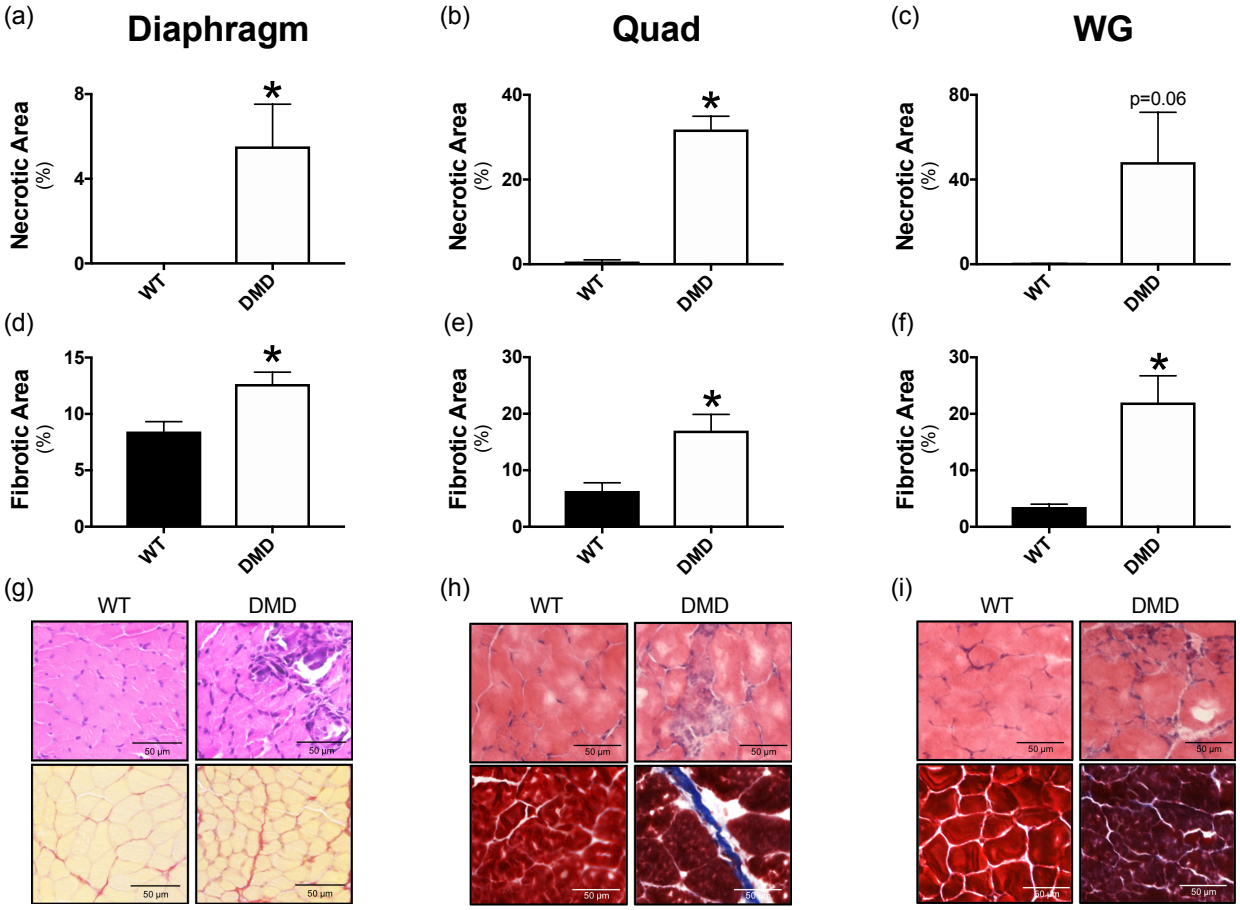

Figure 4-8: Quantification of muscle damage in DMD. Necrosis was evaluated in Diaphragm (a), Quad (b) and WG (c) using haemotoxylin and eosin (H&E) staining in all muscles. Fibrosis was evaluated in Diaphragm (d) using picrosirius red and in Quad (e) and WG (f) using Masson's trichrome. Results represent mean ± SEM; n=3-6; * $p<0.05$ compared to WT. Representative images of Diaphragm (g, magnification, 40x), Quad (h, magnification, 20x) and WG (i, magnification, 20x).

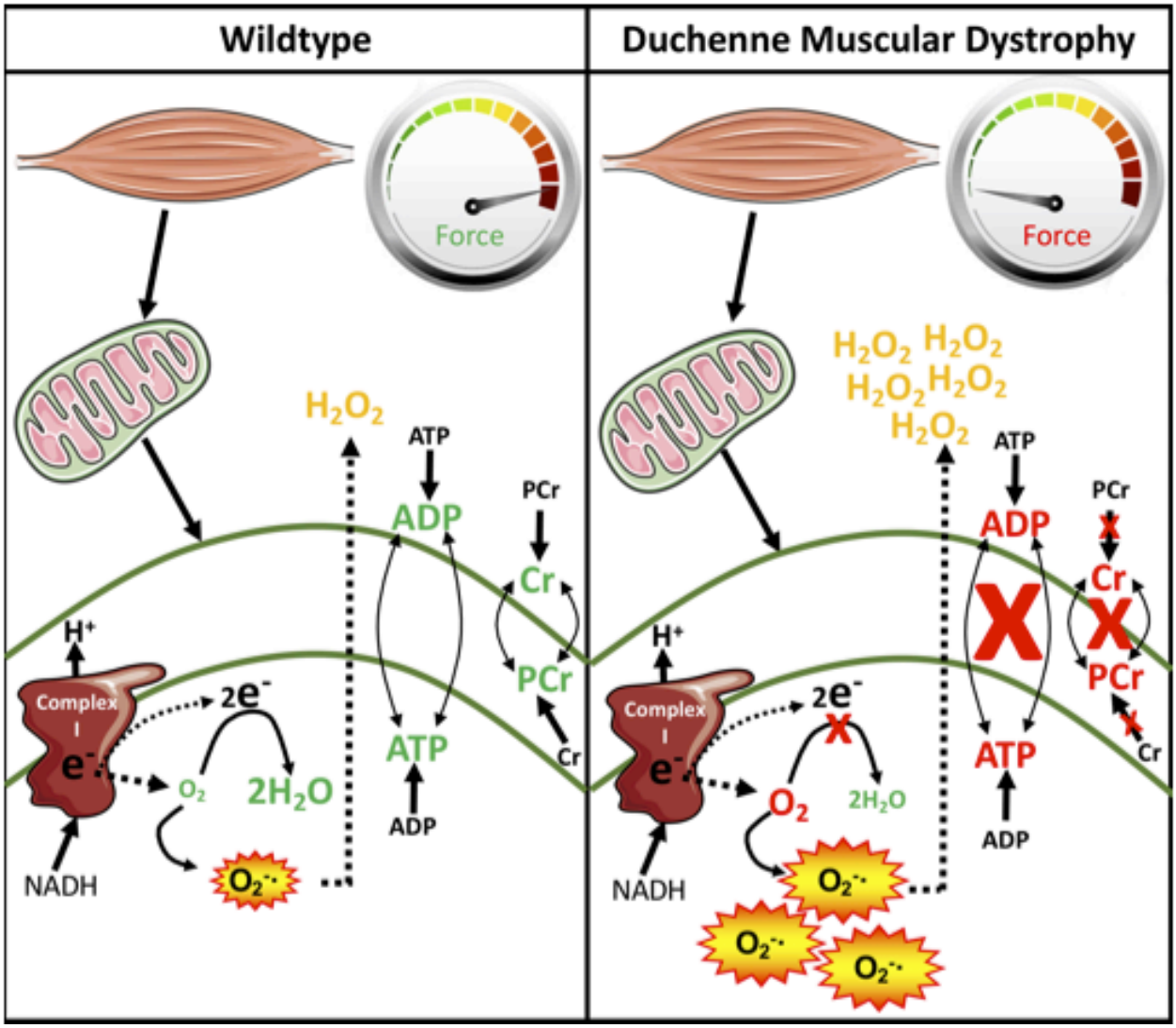

Figure 4-9: Summary of the relationship between impaired mitochondrial bioenergetics and myopathy in DMD. Specific dysfunctions in Complex I and central respiratory control by ADP and creatine cause elevated oxidant generation during impaired oxidative phosphorylation in DMD in association with a loss of muscle force.

Discussion

Oxidative stress has long been implicated as a contributor to the myopathy of Duchenne muscular dystrophy. However, identifying the precise source of elevated oxidants has remained controversial. In this study, we demonstrate that mH_2O_2 is elevated concurrent with impaired oxidative phosphorylation specific to Complex I-supported respiration. An impairment in the ability of ADP to both stimulate respiration and attenuate mH_2O_2 was central to these impairments. These bioenergetic deficits occurred early in the disease process (4 weeks of age) and were associated with severe myopathy in skeletal muscles and Diaphragm. By identifying a potential new relationship between elevated mH_2O_2, impaired oxidative phosphorylation and myopathy in Diaphragm (respiratory) and limb muscle (locomotor; see summary Figure **9)**, these findings suggest that DMD may be a candidate for therapeutics that attenuate mH_2O_2 [258] and improve mitochondrial respiratory control.

Several factors warranted a re-evaluation of mH_2O_2 in DMD. First, an elegant study by Godin et al [33] demonstrated an unexpected decrease in mH_2O_2 in the tibialis anterior of the classic C57bl/10-*mdx* mouse, but this occurred concurrently with increased redox buffering capacity suggesting compensation occurred in response to an underlying redox stress [33]. Furthermore, the degree of mitochondrial dysfunction may differ across muscles in relation to the extent of myopathy which warrants comparisons of muscle types, particularly given the known regenerative capacities of the classic C57bl/10-*mdx* model [51, 52]. The design of *in vitro* protocols to measure mitochondrial respiration and mH_2O_2 must also be considered given 1) ADP governs both processes concurrently, 2) disease-related stressors may alter sensitivity to low ADP concentrations to a different extent than saturating conditions, 3) mitochondrial-cytosolic energy exchange is thought to occur through either direct ADP/ATP cycling or Cr/PCr shuttling via mtCK, and 4) there are multiple sources of oxidant generation that contribute to net mH_2O_2. By controlling

for these factors, a general pattern of impaired Complex I activity, creatine insensitivity and ADP insensitivity in the regulation of mH_2O_2 and respiration was identified in both dystrophic respiratory and locomotor muscles.

Concurrent impairments in Complex I and governance by ADP

At 4 weeks of age, D2.*mdx* Diaphragm, Quad and WG muscle exhibit elevated Complex I-supported mH_2O_2 during oxidative phosphorylation. This pattern appeared to be due to several factors. First, the maximal rate of mH_2O_2 supported by Complex I was increased as seen in the absence of ADP's influence on membrane potential (State II conditions). The impairments at Complex I were not explained by altered protein content of the NDUFB8 subunit. This suggests post-translational modifications may have occurred. Indeed, Complex I activity can be decreased by oxidation of specific cysteine residues [259] but the degree to which this occurs in DMD remains to be determined. Also, while superoxide production prior to dismutation to H_2O_2 was not assessed, the increases in H_2O_2 emission during respiration are suggestive of increased superoxide production particularly given MnSOD was lower in Quad and WG. It is also possible that the lower leak respiration in the absence of ADP reflects less uncoupling, which may contribute to elevated membrane potential-dependent Complex I superoxide production [232].

Furthermore, low/physiological to high concentrations of ADP were unable to attenuate mH_2O_2 to the same extent as WT. The impaired control by ADP in skeletal muscle may not be related to changes in mitochondrial content given ETC markers were unchanged in Diaphragm and WG similar to what has been reported recently in C57bl/10-*mdx* mouse soleus and extensor digitorum longus [260]. Rather, this may be explained partially by limited ADP/ATP exchange due to decreased protein expression of VDAC 2 and ANT 1 in Quad and WG, or octameric mtCK, the regulator of high energy phosphate shuttling. There was no change in the content of these proteins

in Diaphragm which suggests that post-translational regulation of these proteins may have been altered. Indeed, all three proteins are redox sensitive [261-263]. ANT and VDAC also have known phosphorylation sites [264, 265] although the physiological relevance of this regulatory paradigm remains unknown. Furthermore, mtCK is highly susceptible to oxidative modifications, leading to enzymatic inactivation and octamer dissociation, as well as formation of crystalline mitochondrial inclusion bodies, all resulting in loss of function [153, 152]. The present findings suggest future examination of post-translational regulation of Complex I, isoforms of ANT 1 and VDAC 2, as well as mtCK may reveal how multiple cellular stressors in DMD lead to the observed mitochondrial dysfunctions. Lastly, while no other site of mitochondrial oxidant generation tested in this investigation demonstrated altered mH_2O_2 (reverse electron flux from complex II, complex III and pyruvate dehydrogenase), additional sites could be considered in future investigations at this early age [266, 267].

To our knowledge, this is the first study to demonstrate impairments in ADP-stimulated respiration at both low and maximal kinetics in D2.*mdx* Diaphragm muscle. The respiratory impairments in Quad and WG are consistent with previous reports in humans [29, 30] and C57bl/10-*mdx* skeletal muscle [30, 33, 231, 268]. However, the role of creatine-dependent phosphate shuttling through mtCK was not assessed which means these earlier studies only report impairments in creatine-independent ADP/ATP cycling similar to the present findings, albeit with one exception that also reported impaired creatine sensitivity in oxidative muscles [201]. Given the creatine-dependent model is predicted to be the dominant system of energy exchange [157], the lack of effect of creatine on respiration in DMD may be particularly detrimental to muscle function, in particular, at high workloads with repeated contractions (**Table 1**). As noted above, changes in ANT 1, VDAC 2 and mtCK might contribute to this loss of control by ADP in Quad and WG but alternative

mechanisms are likely for Diaphragm, further highlighting the importance of considering post–translational modifications.

Possible relationships between mitochondrial bioenergetics and myopathy in DMD

Mitochondrial induction of apoptosis and necrosis has been linked to several diseases that also exhibit elevated mitochondrial ROS and impaired oxidative phosphorylation [269, 270, 226, 271-273]. It is thought that impairments in both processes can contribute to the induction of PTP formation as can occur under conditions of calcium overload [274]. Such PTP formation has already been implicated in DMD myopathy in response to calcium stress [33, 35]. However, the synergistic link with mH_2O_2 had not been demonstrated. Indeed, an increase in mitochondrial $[Ca^{2+}]$ alone is relatively ineffective at inducing PTP formation, but mitochondrial sensitivity to $[Ca^{2+}]$ can be drastically increased through elevated ROS [172]. Furthermore, the increases in caspase 9 seen in Quad are consistent with previous reports of greater cytochrome *c* release in dystrophic muscle [275] – a process that is known to be triggered in part by mitochondrial ROS during induction of the PTP [276]. Overall, the present findings suggest that elevated mH_2O_2 contributes to this calcium-overload induction of PTP in Quad but not necessarily in Diaphragm or WG at this early stage of the disease (Figure 4). Surprisingly, Quad displayed hypertrophy based on fibre cross sectional area which may be compensation to caspase 9-mediated cell death. Indeed, this early hypertrophy is consistent with observations in Quad of young boys with DMD that was later followed by atrophy in advanced stages of the disease [67].

In contrast to the present study, previous work has shown heightened sensitivity to Ca^{2+}-induced PTP in Diaphragm in C57bl/10-*mdx* mice. Methodological differences may contribute to these divergent findings as previous studies have produced divergent results depending on whether PTP opening was assessed in terms of elapsed time in response to a single bolus of Ca^{2+} [35] or

identifying the minimal concentration required to trigger PTP as in the present study [33, 35]. These discrepant findings suggest the approach used to determine PTP sensitivity to Ca^{2+} can change the conclusion, and that comparison to other proxies of PTP are warranted.

It is possible that calcium-independent modulators of mitochondrial dysfunction and induction of cell death are present in DMD. While not assessed in this study, mH_2O_2 also activates necrosis in a PTP-independent manner by activating nuclear factor-kappa B (NF-κB) [137] and up-regulating the pro-inflammatory cytokine tumour necrosis factor-alpha (TNF-α) [277, 181]. Indeed, antioxidants that lower mH_2O_2 have been shown to prevent muscle wasting in a TNF-α induced model of cachexia [278], and an anti-TNF-α antibody (*Remicade)* reduces muscle necrosis and inflammation in C57bl/10-*mdx* mice [141]. Further examination of alternative mechanisms by which impaired mitochondrial bioenergetics contributes to cell death in DMD may be fruitful considering the necrosis observed in the present study (Diaphragm, WG, Quad) was not consistently linked to a calcium-induction of PTP, particularly in Diaphragm which displayed atrophy without caspase 9 activation.

Perspectives on redox homeostasis in DMD: reconciling with previous literature

While cytoskeletal-based NADPH oxidase activity is increased in DMD skeletal muscle [130], the contribution of mitochondrial-specific ROS across all muscle types has received surprisingly little attention. To our knowledge, only one previous study has directly measured mH_2O_2 in DMD skeletal muscle. Using Tibialis Anterior muscle from 6-week old C57bl/10-*mdx* mice, Godin et al demonstrated a surprising decrease in mH_2O_2 [33]. This decrease appeared to be due to increases in mH_2O_2 scavenging capacity which may be related to extensive muscle regeneration at this age in C57bl/10-*mdx* mice that occurs after an earlier period of peak necrosis at 3-4 weeks [51, 52]. This robust increase in scavenging capacity may reflect a compensation in response to an

underlying elevation in mH_2O_2. As such, we re-evaluated the relationship between mH_2O_2 and myopathy in a model with less regenerative capacity [59, 60] and in muscles displaying membrane damage (Supplemental Figure 1). While a direct comparison of mitochondrial bioenergetics in muscles with and without damaged cell membranes was not performed, heterogeneous rates and degrees of myopathy between muscles should be taken into consideration when evaluating the contribution of the mitochondria to DMD. It is also possible that the differences between these previous observations and the present investigation may be due to the age (6 weeks vs 4 weeks currently) or the muscle analysed (tibialis anterior previously), but this remains to be determined.

Contrary to previous work in young C57bl/10-*mdx* mice which showed a more oxidized GSH:GSSG ratio [279, 21], the present investigation revealed no changes in the glutathione ratio in all muscles analyzed. Despite the differences in mH_2O_2 emission rates, both the present study and the work by Godin et al., demonstrate increases in redox buffering capacity. Similarly, in accordance with previous findings [21, 33], no differences in lipid peroxidation were detected through 4-HNE or protein carbonylation levels between WT and DMD muscles. These results suggest that the increases in buffering capacity are sufficient to tolerate the stress created by elevated mH_2O_2 and prevent detectable oxidative damage from occurring at this early time point. However, it is plausible that the buffering capacity of the cell will become overwhelmed and result in oxidative damage as the disease progresses. Furthermore, 4-HNE and carbonylation are measures of irreversible oxidative damage and therefore, the present investigation does not rule out H_2O_2 acting as a reversible redox signal within the cell. Future investigation into the time-course of redox stress in the context of both reversible and irreversible modifications in this D2.*mdx* model of DMD are warranted.

Conclusions

In summary, this investigation identified elevations in Complex I-supported mH_2O_2 during oxidative phosphorylation concurrent with impaired ADP and creatine control of respiration in DMD Diaphragm, Quad and WG muscle. These impairments were associated with a greater propensity for calcium-induced PTP and caspase 9 activation in Quad but the degree to which they are related to apoptosis in other muscles requires further investigation. The potential association between these mitochondrial impairments and myopathy at an early stage of DMD may guide the pre-clinical testing of mitochondrial-targeted therapeutics to restore normal mH_2O_2 and Complex I-supported oxidative phosphorylation, particularly by rescuing ADP and creatine control of bioenergetics. While such an approach would not target the primary cause of the disease, the addition of mitochondrial therapies warrants consideration given existing standards of care already focus on treating other secondary complications of DMD in the absence of genetic therapies.

Conflicts of interest: none

Funding: Funding was provided to CGRP and TJH by the National Science and Engineering Research Council (#436138-2013 and # 2018-06324, respectively) with infrastructure supported by Canada Foundation for Innovation, the James. H. Cummings foundation and the Ontario Research Fund. MCH was supported by an NSERC CGS-PhD scholarship. SVR was supported by an Ontario Graduate Scholarship. PCT was supported by an NSERC CGS-PhD scholarship. IAR was supported by an Ontario Graduate Scholarship. CMFM was supported by an NSERC PGS-PhD and the Michael DeGroote Doctoral Scholarship of Excellence.

Acknowledgements: The authors certify that they comply with the ethical guidelines for authorship and publishing in the Journal of Cachexia, Sarcopenia and Muscle.

Author Contributions: CGRP, MCH, SVR, JAS and TJH contributed to the rationale and study design. All authors conducted experiments and/or analyzed all data. CGRP and MCH wrote the manuscript. All authors contributed to the interpretation of the data and manuscript preparation. All authors have approved the final version of the manuscript and agree to be accountable for all aspects of the work. All persons designated as authors qualify for authorship, and all those who qualify for authorship are listed.

Supplementary Data – Included in published manuscript

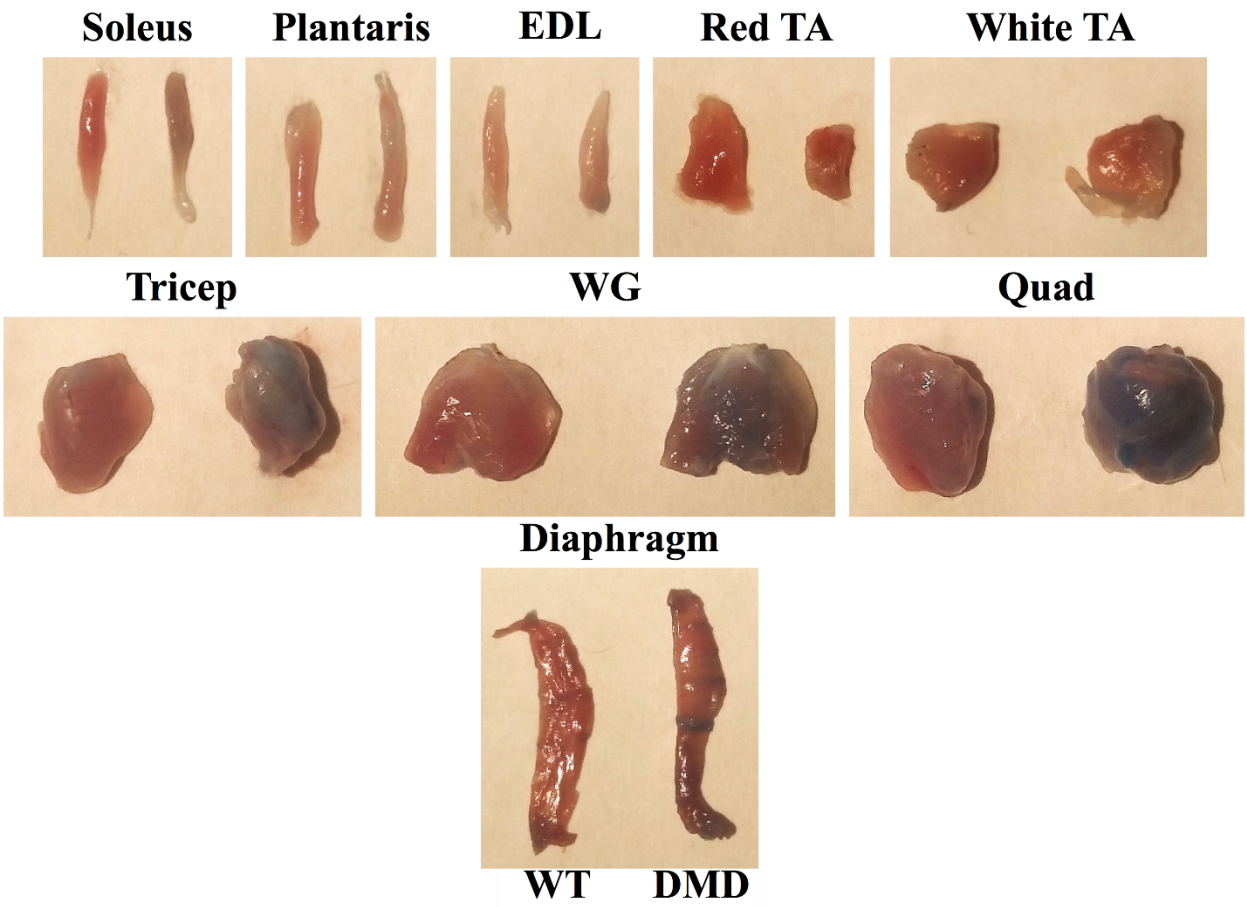

Supplemental Figure 4-1: Evaluation of sarcolemmal damage by Evans Blue Dye staining in DMD. Representative images of Evans Blue Dye staining in WT and DMD skeletal muscles 16 hours following an injection of 1% EBD solution at 5µl/g body weight.

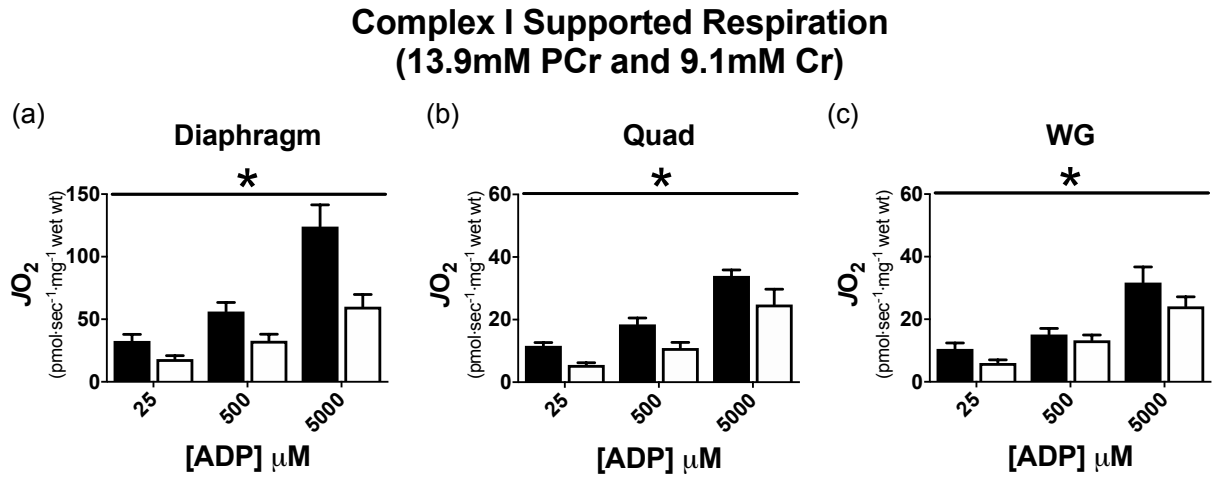

Supplemental Figure 4-2: ADP-stimulated respiration in the presence of phosphocreatine and creatine. 13.9mM phosphocreatine (PCr) and 9.1mM creatine (Cr) were added to the assay media to assess state III respiration supported by Complex-I substrates pyruvate (5mM) and malate (2mM) in Diaphragm (A), Quad (B) and WG (C). Results represent mean ± SEM; n=10-12; * $p<0.05$ compared to WT.

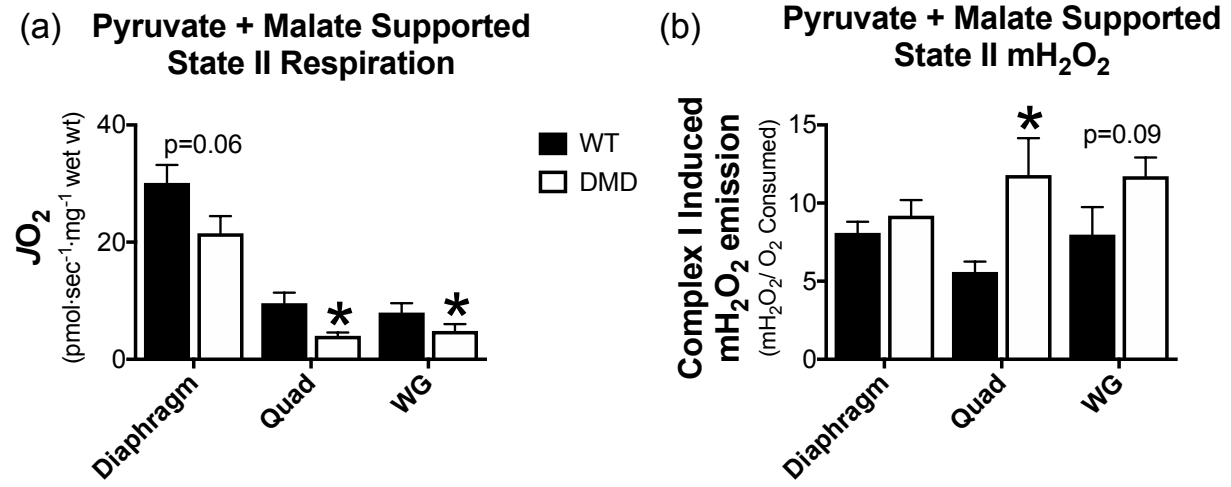

Supplemental Figure 4-3: Evaluation of state II respiration and mH_2O_2. State II (no ADP; proton leak) respiration (A) and mH_2O_2 emission (B) were initiated using Complex-I substrates pyruvate (5mM) and malate (2mM) in Diaphragm, Quad and WG muscles. Results represent mean ± SEM; n=10-12; * $p<0.05$ compared to WT.

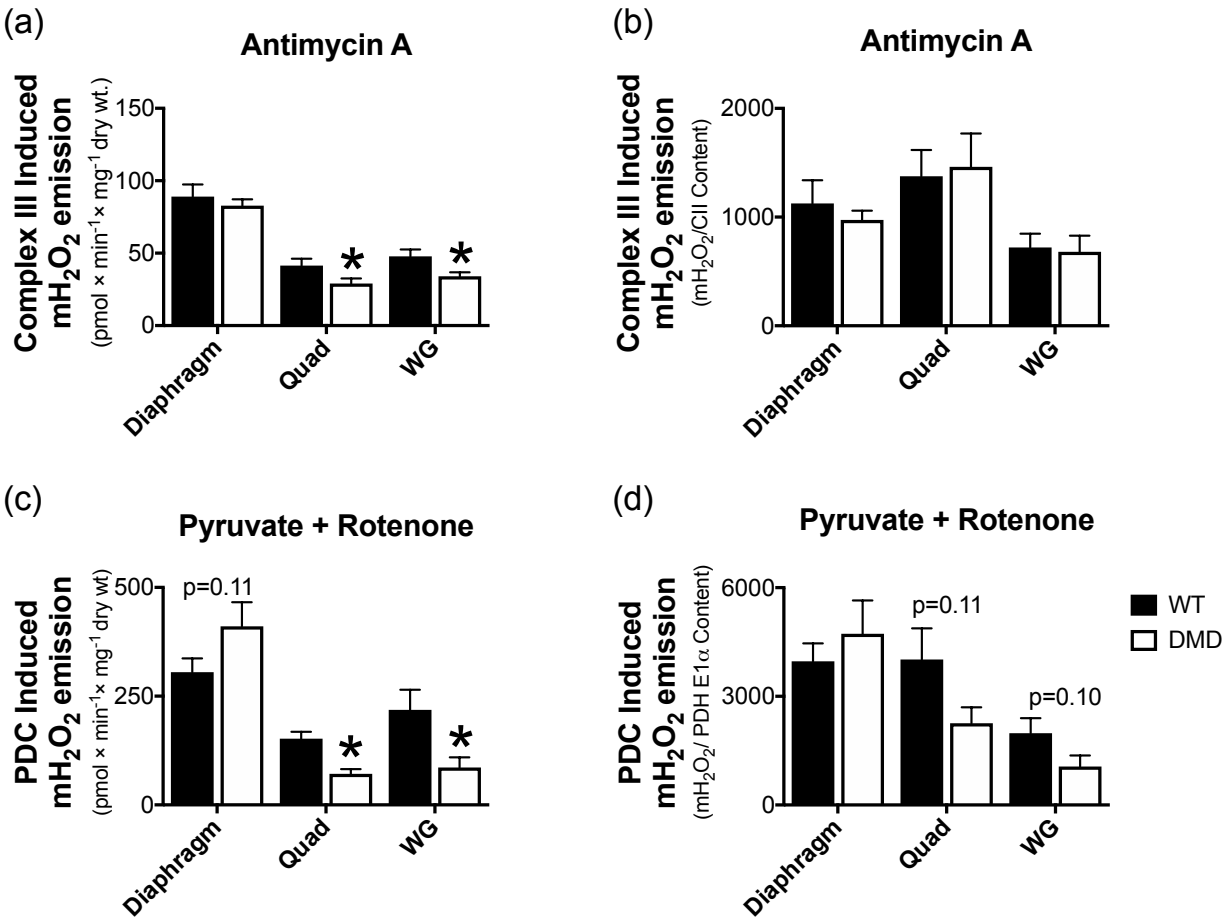

Supplemental Figure 4-4: Additional sites of state II mH_2O_2 emission. Complex-III derived mH_2O_2 was assessed using Complex-III inhibitor antimycin A (2.5μM). Data was expressed per mg muscle weight (A) as well as normalized to Complex-III content (B). Pyruvate dehydrogenase complex (PDC) derived mH_2O_2 was assessed using pyruvate (10mM) and Complex-I inhibitor rotenone (0.5μM). Data was expressed per mg muscle weight (C) as well as normalized to PDH-E1α content (D). Results represent mean ± SEM; n=8-12; * $p<0.05$ compared to WT.

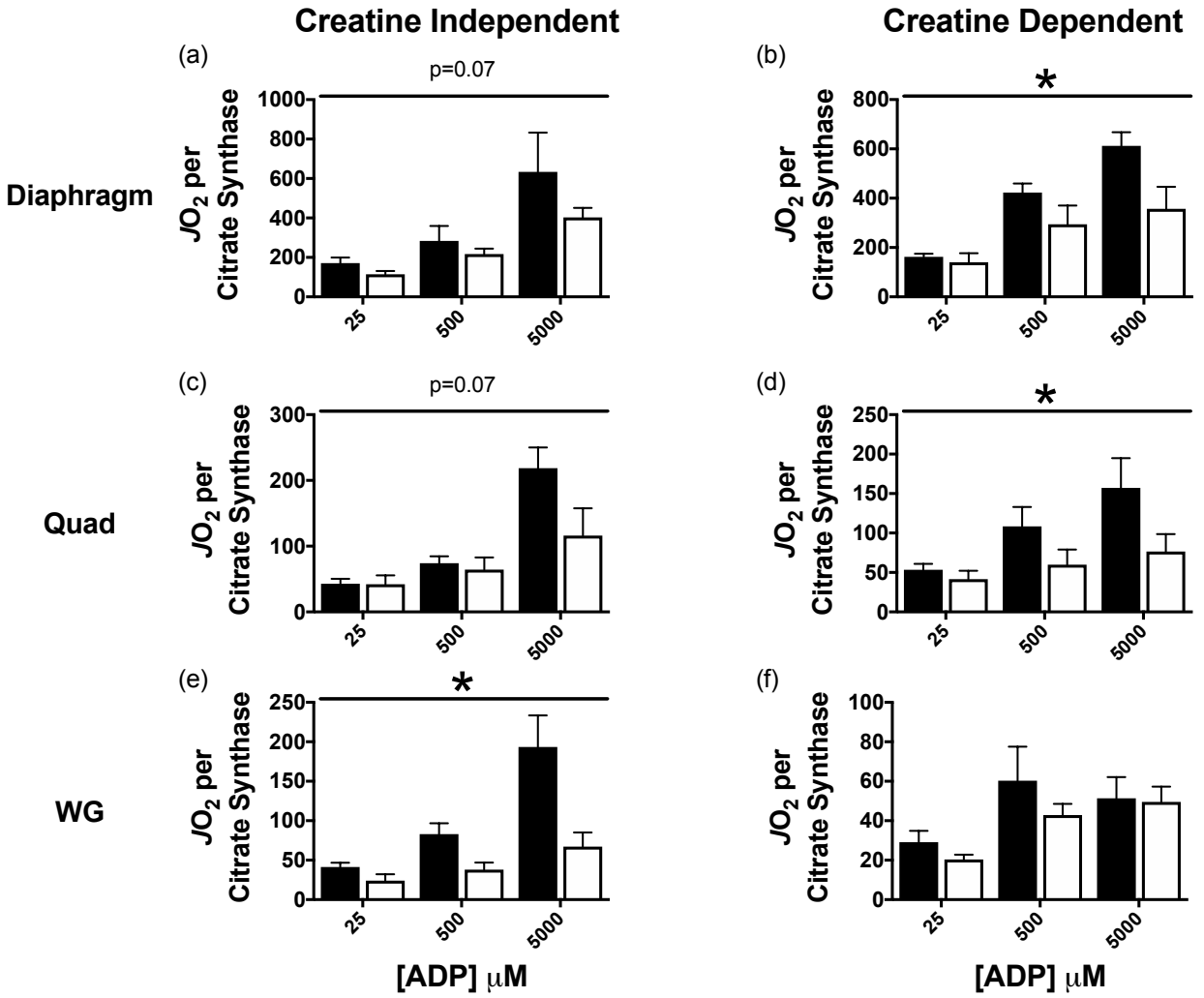

Supplemental Figure 4-5: Intrinsic Respiratory Capacity. State III respiration, supported by Complex-I substrates pyruvate (5mM) and malate (2mM), was assessed in the absence (Creatine Independent) and presence (Creatine Dependent) of 20mM creatine at physiological (25μM), sub-maximal (500μM) and maximal (5000μM) [ADP] and normalized to citrate synthase content. Assessments of bioenergetic function were completed in Diaphragm (a-b), Quad (c-d) and WG (e-f) muscles. Results represent means ± SEM; n=5-8; * $p<0.05$ compared to WT.

Supplemental Data – Not Included in Published Manuscript

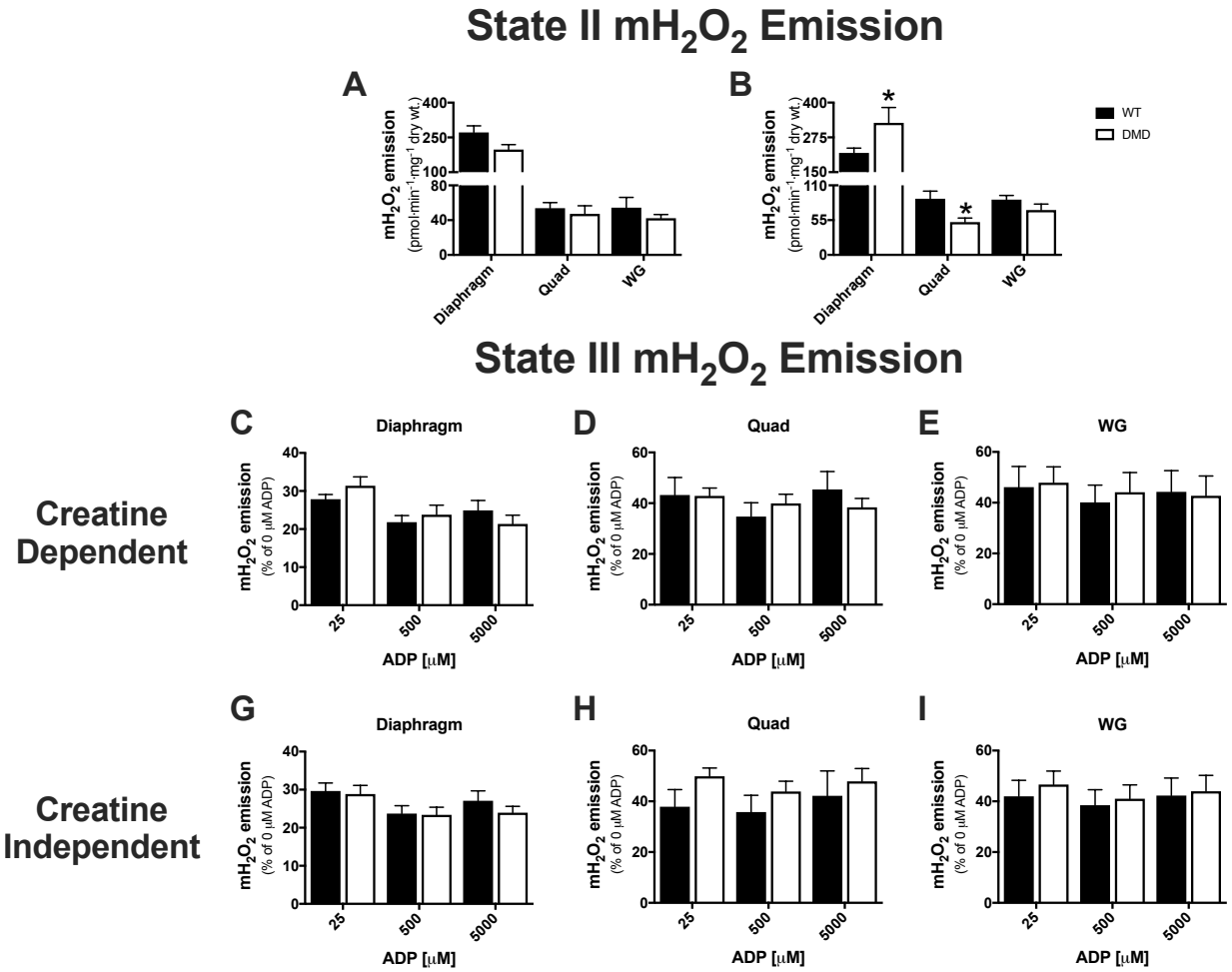

Supplemental Figure 4-6: Absolute rates of Complex-I supported mH_2O_2 emission. State II mH_2O_2 was supported by Complex-I substrates Pyruvate (5mM) and Malate (2mM) in the **A.** presence (Creatine Dependent) and **B**. absence (Creatine Independent) of 20mM creatine. ADP's attenuation of maximal mH_2O_2 emission (state III) was evaluated in the same creatine-dependent (**C-E**) and independent conditions (**G-I**). Results represent mean ± SEM; n=10-12; * $p<0.05$, compared to WT.

5 Impairments in left ventricular mitochondrial bioenergetics precede overt cardiac dysfunction and remodelling in Duchenne muscular dystrophy

This chapter is an original published article. It is presented in its published form.

Impairments in left ventricular mitochondrial bioenergetics precede overt cardiac dysfunction and remodelling in Duchenne muscular dystrophy. MC Hughes, SV Ramos*, PC Turnbull, BA Edgett, JS Huber, N Polidovitch, U Schlattner, PH Backx, JA Simpson and CGR Perry. The Journal of Physiology. doi.org/10.1113/JP277306.*

**Co-first authors*

Author Contributions: The majority of experiments for this project were carried about by Meghan Hughes. As previously mentioned, MH established and maintained the breeding colony required for this project. MH and SVR performed all tissue harvests and mitochondrial bioenergetic assays (respiration, mH_2O_2 emission, calcium retention capacity). MH performed all caspase assays and western blotting experiments. NP performed echocardiography measurements. PCT completed glutathione measurements. BAE and JSH performed all immunohistochemistry staining and analysis. MH and CGRP wrote and revised the manuscript.

Impairments in left ventricular mitochondrial bioenergetics precede overt cardiac dysfunction and remodelling in Duchenne muscular dystrophy

Authors: MC Hughes[1*], SV Ramos[1*], PC Turnbull[1], BA Edgett[2,3,4], JS Huber[2], N Polidovitch[5], U Schlattner[6], PH Backx[5], JA Simpson[2,4] and CGR Perry[1†].

Affiliations:

[1]School of Kinesiology and Health Science and the Muscle Health Research Centre, York University, Toronto, ON, Canada.

[2]Department of Human Health and Nutritional Sciences and Cardiovascular Research Group, University of Guelph, Guelph, ON, Canada.

[3]Department of Pharmacology, Dalhousie Medicine New Brunswick, Saint John, New Brunswick, Canada

[4]IMPART Team Canada Investigator Network, Saint John, New Brunswick, Canada

[5]Department of Biology and the Muscle Health Research Centre, York University, Toronto, ON, Canada.

[6]Laboratory of Fundamental and Applied Bioenergetics (LBFA) and SFR Environmental and Systems Biology (BEeSy), University Grenoble Alpes, Grenoble, France.

*Authors contributed equally to this work

Running Title:

Impaired left-ventricular bioenergetics in Duchenne muscular dystrophy

Table of Contents Category:

Muscle

†Address for Correspondence:

Christopher Perry, PhD
School of Kinesiology and Health Science
Muscle Health Research Centre
344 Norman Bethune College
York University
4700 Keele Street
Toronto, Ontario M3J 1P3
(P) 416 736 2100 ext. 33232
cperry@yorku.ca

Key Points Summary

- 98% of patients with Duchenne muscular dystrophy (DMD) develop cardiomyopathy, with 40% developing heart failure
- While increased propensity for mitochondrial induction of cell death has been observed in left ventricle, it remains unknown whether this is linked to impaired mitochondrial respiratory control and elevated H_2O_2 emission prior to the onset of cardiomyopathy
- Classic mouse models of DMD demonstrate hyper-regeneration in skeletal muscle which may mask mitochondrial abnormalities. Using a model with less regenerative capacities that is more akin to Patients with DMD, we observed elevated left ventricular mitochondrial H_2O_2 and impaired oxidative phosphorylation in the absence of cardiac remodelling or overt cardiac dysfunction at 4 weeks
- These impairments were associated with dysfunctions at Complex I, governance by ADP and creatine-dependent phosphate shuttling which results in a less efficient response to energy demands
- Mitochondria may be a therapeutic target for the treatment of cardiomyopathy in DMD

Abstract

In Duchenne muscular dystrophy (DMD), mitochondrial dysfunction is predicted as a response to numerous cellular stressors yet the degree and contribution of mitochondria to the onset of cardiomyopathy remains unknown. To resolve this uncertainty, we designed *in vitro* assessments of mitochondrial bioenergetics to model mitochondrial control parameters that influence cardiac function. Both left ventricular mitochondrial responsiveness to the central bioenergetic controller ADP as well as the ability of creatine to facilitate mitochondrial-cytoplasmic phosphate shuttling were assessed. These measurements were performed in D2.B10-DMD^{mdx}/2J mice – a model that demonstrates skeletal muscle atrophy and weakness due to limited regenerative capacities and cardiomyopathy more akin to people with DMD than classic models. At 4 weeks of age, there was no evidence of cardiac remodelling or cardiac dysfunction despite impairments in ADP-stimulated respiration and ADP- attenuation of H_2O_2 emission. These impairments were seen at both sub-maximal and maximal ADP concentrations despite no reductions in mitochondrial content markers. The ability of creatine to enhance ADP's control of mitochondrial bioenergetics was also impaired, suggesting an impairment in mitochondrial creatine kinase-dependent phosphate shuttling. Susceptibly to permeability transition pore opening and the subsequent activation of cell death pathways remained unchanged. Mitochondrial H_2O_2 emission was elevated despite no change in markers of irreversible oxidative damage, suggesting alternative redox signalling mechanisms should be explored. These findings demonstrate that selective mitochondrial dysfunction precedes the onset of overt cardiomyopathy in D2.*mdx* mice*,* suggesting that improving mitochondrial bioenergetics by restoring ADP, creatine-dependent phosphate shuttling and Complex I should be considered for treating Patients with DMD.

Keywords: mitochondria, Duchenne muscular dystrophy, reactive oxygen species, respiration, cardiomyopathy

Introduction

Duchenne muscular dystrophy (DMD) is a debilitating disease that causes progressive loss of skeletal and cardiac muscle fibres. Inherited mutations in the gene dystrophin located on chromosome Xp21 disrupts the normal function of this sarcolemmal-cytoskeletal protein in striated muscle. While initial clinical manifestations of DMD are related to skeletal muscle weakness, the development of dilated cardiomyopathy occurs progressively over time, resulting in heart failure and subsequent mortality in approximately 40% of patients [37, 43]. Currently, there are limited treatment approaches for patients with DMD and genetic-based therapies in preclinical models have yielded inconsistent results to date [46]. As such, there is a clear need for unravelling the underlying mechanisms leading to cardiomyopathy in order to identify putative therapeutic targets for the treatment and/or prevention of cardiomyopathy and subsequent heart failure.

By disrupting sarcolemmal stability and cytoskeletal organization, the dystrophin mutation leads to a myriad of cellular stressors which have a significant impact on disease progression in DMD. Two identified contributors to the DMD myopathy include calcium dysregulation and oxidative stress [93, 82, 2]. As such, it is possible these stressors contribute to a mitochondrial dysfunction in DMD which may reciprocate on progression of the disease. However, direct assessments of mitochondrial respiratory function have found no impairments in left ventricle from C57BL10/ScSn^{mdx} mice [199, 32, 30] or changes in mitochondrial H_2O_2 emission [199]. This is surprising given reductions in the activities of the redox-sensitive enzymes aconitase and NADP isocitrate dehydrogenase [280, 199] were reported, which suggests mitochodnrial H_2O_2 emission should be elevated consistent with the oxidative stress reported in dystrophic hearts [93, 82]. Furthermore, increased levels of calcium-induced permeability transition pore (PTP) opening as well as the activation of caspase 9/3, have been reported at a young age prior to the onset of cardiac dysfunction, indicative of mitochondrial derived apoptosis [199]. As noted in an elegant review

by Burelle and colleagues [32], it is surprising that increased PTP susceptibility was not related to mitochondrial respiratory dysfunction or elevated H_2O_2 emission given these responses often occur in tandem in the presence of calcium stress [172, 173, 281, 282]. To date, this discrepancy between the mitochondrial PTP-cell death cascade and reports of normal mitochondrial respiration and H_2O_2 emission has not been resolved.

Recent work by Chang and colleagues suggests the hyper-regeneration that occurs in the *mdx* mouse [51, 52, 202] masks the ability to detect early attenuations in mitochondrial bioenergetics in dystrophic heart [203, 204]. Indeed, shortening telomeres to a more "humanized" length, thereby lowering the stem cell pool, revealed an increase in mitochondrial superoxide production and impairments in respiration in cardiomyocytes relative to the classic *mdx* model [204]. These mitochondrial abnormalities were also related to a more severe cardiac dysfunction [203]. This inverse relationship between regenerative capacities and mitochondrial quality may explain why identifying mitochondrial dysfunction in *mdx* mice has been elusive given the high regenerative capacities demonstrated in this classic model. As such, it remains to be determined if mitochondrial dysfunction is observed in a model of DMD with natural reductions in regenerative capacity, more akin to people with DMD.

The D2.B10-DMD^{mdx}/2J (D2.*mdx)* exhibits attenuated muscle regeneration arising from a natural mutation in TGF-β binding protein 4 in the background D2A strain [60, 59]. In this investigation, we evaluated mitochondrial bioenergetics in dystrophic left ventricle (LV) muscle from the D2.*mdx* mouse relative to wildtype controls. At 4 weeks of age, D2.*mdx* mice exhibit increased Complex I-supported H_2O_2 concurrent with impaired respiration, revealing central impairments in the ability of ADP and creatine to control bioenergetics. These impairments were seen in the

absence of cardiac remodelling and cardiac dysfunction and before the previous reported indices of cardiomyopathy in this model [59].

Materials and Methods

Ethical Approval

All experiments and procedures were approved by the Animal Care Committee at York University (AUP Approval Number 2016-18) in accordance with the Canadian Council on Animal Care.

Animal Care

The 4-week old D2.*mdx* animals originated from a colony maintained at York University (Toronto, Canada) established with breeding pairs from Jackson Laboratories (Bar Harbor, United States). 4-week old DBA/2J WT mice were obtained directly from Jackson Laboratories due to breeding challenges with this strain. Upon arrival, DBA/2J mice were given a minimum of 72 hours to acclimatize before experiments were performed. All animals were provided access to standard chow and water *ad libitum*.

Study Design

Immediately following weaning, D2.*mdx* and WT animals underwent transthoracic echocardiographic analysis (described in detail below) as well as the assessment of body weight. Animals were given minimum 2 days to equilibrate following this analysis. On the day of harvest, animals were maintained under isoflurane while skeletal muscles were harvested for other work as part of another investigation. Animals were then euthanized by exsanguination and a portion of the LV was immediately separated from the rest of the heart and placed in ice-cold BIOPS buffer (described below) for bioenergetic measurements. Remaining muscle was frozen in liquid nitrogen for western blotting and caspase activity measurements. Due to tissue limitation, a separate cohort of animals were used for glutathione and histochemical measurements.

Animals were evaluated at 4 weeks of age to allow for the assessment of mitochondrial bioenergetics prior to the established onset of cardiomyopathy in this model [59].

Echocardiography

All mice were subjected to transthoracic echocardiographic analysis (Vevo 2100, VisualSonics) to measure cardiac function and morphology 2-3 days prior to sacrifice for bioenergetic measurements. The animals were sedated using 3% isoflurane and maintained with 1–2% isoflurane. Mice were placed on a heating pad and body temperature was maintained between 36.9 and 37.3 °C for the duration of the measurements. Left ventricular internal end diastolic diameters (LVDd), left ventricular internal end systolic diameters (LVDs) and left ventricular posterior wall thickness (LVPWTh) were measured in brightness mode (B-Mode) and motion mode (M-Mode) using the parasternal long axis view. Fractional shortening (FS) was calculated as FS(%) = (LVDd - LVDs)/LVDd x 100. Stroke volume (SV) was estimated as SV = Left ventricular diastolic volume (LVVol;d) - Left ventricular systolic volume (LVVol;s), where LVVol;d = ((7.0/(2.4 + LVDd)) x $LVDd^3$ and LVVol;s = ((7.0/(2.4 + LVDs)) x $LVDs^3$. Ejection fraction (EF) was estimated as EF = SV/LVVol;d and cardiac output (CO) was estimated as CO = SV x heart rate. All data analysis was performed using the Visual Sonic data analysis suite.

Mitochondrial Bioenergetic Assessments

Preparation of Permeabilized Muscle Fibre Bundles (PmFB)

This technique is partially adapted from previous methods as described elsewhere [237-240]. Briefly, LV was removed from mice during anaesthesia with isoflurane and immediately placed in ice-cold BIOPS, containing (in mM): 50 MES Hydrate, 7.23 K_2EGTA, 2.77 CaK_2EGTA, 20 imidazole, 0.5 dithiothreitol, 20 taurine, 5.77 ATP, 15 PCr, and 6.56 $MgCl_2 \cdot 6\ H_2O$ (pH 7.1). The epicardium was trimmed away and the remaining muscle was divided into small bundles (~2–7 mm long, 1.0–2.5 mg wet weight). Each bundle was gently separated along the longitudinal axis to form bundles that were treated with 40 μg/ml saponin in BIOPS on a rotor for 30 minutes at 4° C. Bundles for mitochondrial H_2O_2 emission (mH_2O_2) measurements (described below) were also treated with 35 μM 2,4-dinitrochlorobenzene (CDNB) during the permeabilization step to deplete

glutathione and allow for detectable rates of mH_2O_2 [242]. Following permeabilization, the PmFB were divided into three groups; 1) bundles intended for high resolution respirometry were placed in MiR05 containing (in mM): 0.5 EGTA, 10 KH_2PO_4, 3 $MgCl_2 \cdot 6\ H_2O$, 60 K-lactobionate, 20 Hepes, 20 Taurine, 110 sucrose and 1 mg/ml fatty acid free BSA (pH 7.1) while 2) bundles intended for mH_2O_2 were placed in Buffer Z containing (in mM): 105 K-MES, 30 KCl, 10 KH_2PO_4, 5 $MgCl_2 \cdot 6\ H_2O$, 1 EGTA and 5 mg/ml BSA (pH 7.4). PmFB were washed on a rotor at 4°C in MiR05 or Buffer Z until the measurements were initiated. 3) bundles for calcium retention capacity were placed in Buffer Y + 1 mM EGTA containing (in mM): 250 sucrose, 10 tris-HCl, 20 tris-base, 10 KH_2PO_4 and 0.5mg/mL BSA and washed on a rotor at 4° C for 10 minutes, then transferred to a second wash of Buffer Y + 10 μM blebbistatin (BLEB, see below) and washed on a rotor at 4°C until measurements were initiated. Following permeabilization and washing, all mitochondrial bioenergetic measurements were performed in the same order from one animal to another and between groups to ensure consistent durations of the wash step.

Mitochondrial Respiration

High-resolution O_2 consumption measurements were conducted in 2 ml of respiration medium (MiR05) using the Oroboros Oxygraph-2k (Oroboros Instruments, Corp., Innsbruck, Austria) with stirring at 750 rpm at 37 °C [239, 240, 243-245]. Respiration medium contained 20mM creatine (Cr) to saturate mtCK or no Cr to prevent the activation of mtCK [283, 243]. For ADP-stimulated respiratory kinetics, 5 mM pyruvate, accompanied by 2 mM malate, were added as Complex I substrates (via generation of NADH to saturate electron entry into Complex I) followed by a titration of submaximal ADP (25 μM and 500 μM) and maximal ADP (5 mM). Cytochrome *c* was added to test for mitochondrial membrane integrity, with all experiments demonstrating <10% increase in respiration. Finally, succinate (20 mM) was then added to saturate electron entry into

Complex II. All experiments were conducted in the presence of 5μM BLEB in the assay media to prevent spontaneous contraction of PmFB [243, 244, 240]. Each protocol was initiated with a starting [O_2] of approximately 350 μM and was completed before the oxygraph chamber [O_2] reached 150 μM as done previously [239, 240, 243, 244]. Polarographic oxygen measurements were acquired in 2 s intervals with the rate of respiration derived from 40 data points and expressed as pmol/s/mg wet weight. PmFB were weighed in ~1.5 ml of tared BIOPS (ATP-containing relaxing media) to prevent rigor that occurs when weighing PmFB in open air (unpublished observations).

Mitochondrial H_2O_2 Emission (mH_2O_2)

mH_2O_2 was determined fluorometrically (QuantaMaster 40, HORIBA Scientific, Edison, NJ, USA) in a quartz cuvette with continuous stirring at 37°C, in 1 mL of Buffer Z supplemented with 10 μM Amplex Ultra Red, 0.5 U/ml horseradish peroxidase, 1 mM EGTA, 40 U/ml Cu/Zn-SOD1, and 5 μM BLEB. Induction of state II mH_2O_2 was measured through the addition of 10 mM pyruvate and 2 mM malate followed by a titration of ADP which was added to progressively attenuate mH_2O_2. Complex I-supported mH_2O_2 was repeated with and without 20mM Cr in the assay buffer to compare ADP's effects dependent or independent of mtCK-mediated phosphate shuttling. The rate of H_2O_2 emission was calculated from the slope (F/min), from a standard curve established with the same reaction conditions and normalized to fibre bundle wet weight as described above.

Mitochondrial Calcium Retention Capacity

This assay is partially adapted from methods previously described [249]. Mitochondrial calcium retention capacity measurements were completed spectrofluorometrically (QuantaMaster 80, HORIBA Scientific, Edison, NJ, USA) in a cuvette with continuous stirring at 37° C, in 300 μL of Buffer Y containing 1 μM Calcium Green-5N (Invitrogen), 2 μM thapsigargin, 5 mM 2-

deoxyglucose, 2 U/mL hexokinase, 20 mM Cr, 5 μM BLEB and 40 μM EGTA. Prior each experiment, the cuvette was placed on a stir plate with 500 mL water and 10 mM EGTA. The water was then aspirated from the cuvette but not rinsed, leaving the EGTA coating on the cuvette walls to chelate any residual Ca^{2+} in the assay buffer. Minimum fluorescence was obtained following the addition of the PmFB plus 5 mM glutamate +2 mM malate to the assay buffer. Calcium uptake was then initiated by a single 8 nmol pulse of $CaCl_2$. Subsequent 4 nmol pulses of Ca^{2+} were added until mitochondrial permeability transition pore (PTP) opening was evident. Two 0.5 mM pulses of Ca^{2+} were then added to saturate the fluorophore and establish a fluorescent maximum. All experiments were conducted at 37 °C. Changes in free Ca^{2+} in the cuvette during mitochondrial Ca^{2+} uptake were then calculated using the known K_d for Calcium Green 5-N and the equations established for calculating free ion concentrations using ion-sensitive fluorophores [250]. After the experiments, the fibres were rinsed in double deionized H_2O, lyophilized in a freeze-dryer for >4 h and weighed on a microbalance (Sartorius Cubis, Gottingen, Germany).

In Vitro Muscle Analyses

Western Blotting

An aliquot of frozen heart (10–30 mg) from each animal was homogenized in a plastic microcentrifuge tube with a tapered teflon pestle in ice-cold buffer containing (mm): 40 Hepes, 120 NaCl, 1 EDTA, 10 $NaHP_2O_7 \cdot 10H_2O$ pyrophosphate, 10 β-glycerophosphate, 10 NaF and 0.3% CHAPS detergent (pH 7.1 adjusted using KOH). Protein concentrations were determined using a BCA assay (Life Technologies, Carlsbad, CA, USA). 50 μg of denatured and reduced protein was subjected to 6–12% gradient SDS-PAGE followed by transfer to low-fluorescence polyvinylidene difluoride membrane. Membranes were blocked with LI-COR Odyssey Blocking Buffer (LI-COR, Lincoln NE, USA) and immunoblotted overnight (4°C) with antibodies specific

for each protein. A commercially available monoclonal antibody cocktail was used to detect electron transport chain proteins (human OXPHOS Cocktail, ab110411; Abcam, Cambridge, UK, 1:250 dilution), including V-ATP5A (55 kDa), III-UQCRC2 (48 kDa), IV-MTCO1 (40 kDa), II-SDHB (30 kDa) and I-NDUFB8 (20 kDa). Commercially available polyclonal antibodies were used to detect voltage dependent anion carrier 2 (VDAC 2) (32059, 33 kDa; Santa-Cruz, 1:1000), adenine nucleotide translocase 1 (ANT 1) (ab180715, 32 kDa; Abcam, 1:1000), 4-hydroxynoneonal (4-HNE) (ab46545; Abcam, 1:1000) and sarcomeric s-mtCK (Dr Uwe Schlattner, Grenoble, France; 42 kDa, 1:1000). The mtCK antibody has been validated previously to confirm specificity [256]. Protein carbonylation was detected using the OxyBlot Protein Oxidation Detection Kit (Millipore Sigma, Burlington, MA, USA).

After overnight incubation in primary antibodies, membranes were washed three times, for 5 minutes each time, in TBST and incubated for 1 hour at room temperature with the corresponding infrared fluorescent secondary antibody (LI-COR). Immunoreactive proteins were detected by infrared imaging (LI-COR CLx; LI-COR) and quantified by densitometry (ImageJ, http://imagej.nih.gov/ij/). All images were normalized to a whole membrane Amido Black total protein stain (A8181, Sigma, St Louis, MO, USA). A double band was detected at 33 kDa for ANT 1 and as such, both bands were analyzed and reported.

Glutathione

Glutathione was assessed as previously described [255]. GSH was assessed by UV-HPLC monitoring of NEM-GSH while GSSG was assessed by fluorescent-HPLC by tracking O-pthalymide (OPA, Sigma-Aldrich, Oakville, Canada) tagged GSH through a flow-through cuvette following GSSG conversion to GSH (FireflySci 8830, NY, USA) in a QuantaMaster 40

spectrofluorometer (HORIBA, NJ, USA). All values were referenced to protein concentration and reported in μmol/g protein. USA).

Caspase Activity

Enzymatic activities of caspase 3 and caspase 9 were measured fluorometrically using substrates Ac-DVED-AMC and Ac-LEHD-AMC (Enzo Life Sciences, Farmingdale, NY) as previously described [251, 252].

Histochemistry

In a subset of animals, not used for bioenergetic measurements, the lower third of the heart was immediately placed in 10% neutral buffered formalin for 72 hours. After 72 hours, the heart was placed in 70% ethanol where it was preserved until processing using routine procedures. Processed heart tissue was embedded in paraffin wax (Thermo Fisher Scientific, Burlington, Canada) prior to sectioning (5 μm thickness). Sections were stained with picrosirius red to measure fibrotic area (fibrotic regions stain red for extracellular matrix), areas of muscle damage and CSA (quantified only from cardiomyocytes with centralized nuclei). Two to five images (4 on average) were used for analyses (n=7 per group). Sections were imaged using an Olympus FSX100 light microscope (Olympus), Richmond Hill, Canada) and analyzed in cellSens software (Olympus) for necrosis and fibrosis analysis, or ImageJ (http://imagej.nih.gov/ij/) for CSA analysis.

Statistics

Results are expressed as means ± SEM. The level of significance was established as $p<0.05$ for all statistics. Outliers were omitted in accordance with the ROUT test GraphPad Prism Software, La Jolla, CA, USA). D'Agostino-Pearson omnibus normality test revealed that data resembled a Gaussian distribution which justified the application of parametric tests. For all data except the presence of muscle damage, statistical differences were analysed using unpaired t-tests between WT and D2.*mdx*. The design of ADP-titration protocols focused specifically on determining

separate questions regarding mitochondrial bioenergetic responses to low vs high ADP concentrations. As such, t-tests were used at each ADP concentration. Statistical differences in muscle damage in D2.*mdx* vs WT was analysed using Pearson's chi-squared test.

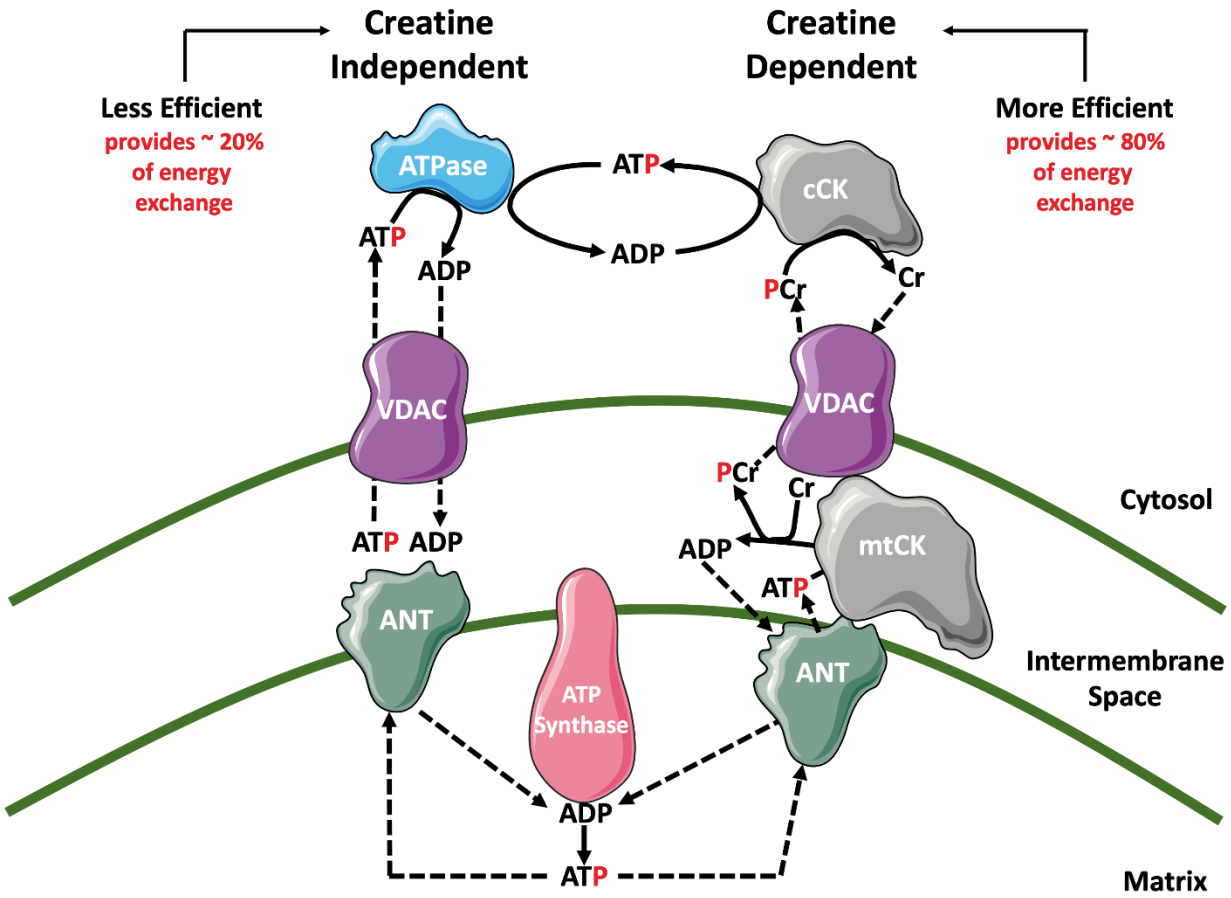

Figure 5-1: Schematic representation of energy transfer between mitochondria and cytosol. The leading model for energy exchange involves a creatine-independent (-Cr) and creatine-dependent (+Cr) pathway. The left side depicts the –Cr pathway whereby the transfer of ADP/ATP occurs solely through diffusion across voltage dependent anion carrier (VDAC) on the outer mitochondrial membrane and adenosine nucleotide translocase (ANT) on the inner mitochondrial membrane. The right side depicts the +Cr 'mitochondrial phosphate shuttling' mechanism of energy transfer. In the presence of Cr, ATP produced during oxidative phosphorylation in the mitochondrial matrix diffuses through ANT into the inner membrane space where mitochondrial creatine kinase (mtCK) facilitates the transfer of the phosphate group from ATP to Cr, producing phosphocreatine (PCr) and ADP. The PCr is exported via VDAC into the cytosol while the ADP is directly recycled back via ANT into the mitochondrial matrix. This schematic has been partially adapted from Hughes et al. (paper in submission at the time of review) using concepts from [146, 150, 147, 157].

Physical Parameters and Echocardiography

At 4 weeks of age, we first determined whether differences in whole body as well as cardiac-specific physical parameters existed. D2.*mdx* animals demonstrate a significant decrease in body weight compared to WT controls (-21%, p=0.006, **Figure 2A**) and left ventricular diameter during both systole (-26%, p=0.00005; **Figure 2B**) and diastole (-14%, p=0.00006; **Figure 2B**) is unchanged when normalized to body weight (Figure 2B). Furthermore, cardiac output is driven in part by lean body mass and lean muscle mass has been shown to be lower in this model [60]. As such, stroke volume and cardiac output were normalized relative to body weight as a strong correlation between these measures has been established [284]. Accordingly, stroke volume per gram body weight was unchanged (**Figure 2D**) while cardiac output per gram body weight was significantly increased in D2.*mdx* animals vs WT controls (+13%, p=0.03, **Figure 2E**). However, heart rate was also significantly increased in D2.*mdx* mice relative to WT (+13%, p=0.02; **Figure 2C**). Ejection fraction was significantly increased in D2.*mdx* mice relative to WT (+13%, p=0.0008; **Figure 2F**) as well as fractional shortening (+19%, p=0.001; **Figure 2G**), indicating overall that there was no overt cardiac dysfunction at 4 weeks of age in D2.*mdx* mice.

Impaired respiration and elevated Complex I-supported mH_2O_2 during oxidative phosphorylation in left ventricle muscle of D2.mdx mice

Key to this investigation is the design of *in vitro* assessments of mitochondrial bioenergetics that model *in vivo* critical parameters controlling respiratory and H_2O_2 emission kinetics. Specifically, we considered that mitochondrial responsiveness to ADP may be different at lower vs higher concentrations, as well as the substantial evidence demonstrating that creatine facilitates mitochondrial phosphate shuttling with the cytoplasm more efficiently than ATP/ADP cycling (**Figure 1**). Specifically, the stimulation of mitochondrial respiration and H_2O_2 emission in left ventricle muscle was initiated using pyruvate (5mM) and malate (2mM) which generates NADH

to stimulate Complex I. In the absence of ADP, state II respiration and mH_2O_2 were assessed in both the presence (+Cr) and absence (-Cr) of 20mM Cr to drive energy transfer dependent or independent of mtCK, respectively **(Figure 1)**. In both +Cr and –Cr conditions, state II respiration was significantly decreased in D2.*mdx* mice (+Cr: -26%, p=0.045; -Cr: -16%, p=0.050; **Figure 3A,E**), suggesting less uncoupling, while mH_2O_2 emission was significantly elevated in D2.*mdx* mice vs WT (+Cr: +75%, p=0.002; -Cr: +65%, p=0.003; **Figure 3B,F**).

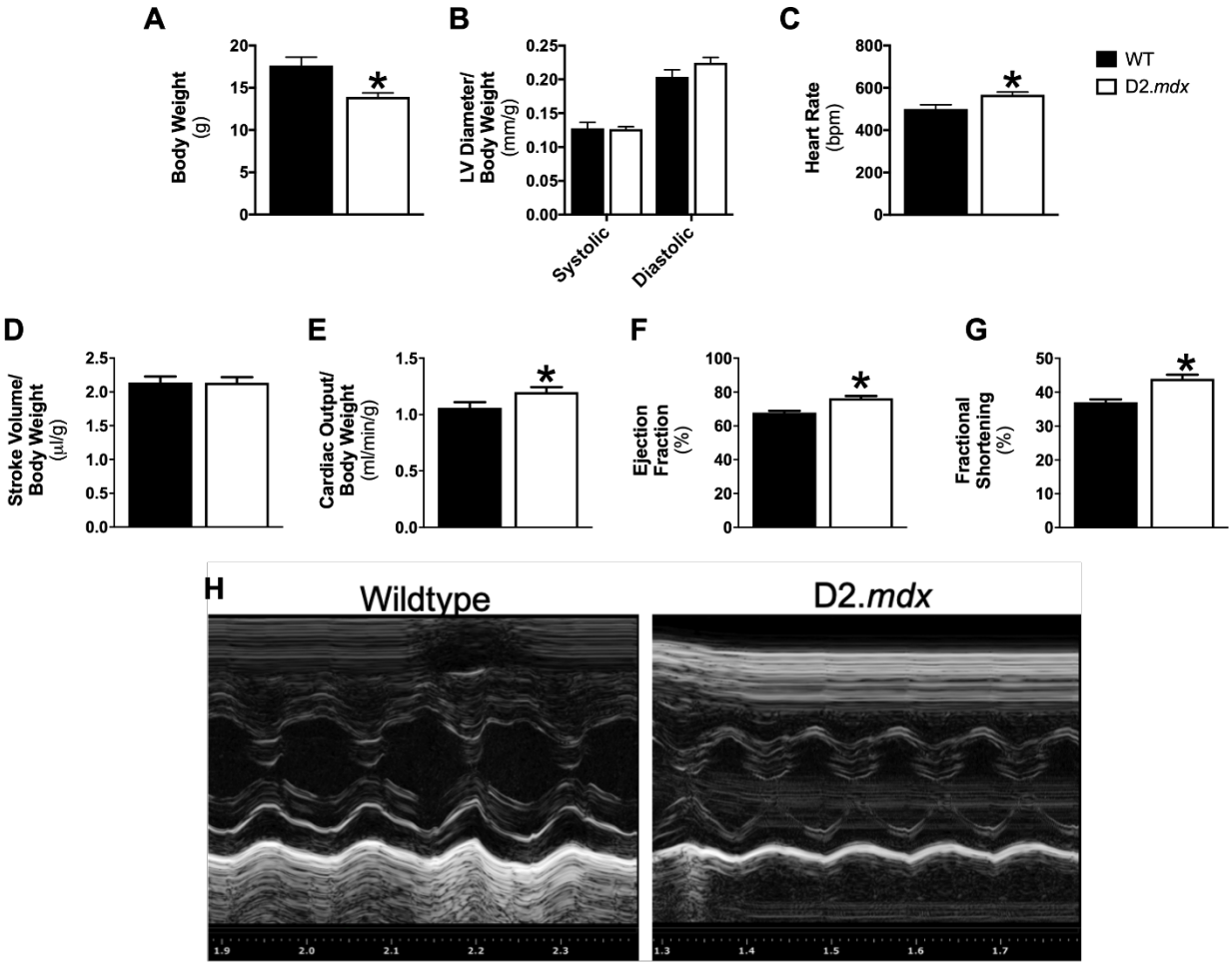

Figure 5-2: Physical parameters and echocardiography in D2.*mdx* mice. (A) Body weight. (B) Left ventricle (LV) diameter was calculated during both systole and diastole. (C) Heart rate (HR) during echocardiographic measurements. LV dimensions and volume along with HR were used to calculate (D) stroke volume and (E) cardiac output as well as (F) ejection fraction and (G) fractional shortening. Results represent means ± SEM; n=5-6; * p<0.05 compared to WT.

We then determined the ability of ADP to simulate coupled respiration and attenuate mH_2O_2 (state III conditions) while concurrently evaluating the function of mtCK by comparing +Cr and –Cr conditions. ADP was titrated beginning with low/physiological (25μM), followed by high sub-maximal (500μM) and finally saturating concentrations (5mM) of ADP. +Cr, state III respiration was impaired at a range of [ADP] (25μM: -20%, p=0.08; 500μM: -37%, p=0.01; 5mM: -37%, p=0.003; **Figure 3C**) while mH_2O_2 during oxidative phosphorylation was elevated at all [ADP] (25μM: +133%, p=0.00002; 500μM: +131%, p=0.0004; 5mM: +133%, p=0.001; **Figure 3D**) in D2.*mdx* vs WT. –Cr, ADP's ability to simulate respiration and concurrently lower mH_2O_2 during oxidative phosphorylation was impaired at low [ADP] only (Respiration: -33%, p=0.007; **Figure 3G**; mH_2O_2: +121%, p=0.0001; **Figure 3H**), indicating an impairment in ADP sensitivity that is not evident at high submaximal and saturating [ADP]. Overall, these findings suggest that there are impairments in ADP stimulated respiration and accompanied attenuation of mH_2O_2 at low [ADP] regardless of the degree of mtCK activation, yet high or saturating [ADP] demonstrates impaired control only in the +Cr pathway. Indeed, comparing sensitivity to Cr reveals an impairment in bioenergetics that is more specific to the predominant phosphate shuttling pathway that is dependent on mtCK (**Table 1**).

Western blotting was performed on the key regulators of energy shuttling to determine if changes in mitochondrial bioenergetics could be attributed to alterations in protein content of these regulators. Adenine nucleotide translocator 1 (ANT 1), located on the inner mitochondrial membrane, was unchanged between D2.*mdx* and WT animals (**Figure 4A**). However, voltage dependent anion carrier 2 (VDAC 2) that is specific to the outer mitochondrial membrane, was significantly elevated in D2.*mdx* heart muscle (+50%, p=0.046; **Figure 4B**). Protein content of mtCK was unchanged in D2.*mdx* relative to WT (**Figure 4C**). Quantification of the proteins

comprising the electron transport chain was also performed. While subunits of Complexes I, III, IV and V as well as the sum of all 5 complexes were unchanged in D2.*mdx* mice, there was an increase in Complex II marker in D2.*mdx* mice (+22%, p=0.01; **Figure 4D**) relative to WT. This increase in Complex II marker content occurred concurrently impaired succinate-stimulated respiration, suggesting partial compensation may have been invoked (data not shown). Overall, alterations in protein content of key regulators of energy shuttling as well as markers of OXPHOS capacity do not explain the decreases seen in mitochondrial respiration and elevations in mH_2O_2 in the left ventricle of D2.*mdx* mice at 4 weeks of age.

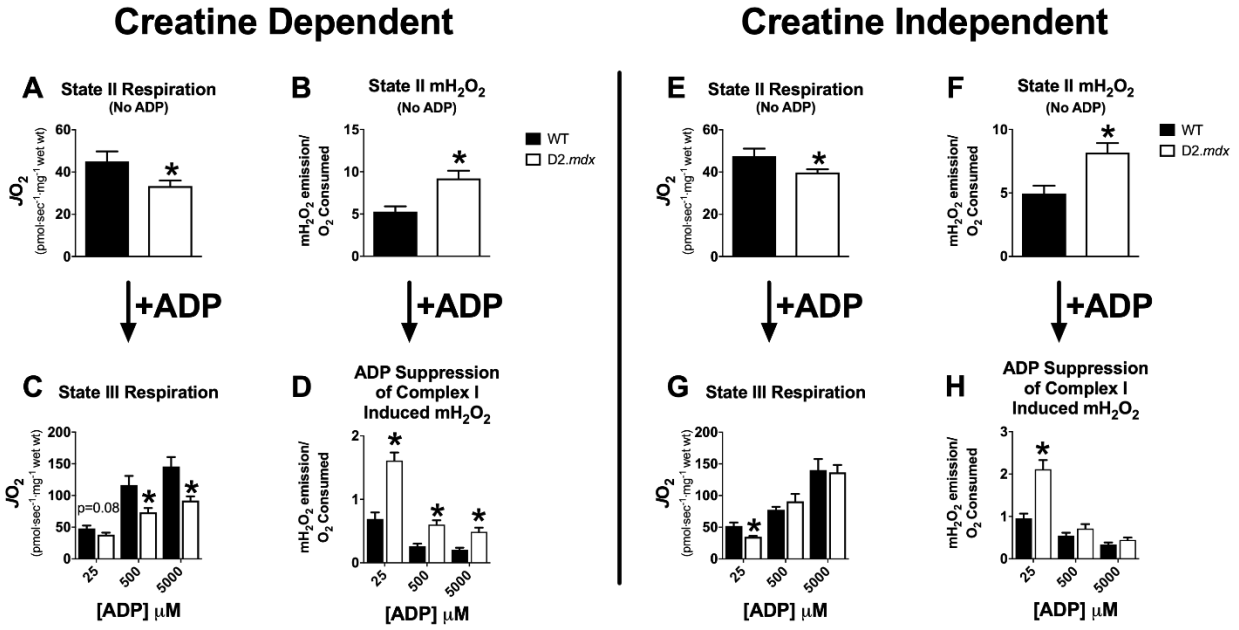

Figure 5-3: Respiration and mH_2O_2 emission in left ventricle of D2.*mdx* mice. State II (no ADP) respiration (proton leak) and mH_2O_2 emission, supported by Complex-I substrates pyruvate (5mM) and malate (2mM), was assessed in the (A-B) presence (Creatine Dependent) and (E-F) absence (Creatine Independent) of 20mM creatine. State III (ADP) respiration and mH_2O_2 emission were evaluated at low (25μM), sub-maximal (500μM) and maximal (5000μM) [ADP] in the presence (C-D) and absence (G-H) of creatine. Results represent means ± SEM; n=12-17; * $p<0.05$ compared to WT.

Table 5-1: Impairment in creatine sensitivity with 500μM ADP in dystrophic heart muscle

	Wildtype		P Value (-Cr vs +Cr)	D2.*mdx*		P Value (-Cr vs +Cr)
	-Cr	+Cr		-Cr	+Cr	
JO_2 (pmol · sec^{-1} · mg^{-1} wet wt)	76.6 ± 4.6	128.8 ± 17.1	P<0.05	90.9 ± 11.7	76.3 ± 8.6	P=0.31
mH_2O_2/O_2 Consumed	0.55 ± 0.07	0.26 ± 0.04	P<0.01	0.62 ± 0.10	0.60 ± 0.07	P=0.37

Creatine Dependent (+Cr), Creatine Independent (-Cr), Values represent mean ± SEM, (n=8-14).

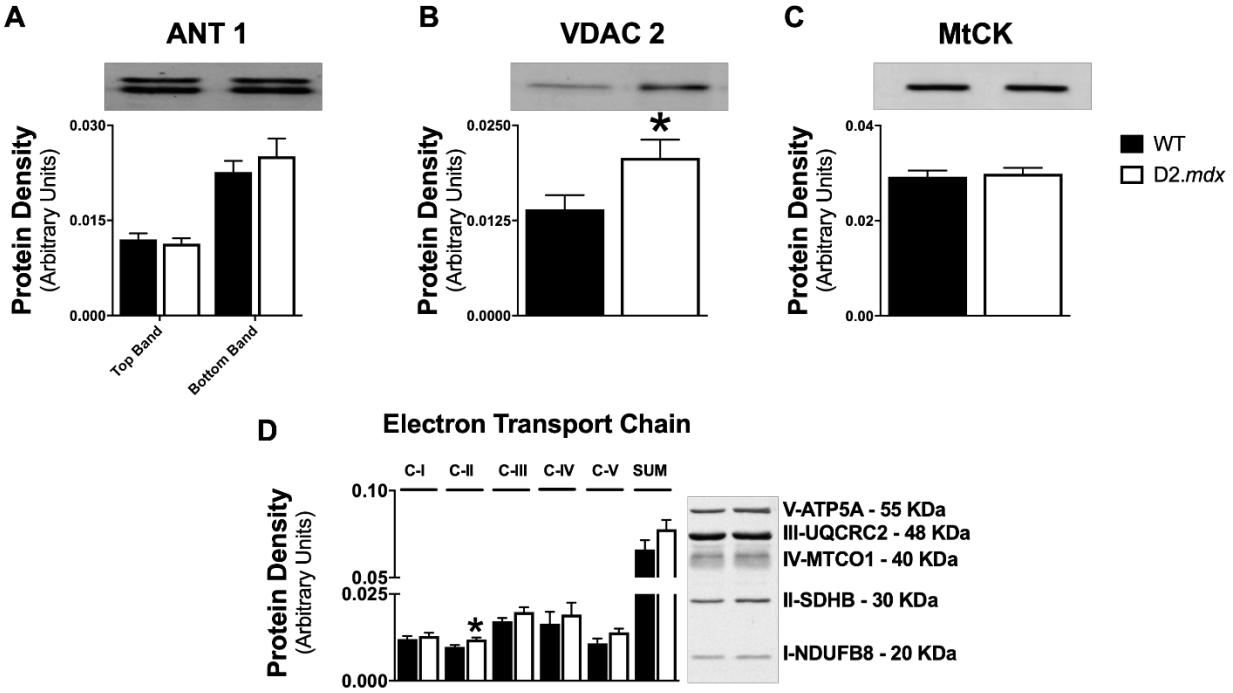

Figure 5-4: Evaluation of essential regulators of mitochondrial bioenergetics. Protein content of (A) adenine nucleotide translocase 1 (ANT 1) on the inner mitochondrial membrane, (B) voltage dependent anion carrier 2 (VDAC 2) on the outer mitochondrial membrane and (C) mitochondrial creatine kinase (mtCK) found in the inner membrane space. (D) Protein content of electron transport chain subunits. Results represent mean ± SEM; n=8-12; * p<0.05 compared to WT.

Elevated mH_2O_2 does not alter markers of irreversible oxidative damage in D2.mdx left ventricle

Despite elevated mH_2O_2 emission in the left ventricle of D2.*mdx* mice, there were no changes in reduced glutathione (GSH, **Figure 5A**), oxidized glutathione (GSSG; **Figure 5B**), total glutathione (GSH + 2xGSSG; **Figure 5C**) or the ratio of GSH:GSSG (**Figure 5D**). Additionally, there was no evidence of changes in lipid peroxidation, as measured through the quantification of 4-hydroxynoneal (**Figure 5E**) or evidence of protein carbonylation (**Figure 5F**) demonstrating that elevations in mH_2O_2 did not change whole cell oxidative status at this early time point.

Bioenergetic impairments are not accompanied by changes in susceptibility to PTP opening or mitochondrial-derived apoptosis

We next determined if elevated mH_2O_2 during impaired oxidative phosphorylation resulted in increased susceptibility to PTP opening at this early time point. D2.*mdx* left ventricle muscle showed no differences in the $[Ca^{2+}]$ required to induce PTP opening relative to WT (**Figure 6A**). Furthermore, there were no differences in mitochondrial-derived caspase 9 activity **(Figure 6B**) and subsequently, no elevations in caspase 3 activity (**Figure 6C**) indicating that elevated mH_2O_2 and impaired mitochondrial respiration do not result in mitochondrial-derived apoptosis.

Impaired mitochondrial bioenergetics precede muscle damage and atrophy in left ventricle of D2.mdx mice

Interstitial fibrosis of the LV was quantified using picrosirius red stain and revealed no differences in degree of fibrosis between D2.*mdx* and WT (**Figure 6D**). Furthermore, quantification of fibre cross sectional area revealed no difference in D2.*mdx* relative to WT (**Figure 6E**) indicating that there is no fibre atrophy or hypertrophy in the LV at this early time point. The presence of muscle damage in the LV was also determined in D2.*mdx* and WT LV. While there were more instances of damage present in D2.*mdx* vs WT, this difference was not statistically significant (**Figure 6F)**.

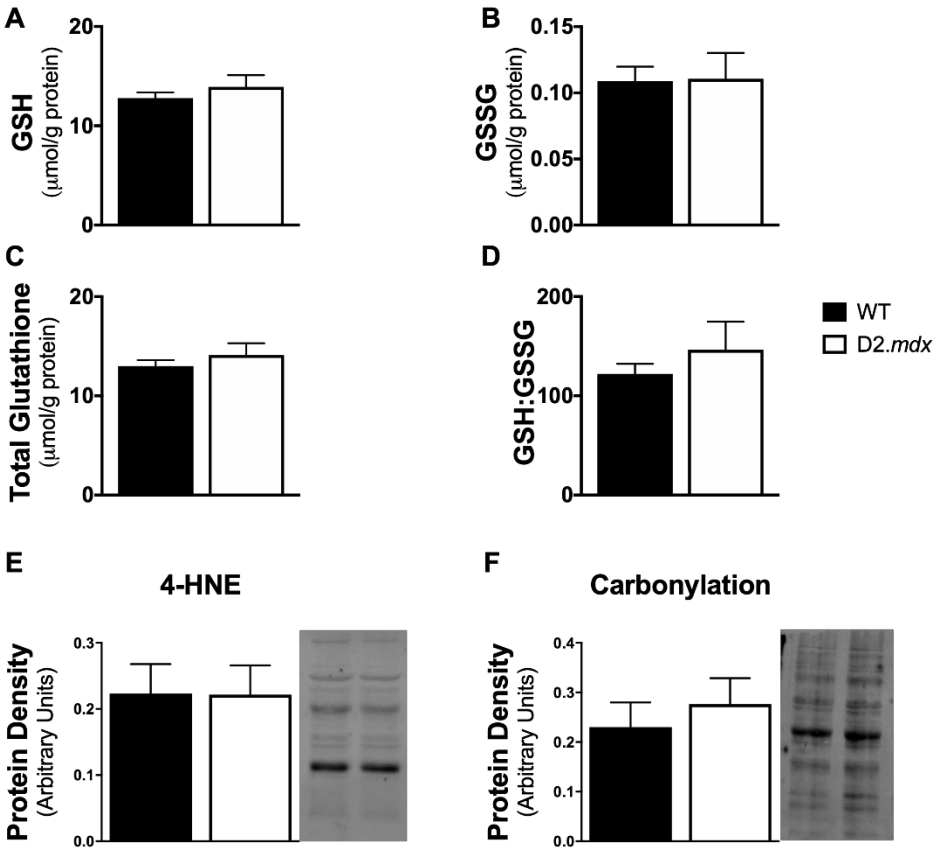

Figure 5-5: Evaluation of redox buffering capacity and whole cell oxidative status. Glutathione was measured in muscle homogenate using (A) HPLC-UV for the detection of GSH and (B) HPLC-Fluorescence for the detection of GSSG. (C) The GSH:GSSG ratio and (D) total glutathione were calculated from GSH and GSSG measurements; n=6. Quantification of proteins modified through (E) lipid peroxidation and (F) carbonylation; n=8. Results represent mean ± SEM; * $p<0.05$ compared to WT.

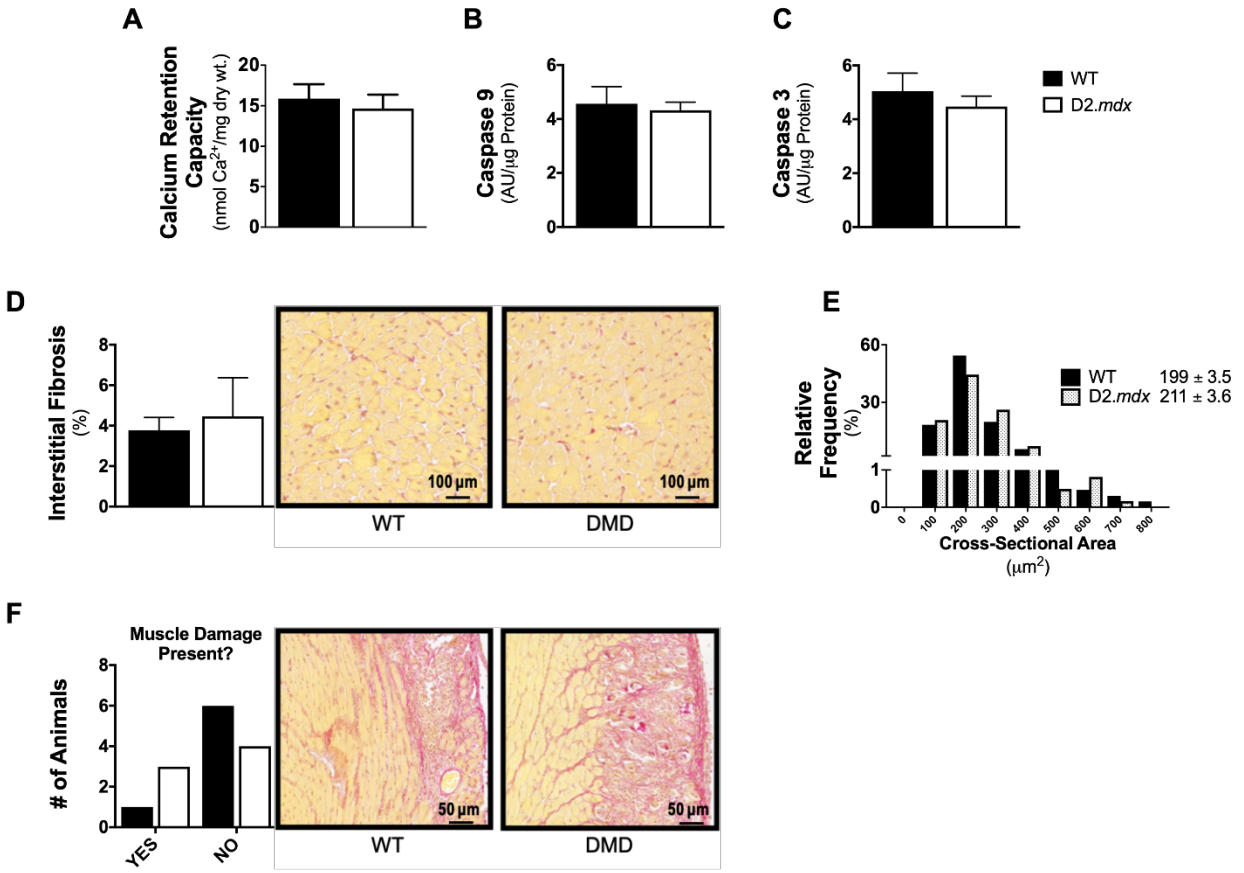

Figure 5-6: Quantification of mitochondrial-associated cell death pathways and overall muscle damage in left ventricle of D2.*mdx* mice. (A) Calcium retention capacity, an index of susceptibility to permeability transition pore opening, was assessed in permeabilized fibres from LV muscle; n=8-9. Mitochondrial-induction of apoptosis was evaluated through (B) caspase 9 activity followed by it's down-stream target (C) caspase 3; n=6-7. (D) Interstitial fibrosis of the LV was quantified using picrosirius red stain. (E) Cross-sectional area was quantified and represented as a relative frequency of fibre diameter with median ± SEM reported. (F) The presence or absence of muscle damage was also identified; n=7. Results represent mean ± SEM; * $p<0.05$ compared to WT.

Discussion

While the early stages of DMD progression are characterized by severe skeletal muscle wasting and weakness, the development of cardiomyopathy occurs in 98% of Patients with DMD by the age of ~18 and progresses to heart failure in approximately 40% of Patients with DMD [77, 4, 37, 43]. Given there is no cure for this condition, identifying secondary contributors to myopathy can guide the development of potential therapeutics in order to slow disease progression and improve quality of life. The present investigation provides evidence of elevated mitochondrial H_2O_2 emission and impaired oxidative phosphorylation in LV muscle of D2.*mdx* mice. These findings also suggest that previous reports of altered substrate metabolism and decreased TCA cycle intermediates [280] may be related specifically to impaired respiratory sensitivity to ADP, loss of phosphate shuttling by creatine, and impaired Complex I activity. Of note, these mitochondrial dysfunctions occurred at a young age of 4 weeks, prior to the onset of overt cardiac dysfunction and remodelling in D2.*mdx*; abnormalities that present at 28 weeks of age in this mouse model [59]. These findings suggest a potential role for mitochondrial dysfunction as a contributing factor to the etiology of cardiomyopathy that manifests at later stages of the disease.

Mitochondrial dysfunction occurs in the absence of overt cardiac dysfunction and remodelling

Despite the clear changes in mitochondrial bioenergetics, D2.*mdx* mice showed no signs of overt cardiac dysfunction at this young age. Moreover, we found that the heart dimensions of D2.*mdx* mice were smaller than WT mice but these size differences were associated with decreased body weights. Thus, unlike most cardiac disease conditions that are typically associated with cardiac hypertrophy and increased interstitial fibrosis, at 4 weeks of age neither heart size nor the degree of interstitial collagen differed between D2.*mdx* and WT mice. In fact, a small increase in cardiac output was observed and this appeared to be related to increased heart rate, as there was no differences in normalized stroke volumes between the two groups of mice. The basis for the

increased heart rate is unclear, but may arise from increased demands for blood flow due to altered peripheral metabolic rate. There was also no difference in the number of animals presenting with muscle damage within the LV between D2.*mdx* and WT groups. While both groups demonstrated fibrosis and muscle damage to the same degree, this infiltration was limited to the epicardium of the heart. Given permeabilized fibres were separated strictly from the endocardium of the LV, all impairments in DMD mitochondrial bioenergetics were found in muscle that did not contain fibrotic or necrotic tissue. As such, the findings indicate that the impairments in mitochondrial bioenergetics occurred in the absence of overt cardiac dysfunction and/or cardiac remodelling.

Specific mechanisms of impaired mitochondrial bioenergetics

At 4 weeks of age D2.*mdx* LV muscle demonstrates elevated H_2O_2 emission as seen in ADP-free conditions. In this state, the absence of ADP results in a higher membrane potential that promotes electron leak at various sites of the electron transport chain, including Complex I, which generates superoxide that is dismutated to H_2O_2 prior to its emission to the cytosolic compartment [232]. Respiration is driven by proton leak through uncoupling proteins, such that greater uncoupling lowers membrane potential and attenuates H_2O_2 emission without ATP synthesis. The observation that D2.*mdx* LV muscle had elevated maximal rates of H_2O_2 emission and lower uncoupled respiration supported by Complex I suggests compromised uncoupling mechanisms may contribute to the increased H_2O_2 emission. Furthermore, the impairments at Complex I were not explained by altered protein content of the NDUFB8 subunit, suggesting that post-translational modifications may also have occurred. Indeed, Complex I activity can be decreased by oxidation of specific cysteine residues [259] but the degree to which this occurs in DMD remains to be determined.

After supporting electron flux with Complex-I substrates, ADP was titrated to reflect an increased cellular energy demand in order to challenge oxidative phosphorylation and lower H_2O_2 emission. In the dystrophic left ventricle, mitochondrial insensitivity to ADP was seen in +Cr and -Cr conditions suggesting both mtCK-dependent PCr/Cr cycling and ADP/ATP cycling were compromised. Impaired ADP sensitivity is detrimental given ADP regulates both oxidative phosphorylation and H_2O_2 emission through governance of membrane potential as noted above [232]. These data suggest that mitochondria are less capable of responding to low and high states of energy demand in that less ATP synthesis would occur while H_2O_2 emission would be greater, and that mitochondrial-cytosolic phosphate shuttling through both PCr/Cr cycling and ATP/ADP cycling (-Cr condition) are compromised.

It is thought that both PCr/Cr and ATP/ADP cycling occur through ANT and VDAC isoforms on the mitochondrial inner and outer membranes respectively (depicted in Figure 1). Given ANT 1 (dominant ANT isoform in muscle) content was not different while VDAC 2 (mitochondrial-specific isoform) content was increased despite impairments in ADP sensitivity in both +Cr and -Cr conditions, it is possible that the ADP-insensitivities may be due to post-translational modifications of these proteins. Indeed, ANT and VDAC also have known phosphorylation sites [264, 265] and acetylation has been associated with ADP insensitivity [285], although the physiological relevance of this regulatory paradigm remains unknown.

A robust impairment in the ability of creatine to govern mitochondrial bioenergetics was noted in D2.*mdx* LV. Specifically, in +Cr, ADP's governance of bioenergetics was impaired across a range of low and high ADP concentrations which suggests a pronounced impairment in mtCK-dependent energy exchange. A study that compared both Cr-dependent and independent models of energy exchange [201] noted an impairment in LV Cr sensitivity, albeit in older C57BL10/ScSn^{mdx} mice

(10-11 months). The present findings indicate this is an early event in the disease process. The cause of the creatine-insensitivity is uncertain as mtCK content was unchanged. However, mtCK is highly susceptible to oxidative modifications, leading to enzymatic inactivation and octamer dissociation, as well as formation of crystalline mitochondrial inclusion bodies, all resulting in loss of function [153, 152]. Future investigations could determine if the predominantly greater dysfunction seen in +Cr (Table 1) is driven by such modifications to mtCK. Finally, these impairments in both Cr conditions were not explained by changes in ETC marker contents which further suggests the dysfunctions are due to unknown post-translational modifications to mtCK and/or ANT and VDAC. Nevertheless, the importance of modelling mtCK equilibrium to capture the mitochondrial dysfunction is apparent given the Cr-dependent model is predicted to be the dominant system of energy exchange [157, 286].

Relationship between the DMD myopathy and impaired mitochondrial bioenergetics

Inherited mutations in the gene dystrophin causes a loss in the normal function of this sarcolemmal-cytoskeletal protein [229]. Subsequent disruptions to cell membrane stability and cytoskeletal organization are linked to a myriad of cellular defects including increased cytosolic calcium, oxidative stress and cell death [93, 2]. Based on these hallmark features of DMD, it has been proposed that mitochondrial dysfunctions arise from these multiple cellular stressors and may ultimately contribute to muscle fibre degeneration [34, 195, 33]. It is thought that impairments in both mitochondrial respiration and H_2O_2 emission can contribute to the induction of PTP formation and subsequently activate mitochondrial derived cell death pathways. Indeed, mitochondrial induction of apoptosis and necrosis has been linked to several diseases that also exhibit elevated mitochondrial ROS and impaired oxidative phosphorylation [269, 270, 226, 271-273]. Such PTP formation has also already been implicated in DMD myopathy in response to calcium stress [33, 35].

In contrast to the present findings of similar PTP sensitivities to calcium, previous work has shown increased susceptibility to PTP opening in both intact dystrophic hearts as well as LV muscle fibres from C57BL10/ScSn^{mdx} mice [199, 32]. Differences in methodology may contribute to these divergent findings. For example, when intact hearts from C57BL10/ScSn^{mdx} are subjected to I/R injury, the number of mitochondria undergoing PTP opening is increased compared to normal hearts. However, this physiological stressor was required to unmask differences, as PTP opening was unchanged prior to the induction of I/R relative to WT controls [199, 32]. Also, only one study to date has assessed PTP opening in permeabilized fibres but evaluated PTP opening in terms of elapsed time in response to a single bolus of Ca^{2+} [199], as opposed to determining the concentration of Ca^{2+} required to trigger PTP opening as was done in the present study. This difference in assessment approaches could alter conclusions, particularly given time to PTP opening was lower in *mdx* mouse Tibialis Anterior, yet the [Ca^{2+}] required to induce PTP was unchanged [33]. This observation suggests that comparing methods of PTP assessment may be necessary to better understand PTP responses. Alternatively, our observations of increased H_2O_2 emission and decreased respiration may be preceding compromised calcium sensitivity seen at later stages in DMD.

In line with this speculation, elevated mH_2O_2 emission and impaired respiration at 4 weeks of age were not associated with changes in the redox status of the cell, as measured through glutathione, lipid peroxidation and protein carbonylation. This pattern suggests that the intrinsic buffering capacity of the muscle is sufficient to tolerate the stress induced by these bioenergetic impairments. As a result, no detectable oxidative damage is evident at this early time point. Furthermore, the lack of irreversible oxidative damage and activation of cell death pathways is consistent with the absence of an overt cardiomyopathy at this early time point. However, it is plausible to believe

that as the disease progresses, the buffering capacity of the cell will become overwhelmed, resulting in the documented oxidative damage of dystrophic cardiac muscle [93, 111] and the subsequent contribution of this damage to cardiomyopathy.

The present findings implicate mitochondrial dysfunction as a potential contributor to cardiac dysfunction. Indeed, pre-clinical tests showed that Idebenone – a quinone based electron shuttler [206, 207] - improved cardiac function and exercise performance in *mdx* mice [208] as well as cardiac and respiratory function in persons with DMD during clinical trials [210, 211, 287, 209], directly implicating the mitochondria in cardiac dysfunction in DMD. While promising at high doses, there are concerns over idebenone's limited bioavailability [212]. Given other mitochondrial-targeted therapeutics were shown to be effective at preventing mitochondrial dysfunction in conditions such as ischaemia-reperfusion injury [258, 224], the present findings suggest these compounds should be explored for their potential in preserving mitochondrial bioenergetics and muscle quality in DMD, particularly prior to the onset of cardiac dysfunction.

Conclusions

In summary, elevations in Complex I-supported mitochondrial H_2O_2 emission during impaired oxidative phosphorylation were identified in the LV of dystrophin-deficient mice. These mitochondrial abnormalities occur at any early age prior to the onset of overt cardiac dysfunction and remodelling [60, 59] given fibrosis and necrosis were unchanged, and cardiac functional indices were not impaired. Identifying these mitochondrial-specific impairments at this early age may guide the development of mitochondrial-targeted therapeutics that restore normal Complex I activity as well as bioenergetic control by ADP and creatine in order to delay the onset of cardiomyopathy and subsequent development of heart failure in DMD.

Additional Information

Competing Interests

There are no competing interests or conflicts of interest.

Author Contributions

M.H., S.V.R., P.B., J.S. and C.G.R.P. contributed to the conception or design of the work. M.H., S.V.R., P.C.T., N.P., B.E., J.H., U.S., P.B., J.S. and C.G.R.P. contributed to acquisition, analysis or interpretation of data. All authors contributed to drafting the work or revising it critically for important intellectual content. All authors approved the final version of the manuscript, agree to be accountable for all aspects of the work in ensuring that questions related to the accuracy or integrity of any part of the work are appropriately investigated and resolved and all persons designated as authors qualify for authorship, and all those who qualify for authorship are listed.

Funding

Funding was provided to C.G.R.P. by the National Science and Engineering Research Council (NSERC #436138-2013) with infrastructure supported by Canada Foundation for Innovation, the Ontario Research Fund, NSERC Research Tools and Instruments, and the James H. Cummings Foundation. J.A.S. is a new investigator with Heart and Stroke Foundation of Canada and the Heart and Stroke Foundation of Canada (HSFC; S13 SI 0592). P.B. was supported by Canadian Institutes of Health Research, Project Grant (PJT 153159) and a Canada Research Chair in Cardiovascular Biology. M.C.H. and P.C.T. were supported by a NSERC CGS-PhD scholarship. S.V.R. was supported by an Ontario Graduate Scholarship.

Acknowledgements

We thank Dr. Robert Tsushima, York University, for his kind provision of access to the Vevo 2100 system.

Supplemental Data – Not included in published manuscript

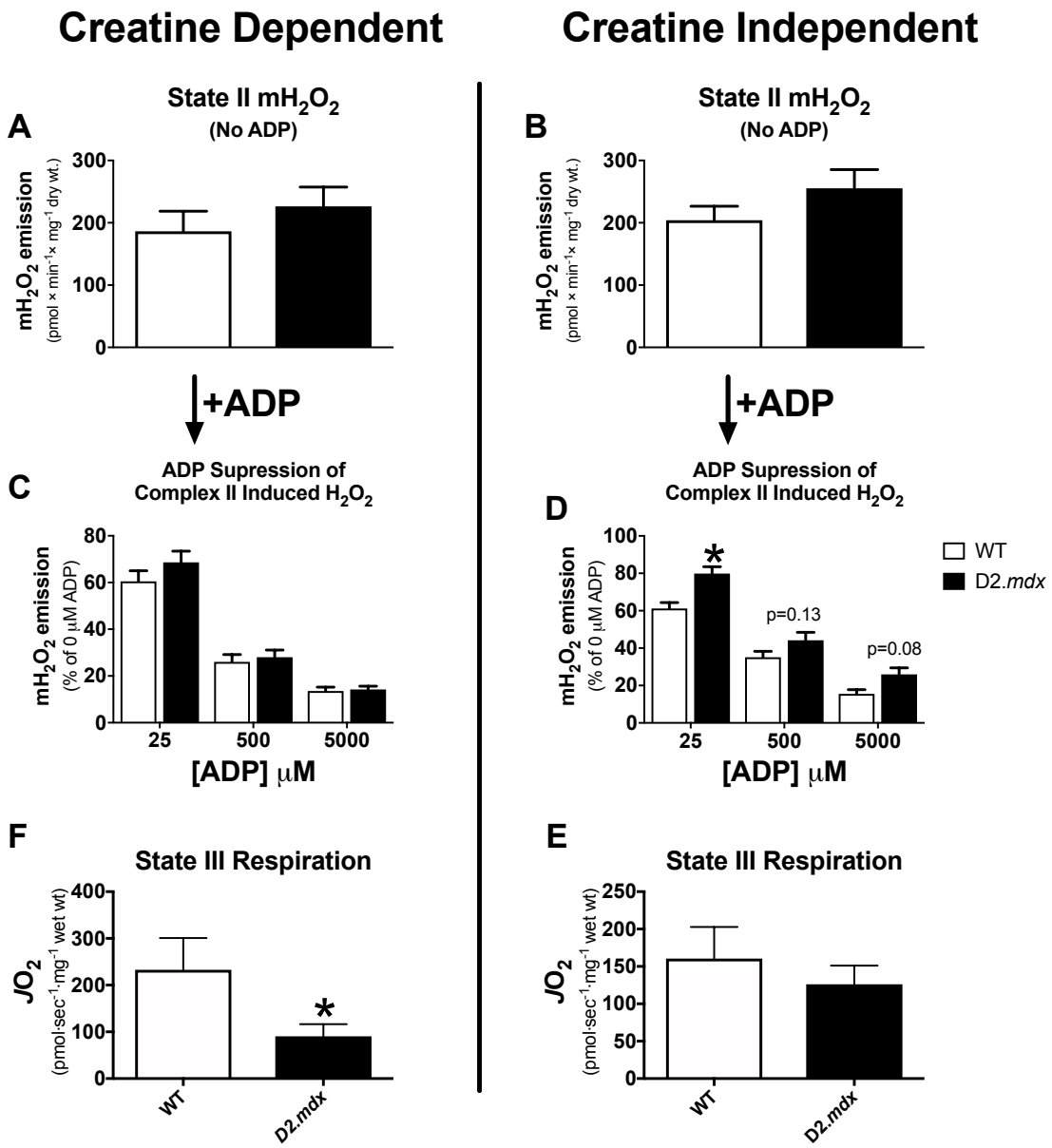

Supplemental Figure 5-1: Complex II supported mH_2O_2 emission and state III respiration in LV muscle. State II (no ADP) mH_2O_2 emission, supported by Complex-II substrate succinate (10mM), was assessed in the (A) presence (Creatine Dependent) and (B) absence (Creatine Independent) of 20mM creatine. State III (ADP) mH_2O_2 emission was evaluated at low (25μM), sub-maximal (500μM) and maximal (5000μM) [ADP] in the presence (C) and absence (D) of creatine; n=12-17. State III respiration, supported by complex-II substrate succinate (20mM) was evaluated in the presence (F) and absence (E) of 20mM creatine; n= 6-9. Results represent means ± SEM; * $p<0.05$ compared to WT.

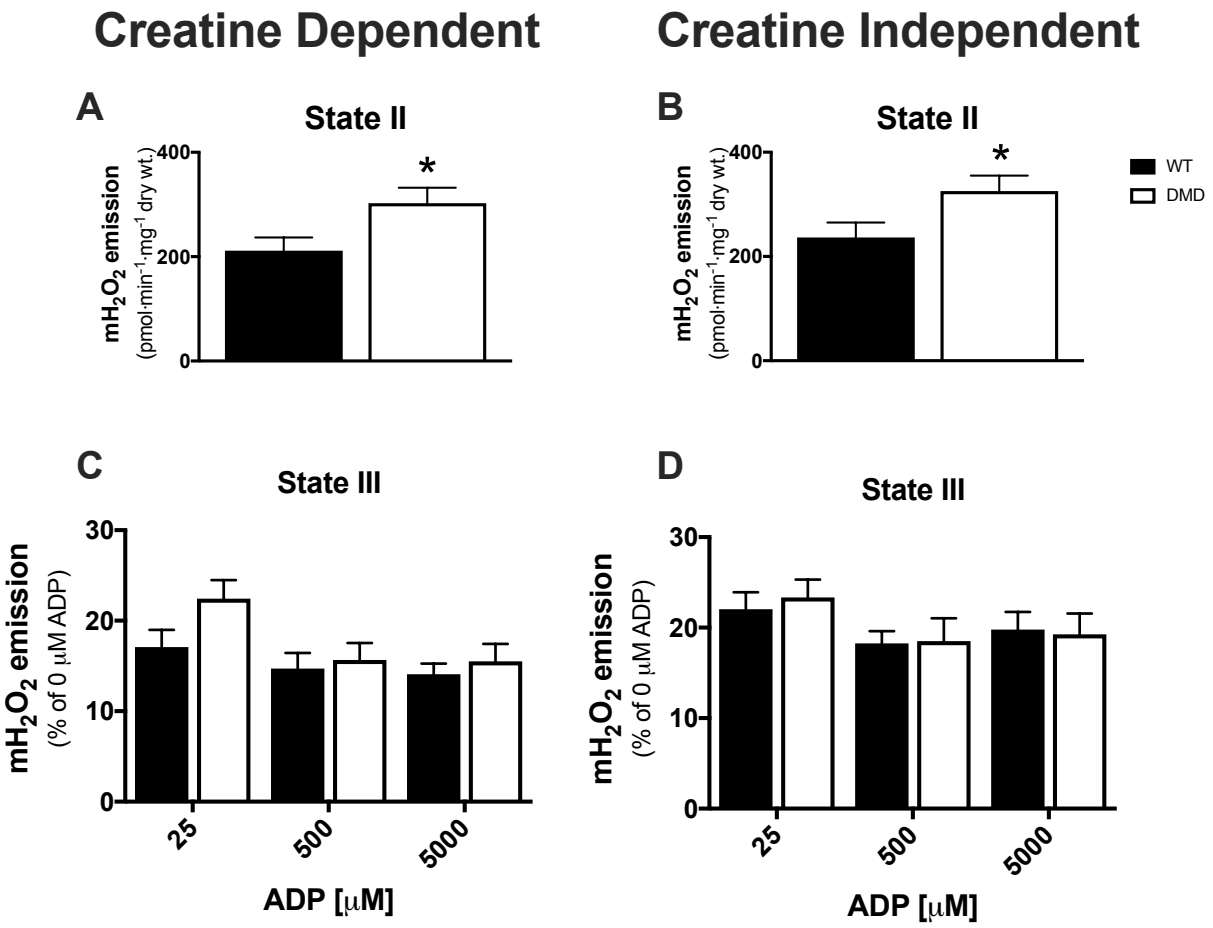

Supplemental Figure 5-2: Absolute rates of Complex-I supported mH_2O_2 emission. State II mH_2O_2 was supported by Complex-I substrates Pyruvate (5mM) and Malate (2mM) in the **A.** presence (Creatine Dependent) and **B**. absence (Creatine Independent) of 20mM creatine. ADP's attenuation of maximal H_2O_2 emission (state III) was evaluated in the same **C.** creatine-dependent and **D.** creatine-independent conditions. Results represent mean ± SEM; n=10-12; * $p<0.05$, compared to WT.

6 The mitochondrial targeted peptide SBT-20 improves diaphragm and skeletal muscle pathophysiology in dystrophin-deficient mice

Assay Development Prior to the start of Project 3:

1. *In Situ* Quadriceps Force Production – in collaboration with SVR
2. *In Vitro* Diaphragm Force Production – in collaboration with CAB

Author Contributions: The majority of experiments for this project were carried about by Meghan Hughes. MH maintained the breeding colony required for this project. As tissue from the animals in this project was being used for the theses of both MH and SVR, the following tasks were shared amongst the two students. MH and SVR completed daily drug injections. MH and SVR completed all whole body *in vivo* testing, *in situ* quadriceps force production experiments and all μCT scans. MH and SVR performed all tissue harvests and mitochondrial bioenergetic assays (respiration, mH_2O_2 emission, calcium retention capacity). PT completed the analysis of μCT data. CAB ran *in vitro* diaphragm force production while MH completed the analysis of this data and assisted with the method development. MH completed serum creatine kinase experiments. MH performed all caspase assays and western blotting experiments. PCT completed glutathione measurements. AD, ET and TH completed all immunohistochemistry and TEM imaging and analysis.

The mitochondrial targeted peptide SBT-20 improves diaphragm and skeletal muscle pathophysiology in dystrophin-deficient mice

Authors: MC Hughes[a*], SV Ramos[a*], C Bellissimo[a], AG Dial[b], E Tin[b], PC Turnbull[a], P Tadi[a], U Schlattner[c], TJ Hawke[b] and CGR Perry[a†].

Affiliations:

[a]Muscle Health Research Centre, School of Kinesiology, York University, 4700 Keele Street, Toronto, ON, Canada, M6J 1P3.

[b]Department of Pathology and Molecular Medicine, McMaster University, 1280 Main St W, Hamilton, ON, Canada L8N 3Z5.

[c]Laboratory of Fundamental and Applied Bioenergetics (LBFA) and SFR Environmental and Systems Biology (BEeSy), University Grenoble Alpes, 621 Avenue Centrale, 38400 Saint-Martin-d'Hères, Grenoble, France

*Authors contributed equally to this work

Figure count: 7 + 2 supplemental

[†]Address for Correspondence:

Christopher Perry, PhD
School of Kinesiology and Health Science
Muscle Health Research Centre
344 Norman Bethune College
York University
4700 Keele Street
Toronto, Ontario M3J 1P3
(P) 416 736 2100 ext. 33232
cperry@yorku.ca

Abstract

Duchenne muscular dystrophy (DMD) is a genetic-based disease which causes severe muscle wasting and weakness, resulting in loss of ambulation and premature death due to cardiac and/or respiratory failure. Current standard of care focuses on treating secondary contributors to the DMD myopathy and as such, there is a clear need to develop a portfolio of potential therapeutic candidates that target the underlying causes of muscle degeneration in this disease. Here we evaluate the efficacy of the mitochondrial-targeted peptide SBT-20 in improving DMD pathophysiology through the amelioration of impairments in mitochondrial bioenergetics. Beginning at 4 days of age, D2.B10-DMD^{mdx}/2J (D2.*mdx*) mice received daily injections of 5mg/kg SBT-20 or volume equivalent saline for 28 days. A WT group was also evaluated at this time point. Following treatment, mitochondrial bioenergetics (oxidative phosphorylation, mitochondrial H_2O_2 emission) were improved in diaphragm and quadriceps muscle. These improvements were associated with elevated force production in the diaphragm and decreased fibrosis in the quadriceps. The ultra-structure of quadriceps mitochondria was also improved following treatment, despite a surprising increase in susceptibility to calcium-induced permeability transition pore opening and mitochondrial-derived caspase activity. Furthermore, while body weight was unchanged, lower limb muscle volume improved, as did forelimb grip strength. These improvements were evident at a very early stage in disease progression. Collectively, these findings demonstrate that SBT-20 improved specific bioenergetic and muscle quality indices and should be considered further for its potential therapeutic efficacy.

Introduction

Duchenne muscular dystrophy (DMD), caused by defective expression of the structural protein dystrophin, is the most common form of muscular dystrophy, affecting 1 in 3500 boys [45, 2]. Dystrophin acts as an anchor between the cytoskeleton and sarcolemma, providing structural stability to smooth, cardiac and skeletal muscle fibres [229]. While at a clinical level, a lack of dystrophin causes progressive muscle wasting and weakness, the cascade initiated by this loss of dystrophin, which culminates in robust muscle degeneration, is not fully understood. There is currently no cure for DMD and the progressive nature of the disease results in early loss of ambulation (mid-teenage years) followed by premature death due to cardiac and/or respiratory failure (early adulthood). To date, gene based therapies have had limited success in treating patients with DMD [47]. Indeed, current clinical practice involves the use of glucocorticoids for treatment, which target inflammation as opposed to the genetic defect itself [7]. Unfortunately, long term treatment with glucocorticoids is associated with several negative side effects [48]. As such, identifying the mechanisms underlying muscle degeneration has been a major focus for guiding therapy development [46].

Muscle lacking dystrophin is highly susceptible to tearing of the cell membrane, a process that has been linked to subsequent cytosolic calcium overload, oxidative stress and cell death [93, 2]. Additionally, a highly pro-inflammatory environment is believed to worsen the myopathy [230]. Recent work from our laboratory has identified the mitochondria as a source of ROS during impaired oxidative phosphorylation in respiratory and skeletal muscles from D2.B10-DMD^{mdx}/2J (D2.*mdx)* mice [286, 155], a mouse model of DMD more closely mimicking human disease progression [59, 60]. These impairments were associated with heightened muscle wasting and weakness suggesting the mitochondria may be an important secondary contributor to disease

pathology. This notion is supported by previous work demonstrating that compounds inhibiting mitochondrial-derived cell death through the blocking of mitochondrial permeability transition pore opening have attenuated the DMD myopathy in mouse models [215, 199, 288], although subsequent clinical trials were less promising with reports of no changes or worsening of the DMD myopathy [219, 289].

Recent clinical trials involving the quinone-based electron shuttler idebenone [207] suggest that targeting the bioenergetic deficits that activate mitochondrial-derived cell death may be more efficacious. Indeed, idebenone has been shown to improve cardiac and respiratory function in DMD patients, presenting some of the more promising outcomes of clinical trials in recent years [210, 211, 209]. However, whether this is related to improved mitochondrial bioenergetics remains unknown as these trials focused on clinical outcomes as opposed to mechanisms of action. Furthermore, as a synthetic analog to coenzyme Q_{10}, structurally idebenone is not mitochondrial-targeted and there are concerns over its limited bioavailability [212]. To date, while the mitochondria appear to be a potential therapeutic target, it remains unknown if a mitochondrial-targeted compound can improve DMD pathophysiology through the attenuation of impaired mitochondrial bioenergetics.

The mitochondrial-targeted peptide SBT-20, an aromatic-cationic compound that targets cardiolipin on the inner mitochondrial membrane, has been shown to increase mitochondrial oxidative phosphorylation [224], attenuate mitochondrial H_2O_2 emission [224] and prevent against the activation of cell death pathways [223] as well as oxidant-induced damage [225] in rodent models of ischemia reperfusion [224] and myocardial infarction [225]. Each of the aforementioned cellular dysfunctions have previously been identified in DMD [93, 2, 195, 156]. Furthermore, cardiolipin plays an important role in the control of mitochondrial bioenergetics through its binding

with key regulators of energy exchange (Figure 2C), forming a proteolipid complex that provides efficient energy exchange into and out of the mitochondria [200]. However, both cardiolipin and mtCK are highly redox sensitive whereby oxidative modifications render them dysfunctional [200]. Given the known elevations in mitochondrial ROS emission during impaired oxidative phosphorylation in DMD [156], SBT-20 may represent a viable therapeutic option for targeting mitochondrial bioenergetics to improve pathophysiology in DMD.

In this investigation, we evaluated the efficacy of the cardiolipin-targeted peptide SBT-20 in improving muscle quality and function in respiratory and skeletal muscle from D2.*mdx* mice in the early stages of disease progression. 4 weeks of treatment with SBT-20 improved mitochondrial bioenergetics in both diaphragm and quadriceps muscle, which was associated with muscle specific improvements in pathophysiology as well as increases in lower limb muscle volume and forelimb grip strength.

Material and Methods

Animal Care

D2.*mdx* mice originated from a breeding colony maintained at York University (Toronto, Canada) and sourced from Jackson Laboratories (Bar Harbor, United States). Beginning at 4-days of age, all animals within a litter received a daily subcutaneous injection of SBT-20 (Stealth Biotherapeutics; Newton, MA, USA) at a dose of 5 mg/kg. At 10 days of age, pups were sexed and treatment commenced in male offspring. Age matched litters received the volume equivalent dose of vehicle (0.9% NaCl) through subcutaneous injection. Animals were treated for 28 days followed by functional testing and subsequent muscle harvest. 4-week old DBA/2J wildtype (WT) mice were obtained directly from Jackson Laboratories due to breeding challenges with this strain. Upon arrival, DBA/2J mice were given a minimum of 72 hours to acclimatize before experiments were performed. All animals were provided access to standard chow and water ad libitum. All experiments and procedures were approved by the Animal Care Committee at York University (AUP Approval Number 2016-18) in accordance with the Canadian Council on Animal Care.

Body Composition and Functional Assays

Timeline of measurements and muscle allocation

Various functional assessments were performed on mice before surgical removal of muscle for *in vitro* analyses. Specifically, 2 days prior to surgery, whole body functional testing (Cage Hang Time, Forelimb Grip Strength and Voluntary Wheel Running) were performed. On the day of surgery, prior to muscle harvest, animals underwent a μCT scan for muscle volume followed by *in situ* assessment of quadriceps (Quad) force production. Immediately following tissue harvest, a portion of the Diaphragm from used for *in vitro* assessment of Diaphragm force production. Due to tissue limitations, a separate subset of animals was used for histochemistry, TEM, caspase

activity and glutathione measurements. Methods for these assessments are described in detail below.

Voluntary Wheel Running

Animals were placed in individual cages equipped with a locked 14 cm diameter running wheel and rotation counter (VDO m3 bike computer, Mountain Equipment Co-Op, Vancouver, Canada). After 24 hours of acclimatization, wheels were unlocked and distance run over 24 hours was recorded.

Cage Hang Time

Animals were placed on top of a metal cage lid and positioned so that all four limbs grasped the cage. The cage lid was inverted so that the mouse was hanging and cage hang time was recorded for a maximum of 180 seconds as previously described [156].

Forelimb Grip Strength

Forelimb grip strength was assessed using a force transducer (Mark 10 Digital Force Gauge, Copiague, NY) and has been described in detail previously [156]. Briefly, mice were removed from their cages by the tail and brought towards a grid attached to the force transducer until such time that the mice grasped the grid with their forepaws. Upon grasping, animals were pulled away from the grid until their grasp was broken. Peak tension was recorded, and the trial was repeated twice more. If the animal did not show resistance to the experimenter, the trial was not recorded. Maximum peak tension from the best of 3 trials was used for analysis [233].

In Vivo μCT Scans

In vivo body scans were performed using μCT (SkyScan 1278, Bruker-microCT, Kontick, Belgium) as previously described [156]. Following scans, lower limb muscle volume was analyzed through reconstruction of the image using NRecon (software version 1.7.0.4, Bruker-microCT,

Kontick, Belgium) followed by the analysis of a selected region of interest using CTAn (software version 1.15.4.0, Bruker-microCT, Kontick, Belgium). The region of interest for hind-limb muscle volume was landmarked from the top of the patella to the ankle joint and was quantified by setting thresholds for fat free mass (76-102), expressed as volume (mm^3) of lean mass/g body weight.

In Situ Quadriceps Force Production

In situ force production of the Quad muscle was partially adapted from previous methods [2]. In brief, mice were anesthetized with isoflurane and placed on a platform maintained at 37° C. Hair around the knee was removed and an incision was made above the patella to expose the femoral tendon which was then tightly secured with suture. Once the knot was in place, the tendon was carefully severed and the suture was attached to an Aurora Scientific 305C muscle lever arm with s hook (Aurora, Ontario, Canada). The knee was secured with a vertical knee clamp immobilizing the knee joint with a 27 G needle. Contraction of the Quad was controlled through percutaneous stimulation of the femoral nerve anterior to the hip joint. Optimal resting length (L_o) was determined using single twitches (pulse width = 0.2ms) at varying muscle lengths. Once L_o was established, force as a function of stimulation frequency was measured during 7 isometric contractions at varying stimulation frequencies (1, 40, 60, 80, 100, 120, 140, 160 Hz). Following the force-frequency protocol, a 5 minute recovery period was provided followed by a maximum torque test, performed at the frequency by which maximum force was achieved during the force-frequency curve. The quadriceps muscle was then harvested and weighed to allow for normalization of force production to muscle weight in mg.

In Vitro Diaphragm Force Production

Assessment of contractile force in Diaphragm strips was partially adapted from previously described methods [290, 291]. The entire Diaphragm was removed and placed in a petri dish of

ice cold Ringer solution containing (in mM):121 NaCl, 5 KCl, 1.8 $CaCl_2$, 0.5 $MgCl_2$, 0.4 $NaHPO_4$, 24 $NaHCO_3$, 5.5 glucose and 0.1 EDTA; pH 7.3 [292] oxygenated with 95% O_2 and 5% CO_2. Diaphragm strips were cut from the central region of the lateral costal hemidiaphragm. The strips included an adjacent section of rib on either side of the strip and part of a central tendon. Silk suture was tied to the central tendon as well the ribs, and the preparation was transferred to an oxygenated bath filled with Ringer solution, maintained at 25°C. The suture secured to the central tendon was then attached to a lever arm while the suture loop secured to the ribs was attached to a force transducer. The Diaphragm strip was situated between flanking platinum electrodes driven by a biphasic simulator (Model 305C; Aurora Scientific, Inc., Aurora, ON, Canada). Optimal resting length (L_o) was determined using single twitches (pulse width = 0.2ms) at varying muscle lengths. Once L_o was established, force as a function of stimulation frequency was measured during 7 isometric contractions at varying stimulation frequencies (1, 10, 20, 40, 60, 80, 100, 120, 140 Hz). Following the force-frequency protocol, a 5 minute recovery period was provided followed by a maximum torque test, performed at the frequency by which maximum force was achieved during the force-frequency curve. Force production was normalized to the calculated CSA of the muscle strip (m/l*d) where m is the muscle mass, l is the length, and d is mammalian skeletal muscle density (1.06 mg/mm^3).

Mitochondrial Bioenergetic Assessments

Preparation of Permeabilized Muscle Fibre Bundles (PmFB)

This technique is partially adapted from previous methods and has been described elsewhere [237-240]. Briefly, muscles were removed from mice during anaesthesia with isoflurane. The Quad from the non-stimulated leg as well as a strip of Diaphragm were removed and immediately placed in ice-cold BIOPS, containing (in mM): 50 MES Hydrate, 7.23 K_2EGTA, 2.77 CaK_2EGTA, 20

imidazole, 0.5 dithiothreitol, 20 taurine, 5.77 ATP, 15 PCr, and 6.56 $MgCl_2 \cdot 6\ H_2O$ (pH 7.1). Each muscle was trimmed of connective tissue and fat and divided into several small muscle bundles (~2–7 mm, 1.0–2.5 mg wet weight). Each bundle was gently separated along the longitudinal axis to form bundles that were treated with 40 μg/ml saponin in BIOPS on a rotor for 30 minutes at 4° C. Bundles destined for mitochondrial H_2O_2 emission (mH_2O_2) measurements (described below) were also treated with 35 μM 2,4-dinitrochlorobenzene (CDNB) during the permeabilization step to deplete glutathione and allow for detectable rates of mH_2O_2 [242]. Following permeabilization, the PmFB were divided into three groups; 1) bundles intended for high resolution respirometry were placed in MiR05 containing (in mM): 0.5 EGTA, 10 KH_2PO_4, 3 $MgCl_2 \cdot 6\ H_2O$, 60 K-lactobionate, 20 Hepes, 20 Taurine, 110 sucrose and 1 mg/ml fatty acid free BSA (pH 7.1) while 2) bundles intended for mH_2O_2 were placed in Buffer Z containing (in mM): 105 K-MES, 30 KCl, 10 KH_2PO_4, 5 $MgCl_2 \cdot 6\ H_2O$, 1 EGTA and 5mg/ml BSA (pH 7.4) . PmFB were washed on a rotor at 4°C in MiR05 or Buffer Z until the measurements were initiated. 3) Bundles intended for calcium retention capacity were placed in Buffer Y + 1 mM EGTA containing (in mM): 250 sucrose, 10 tris-HCl, 20 tris-base, 10 KH_2PO_4 and 0.5mg/mL BSA and washed on a rotor at 4° C for 10 minutes. PmFB were then transferred to a second wash of Buffer Y + 10 μM blebbistatin (BLEB, see below) and were washed on a rotor at 4°C until measurements were initiated. Following permeabilization and washing, all mitochondrial bioenergetic measurements were performed in the same order from one animal to another and between groups to ensure consistent durations of the wash step.

Mitochondrial Respiration

High-resolution O_2 consumption measurements were conducted in 2 ml of respiration medium (MiR05) using the Oroboros Oxygraph-2k (Oroboros Instruments, Corp., Innsbruck, Austria) with

stirring at 750 rpm at 37 °C [239, 240, 243-245]. Respiration medium contained 20mM Cr to saturate mitochondrial creatine kinase or no creatine to prevent the activation of mtCK [283, 243]. A third condition of 13.9mM PCr and 9.1mM Cr was used to provide an equilibrium across mtCK as occurs in skeletal muscle at rest *in vivo* [247]. For ADP-stimulated respiratory kinetics, 5 mM pyruvate, accompanied by 2 mM malate, were added as Complex I substrates (via generation of NADH to saturate electron entry into Complex I) followed by a titration of submaximal ADP (25 μM and 500 μM) and maximal ADP (5 mM). Cytochrome *c* was added to test for mitochondrial membrane integrity, with all experiments demonstrating <10% increase in respiration. Finally, succinate (20 mM) was then added to saturate electron entry into Complex II. All experiments were conducted in the presence of 5μM BLEB in the assay media to prevent spontaneous contraction of PmFB [243, 248, 244]. Each protocol was initiated with a starting [O_2] of approximately 350 μM and was completed before the oxygraph chamber [O_2] reached 150 μM as done previously [239, 240, 243-245]. Polarographic oxygen measurements were acquired in 2 s intervals with the rate of respiration derived from 40 data points and expressed as pmol/s/mg wet weight. PmFB were weighed in ~1.5 ml of tared BIOPS (ATP-containing relaxing media) to prevent rigor that occurs when weighing PmFB in open air (unpublished observations).

Mitochondrial H_2O_2 Emission (mH_2O_2)

mH_2O_2 was determined fluorometrically (QuantaMaster 40, HORIBA Scientific, Edison, NJ, USA) in a quartz cuvette with continuous stirring at 37°C, in 1 mL of Buffer Z supplemented with 10 μM Amplex Ultra Red, 0.5 U/ml horseradish peroxidase, 1 mM EGTA, 40 U/ml Cu/Zn-SOD1,5 μM BLEB and 20mM Cr. State II mH_2O_2 was induced using complex I substrates pyruvate (10mM) and malate (2mM) to assess maximal emission potential. Following the induction of state II mH_2O_2, a titration of ADP was added to progressively attenuate mH_2O_2. This assay was repeated

with no creatine in the assay buffer to compare ADP's effects without mtCK-mediated phosphate shuttling. All measurements were made in the presence of 1 μM BLEB to prevent ADP-induced rigor as described above. After the experiments, the fibres were rinsed in double deionized H_2O, lyophilized in a freeze-dryer (Labconco, Kansas City, MO, USA) for >4 h and weighed on a microbalance (Sartorius Cubis Microbalance, Gottingen, Germany). The rate of H_2O_2 emission was calculated from the slope (F/min), from a standard curve established with the same reaction conditions and normalized to fibre bundle dry weight.

Mitochondrial Calcium Retention Capacity

This assay is partially adapted from previous methods [249] and has been described in detail elsewhere [156]. Briefly, mitochondrial calcium retention capacity measurements were completed spectrofluorometrically (QuantaMaster 80, HORIBA Scientific, Edison, NJ, USA) in a cuvette with continuous stirring at 37° C, in 300 μL of Buffer Y containing 1 μM Calcium Green-5N (Invitrogen), 2 μM tharpsigargin, 5 mM 2-deoxyglucose, 2 U/mL hexokinase, 20mM creatine, 5 μM BLEB and 40 μM EGTA. Minimum fluorescence was obtained following the addition of the PmFB, 5 mM glutamate + 2 mM malate and 5 mM ADP to the assay buffer. Calcium uptake was then initiated by a single 8 nmol pulse of $CaCl_2$. Subsequent 4 nmol pulses of Ca^{2+} were added until mitochondrial permeability transition pore (PTP) opening was evident. Two 0.5 mM pulses of Ca^{2+} were then added to saturate the fluorophore and establish a fluorescent maximum. All experiments were conducted at 37 °C. Changes in free Ca^{2+} in the cuvette during mitochondrial Ca^{2+} uptake were then calculated using the known K_d for Calcium Green 5-N and the equations established for calculating free ion concentrations using ion-sensitive fluorophores [250]. After the experiments, the fibres were dried and weighed as described above.

In Vitro Muscle and Blood Analyses

Caspase Activity

Enzymatic activities of caspase 3 and caspase 9 were measured fluorometrically using substrates Ac-DVED-AMC and Ac-LEHD-AMC (Enzo Life Sciences, Farmingdale, NY) as previously described [251, 252].

Glutathione

Glutathione was assessed as previously described [255]. GSH was assessed by UV-HPLC monitoring of NEM-GSH while GSSG was assessed by fluorescent-HPLC by tracking O-pthalymide (OPA, Sigma-Aldrich, Oakville, Canada) tagged GSH through a flow-through cuvette following GSSG conversion to GSH (FireflySci 8830, NY, USA) in a QuantaMaster 40 spectrofluorometer (HORIBA, NJ, USA). All values were normalized to protein concentration and reported in μmol/g protein.

Western Blotting

An aliquot of frozen Quad and Diaphragm (10–30 mg) from each animal was homogenized in a plastic microcentrifuge tube with a tapered teflon pestle in ice-cold buffer containing (mm): 40 Hepes, 120 NaCl, 1 EDTA, 10 $NaHP_2O_7 \cdot 10H_2O$ pyrophosphate, 10 β-glycerophosphate, 10 NaF and 0.3% CHAPS detergent (pH 7.1 adjusted using KOH). Protein concentrations were determined using a BCA assay (Life Technologies, Carlsbad, CA, USA). Fifty μg of denatured and reduced protein was subjected to 10–12% gradient SDS-PAGE followed by transfer to low- fluorescence polyvinylidene difluoride membrane. Membranes were blocked with LI-COR Odyssey Blocking Buffer (LI-COR, Lincoln NE, USA) and immunoblotted overnight (4°C) with antibodies specific for each protein. A commercially available monoclonal antibody was used to detect electron transport chain proteins (human OXPHOS Cocktail, ab110411; Abcam, Cambridge, UK, 1:250 dilution), including V-ATP5A (55 kDa), III-UQCRC2 (48 kDa), IV-MTCO1 (40 kDa), II-SDHB

(30 kDa) and I-NDUFB8 (20 kDa). Commercially available polyclonal antibodies were used to detect voltage dependent anion carrier 2 (VDAC 2) (32059, 33 kDa; Santa-Cruz, 1:1000), adenine nucleotide translocase 1 (ANT 1) (ab180715, 32 kDa; Abcam, 1:1000) and sarcomeric s-mtCK (generous gift from Dr Uwe Schlattner, Grenoble, France; 42 kDa, 1:1000). The mtCK antibody has been validated previously to confirm specificity[256].

After overnight incubation in primary antibodies, membranes were washed three times, for 5 minutes each time, in TBST and incubated for 1 hour at room temperature with the corresponding infrared fluorescent secondary antibody (LI-COR Biotechnology, Lincoln, NE, USA). Immunoreactive proteins were detected by infrared imaging (LI-COR CLx; LI-COR) and quantified by densitometry (ImageJ, http://imagej.nih.gov/ij/). All images were normalized to a whole membrane Amido Black total protein stain (A8181, Sigma, St Louis, MO, USA).

Histochemistry

Immediately after removal from the animal, a strip of Quad and Diaphragm muscle was embedded in O.C.T compound (Tissue Tek), frozen in liquid nitrogen-cooled isopentane and stored at -80°C until analysis. To determine fibrotic area, skeletal muscle sections were stained with Picrosirius Red (fibrotic regions stain red for collagen). Diaphragm and quad sections were imaged on a Nikon 90i-eclipse microscope (Nikon Inc.; Melville, NY) and analyzed with the NIS Elements AR software (v 4.6; Nikon). All images were obtained with a ×20 objective. The operator was blinded with respect to the experimental group of each sample. Images were taken of the entire 8-µm section. To determine collagen content, one large region of interest (ROI) was created, representing the majority of the area of the section, with the exception of the periphery and any obvious artifact. A threshold was applied to create a binary layer to remove background fluorescence, and collagen content was expressed as a ratio of binary area / ROI area. To determine

muscle fiber size, 100 muscle fibers were manually circled per image, and minimum ferret diameter was measured using from NIS Elements software.

Transmission Electron Microscopy (TEM)

A thin strip of Quad and Diaphragm tissue was immediately fixed in 2% (v/v) glutaraldehyde in 0.1 mol/l sodium cacodylate buffer and processed as described previously [253]. Seven unique fibers were represented by nine non-overlapping micrographs (3 subsarcolemmal, 6 intramyofibrillar) each per animal. All images were acquired at x30,000 magnification. Quantification was achieved using object measurements in Nikon Elements software by manually outlining mitochondria and converting these to actual size using a calibration grid [254].

Serum Creatine Kinase

Serum creatine kinase activity was quantified as described previously [156]. In brief, creatine kinase activity was measured spectrofluorometrically (QuantaMaster 80, HORIBA Scientific, Edison, NJ, USA) based on the autofluorescence of NADPH (excitation – 340 nm, emission – 450 nm) using the Pointe Scientific Serum Creatine Kinase kit (Pointe Scientific, Canton, MI, USA). Creatine kinase activity (U/L) was calculated from the rate of NADPH production (F/min) applied to a standard curve produced under the same conditions and normalized to volume dilution.

Statistics

Results are expressed as means ± SEM. The level of significance was established as $p<0.05$ for all statistics. The D'Agostino – Pearson omnibus normality test was first performed to determine whether data resembled a Gaussian distribution. If data failed the normality test, a Kruskal-Wallis non-parametric test followed by a Dunn's post-hoc test were performed (cage hang time, % body fat, seum CK, creatine-dependent state II mH_2O_2 emission in the Diaphragm and Quad, creatine-independent state III mH_2O_2 emission in the Diaphragm, Diaphragm caspase 9, Quad ANT1 and VDAC 2 and Diaphragm GSH:GSSG). When data (all other data) passed normality, a 1-way

ANOVA followed by an LSD post-hoc test was performed for all data excluding state III respiration, state III mH_2O_2, force frequency curves and TEM. The aforementioned data sets underwent a 2-way ANOVA followed by an LSD post-hoc test (GraphPad Prism Software, La Jolla, CA, USA).

Results

SBT-20 treatment improves Diaphragm force production and lowers fibrosis in D2.mdx mice

Evaluation of force production in Diaphragm strips *in vitro* revealed an increase in specific force as a function of frequency in D2.*mdx* mice relative to saline treated D2.*mdx* mice (SAL) (main effect across frequencies, $p<0.05$) but remained lower than WT controls (main effect across frequencies, $p<0.01$; **Figure 1A**). Maximum force produced by SAL was significantly lower relative to WT (-53% vs WT, $p<0.05$). SBT-20 treatment improved maximum force production such that differences relative to WT were no longer evident (**Figure 1B**). Muscle fibre size, evaluated using minimum feret diameter, was not different among the three groups (**Figure 1C**). The degree of fibrosis in SAL animals was significantly higher relative to WT (+44%, $p<0.05$). SBT-20 did not alter degree of fibrosis in the Diaphragm as the degree of fibrosis was still elevated relative to WT (+63%, $p<0.05$; **Figure 1D**).

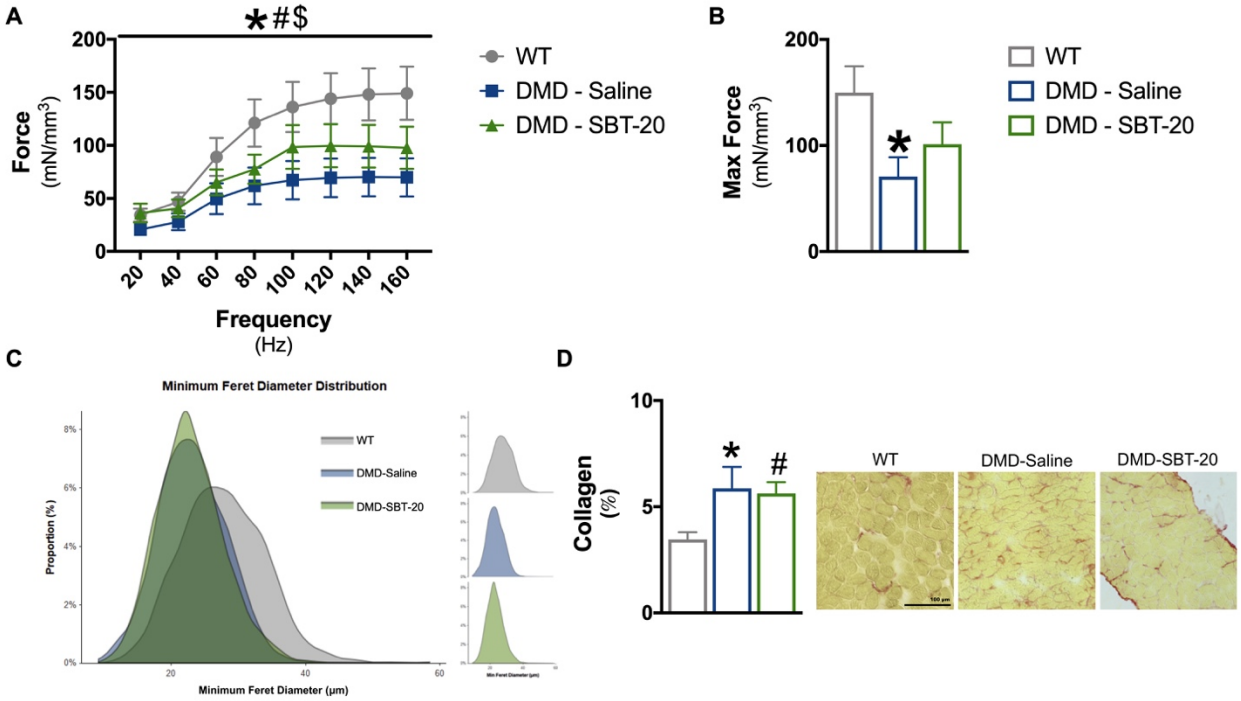

Figure 6-1:Evaluation of muscle quality in Diaphragm following treatment with SBT-20. Diaphragm specific force was evaluated **(A)** across a range of frequencies and through (**B)** maximal tetanic force. Fibre diameter was assessed using (**C)** minimum feret diameter. Degree of fibrosis (**D)** was quantified using picrosirius red staining. Results represent mean ± SEM; n=10-12 (A-B) and n=6 (C-D); * p<0.05, DMD-Saline vs WT; # p<0.05, DMD-SBT-20 vs WT; $ p<0.05, DMD-SBT-20 vs DMD-Saline.

Improvements in Diaphragm force and histopathology are associated with altered creatine-independent mitochondrial bioenergetics

An important consideration in this investigation is the design of *in vitro* assessments of mitochondrial bioenergetics that model *in vivo* critical parameters controlling respiratory and H_2O_2 emission kinetics. Indeed, our previous work identified Complex I dysfunction and loss of central respiratory control by ADP and creatine as the cause of elevated oxidant generation during impaired oxidative phosphorylation. Based on these findings, we believe that a comprehensive assessment of mitochondrial responsiveness to ADP in the context of oxidative phosphorylation and mH_2O_2 emission may be necessary to fully elucidate the effects of SBT-20 on mitochondrial

bioenergetics. Specifically, the stimulation of mitochondrial respiration and mitochondrial H_2O_2 (mH_2O_2) emission during oxidative phosphorylation in Diaphragm were initiated using pyruvate (5mM) and malate (2mM) which generates NADH to stimulate Complex I and were assessed in both the presence (+Cr) and absence (-Cr) of 20mM creatine to drive energy transfer dependent (**Figure 2C**) or independent of mtCK, respectively **(Figure 2F)**.

We first determined whether SBT-20 altered ADP-independent (state II) respiration and mH_2O_2 emission during oxidative phosphorylation. State II respiration is driven by proton leak through uncoupling pathways independent of ATP synthase. Proton leak-dependent respiration both +Cr and -Cr was lower in SAL relative to WT (+Cr: -21%, $p=0.07$; –Cr: -26%, $p<0.05$). SBT-20 treatment did not alter state II respiration rates such that respiration rates remained impaired relative to WT both +Cr (-28%, $p<0.05$; **Supplemental Figure 1A**) and -Cr (-33%, $p<0.05$; **Supplemental Figure 1C**). State II mH_2O_2 emission during oxidative phosphorylation reveals the capacity of oxidant generation by Complex I during oxidative phosphorylation, independent of the influence of ADP. State II mH_2O_2 emission was unchanged across all 3 groups +Cr (**Supplemental Figure 1B)** yet –Cr, SAL was significantly lower relative to WT (-26%, $p<0.05$) and SBT-20 treatment tended to be lower relative to WT (-22%, $p=0.06$; **Supplemental Figure 1D**) while no difference between SBT-20 and SAL were evident. These findings highlight that any SBT-20-derived changes in mitochondrial bioenergetics are ADP-dependent in nature.

We then determined whether SBT-20 resulted in alterations to the central role of ADP in stimulating respiration and attenuating mH_2O_2 emission during oxidative phosphorylation. ADP-supported (state III) respiration and mH_2O_2 emission was evaluated in the presence of low/physiological (25μM), high sub-maximal (500μM) and saturating concentrations (5mM) of ADP, creating a titration curve mimicking low and high metabolic stress. +Cr, SAL ADP-

supported respiration was significantly impaired across all [ADP] relative to WT (-22 to -31%, main effect across ADP, $p<0.05$). SBT-20 did not rescue the impaired respiration such that rates across all [ADP] were no different from SAL and significantly lower relative to WT (-20 to -25%, main effect across ADP, $p<0.05$; **Figure 2A**). mH_2O_2 emission was no different between SAL and WT groups during oxidative phosphorylation +Cr, and no effect of SBT-20 was seen on mH_2O_2 emission in the presence of creatine (**Figure 2B**).

Alternatively, -Cr, SBT-20 treatment rescued both impaired ADP-dependent respiration and mH_2O_2 emission during oxidative phosphorylation. SAL respiration rates were significantly lower relative to WT (-10 to -36%, main effect across ADP, $p<0.05$) while SBT-20 treatment resulted in respiration rates higher relative to SAL (+9 to 21%, main effect across ADP, $p<0.05$) that were no different compaired to WT controls (**Figure 2D**). SAL mH_2O_2 emission was also significantly elevated relative to WT during oxidative phosphorylation (+31 to +47%, main effect across ADP, $p<0.05$) and SBT-20 treatment significantly decreased mH_2O_2 emission compared to SAL (-9 to -10%, main effect across ADP, $p<0.05$), however emission rates remained significantly elevated relative to WT controls (+13 to +34%, main effect across ADP, $p<0.05$; **Figure 2E**).

We also assessed state III respiration in the presence of 13.9mM PCr and 9.1mM Cr, concentrations found *in vivo* in resting skeletal muscle. State III respiration was impaired in SAL animals in Diaphragm (-5 to -17%, main effect across ADP, $p<0.05$; **Supplemental Figure 2A**). SBT-20 further impaired respiration in the Diaphragm such that respiration rates in SBT-20 treated muscle were significantly lower than SAL (-8 to -12%, main effect across ADP, $p<0.05$) and WT (-12 to -28%, main effect across ADP, $p<0.05$; **Supplemental Figure 2A)** indicating some form of heightened sensitivity to phosphocreatine following treatment with SBT-20.

Improvements in mitochondrial bioenergetics following treatment with SBT-20 are not due to changes in protein content of the regulators of energy exchange in Diaphragm

Given the improvements in respiration and mH_2O_2 emission during oxidative phosphorylation that resulted from SBT-20 treatment, the protein content of key regulators of energy exchange was quantified in all 3 groups. Protein content of ANT 1 and VDAC 2, situated in the inner and outer mitochondrial membrane respectively, are significantly decreased in SAL Diaphragm (ANT 1: -26%, $p<0.05$; VDAC 2: -36%, $p<0.05$) relative to WT. SBT-20 treatment did not alter ANT 1 or VDAC 2 content relative to SAL such that content remained reduced relative to WT (ANT 1: -25%, $p<0.05$; VDAC 2: -28%, $p<0.05$; **Figure 2G**). MtCK content was no different among groups in Diaphragm muscle (**Figure 2G**). Quantification of the complexes comprising the electron transport chain (ETC) was also completed to provide an index of mitochondrial content. Individual ETC subunit content was unchanged across groups in the Diaphragm (**Figure 2H)**. However, the sum of all 5 subunits was significantly decreased in SAL relative to WT (-13%, $p<0.05$; **Figure 2H**). SBT-20 treatment did not alter the sum of 5 subunits relative to SAL such that total content was still reduced relative to WT (-16%, $p<0.05$; **Figure 2H**).

SBT-20 reduces content of oxidized glutathione in Diaphragm muscle

The content of the reduced form of glutathione (GSH) was unchanged across all groups in Diaphragm muscle (**Figure 2I**). However, content of the oxidized form of glutathione (GSSG) was significantly elevated in SAL relative to WT (+75%, $p<0.05$) (**Figure 2J**). SBT-20 treatment reduced the content of GSSG in Diaphragm to levels no different from WT controls (**Figure 2J**). Total glutathione **(Figure 2K**) and the ratio of GSH:GSSG **(Figure 2L**) were unchanged across all groups.

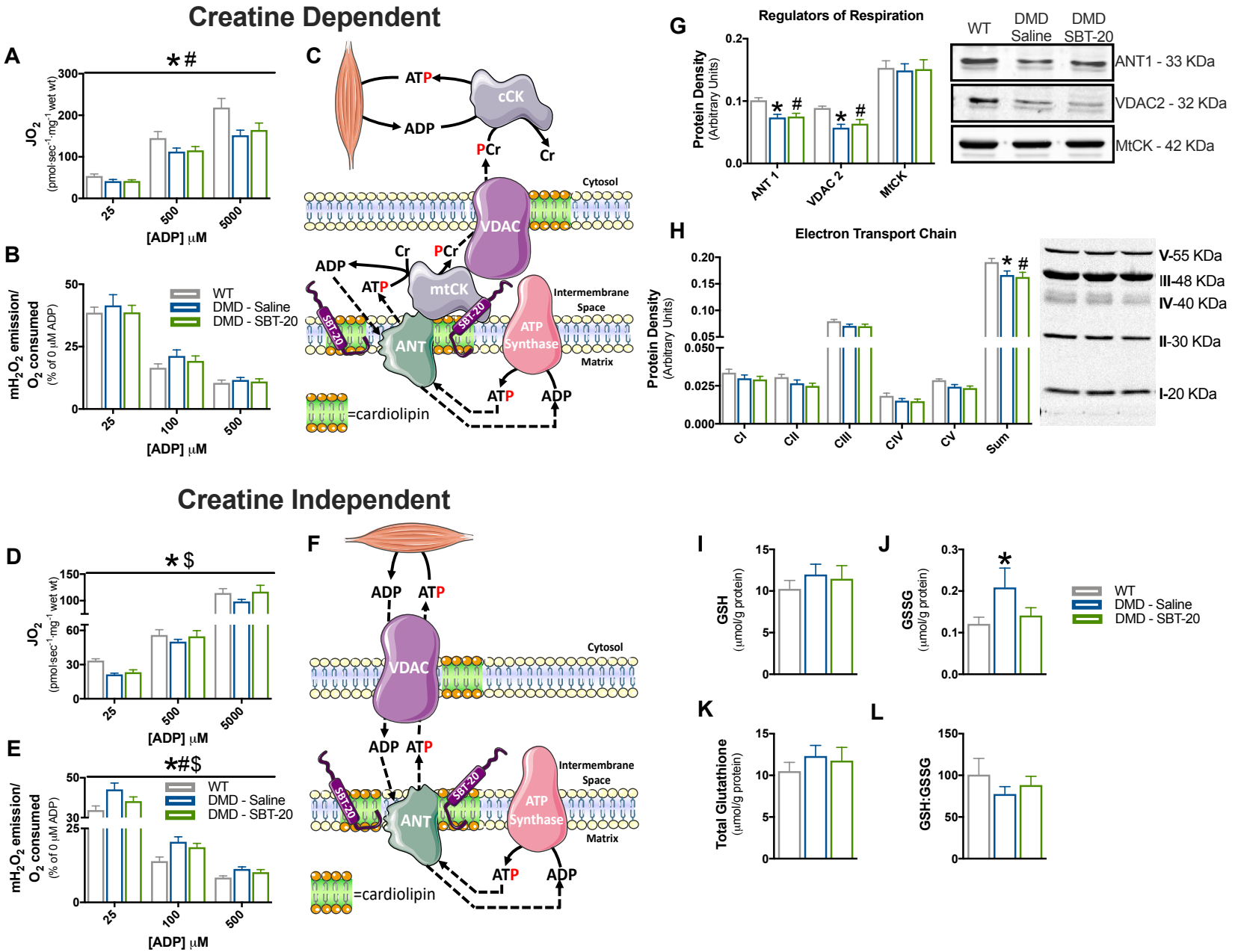
Creatine Dependent
A
*#
JO2 (pmol·sec-1·mg-1 wet wt)
300
200
100
0
25
500
5000
[ADP] μM
B
mH2O2 emission/ O2 consumed (% of 0 μM ADP)
50
25
0
WT
DMD - Saline
DMD - SBT-20
25
100
500
[ADP] μM
C
ATP
ADP
cCK
PCr
Cr
Cytosol
VDAC
Cr
PCr
ADP
ATP
mtCK
Intermembrane Space
SBT-20
ANT
ATP Synthase
Matrix
ATP
ADP
=cardiolipin
G
Regulators of Respiration
Protein Density (Arbitrary Units)
0.2
0.1
0.0
*
#
ANT 1
VDAC 2
MtCK
WT
DMD Saline
DMD SBT-20
ANT1 - 33 KDa
VDAC2 - 32 KDa
MtCK - 42 KDa
H
Electron Transport Chain
Protein Density (Arbitrary Units)
0.20
0.15
0.10
0.05
0.050
0.025
0.000
CI
CII
CIII
CIV
CV
Sum
V-55 KDa
III-48 KDa
IV-40 KDa
II-30 KDa
I-20 KDa
Creatine Independent
D
*$
JO2 (pmol·sec-1·mg-1 wet wt)
150
100
60
30
0
25
500
5000
[ADP] μM
E
*#$
mH2O2 emission/ O2 consumed (% of 0 μM ADP)
50
30
25
0
WT
DMD - Saline
DMD - SBT-20
25
100
500
[ADP] μM
F
ADP
ATP
VDAC
Cytosol
ADP
ATP
Intermembrane Space
SBT-20
ANT
ATP Synthase
Matrix
ATP
ADP
=cardiolipin
I
GSH (μmol/g protein)
15
10
5
0
J
GSSG (μmol/g protein)
0.3
0.2
0.1
0.0
*
WT
DMD - Saline
DMD - SBT-20
K
Total Glutathione (μmol/g protein)
15
10
5
0
L
GSH:GSSG
150
100
50
0

Figure 6-2: Evaluation of mitochondrial bioenergetics and regulators of energy exchange in Diaphragm muscle following treatment with SBT-20. The leading model for energy exchange involves a (**C)** creatine-dependent and (**D)** creatine-independent pathway. ADP stimulated respiration and mH_2O_2 emission during oxidative phosphorylation, supported by Complex-I substrates pyruvate (5mM) and malate (2mM), were assessed in the presence (Creatine Dependent, **A-B**) and absence (Creatine Independent, **D-E**) of 20mM creatine across a range of low and high [ADP], n=10-12. Protein content of adenine nucleotide translocase 1 (ANT 1) on the inner mitochondrial membrane, voltage dependent anion carrier 2 (VDAC 2) on the outer mitochondrial membrane and mitochondrial creatine kinase (mtCK) found in the inner membrane space (**G**) n=8. Protein content of electron transport chain components were also quantified (**H**) n=8. Glutathione was measured in muscle homogenate using HPLC-UV for the detection of GSH (**I**) and HPLC-Fluorescence for the detection of GSSG (**J**). The GSH:GSSG ratio (**K**) and total glutathione (**L**) were calculated from GSH and GSSG measurements n=8. Results represent means ± SEM; * $p<0.05$, DMD-Saline vs WT; # $p<0.05$, DMD-SBT-20 vs WT; $ $p<0.05$, DMD-SBT-20 vs DMD-Saline.

SBT-20 reduces mitochondrial-derived caspase activity but does not alter mitochondrial ultra-structure in Diaphragm

We next determined whether alterations in respiration and mH_2O_2 emission following SBT-20 treatment were associated with changes in markers of mitochondrial-derived cell death. In Diaphragm muscle, there was no difference in the $[Ca^{2+}]$ required to induce PTP opening across the 3 groups (**Figure 3A**). However, SBT-20 significantly decreased caspase 9, a marker of mitochondrial-derived apoptosis relative to both SAL (-23%, $p<0.05$) and WT (-14%, $p<0.05$; **Figure 3B**) yet there was a significant increase in caspase 3 activity in both SBT-20 (+64%, $p<0.005$) and SAL (+60%, $p<0.005$; **Figure 3B**) groups relative to WT and no difference between SBT-20 and SAL.

We then evaluated mitochondrial structure and morphology following treatment with SBT-20. SS mitochondria were unaltered in SAL animals and as such, SBT-20 had no effect on SS ultra-structure in Diaphragm muscle. IMF mitochondria were found to be swollen in SAL muscle and SBT-20 did not prevent this alteration in morphology (**Figure 3C**). SAL animals also demonstrated less IMF mitochondria per unit area than WT controls, however, this alteration was rescued by SBT-20 treatment (**Figure 3D**). Mitochondria density, likely driven by the enlarged mitochondria was elevated in SAL relative to WT and SBT-20 did not affect this marker (**Figure 3E**).

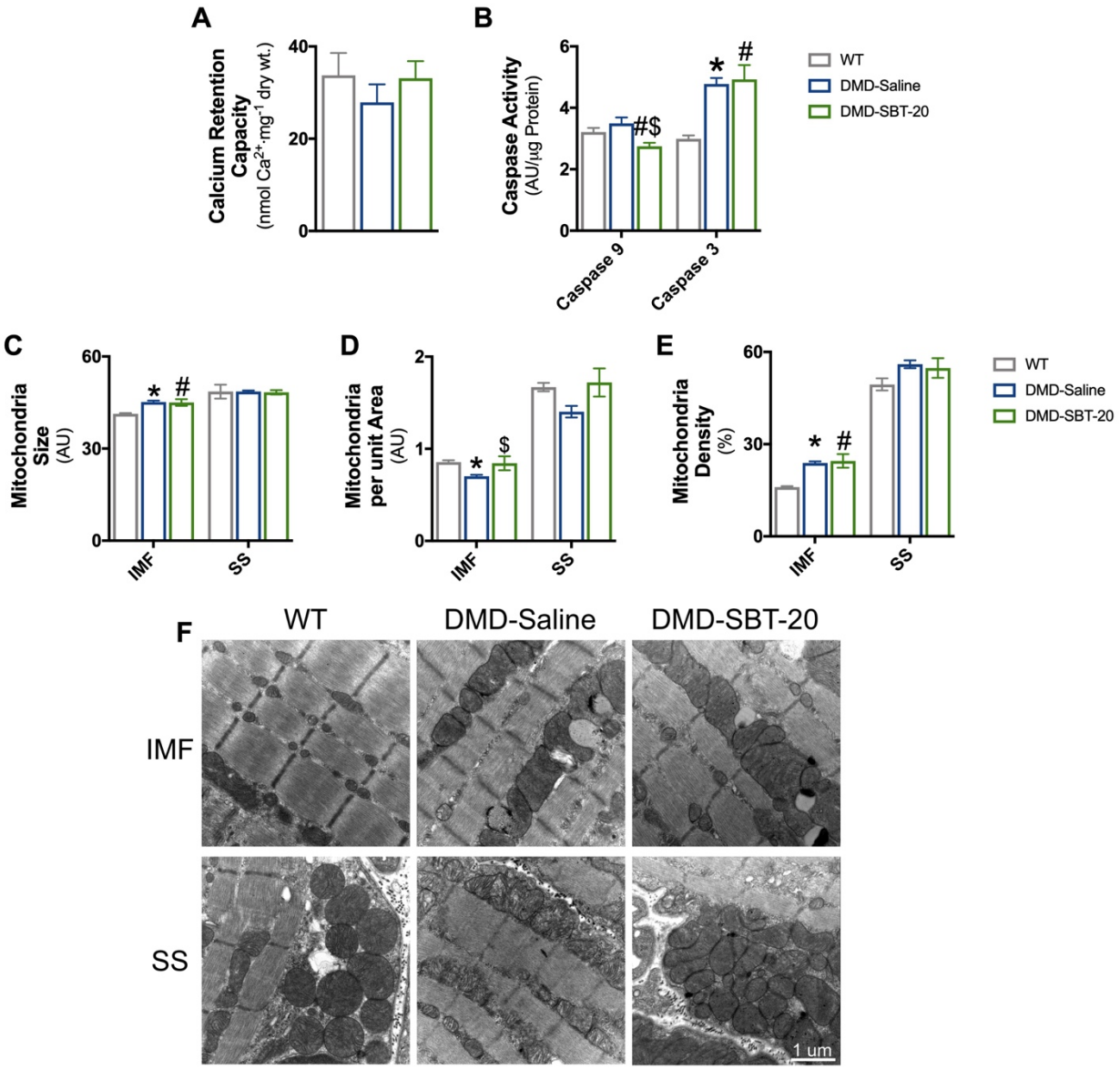

Figure 6-3: Evaluation of mitochondrial quality in Diaphragm muscle following treatment with SBT-20. Calcium retention capacity, an index of susceptibility to permeability transition pore opening was assessed in permeabilized fibres from Diaphragm muscle (**A**); n=10-12. Mitochondrial-induction of apoptosis was evaluated through caspase 9 activity followed by it's down-stream target caspase 3 (**B**); n=8. Transmission electron micrographs were acquired in the and analyzed for mitochondrial size (**C**), distribution (**D**) and density (**E**) within the intermyofibrillar (IMF) and subsarcolemmal (SS) area of the muscle; scale bar = 1 μm, n=3. Results represent mean ± SEM; * p<0.05, DMD-Saline vs WT; # p<0.05, DMD-SBT-20 vs WT; $ p<0.05, DMD-SBT-20 vs DMD-Saline.

SBT-20 decreases the degree of fibrosis in Quad muscle yet has no effect on force production

Evaluation of Quad force production *in situ* revealed that SBT-20 did not increase force as a function of frequency relative to SAL such that both groups displayed significantly lower force production for a given frequency relative to WT controls (main effect across frequencies, $p<0.05$; **Figure 4A).** Based on the frequency at which maximum force was produced for a given animal, maximum tetanic force was then evaluated in each animal. SBT-20 treatment did not improve maximum tetanic force in Quad of D2.*mdx* mice (**Figure 4B**). Muscle fibre size, evaluated using minimum feret diameter, was no different among the three groups (**Figure 4C**) although qualitatively, there appeared to be a rightward shift in fibre distribution, seemingly normalizing fibre distribution following SBT-20 treatment. The degree of fibrosis in SAL animals was significantly higher relative to WT (+43%, $p<0.05$). SBT-20 decreased degree of fibrosis in relative to SAL (-66%, $p=0.052$) such that no differences were evident relative to WT controls (**Figure 1D**).

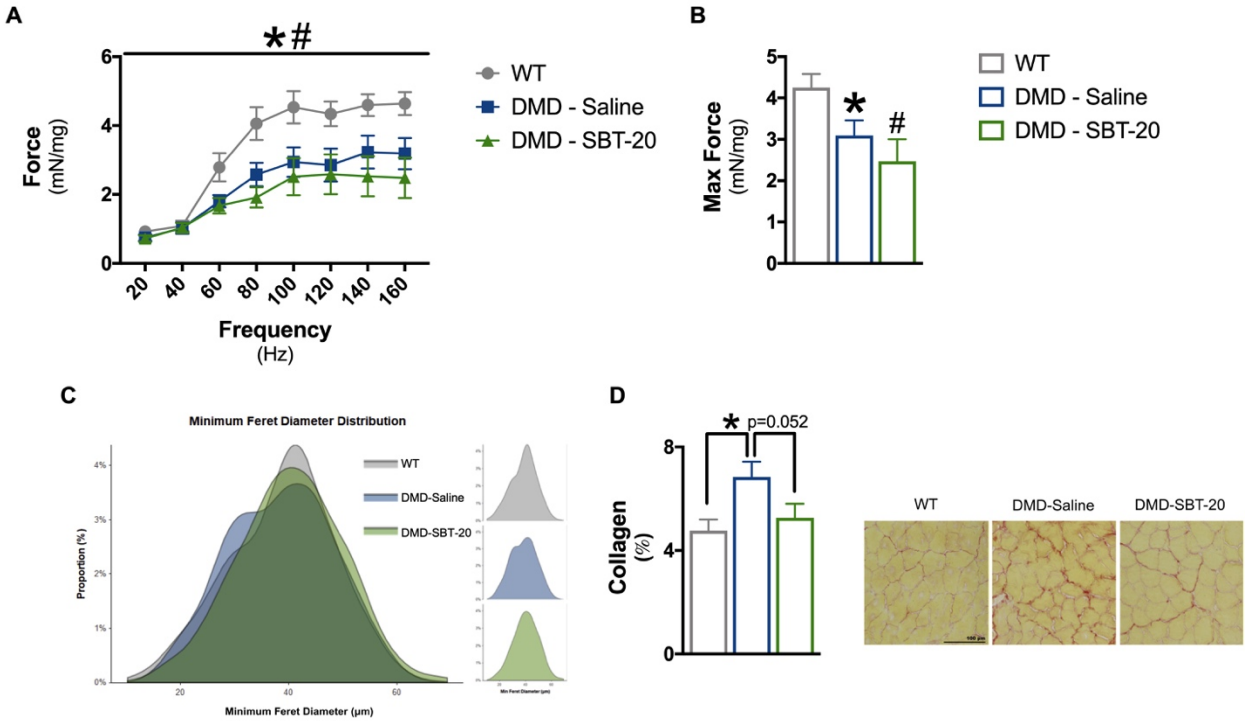

Figure 6-4: Evaluation of muscle quality in Quad following treatment with SBT-20. Quad specific force was evaluated **(A).** across a range of frequencies and through (**B**) maximal tetanic force, n=10-12. Fibre diameter was assessed using (**C**) minimum feret diameter, n=6. (**D**) Degree of fibrosis was quantified using picrosirius red staining, n=6. Results represent mean ± SEM; * p<0.05, DMD-Saline vs WT; # p<0.05, DMD-SBT-20 vs WT; $ p<0.05, DMD-SBT-20 vs DMD-Saline.

SBT-20 improves mitochondrial bioenergetics in a creatine-dependent manner in Quad muscle from D2.mdx mice

The aforementioned bioenergetic experiments in Diaphragm muscle were repeated in Quad muscle across all three groups. +Cr, State II respiration and mH_2O_2 emission during oxidative phosphorylation were no different across the 3 groups (**Supplemental Figure 1E and F**) yet –Cr respiration was significantly lower in SAL vs WT (-41%, p<0.05) and SBT-20 did not rescue this impairment (-44% vs WT, p<0.05; **Supplemental Figure 1G**). –Cr mH_2O_2 emission during oxidative phosphorylation was no different across groups (**Supplemental Figure 1F**). These findings once again highlight the ADP-dependency of SBT-20's effect.

We then determined whether SBT-20 resulted in alterations to the central role of ADP in stimulating respiration and attenuating mH_2O_2 emission during oxidative phosphorylation in the

presence of varying [ADP]. +Cr, ADP-supported (state III) respiration was impaired in SAL relative to WT (-21 to -44%, main effect across ADP, $p<0.05$). SBT-20 treatment improved state III respiration relative to SAL (+18 to +25%, main effect across ADP, $p<0.05$) but rates remained lower than WT controls (-17 to -33%, main effect across ADP, $p<0.05$; **Figure 5A**). Similarly, +Cr ADP-stimulated mH_2O_2 emission is elevated during oxidative phosphorylation in SAL relative to WT (+42 to +82%, main effect across ADP, $p<0.05$) and SBT-20 treatment decreased mH_2O_2 emission relative to SAL (-10 to -25%, main effect across ADP, $p<0.05$) yet emission remained elevated compared to WT controls (+28 to +40%, main effect across ADP, $p<0.05$; **Figure 5B**). Alternatively, -Cr, while ADP-supported respiration was reduced in SAL relative to WT (-33 to -45%, main effect across ADP, $p<0.05$), SBT-20 had no effect on –Cr respiration relative to SAL with rates remaining significantly impaired relative to WT controls (-37 to -50%, main effect across ADP, $p<0.05$; **Figure 5C**). –Cr, mH_2O_2 emission was elevated in SAL relative to WT during oxidative phosphorylation (+23 to +31%, main effect across ADP, $p<0.05$). SBT-20 treatment attenuated this impairment such that there were no differences in emission rates relative to WT (**Figure 5D**).

Similar to Diaphragm, ADP-supported respiration in the presence of *in vivo* concentrations of PCr and Cr was impaired in SAL animals (-30 to -32%, main effect across ADP, $p<0.05$; **Supplemental Figure 2B**) relative to WT and SBT-20 further impaired this respiration in Quad muscle such that respiration rates in SBT-20 treated muscle were significantly lower than SAL (-19 to -27%, main effect across ADP, $p<0.05$;) and WT (-43 to -50%, main effect across ADP, $p<0.05$; **Supplemental Figure 2B**).

Improvements in mitochondrial bioenergetics following treatment with SBT-20 are not due to changes in protein content of the regulators of energy exchange in Quad

Protein content of ANT 1 and VDAC 2, were significantly decreased in SAL (ANT 1: -29%, $p<0.05$; VDAC 2: -29%, $p<0.05$) relative to WT. SBT-20 treatment did not alter ANT 1 or VDAC 2 content relative to SAL such that content remained reduced relative to WT (ANT 1: -36%, $p<0.001$; VDAC 2-36%, $p<0.001$; **Figure 5E**). MtCK content was significantly decreased in SAL relative to WT (-41%, $p<0.01$) and SBT-20 did not alter MtCK relative to SAL such that content remained reduced relative to WT (-47%, $p<0.01$; **Figure 5E**). Individual ETC subunit content was unchanged however, the sum of all 5 subunits was significantly decreased in SAL relative to WT (-21%, $p<0.001$; **Figure 5F**). SBT-20 treatment did not alter the sum of 5 subunits relative to SAL such that total content was still reduced relative to WT (: -14%, $p<0.05$; **Figure 5F**).

Glutathione (reduced, oxidized, total glutathione and ratio of reduced: oxidized) in Quad muscle was unaltered in SAL relative to WT (**Figure 5G-J**) and as such, SBT-20 did not alter the intercellular oxidative environment in this muscle.

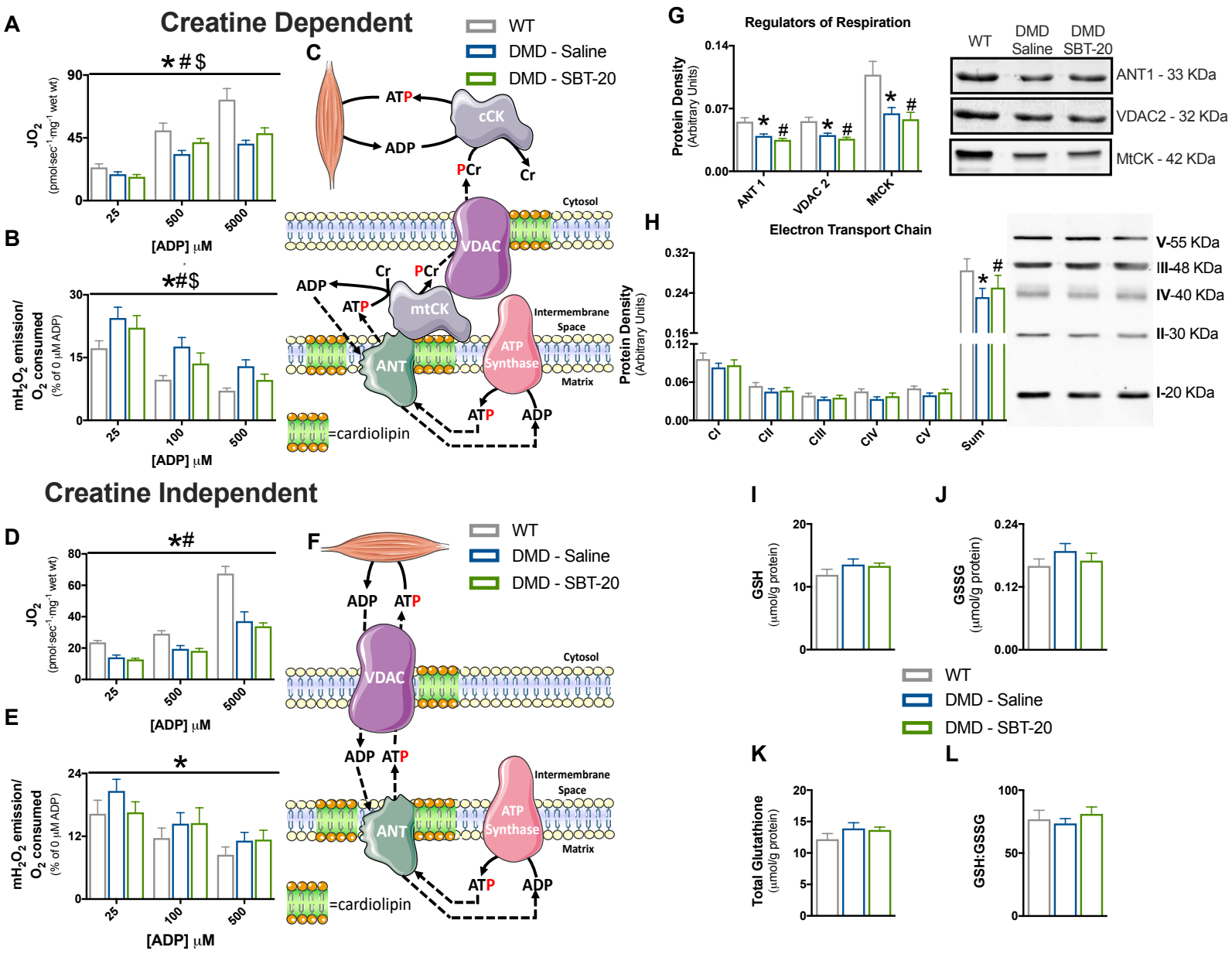
A
Creatine Dependent
WT
DMD - Saline
DMD - SBT-20
*#$
JO2 (pmol·sec-1·mg-1 wet wt)
[ADP] μM
B
*#$
mH2O2 emission/ O2 consumed (% of 0 μM ADP)
[ADP] μM
C
ATP
ADP
cCK
PCr
Cr
Cytosol
VDAC
Cr
PCr
ADP
ATP
mtCK
Intermembrane Space
ANT
ATP Synthase
Matrix
ATP
ADP
=cardiolipin
G
Regulators of Respiration
Protein Density (Arbitrary Units)
ANT 1
VDAC 2
MtCK
WT
DMD Saline
DMD SBT-20
ANT1 - 33 KDa
VDAC2 - 32 KDa
MtCK - 42 KDa
H
Electron Transport Chain
Protein Density (Arbitrary Units)
CI
CII
CIII
CIV
CV
Sum
V-55 KDa
III-48 KDa
IV-40 KDa
II-30 KDa
I-20 KDa
Creatine Independent
D
*#
JO2 (pmol·sec-1·mg-1 wet wt)
[ADP] μM
E
*
mH2O2 emission/ O2 consumed (% of 0 μM ADP)
[ADP] μM
F
WT
DMD - Saline
DMD - SBT-20
ADP
ATP
VDAC
Cytosol
ADP
ATP
Intermembrane Space
ANT
ATP Synthase
Matrix
ATP
ADP
=cardiolipin
I
GSH (μmol/g protein)
J
GSSG (μmol/g protein)
WT
DMD - Saline
DMD - SBT-20
K
Total Glutathione (μmol/g protein)
L
GSH:GSSG

Figure 6-5: Evaluation of mitochondrial bioenergetics and regulators of energy exchange in Quad muscle following treatment with SBT-20. The leading model for energy exchange involves a (**C**) creatine-dependent and (**D**) creatine-independent pathway. ADP stimulated respiration and mH_2O_2 emission, supported by Complex-I substrates pyruvate (5mM) and malate (2mM), were assessed in the presence (Creatine Dependent, **A-B**) and absence (Creatine Independent, **D-E**) of 20mM creatine with low and high [ADP], n=10-12. Protein content of adenine nucleotide translocase 1 (ANT 1) on the inner mitochondrial membrane, voltage dependent anion carrier 2 (VDAC 2) on the outer mitochondrial membrane and mitochondrial creatine kinase (mtCK) found in the inner membrane space (**G**), n=8. Protein content of electron transport chain components were also quantified (**H**), n=8. Glutathione was measured in muscle homogenate using HPLC-UV for the detection of GSH (**I**) and HPLC-Fluorescence for the detection of GSSG (**J**). The GSH:GSSG ratio (**K**) and total glutathione (**L**) were calculated from GSH and GSSG measurements, n=8. Results represent means ± SEM; * $p<0.05$, DMD-Saline vs WT; # $p<0.05$, DMD-SBT-20 vs WT; $ $p<0.05$, DMD-SBT-20 vs DMD-Saline.

SBT-20 increases mitochondrial-derived caspase activity yet improves mitochondrial ultra-structure in Quad

We next determined whether alterations in respiration and mH_2O_2 emission following SBT-20 treatment were associated with changes in markers of mitochondrial-derived cell death. Surprisingly, the [Ca^{2+}] required to induce PTP opening was lower in SAL relative to WT (+60%, p=0.06) and SBT-20 reduced the [Ca^{2+}] required to induce PTP opening relative to SAL (-60%, p<0.01) such that there was no difference relative to WT (**Figure 6A**). SBT-20 tended to increase caspase 9 activity relative to SAL (+29%, p=0.09) and was no different relative to WT (**Figure 6B**) while caspase 3 activity was significantly elevated relative to both SAL (+51%, p<0.05) and WT (+54%, p<0.05) despite no difference in activity between SAL and WT (**Figure 6B**). Overall these findings indicate that SBT-20 enhances mitochondrial-derived apoptosis in Quad muscle.

We then evaluated mitochondria structure and morphology. IMF mitochondria from SAL Quad demonstrate a decrease in size (**Figure 6C**) and density (**Figure 6E**) relative to WT. SBT-20 has no effect on mitochondria size but significantly increases the number of mitochondria per unit area relative to both SAL and WT (**Figure 6D**) and density relative to SAL (**Figure 6E**). SS mitochondria also exhibit a decrease in size (**Figure 6C**) and density (**Figure 6E**) relative to WT. SBT-20 treatment increases SS mitochondria size, number of mitochondria per unit area and density relative to SAL.

SBT-20 treatment improves limb muscle volume and specific markers of in vivo muscle function.

Finally, we assessed the impact of SBT-20 treatment on body composition and whole body *in vivo* muscle function. Following 4 weeks of treatment with SBT-20, body weight was no different relative to saline treated SAL and both groups demonstrated significantly decreased body weight relative to WT controls (SAL: -9%, p<0.05; SBT-20: -12%, p<0.05; **Figure 7A**). Despite no

difference in muscle volume between SAL and WT controls, SBT-20 treatment resulted in a significant increase in lower limb muscle volume relative to SAL (+9%, p=0.08) and WT (+10%, p<0.05; **Figure 7B**). However, SBT-20 treatment did not have an effect on % fat mass such that there was no difference between SBT-20 and SAL and both groups were significantly lower than WT controls (SAL: -35%, p<0.001; SBT-20: -35%, p<0.05; **Figure 7C**). Additionally, SBT-20 did not reduce serum creatine kinase levels relative to SAL and both SAL and SBT-20 rates were significantly elevated relative to WT (SAL: (+356%, p<0.05; SBT-20: +393%, p<0.05; **Figure 1D).**

We then evaluated muscle strength through a series of whole body *in vivo* measures. SBT-20 treatment caused a significant increase in forelimb grip strength (+82% vs SAL, p<0.05) such that SBT-20 treated animals were no longer different than WT controls (**Figure 1E)**. However, SBT-20 did not result in increases in cage hang time relative to SAL and both DMD groups had significantly lower hang times relative to WT controls (SAL: -46%, p<0.05; SBT-20: -42%, p<0.05; **Figure 1F**). Distance covered during 24-hours of voluntary wheel running also did not increase following SBT-20 treatment relative to SAL and both groups ran significantly less than WT (SAL: -83%, p<0.05; SBT-20: -87%, p<0.05; **Figure 1G**).

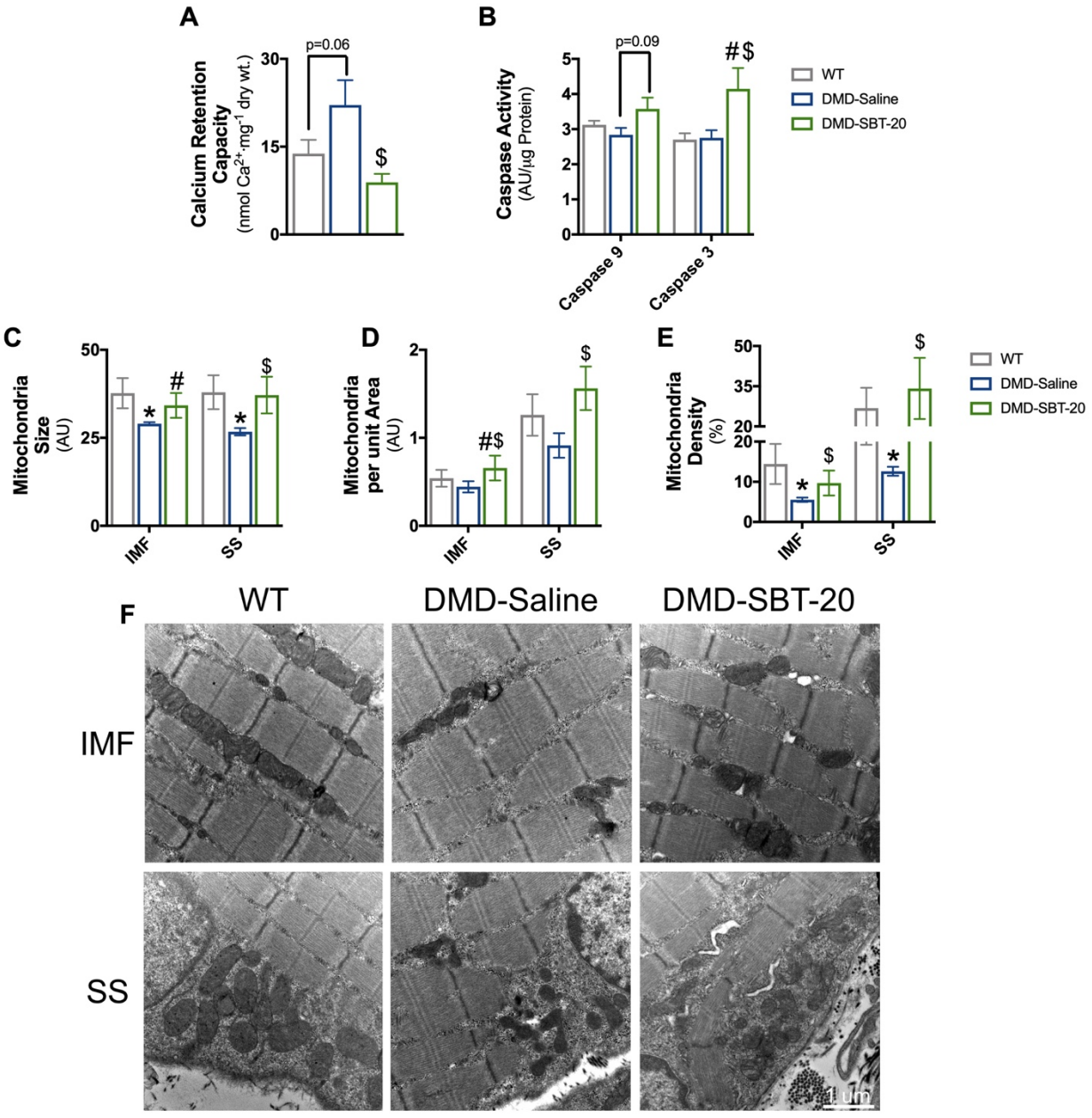

Figure 6-6: Evaluation of mitochondrial quality in Quad muscle following treatment with SBT-20. Calcium retention capacity, an index of susceptibility to permeability transition pore opening was assessed in permeabilized fibres from Quad muscle (**A**); n=10-12. Mitochondrial-induction of apoptosis was evaluated through caspase 9 activity followed by it's down-stream target caspase 3 (**B**); n=8. Transmission electron micrographs were acquired in the and analyzed for mitochondrial size (**C**), distribution (**D**) and density (**E**) within the intermyofibrillar (IMF) and subsarcolemmal (SS) area of the muscle; scale bar = 1 μm, n=3. Results represent mean ± SEM; * p<0.05, DMD-Saline vs WT; # p<0.05, DMD-SBT-20 vs WT; $ p<0.05, DMD-SBT-20 vs DMD-Saline.

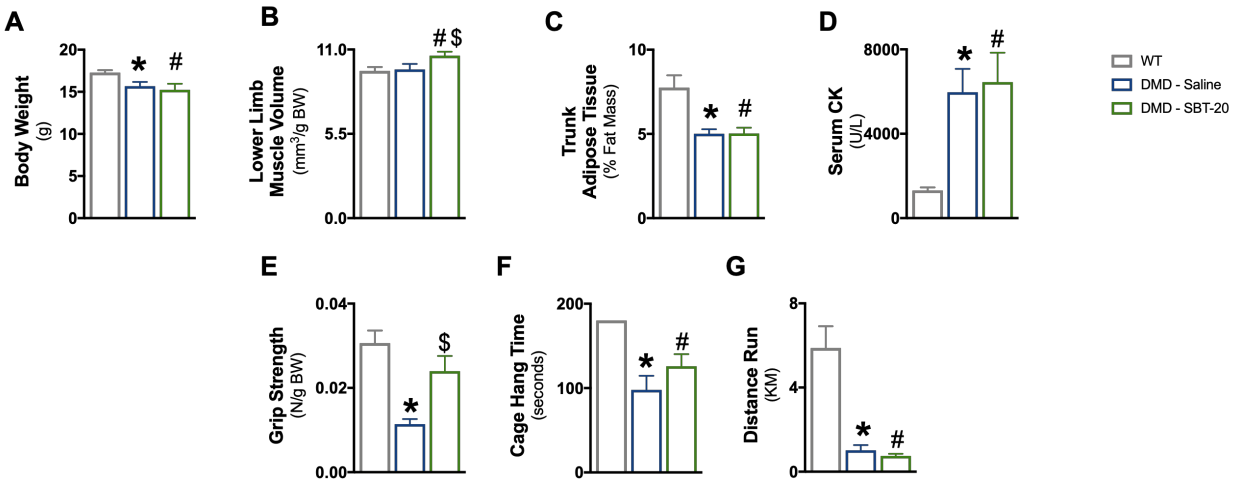

Figure 6-7: Evaluation of body composition and *in vivo* muscle function following treatment with SBT-20. Body weight (**A**), microCT analysis of lower limb muscle volume (**B**) and % fat mass (**C**). Whole body muscle damage was quantified by serum creatine kinase (CK) activity (**D**). Indices of muscle function were assessed by forelimb grip strength (**E**), cage hang time (**F**) and 24-hour voluntary wheel running (**G**), Results represent mean ± SEM; n=12; * $p<0.05$, DMD-Saline vs WT; # $p<0.05$, DMD-SBT-20 vs WT; $ $p<0.05$, DMD-SBT-20 vs DMD-Saline.

Discussion

Despite the extensive evidence suggesting the mitochondria contribute to DMD myopathy, the direct implications of improving mitochondrial bioenergetics through the use of a mitochondrial-targeted therapeutic for the treatment of this pathophysiology remains unknown. The present investigation presents data to support SBT-20 as a potential mitochondrial targeted therapy for the treatment of DMD myopathy through the improvement of mitochondrial bioenergetics. D2.*mdx* mice were injected daily with the mitochondrial-targeted peptide SBT-20, beginning at 4 days of age, for 28 days. Following treatment, SBT-20 improved mitochondrial bioenergetics in Diaphragm and Quad muscle and subsequently lowered mitochondrial-derived cell death in the Diaphragm while improving mitochondrial ultrastructure in the Quad, despite surprising increases in apoptosis in this muscle. These improvements in mitochondrial quality were associated with improved force production in the Diaphragm and decreased fibrosis in the Quad.

Improvements in Diaphragm force production may be due to protection against fatigue-induced declines in contractility

While beneficial overall to both the Diaphragm and Quad, SBT-20 had muscle-specific effects on certain indices of DMD myopathy. Firstly, force production was improved in Diaphragm muscle only. The Diaphragm presents a unique set of challenges in DMD as it is effected early and more severely than other skeletal muscles, however, the onset of respiratory failure in patients with DMD does not occur until the later stages of disease progression [293]. This is believed to be due to the compensatory recruitment of accessory respiratory muscles to carry the workload for the Diaphragm [53, 294]. Nevertheless, the Diaphragm undergoes progressive deterioration throughout lifespan in both rodent models and patients with DMD, likely due to its heavy use as a primary driver of ventilation at rest [294]. As such, even entirely inactive animals require the chronic contraction and relaxation of the Diaphragm, ultimately accelerating muscle degeneration.

Given the weakened state of the respiratory muscles in D2.*mdx* mice, even at this early time point [155], the Diaphragm is likely in a state of chronic fatigue by 4 weeks of age. Previous work using the general antioxidant n-acetylcysteine (NAC) demonstrated a protective effect against fatigue-induced reductions in force production in the Diaphragm of rodents [295-297] as well as in humans following acute and chronic fatiguing protocols [298, 299]. However, the benefits of NAC were non-existent in un-fatigued muscle [295-297].

While the Diaphragm muscle in D2.*mdx* mice is involuntarily chronically active, these animals exhibit little movement or activity from day to day. Therefore, it is plausible that the benefits of SBT-20 were evident in Diaphragm due to its underlying state of fatigue yet masked in Quad due the rested state of this muscle and that the induction of fatigue in Quad may have uncovered a protective effect of this peptide. Furthermore, SBT-20 lowered the intercellular content of oxidized glutathione (GSSG) in the Diaphragm only. It has been reported that inspiratory loading causes decreases in reduced glutathione and increases in GSSG content [300] while augmenting GSH and lowering GSSG pharmacologically increases respiratory muscle function [301]. Additionally, an oxidized intercellular environment has been positively correlated to disease pathology in patients with DMD [302]. Therefore, it is possible that the decrease in GSSG in Diaphragm muscle resulted in evident improvements in force production following SBT-20 treatment.

On the contrary, the degree of fibrosis was unchanged in Diaphragm but decreased in Quad following treatment with SBT-20. While SBT-20 decreased the activation of mitochondrial-derived apoptosis (decreased caspase 9 activity) in the Diaphragm, there was no effect on susceptibility to mitochondrial permeability transition pore (PTP) opening, which can trigger mitochondrial-derived necrosis. Additionally, caspase 3, the downstream effector caspase which is activated by both caspase 9 as well as non-mitochondrial targeted caspases [182], was still

significantly elevated relative to WT following treatment with SBT-20. As such, while SBT-20 attenuated one cell death pathway, there were several other avenues through which cell death may have been occurring in Diaphragm muscle. Given the previously discussed fact that the diaphragm is in a constant state of activation, contraction-induced membrane tearing is likely heightened and it is possible that the mitochondria are not the only source of cellular dysfunction. While targeting the mitochondria proves partially beneficial, a combination of therapeutics targeting several dysfunctional pathways in the Diaphragm will likely provide greater benefits in this highly active muscle.

SBT-20 treatment activates mitochondrial-derived apoptosis yet decreases fibrosis and improves mitochondria ultra-structure in Quad muscle

As previously discussed, while no improvements in Quad force production were evident following SBT-20 treatment, improvements in muscle and mitochondria quality were robust. SBT-20 has a demonstrated ability to prevent mitochondrial-derived apoptosis through the stabilization of cytochrome *c* on the inner mitochondrial membrane. Based on this notion, we were surprised to find that SBT-20 increased mitochondrial derived apoptosis in Quad muscle which was accompanied by an increased susceptibility to mitochondrial PTP opening. However, there were also subsequent improvements to mitochondria ultra-structure and decreased fibrosis. Taken together, these findings suggest that SBT-20 induced the preferential activation of mitochondrial-derived apoptosis over necrosis which resulted in the removal of damaged mitochondria and an overall decrease in fibrosis. Indeed, previous work by Pauly and colleagues demonstrated that the pharmacological removal of defective mitochondria in *mdx* Diaphragm resulted in improved mitochondria morphology and histopathology, albeit through the induction of mitophagy as opposed to apoptosis [35].

Apoptosis has often been viewed as the preferential form of cell death over necrosis given it is a controlled process as it selectively targets individual damaged cells for degradation and furthermore, does not elicit an inflammatory response [180]. Early work by Tidball et al., proposed that apoptosis was the mode of cell death that occurred during the symptom free stage of disease progression (0-3 years) in patients with DMD. A notion that was confirmed in *mdx* mice whereby apoptosis was evident in the "pre-necrotic" phase of disease, and occurred in the absence of markers of muscle damage (ie. Fibrosis) [303]. Seemingly, it is possible that SBT-20 induced a switch to apoptosis, which has a somewhat protective effect, at least in the early stages of disease progression. Given that apoptosis is an ATP-dependent process [183] and Quad from D2.*mdx* mice has evident impairments in oxidative phosphorylation, we propose that SBT-20 enhanced creatine-dependent exergy exchange (discussed below) which improved ADP's ability to govern oxidative phosphorylation, allowing for the preferential selection of apoptosis over necrosis when cell death was induced within a cell.

Modeling in vivo conditions in vitro reveal pathway specific alterations in mitochondrial bioenergetics

Recent work from our laboratory has demonstrated the necessity of modeling *in vivo* conditions when designing *in vitro* assays in order to fully capture the source and degree of mitochondrial dysfunction that occurs in rodent models of DMD [304, 156]. Similarly, in the present investigation, treatment with SBT-20 revealed creatine-independent improvements in Diaphragm muscle and creatine-dependent improvements in Quad muscle with an underlying improvement in ADP's ability to govern oxidative phosphorylation and attenuation of mH_2O_2 emission. SBT-20 treatment had no effect on ADP-independent (state II) oxidative phosphorylation or mH_2O_2 emission in either muscle. Given that SBT-20 binds to cardiolipin on the IMM, it is likely that this

peptide altered the regulation of energy exchange, thereby improving ADP's provision of bioenergetics.

Cardiolipin binds to ANT and mtCK as well as VDAC, forming a proteolipid complex across the mitochondrial membranes [200]. This complex creates stable contact sites between the IMM and OMM, and is shown to regulate energy exchange, reduce ROS formation and prevent permeability transition pore opening [200]. However, cardiolipin is highly susceptible to oxidative modifications and when oxidized, loses its binding affinity, resulting in the dissociation of the proteolipid complex [305, 261]. Given that SBT-20 did not alter protein content of the key regulators of energy exchange, improved bioenergetics are likely due to SBT-20's effect on ANT and VDAC permeability and/or altered mtCK functionality. ANT, VDAC and mtCK are all known to be redox sensitive [261-263] and additionally, mtCK is highly susceptible to oxidative modifications, leading to enzymatic inactivation and octamer dissociation, as well as formation of crystalline mitochondrial inclusion bodies, all resulting in loss of function [153, 152]. Given the creatine-dependent improvements in Quad muscle, it is likely that SBT-20 stabilized this proteolipid complex through the prevention of oxidative modifications of these key regulators of energy exchange.

It is somewhat perplexing that SBT-20 improved Diaphragm bioenergetics in a creatine-independent manner given this muscle is highly oxidative and therefore, relies predominantly on creatine-dependent energy exchange [286]. Nevertheless, ANT and VDAC are also susceptible to several post-translational modifications including phosphorylation, acetylation [264, 265] and in ANT specifically, glutathionylation [306]. Spontaneous glutathionylation occurs when GSSG levels are elevated, a noted abnormality in D2.*mdx* Diaphragm tissue. It is possible that SBT-20 lowered glutathionylation of ANT in Diaphragm muscle, thereby improving the cycling of

ADP/ATP into and out of the mitochondrial matrix respectively. While this is highly speculative, post translational modifications should be considered when trying to elucidate the mechanisms surrounding SBT-20 derived improvements in mitochondrial bioenergetics.

Finally, in both Diaphragm and Quad muscle, SBT-20 treatment significantly impaired mitochondrial respiration in the presence of *in vivo* resting concentrations of PCr and Cr, suggesting that SBT-20 treatment results in a heightened sensitivity to PCr-induced inhibition of respiration. It has been demonstrated that Cr enhances mtCK-dependent ADP-stimulated respiration while PCr inhibits it [246]. Our results suggest that SBT-20 sensitized mtCK to PCr inhibition, a finding previously demonstrated following endurance training in humans [239]. While this is difficult to reconcile given the clear benefits of SBT-20 at the mitochondrial and pathological level, this finding certainly highlights a direct effect of SBT-20 on mtCK functionality, likely through the alteration of its redox status. Future work should consider exploring this mechanism further through the direct evaluation of the oxidative status of mtCK.

Conclusions

In summary, this investigation identified the mitochondrial-targeted peptide SBT-20 as a potential therapeutic candidate for the treatment and prevention of DMD disease pathology. Specifically, 4 weeks of treatment with SBT-20 resulted in improved mitochondrial bioenergetics in Diaphragm and Quad muscle from D2.*mdx* mice. These improvements were associated with increased force production and decreased mitochondrial derived apoptosis in Diaphragm as well as decreased fibrosis and improved mitochondria morphology in Quad. This short-term treatment provides direct evidence that attenuating impaired mitochondrial bioenergetics improves DMD pathophysiology, an important finding given the need to develop additional therapies for this debilitating disease.

Conflicts of interest: none

Funding: Funding was provided to CGRP and TJH by the National Science and Engineering Research Council (#436138-2013 and # 2018-06324, respectively) and Stealth Biotherapeutics with infrastructure supported by Canada Foundation for Innovation, the James. H. Cummings foundation and the Ontario Research Fund. MCH was supported by an NSERC CGS-PhD scholarship. SVR was supported by an Ontario Graduate Scholarship. PCT was supported by an NSERC CGS-PhD scholarship.

Acknowledgements: none

Author Contributions: MCH, SVR, TJH and CGRP contributed to the rationale and study design. All authors conducted experiments and/or analyzed all data. CGRP and MCH wrote the manuscript. All authors contributed to the interpretation of the data. All persons designated as authors qualify for authorship, and all those who qualify for authorship are listed.

Supplemental Figures – Included in Manuscript

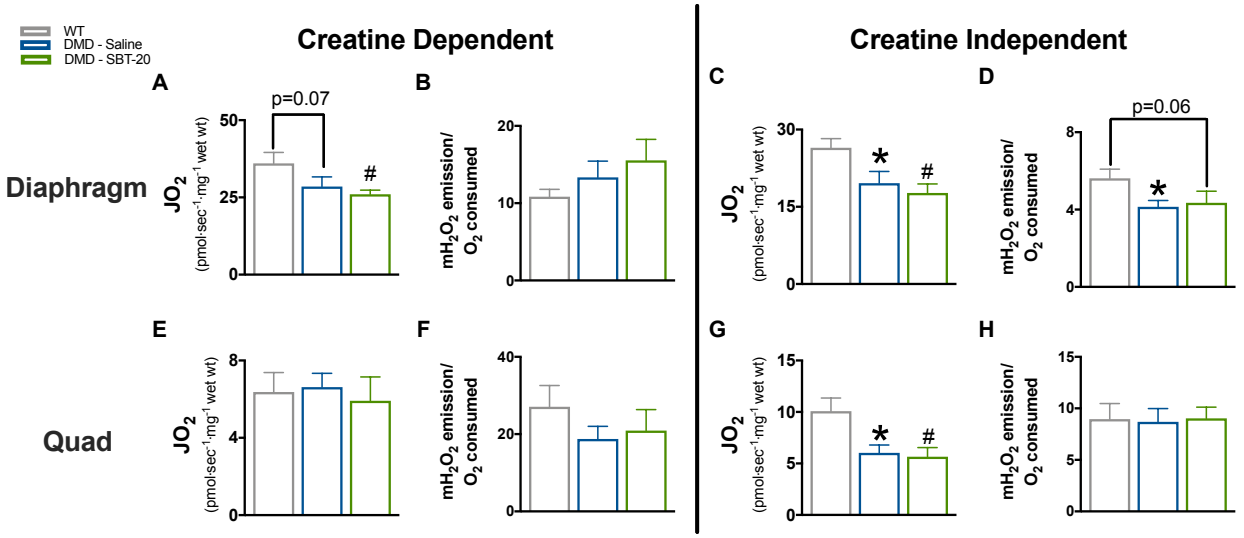

Supplemental Figure 6-1: State II respiration and mH_2O_2 emission following SBT-20 treatment. State II (no ADP; proton leak) respiration and mH_2O_2 emission during oxidative phosphorylation were initiated using Complex-I substrates pyruvate (5mM) and malate (2mM) in Diaphragm (**A-D**) and Quad (**E-H**) in the presence and absence of 20mM Creatine. Results represent mean ± SEM; n=10-12; * p<0.05, DMD-Saline vs WT; # p<0.05, DMD-SBT-20 vs WT; $ p<0.05, DMD-SBT-20 vs DMD-Saline.

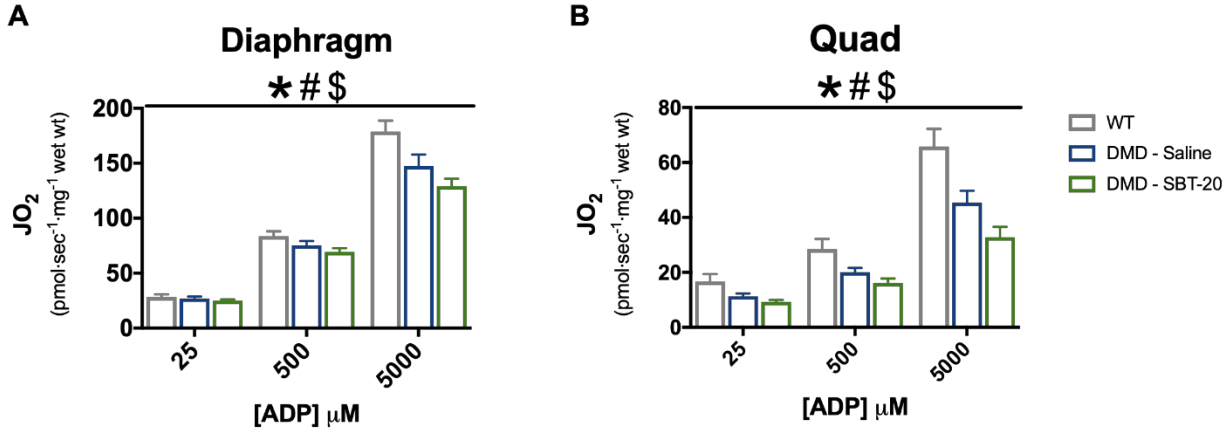

Supplemental Figure 6-2: ADP-stimulated respiration in the presence of phosphocreatine and creatine. 13.9mM phosphocreatine (PCr) and 9.1mM creatine (Cr) were added to the assay media to assess state III respiration supported by Complex-I substrates pyruvate (5mM) and malate (2mM) in Diaphragm (**A**), Quad (**B**). Results represent mean ± SEM; n=10-12; * p<0.05, DMD-Saline vs WT; # p<0.05, DMD-SBT-20 vs WT; $ p<0.05, DMD-SBT-20 vs DMD-Saline.

Supplemental Figures – not included in manuscript

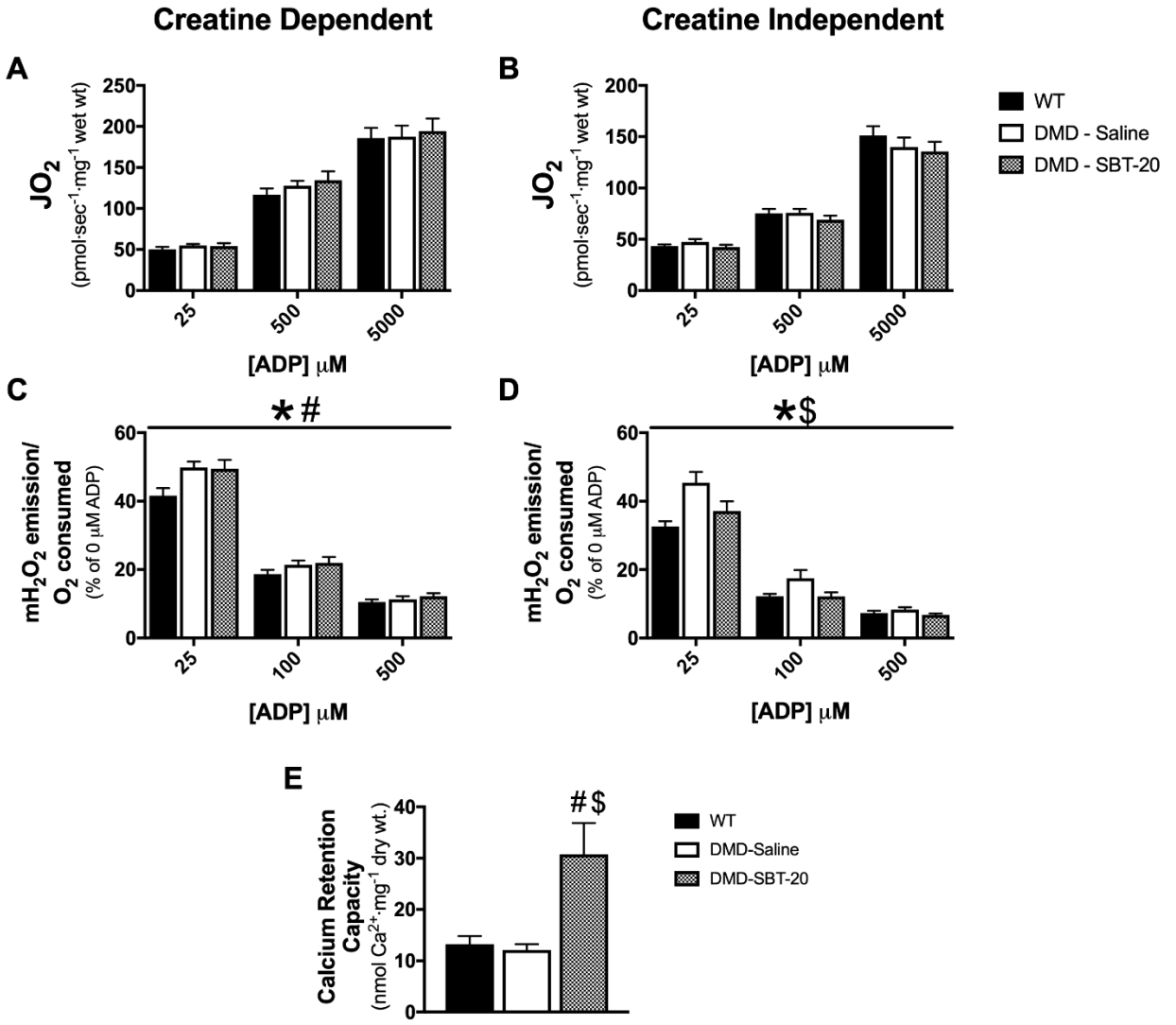

Supplemental Figure 6-3: Evaluation of mitochondrial bioenergetics in left ventricle muscle following SBT-20 treatment. ADP-supported respiration stimulated through Complex-I substrates pyruvate (5mM) and malate (2mM) was assessed in left ventricle muscle in the presence (**A**) and absence (**B**) of creatine. The ability of ADP to suppress mH_2O_2 emission during oxidative phosphorylation was evaluated under the same creatine-dependent (**C**) and independent (**D**) conditions. Mitochondrial susceptibly to permeability transition pore opening was evaluated through calcium retention capacity measurements (**E**). Results represent mean ± SEM; n=10-12; * $p<0.05$, DMD-Saline vs WT; # $p<0.05$, DMD-SBT-20 vs WT; $ $p<0.05$, DMD-SBT-20 vs DMD-Saline.

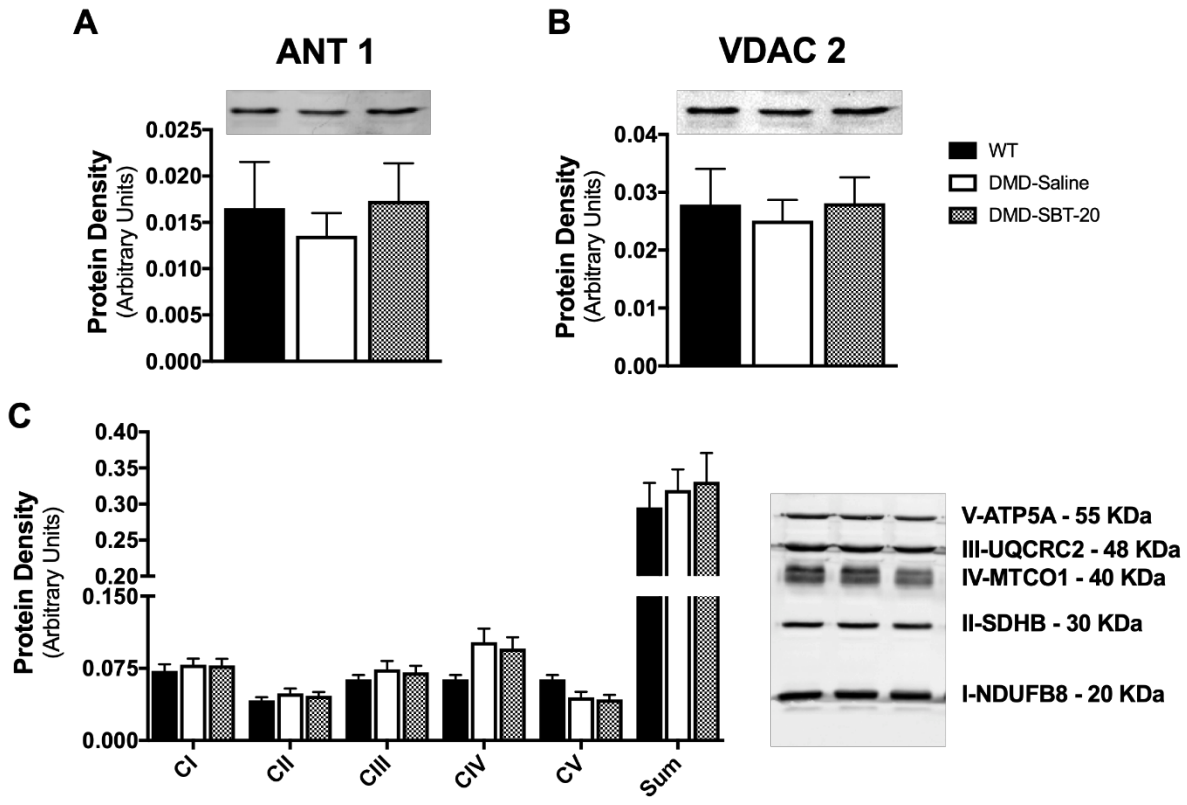

Supplemental Figure 6-4: Protein content of the key regulators of energy exchange in heart muscle following SBT-20 treatment. Protein content of adenine nucleotide translocase 1 (ANT 1) on the inner mitochondrial membrane (**A**), voltage dependent anion carrier 2 (VDAC 2) on the outer mitochondrial membrane (**B**) and electron transport chain components were quantified (**C**). Results represent means ± SEM; n=8.

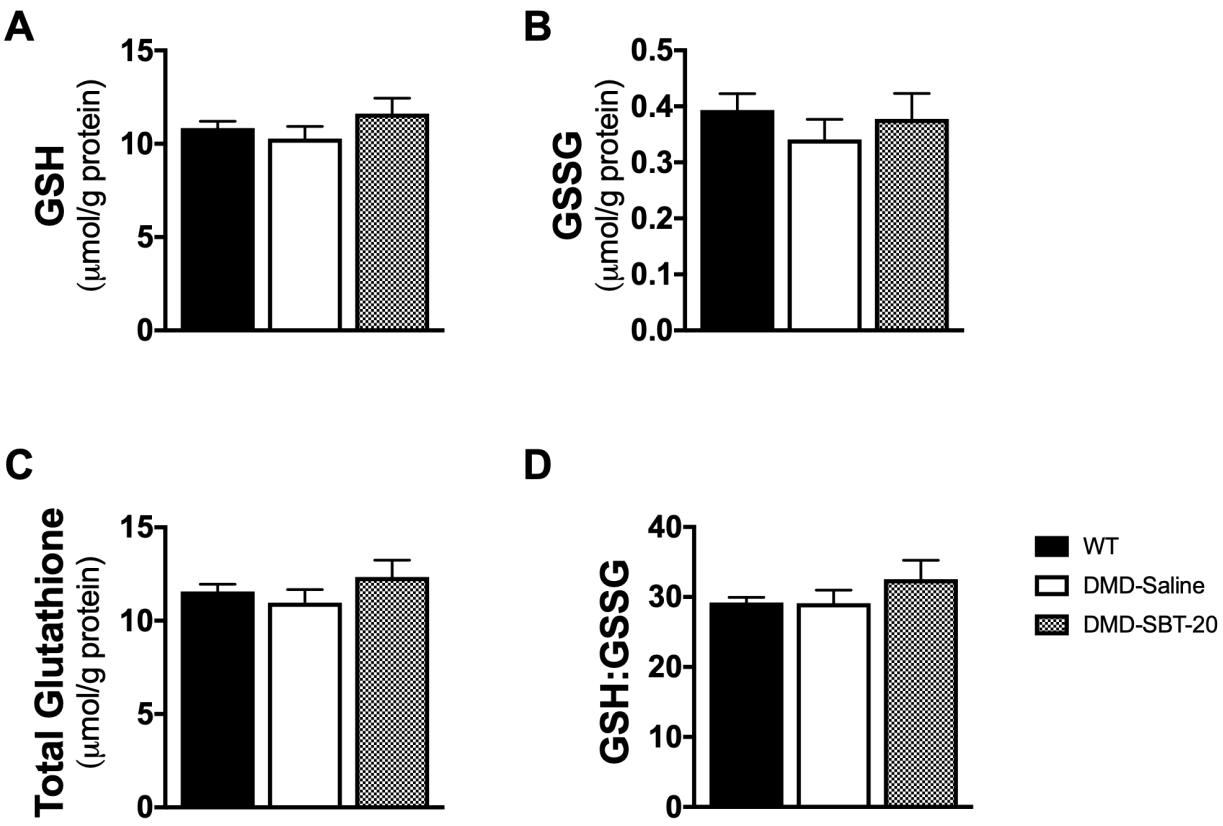

Supplemental Figure 6-5: Evaluation of glutathione in heart muscle following treatment with SBT-20. Glutathione was measured in muscle homogenate using HPLC-UV for the detection of GSH (**A**) and HPLC-Fluorescence for the detection of GSSG (**B**). The GSH:GSSG ratio (**D**) and total glutathione (**C**) were calculated from GSH and GSSG measurements. Results represent means ± SEM; n=6-8.

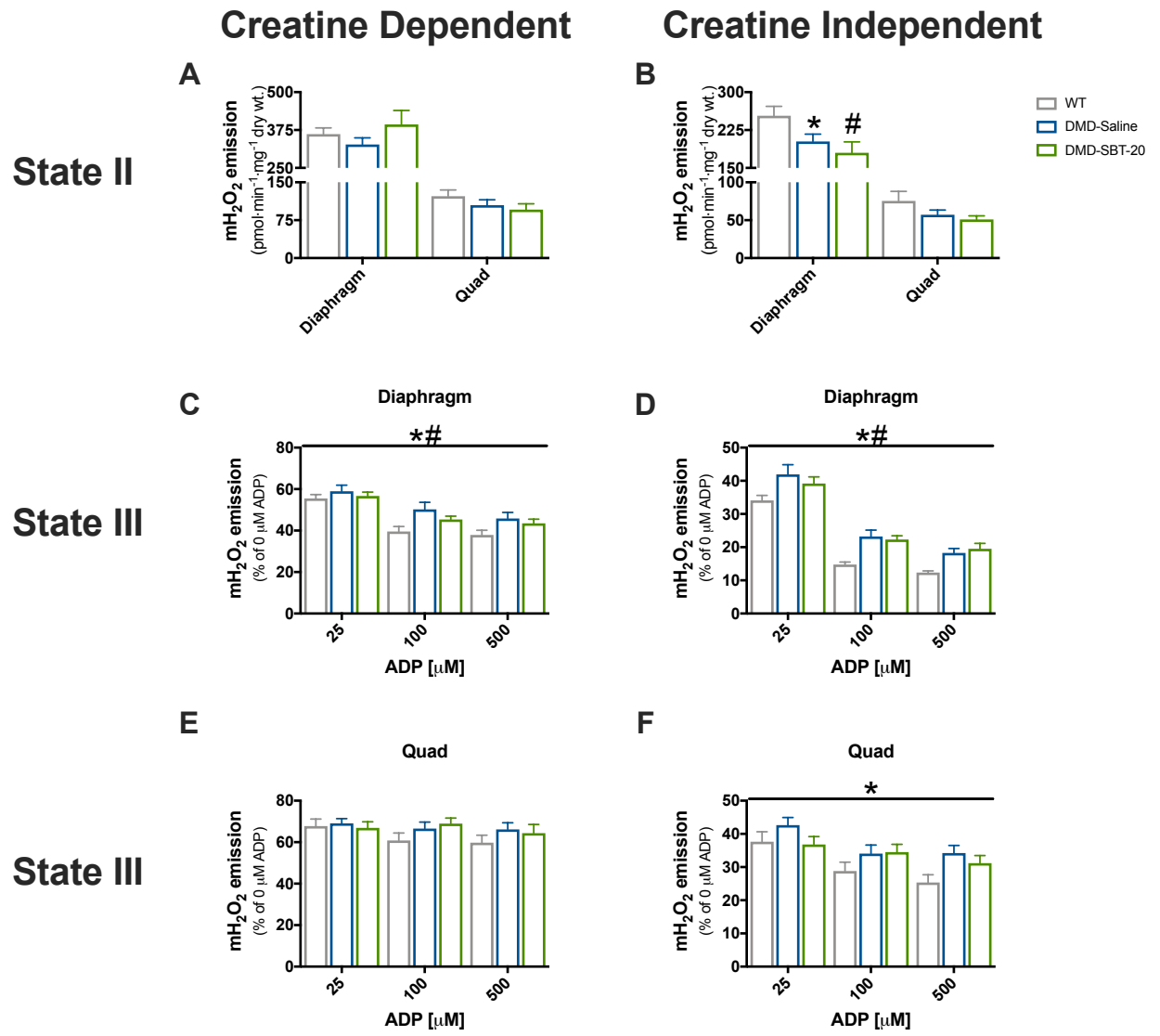

Supplemental Figure 6-6: Absolute rates of complex-1 supported mH_2O_2 Emission. State II mH_2O_2 was supported by Complex-I substrates Pyruvate (5mM) and Malate (2mM) in Diaphragm and Quad muscle in the **A.** presence (Creatine Dependent) and **B**. absence (Creatine Independent) of 20mM creatine. ADP's attenuation of maximal mH_2O_2 emission (state III) was evaluated in the Diaphragm (**C – D**) and Quad (**E – F**) in the same creatine-dependent and independent conditions. Results represent mean ± SEM; n=10-12; * p<0.05, DMD-Saline vs WT; # p<0.05, DMD-SBT-20 vs WT; $ p<0.05, DMD-SBT-20 vs DMD-Saline.

7 Mitochondrial creatine kinase deficits evident in Duchenne muscular dystrophy are ameliorated through treatment with cardiolipin-targeting peptide SBT-20

Assay Development Prior to the start of Project 4:

1. Immunoprecipitation
2. Licor 800CW Malemide IR Dye protein labelling methodology

Author Contributions: Part 1: Aging work - MH maintained the breeding colony required for this project and monitored the animals on a bi-weekly basis from 4-52 weeks. Time-course analysis (4,8,12,16,24,32,40,52 weeks) of body weight, body composition (μCT scans) and whole-body function was completed by MH. Tissue harvest and mitochondrial bioenergetics experiments (respiration, mH_2O_2 emission, calcium retention capacity) were performed by MH with the assistance of TT. MH completed all western blotting and immunoprecipitation experiments. PT completed the analysis of μCT data. PCT completed glutathione measurements. **Part 2: In Vitro work** – MH performed all tissue harvest, bundle preparation and drug treatment for this work. MH completed all respiration experiments and analysis. **Part 3: SBT-20 Treatment** – MH maintained the breeding colony required for this project and performed all daily drug injections over the course of 12 weeks. Time-course analysis (4,6,8,10,12 weeks) of body weight, body composition (μCT scans) and whole-body function was completed by MH. MH and SVR performed all tissue harvests and mitochondrial bioenergetic assays (respiration, mH_2O_2 emission, calcium retention capacity). MH completed all western blotting and immunoprecipitation experiments. PT completed the analysis of μCT data.

Mitochondrial creatine kinase deficits evident in Duchenne muscular dystrophy are ameliorated through treatment with cardiolipin-targeting peptide SBT-20

Authors: MC Hughes[a*], SV Ramos[a], T. Teich[a], P Tadi[a], PC Turnbull[a], N. N Polidovitch[b], U Schlattner[c], PH Backx[b], JA Simpson[d,e], and CGR Perry[a†].

Affiliations:

[a]School of Kinesiology and Health Science and the Muscle Health Research Centre, York University, Toronto, ON, Canada.

[b]Department of Biology and the Muscle Health Research Centre, York University, Toronto, ON, Canada.

[c]Laboratory of Fundamental and Applied Bioenergetics (LBFA) and SFR Environmental and Systems Biology (BEeSy), University Grenoble Alpes, Grenoble, France.

[d]Department of Human Health and Nutritional Sciences and Cardiovascular Research Group, University of Guelph, Guelph, ON, Canada.

[e]IMPART Team Canada Investigator Network, Saint John, New Brunswick, Canada

Figure count: 5 + 4 supplemental

[†]Address for Correspondence:

Christopher Perry, PhD
School of Kinesiology and Health Science
Muscle Health Research Centre
344 Norman Bethune College
York University
4700 Keele Street
Toronto, Ontario M3J 1P3
(P) 416 736 2100 ext. 33232
cperry@yorku.ca

Abstract

In Duchenne muscular dystrophy (DMD), the mitochondria have been identified as a source of ROS during impaired oxidative phosphorylation in cardiac, respiratory and skeletal muscle. Furthermore, there is a specific impairment in mitochondrial creatine sensitivity, indicating a potential dysfunction in the enzyme mitochondrial creatine kinase (mtCK). MtCK is crucial in facilitating ADP's ability to lower mitochondrial H_2O_2 emission while stimulating oxidative phosphorylation through the process of 'high energy phosphate shuttling'. Additionally, mtCK is highly redox sensitive and susceptible to oxidant-induced dysfunction. The present study first sought to determine if altered mtCK functionality was the underlying cause of impaired mitochondrial bioenergetics in DMD. The second aim of this work was to determine whether the cardiolipin-binding peptide SBT-20, known for its ability to improve mitochondrial bioenergetics and protect against oxidative damage, could ameliorate these bioenergetic impairments, specifically through the protection of mtCK from oxidant-induced dysfunction. At late stages of disease progression (52 weeks) in D2.*mdx* mice, cardiac, respiratory and skeletal muscle exhibit creatine-dependent elevations in mitochondrial H_2O_2 emission during impaired oxidative phosphorylation which is associated with oxidized mtCK in cardiac muscle. *In vitro* treatment with SBT-20 improved creatine-dependent oxidative phosphorylation and protected against oxidant-induced impairments in creatine-dependent respiration. Similarly, *in vivo* treatment with SBT-20 resulted in improvements in mitochondrial bioenergetics in a creatine-dependent manner, specifically in muscles that are sensitive to creatine. These findings demonstrate that DMD is a disease characterized by alterations in mtCK functionality and highlight a potential therapeutic target for the treatment and prevention of disease progression in DMD.

Keywords: mitochondria, Duchenne muscular dystrophy, reactive oxygen species, respiration, mitochondrial creatine kinase, creatine

Introduction

Affecting 1 in 3500 live male births, Duchenne muscular dystrophy (DMD) is a progressive muscle wasting disease resulting in early loss of ambulation and eventual premature death due to cardiac and/or respiratory complications [45, 2]. DMD is characterized by a lack of dystrophin due to mutations in the X-linked gene (Xp21) encoding for this structural protein [229]. At the cellular level, dystrophin acts as an anchoring protein between the cytoskeleton and the sarcolemma. In the absence of dystrophin, muscle becomes susceptible to membrane fragility and a myriad of cellular defects including disrupted calcium (Ca^{2+}) homeostasis, oxidative stress, inflammation as well as the heightened activation of cell death pathways [93, 2]. Altogether, these impairments lead to chronic muscle degeneration causing the progressive replacement of muscle with fibrotic tissue and fat, resulting in an overall loss of muscle function.

There is currently no cure for DMD. Given the genetic nature of this disease, extensive research has been conducted in attempts to establish gene based therapies to cure this condition. While recent reports have proved more promising [47], in general, gene based therapies have had limited impact on the treatment of DMD to date [45]. As such, there is a need to identify secondary therapeutic targets within the muscle in order to guide therapy development. Indeed, current standard of care targets inflammation rather than the genetic mutation itself [46].

Recent work from our laboratory revealed the mitochondria are a source of ROS during impaired oxidative phosphorylation in cardiac, respiratory and skeletal muscles from young D2.B10-DMD^{mdx}/2J (D2.*mdx*) mice [156, 304]. These impairments in bioenergetics were associated with muscle damage and loss of function in respiratory and skeletal muscles and preceded the onset of cardiac dysfunction and remodelling. Furthermore, in oxidative muscles specifically, we identified an impairment in creatine sensitivity, as has previously been shown at later stages (10-11 months)

of disease progression [201], highlighting a potential dysfunction in the enzyme mitochondrial creatine kinase (mtCK) in dystrophic muscle (6, 7).

The leading model of energy exchange involves a creatine-dependent (Figure 2A) and creatine-independent (Figure 2B) pathway. Creatine-dependent energy exchange is facilitated by mtCK through the transfer of the phosphate group from ATP to Cr, producing phosphocreatine (PCr) and ADP in the inner membrane space. The PCr is exported via VDAC into the cytosol while the ADP is directly recycled back via ANT into the mitochondrial matrix (Figure 2A). Creatine-independent energy exchange involves ADP/ATP transfer through diffusion across voltage dependent anion carrier (VDAC) on the outer mitochondrial membrane and adenosine nucleotide translocase (ANT) on the inner mitochondrial membrane bypassing mtCK (Figure 2B) [200, 146, 150, 147].

MtCK is believed to facilitate ADP's role in lowering mitochondrial H_2O_2 emission while stimulating oxidative phosphorylation through this process of 'high energy phosphate shuttling' whereby the rapidly diffusing PCr export ultimately accelerates mitochondrial matrix ADP cycling, reduces H_2O_2 emission and stimulates oxidative phosphorylation [205, 157]. As such, diseases of altered mitochondrial bioenergetics are increasingly being identified as having a specific impairment in mtCK functionality [200, 152]. Furthermore, cardiolipin plays an important role in mtCK functionality through contact sites with mtCK and key regulators of energy exchange, forming a proteolipid complex that provides efficient energy exchange into and out of the mitochondria [200]. However, mtCK is extremely redox sensitive and therefore is susceptible to oxidative modifications, structural changes (crystallization) and the compensatory upregulation of its expression, all of which alter the enzyme's functionality specifically through the dissociation from cardiolipin [200, 152, 153]. Given the elevated mitochondrial H_2O_2 emission during oxidative phosphorylation and impaired creatine sensitivity in young D2.*mdx* mice, it is plausible

that oxidant-induced impairments in mtCK functionality underlies mitochondrial dysfunction in dystrophic muscle, yet this remains to be elucidated.

The mitochondrial-targeted peptide SBT-20, which binds to cardiolipin on the IMM, has been shown attenuate mH_2O_2 emission [224], prevent oxidative damage [225] increase mitochondrial oxidative phosphorylation [224] and prevent the dissociation of cytochrome c from cardiolipin, thereby preventing the activation of cell death pathways [223] in rodent models of ischemia reperfusion [224] and myocardial infarction [225]. Each of the aforementioned cellular dysfunctions have previously been identified in DMD [93, 2, 195, 156] suggesting that SBT-20 may have beneficial effects on impaired mitochondrial bioenergetics in DMD, specifically through its improvement of mtCK functionality.

The present study first determined whether alterations in mitochondrial bioenergetics were due to mtCK dysfunction at the late stages of disease progression in D2.*mdx* mice. We then assessed the efficacy of SBT-20 to alter mitochondrial bioenergetics following *in vitro* and *in vivo* treatment. Collectively, our findings demonstrate that mtCK is oxidized in dystrophic muscle, causing impairments in creatine-dependent mitochondrial bioenergetics and furthermore, that the cardiolipin-binding peptide SBT-20 improves mitochondrial bioenergetics in a creatine-dependent manner, potentially through the protection of mtCK from oxidant-induced dysfunction.

Material and Methods

Animal Care and Timeline of measurements

Part 1 – Aged Animals: D2.*mdx* and DBA/2J wildtype (WT) mice originated from breeding colonies maintained at York University (Toronto, Canada) and sourced from Jackson Laboratories (Bar Harbor, United States). At 4 weeks of age, body composition and whole body *in vivo* muscle function was evaluated. These assessments were repeated at 8, 16, 24, 32, 40 and 52 weeks respectively. At 52 weeks of age and two days following the last muscle function assessment, animals were sacrificed and tissue was harvested. Methods for the assessments completed with harvested tissue are described in detail below.

Part 2 – *In Vitro* SBT-20 Treatment: D2.*mdx* mice originated from breeding colonies maintained at York University (Toronto, Canada) and sourced from Jackson Laboratories (Bar Harbor, United States). At 4 weeks of age, animals were sacrificed and quadriceps (Quad) muscle was harvested for the completed of *in vitro* SBT-20 assays. Methods for the assessments completed with harvested tissue are described in detail below.

Part 3 – *In Vivo* SBT-20 Treatment: D2.*mdx* mice originated from breeding colonies maintained at York University (Toronto, Canada) and sourced from Jackson Laboratories (Bar Harbor, United States). Beginning at 4-days of age, all animals within a litter received a daily subcutaneous injection of SBT-20 (Stealth Biotherapeutics; Newton, MA, USA) at a dose of 5 mg/kg. At 10 days of age, pups were sexed and treatment of only males within a litter continued. Age matched litters received the volume equivalent dose of vehicle (0.9% NaCl) through subcutaneous injection. Following 12 weeks of daily injections, all animals underwent whole body *in vivo* muscle functional analysis. Half of the animals were allocated for cardiac function analysis through echocardiography and the half of the animals were allocated for respiratory function analysis through esophageal pressure transduction. Animals were allowed to recover for 2 days following

their respective test. On the day of sacrifice, prior to tissue harvest, animals underwent a μCT scan for muscle volume in all animals followed by *in vivo* hindlimb plantar flexor force production measurements in a small subset of animals. These methods as well as methods for the assessments completed with harvested tissue are described in detail below.

All animals were provided access to standard chow and water ad libitum. All experiments and procedures were approved by the Animal Care Committee at York University (AUP Approval Number 2016-18) in accordance with the Canadian Council on Animal Care.

Body Composition and Functional Assays

Voluntary Wheel Running

Animals were placed in individual cages equipped with a locked 14 cm diameter running wheel and rotation counter (VDO m3 bike computer, Mountain Equipment Co-Op, Vancouver, Canada). After 24 hours of acclimatization, wheels were unlocked and distance run over 24 hours was recorded.

Cage Hang Time

Animals were placed on top of a metal cage lid and positioned so that all four limbs grasped the cage. The cage lid was inverted so that the mouse was hanging and cage hang time was recorded for a maximum of 180 seconds as previously described [156].

Forelimb Grip Strength

Forelimb grip strength was assessed using a force transducer (Mark 10 Digital Force Gauge, Copiague, NY) and has been described in detail previously [156]. Briefly, mice were removed from their cages by the tail and brought towards a grid attached to the force transducer until such time that the mice grasped the grid with their forepaws. Upon grasping, animals were pulled away from the grid until their grasp was broken. Peak tension was recorded, and the trial was repeated

twice more. If the animal did not show resistance to the experimenter, the trial was not recorded. Maximum peak tension from the best of 3 trials was used for analysis [233].

In Vivo μCT Scans

In vivo body scans were performed using μCT (SkyScan 1278, Bruker-microCT, Kontick, Belgium) as previously described [156]. Following scans, lower limb muscle volume was analyzed through reconstruction of the image using NRecon (software version 1.7.0.4, Bruker-microCT, Kontick, Belgium) followed by the analysis of a selected region of interest using CTAn (software version 1.15.4.0, Bruker-microCT, Kontick, Belgium). The region of interest for hind-limb muscle volume was landmarked from the top of the patella to the ankle joint and was quantified by setting thresholds for fat free mass (76-102), expressed as volume (mm^3) of lean mass/g body weight.

Esophageal Pressure Transduction

Esophageal pressure measurements were performed as previously described [234, 156]. Briefly, mice were anesthetized with an isoflurane/oxygen mix (2%:100%) and body temperature was maintained at 37°C. Mice were intubated using a 20-gauge angiocatheter (Becton, Dickinson and Company) to maintain an open/unobstructed airway. Compressible tubing was attached to the angiocatheter to facilitate inducible airway occlusions. Esophageal pressure (P_{es}) was measured with a 1.2F catheter (Transonic) recorded on LabScribe2 software (iWorx) and analyzed with Spike2 software (Cambridge Electronic Design). Immediately after 2 min of baseline P_{es} recording, the trachea was occluded, and P_{es} was monitored for changes. Tracheal occlusions were initiated at end expiratory volume to ensure consistency of the Diaphragm length-tension relationship. Maximum inspiratory pressure (P_{Iocc}) was evaluated after 30s of occlusion when pressure generation reached a plateau.

Echocardiography

All mice were subjected to transthoracic echocardiographic analysis (Vevo 2100, VisualSonics) to measure cardiac function and morphology 2-3 days prior to sacrifice for bioenergetic measurements as previously described [304]. The animals were sedated using 3% isoflurane and maintained with 1–2% isoflurane. Mice were placed on a heating pad and body temperature was maintained between 36.9 and 37.3 °C for the duration of the measurements. Left ventricular internal end diastolic diameters (LVDd), left ventricular internal end systolic diameters (LVDs) and left ventricular posterior wall thickness (LVPWTh) were measured in brightness mode (B-Mode) and motion mode (M-Mode) using the parasternal long axis view. Fractional shortening (FS) was calculated as FS(%) = (LVDd - LVDs)/LVDd x 100. Stroke volume (SV) was estimated as SV = Left ventricular diastolic volume (LVVol;d) - Left ventricular systolic volume (LVVol;s), where LVVol;d = ((7.0/(2.4 + LVDd)) x $LVDd^3$ and LVVol;s = ((7.0/(2.4 + LVDs)) x $LVDs^3$. Ejection fraction (EF) was estimated as EF = SV/LVVol;d and cardiac output (CO) was estimated as CO = SV x heart rate. All data analysis was performed using the Visual Sonic data analysis suite.

In Vivo Hind-limb Force Production

In vivo force production of the hind-limb plantarflexor muscles was partially adapted from previous methods and has been described previously [235, 156]. In brief, mice were anesthetized with isoflurane and placed on a platform maintained at 37° C. Contraction of the plantarflexors was controlled through percutaneous stimulation of the sciatic nerve with left foot secured to a footplate attached to an Aurora Scientific 305C muscle lever (Aurora, Ontario, Canada) so that the ankle's axis of rotation coincided with that of the servomotor shaft and the knee clamped in place such that the knee and ankle angles were both 90°. Peak isometric torque was determined by varying the voltage delivered to the sciatic nerve at a frequency of 60 Hz and 0.2-ms square wave

pulse. Torque as a function of stimulation frequency was measured during 9 isometric contractions at varying stimulation frequencies (40, 60, 80, 100, 120, 140, 160 180, 200 Hz). Maximum torque produced during the torque-frequency protocol was recorded and compared between groups. Animals then underwent a fatiguing protocol whereby the muscle was stimulated at a frequency of 60 Hz, every second for a total of 120 seconds. Animals were then allowed 10 minutes to recover before recovery from fatigue was assessed by stimulating maximum torque production at the same frequency used prior to fatigue [235]. Following a five-minute recovery period, animals then underwent eccentric contraction induced injury as previously described. Eccentric contractions were achieved by translating the footplate backward 30° at a velocity of 40mm/s after the first 200ms of an isometric contraction. This was repeated 20 times with 45 seconds in between contractions. Maximal torque production was assessed following the injury protocol to assess damage.

Mitochondrial Bioenergetic Assessments

Preparation of Permeabilized Muscle Fibre Bundles (PmFB)

This technique is partially adapted from previous methods and has been described elsewhere [237-240]. Briefly, muscles were removed from mice during anaesthesia with isoflurane. Heart, Diaphragm, quadriceps (Quad) and white gastrocnemius (WG) muscles were removed and immediately placed in ice-cold BIOPS, containing (in mM): 50 MES Hydrate, 7.23 K_2EGTA, 2.77 CaK_2EGTA, 20 imidazole, 0.5 dithiothreitol, 20 taurine, 5.77 ATP, 15 PCr, and 6.56 $MgCl_2 \cdot 6\ H_2O$ (pH 7.1). Each muscle was trimmed of connective tissue and fat and divided into several small muscle bundles (~2–7 mm, 1.0–2.5 mg wet weight). Each bundle was gently separated along the longitudinal axis to form bundles that were treated with 40 μg/ml saponin in BIOPS on a rotor for 30 minutes at 4° C. Bundles destined for Complex I, Complex III or pyruvate dehydrogenase supported mitochondrial H_2O_2 emission (mH_2O_2) measurements (described below) were also

treated with 35 μM 2,4-dinitrochlorobenzene (CDNB) during the permeabilization step to deplete glutathione and allow for detectable rates of mH_2O_2 [242]. For Part 1 and Part 2, following permeabilization, the PmFB were divided into three groups; 1) bundles intended for high resolution respirometry were placed in MiR05 containing (in mM): 0.5 EGTA, 10 KH_2PO_4, 3 $MgCl_2 \cdot 6\ H_2O$, 60 K-lactobionate, 20 Hepes, 20 Taurine, 110 sucrose and 1 mg/ml fatty acid free BSA (pH 7.1) while 2) bundles intended for mH_2O_2 were placed in Buffer Z containing (in mM): 105 K-MES, 30 KCl, 10 KH_2PO_4, 5 $MgCl_2 \cdot 6\ H_2O$, 1 EGTA and 5mg/ml BSA (pH 7.4). PmFB were washed on a rotor at 4°C in MiR05 or Buffer Z until the measurements were initiated. Following permeabilization and washing, all mitochondrial bioenergetic measurements were performed in the same order from one animal to another and between groups to ensure consistent durations of the wash step.

For assessment of mitochondrial bioenergetics following *in vitro* incubation with SBT-20, Quad muscle was separated in BIOPS buffer and permeabilized as described above. Following permeabilization with saponin, bundles were transferred to MiRO wash buffer supplemented with either 1 μM SBT-20 [224] or volume equivalent saline and were incubated at 4°C for two hours followed by the initiation of experiments.

Mitochondrial Respiration in Aged Animals (Part 1) and in Animals following In Vivo Treatment with SBT-20 (Part 2)

High-resolution O_2 consumption measurements were conducted in 2 ml of respiration medium (MiR05) using the Oroboros Oxygraph-2k (Oroboros Instruments, Corp., Innsbruck, Austria) with stirring at 750 rpm at 37 °C [239, 240, 243-245]. Respiration medium contained 20mM Cr to saturate mitochondrial creatine kinase or no creatine to prevent the activation of mtCK [283, 243]. A third condition of 13.9mM PCr and 9.1mM Cr was used to provide an equilibrium across mtCK as occurs in skeletal muscle at rest *in vivo* [247]. For ADP-stimulated respiratory kinetics, 5 mM

pyruvate, accompanied by 2 mM malate, were added as Complex I substrates (via generation of NADH to saturate electron entry into Complex I) followed by a titration of physiological ADP (25 μM) and supraphysiological (500 μM) ADP to mimic low and high metabolic stress respectively. Cytochrome *c* was added to test for mitochondrial membrane integrity, with all experiments demonstrating <10% increase in respiration. All experiments were conducted in the presence of 5μM BLEB in the assay media to prevent spontaneous contraction of PmFB [243, 248, 244]. Each protocol was initiated with a starting [O_2] of approximately 350 μM and was completed before the oxygraph chamber [O_2] reached 150 μM as done previously [239, 240, 243-245]. Polarographic oxygen measurements were acquired in 2 s intervals with the rate of respiration derived from 40 data points and expressed as pmol/s/mg wet weight. PmFB were weighed in ~1.5 ml of tared BIOPS (ATP-containing relaxing media) to prevent rigor that occurs when weighing PmFB in open air (unpublished observations).

Mitochondrial Respiration Following In Vitro Treatment with SBT-20

High-resolution O_2 consumption measurements were conducted as described above with slight modifications. Following treatment with SBT-20 or volume equivalent saline, Quad muscle was placed in the Oroboros Oxygraph-2k (Oroboros Instruments, Corp., Innsbruck, Austria) in either 20mM Cr to saturate mitochondrial creatine kinase or no creatine to prevent the activation of mtCK [283, 243]. State III respiration supported by Complex I substrates pyruvate (5 mM and malate 2 mM) and 500 μM ADP was induced followed by the titration of 100 μM and 250 μM H_2O_2 to evaluate the % decrease in respiration following the addition of an oxidant. Cytochrome *c* was added to test for mitochondrial membrane integrity, with all experiments demonstrating <10% increase in respiration. After the experiments, the fibres were rinsed in double deionized H_2O, lyophilized in a freeze-dryer (Labconco, Kansas City, MO, USA) for >4 h and weighed on a microbalance (Sartorius Cubis Microbalance, Gottingen, Germany).

Mitochondrial H_2O_2 Emission (mH_2O_2)

mH_2O_2 was determined fluorometrically (QuantaMaster 40, HORIBA Scientific, Edison, NJ, USA) in a quartz cuvette with continuous stirring at 37°C, in 1 mL of Buffer Z supplemented with 10 μM Amplex Ultra Red, 0.5 U/ml horseradish peroxidase, 1 mM EGTA, 40 U/ml Cu/Zn-SOD1,5 μM BLEB and 20mM Cr. Site specific induction of mH_2O_2 was measured through the addition of either 10 mM pyruvate and 2 mM malate (NADH, Complex I), 10 mM succinate ($FADH_2$, Complex I via reverse electron flux from Complex II) or 2.5 μM antimycin A (Complex III). Additionally, using 0.5 μM rotenone, a complex I inhibitor, plus 10 mM pyruvate, electron slip specific to pyruvate dehydrogenase complex was also measured in CDNB-treated fibres as noted above [242]. Following the induction of state II mH_2O_2 by Complex I and Complex II substrates, a titration of ADP was added to progressively attenuate mH_2O_2. Complexes I and II-supported mH_2O_2 were repeated with no creatine in the assay buffer to compare ADP's effects without mtCK-mediated phosphate shuttling. All measurements were made in the presence of 1 μM BLEB to prevent ADP-induced rigor as described above. After the experiments, the fibres dried and weighed as described above. The rate of H_2O_2 emission was calculated from the slope (F/min), from a standard curve established with the same reaction conditions and normalized to fibre bundle dry weight.

In Vitro Muscle and Blood Analyses

Western Blotting

An aliquot of frozen Heart, Diaphragm, Quad and WG (10–30 mg) from each aged animal was homogenized in a plastic microcentrifuge tube with a tapered teflon pestle in ice-cold buffer containing (mm): 40 Hepes, 120 NaCl, 1 EDTA, 10 $NaHP_2O_7 \cdot 10H_2O$ pyrophosphate, 10 β-glycerophosphate, 10 NaF and 0.3% CHAPS detergent (pH 7.1 adjusted using KOH). Protein concentrations were determined using a BCA assay (Life Technologies, Carlsbad, CA, USA). Fifty

μg of denatured and reduced protein was subjected to 10–12% gradient SDS-PAGE followed by transfer to low- fluorescence polyvinylidene difluoride membrane. Membranes were blocked with LI-COR Odyssey Blocking Buffer (LI-COR, Lincoln NE, USA) and immunoblotted overnight (4°C) with antibodies specific for each protein. A commercially available monoclonal antibody was used to detect electron transport chain proteins (human OXPHOS Cocktail, ab110411; Abcam, Cambridge, UK, 1:250 dilution), including V-ATP5A (55 kDa), III-UQCRC2 (48 kDa), IV-MTCO1 (40 kDa), II-SDHB (30 kDa) and I-NDUFB8 (20 kDa). Commercially available polyclonal antibodies were used to detect voltage dependent anion carrier 2 (VDAC 2) (32059, 32 kDa; Santa-Cruz, 1:1000), adenine nucleotide translocase 1 (ANT 1) (ab180715, 33 kDa; Abcam, 1:1000) and sarcomeric s-mtCK (generous gift from Dr Uwe Schlattner, Grenoble, France; 42 kDa, 1:1000). The mtCK antibody has been validated previously to confirm specificity [256].

After overnight incubation in primary antibodies, membranes were washed three times, for 5 minutes each time, in TBST and incubated for 1 hour at room temperature with the corresponding infrared fluorescent secondary antibody (LI-COR Biotechnology, Lincoln, NE, USA). Immunoreactive proteins were detected by infrared imaging (LI-COR CLx; LI-COR Biotechnology, Lincoln, NE, USA) and quantified by densitometry (ImageJ, http://imagej.nih.gov/ij/). All images were normalized to a whole membrane Amido Black total protein stain (A8181, Sigma, St Louis, MO, USA).

Redox Status of MtCK

Free reactive thiol (SH) groups on mtCK were labeled using IR-Dye 800CW-Maleimide (LiCor Biotechnology, Lincoln, NE, USA) by a modification of the technique previously described [307, 308]. Heart tissue from animals from Part 1 was homogenized in CHAPS buffer plus inhibitors as described above. Samples were incubated overnight at 4°C with the IR-Dye at a concentration of

100nM/200µg total protein. Excess dye was removed from labeled proteins over Zeba Desalting Spin Columns (Thermo Fisher Scientific, Burlington, Canada) and protein concentration was determined using a BCA assay (Life Technologies, Carlsbad, CA, USA). MtCK was incubated at a ratio of 1:50 with 1mg of SureBead Protein G Magnetic Beads (Biorad, Mississauga, Canada) for 10 minutes at room temperature. 600µg of labeled proteins were then incubated with the SureBeads for 1 hour at room temperature. The bound proteins were eluted with 20mM Glyicine (pH 2.0) and were subjected to 10% SDS-PAGE. The gels were scanned using infrared imaging (LI-COR CLx; LI-COR Biotechnology, Lincoln, NE, USA) and quantified by densitometry (ImageJ, http://imagej.nih.gov/ij/).

Statistics

Results are expressed as means ± SEM. The level of significance was established as $p<0.05$ for all statistics. Outliers were omitted in accordance with the ROUT test GraphPad Prism Software, La Jolla, CA, USA). D'Agostino-Pearson omnibus normality test revealed that data resembled a Gaussian distribution which justified the application of parametric tests. In Part 1 and Part 3, all statistical differences were analyzed using unpaired t-tests between WT and D2.*mdx* (Part 1) or Saline and SBT-20 (Part 3) for all experiments except the time course functional data. Statistical differences in time course functional data were analyzed using a two-way ANOVA followed by an LSD post-hoc when an interaction was present (GraphPad Prism Software, La Jolla, CA, USA). All data from Part 2 underwent statistical analysis using a two-way ANOVA followed by an LSD post-hoc when an interaction was present (GraphPad Prism Software, La Jolla, CA, USA).

Results

D2.mdx mice display muscle wasting and weakness across lifespan

D2.*mdx* mice exhibit significantly lower body weights relative to WT controls at all time points from 4-52 weeks of age (-13 to -21%, main effect for group, $p<0.05$; **Figure 1A**). Lower limb muscle volume is reduced by 15% relative to WT at 4 weeks of age ($p<0.05$**)** but this reduction is restored from weeks 8-16 as no differences are evident between DMD and WT groups. Loss of muscle volume is once again apparent at 24 weeks of age (-15% vs WT, $p<0.05$) and muscle volume remains lower relative to WT at all subsequent time points (-28 to -35%, $p<0.05$; main effect for group, $p<0.05$; **Figure 1B**). Cage hang time (**Figure 1C**), forelimb grip strength (**Figure 1D**) and distance covered during 24 hours of voluntary wheel running (**Figure 1E**) are all significantly lower relative to WT controls (main effect for group, $p<0.05$).

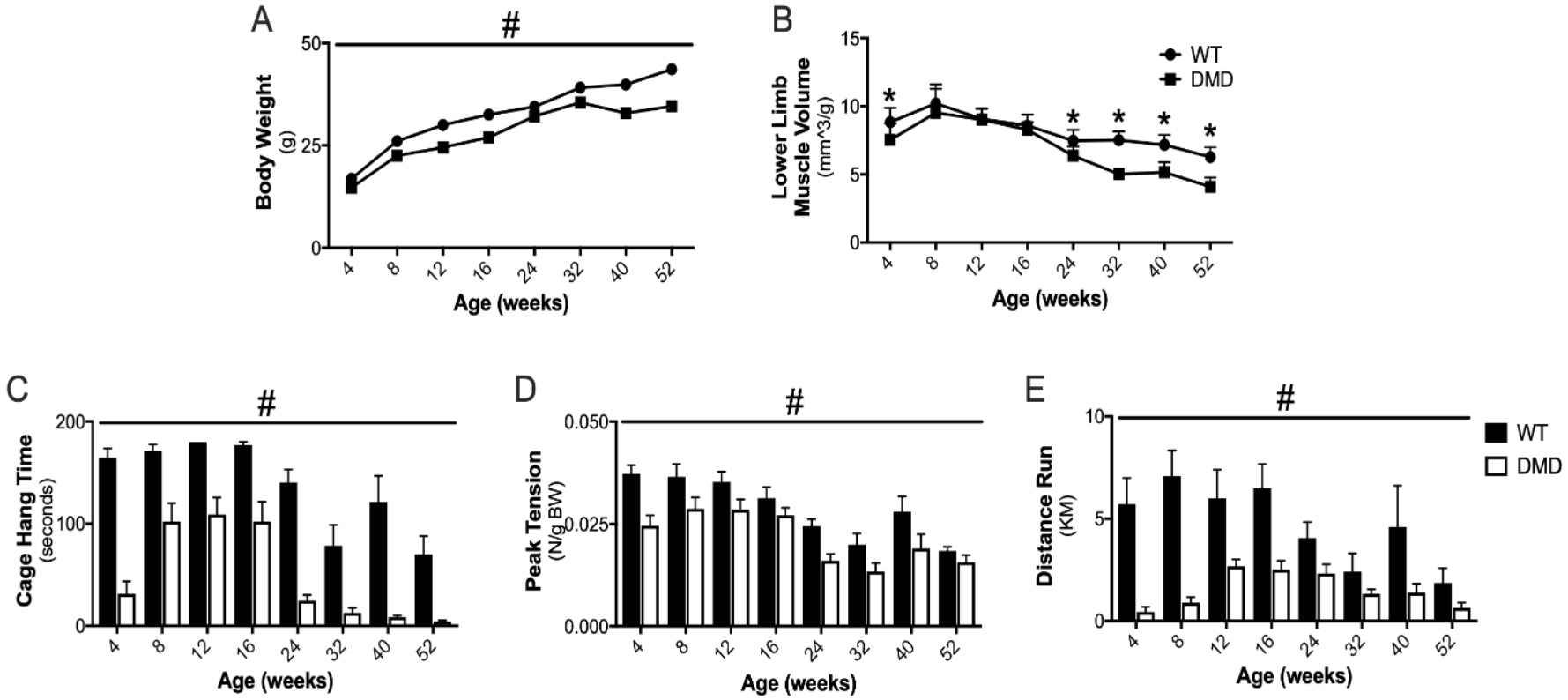

Figure 7-1: Evaluation of muscle wasting and weakness in D2.*mdx* mice throughout lifespan. Body weight (**A,** n=8-10) and μCT analysis of lower limb muscle volume (**B,** n=5-9) were used to evaluate body composition. Indices of muscle function were assessed by cage hang time (**C,** n=6-12), forelimb grip strength (**G**, n=6-12) and 24-hour voluntary wheel running (**E,** n=6-12). Results represent mean ± SEM; # $p<0.05$ main effect for group compared to WT; * $p<0.05$ compared to WT.

Alternations in mitochondrial bioenergetics are creatine-dependent in aged D2.mdx mice

Previous work in our laboratory demonstrated elevated mitochondrial H_2O_2 (mH_2O_2) emission during impaired oxidative phosphorylation in young D2.*mdx* mice specifically highlighting an impairment in the central role of ADP in stimulating controlling bioenergetics [304, 156]. We first determined whether this impairment still exists in aged D2.*mdx* mice across a spectrum of oxidative and glycolytic muscles. Complex I-supported respiration and mH_2O_2 emission during oxidative phosphorylation were stimulated with NADH generated by pyruvate (5mM) and malate (2mM) in the presence of physiological (25μM) and supraphysiological (500μM) concentrations of ADP to mimic a low and high metabolic stress respectively. This titration was repeated with (+Cr) and without (-Cr) 20mM creatine to drive energy transfer dependent (**Figure 2A)** or independent of mtCK (**Figure 2B**), respectively. In the presence of a low (**Figure 2C)** or high (**Figure 2G**) metabolic stress, +Cr oxidative phosphorylation was impaired in D2.*mdx* Heart (-35% to -36% vs WT, $p<0.05$), Diaphragm (-48% to -52% vs WT, $p<0.05$), Quad (-35% to - 41% vs WT, $p<0.05$) and WG (-31 to -50% vs WT, $p<0.0$) relative to WT controls. On the contrary -Cr oxidative phosphorylation was improved in D2.*mdx* Heart at both low (+102% vs WT, $p<0.05$; **Figure 2D**) and high (+90% vs WT, p<0.05l **Figure 2H**) [ADP] and unchanged between D2.*mdx* and WT Diaphragm, Quad and WG muscles, highlighting a creatine-dependent impairment and creatine-independent compensation in mitochondrial oxidative phosphorylation.

During creatine-dependent oxidative phosphorylation, mH_2O_2 emission was elevated in D2.*mdx* muscle in the presence of either low metabolic stress (Heart: +43% vs WT, $p=0.06$; **Figure 2E**), high metabolic stress (WG: +117% vs WT, $p<0.05$; **Figure 2I**) or both (Diaphragm: +36 to +76% vs WT, $p<0.05$ and Quad: +54% to +57% vs WT, $p=0.08$ to $p<0.05$) relative to WT controls. However, during creatine-independent oxidative phosphorylation, mH_2O_2 emission was

unchanged in the Quad (**Figure 2F and J**), lower in D2.*mdx* Heart with supraphysiological ADP (-39% vs WT, $p<0.05$) and lower in D2.*mdx* Diaphragm muscle at both [ADP] (-30 to 51% vs WT, $p<0.05$) relative to WT controls. The WG from D2.*mdx* mice exhibited higher rates of creatine-independent mH_2O_2 emission with low [ADP] (+55% vs WT, $p<0.05$; **Figure 2F**) but this impairment is no longer evident in the presence of a high metabolic stress (**Figure 2J**). Similar elevations in complex-II supported state III mH_2O_2 emission were present in a creatine-dependent manner across all D2.*mdx* muscles regardless of metabolic stress (**Supplemental Figure 1A and C**) while creatine-independent mH_2O_2 emission was unchanged (Diaphragm and WG) or lower (Heart, Quad) in D2.*mdx* muscle relative to WT controls (**Supplemental Figure 1B and D**).

Complex III and pyruvate dehydrogenase complex (PDC)-supported mH_2O_2 emission were also assessed in the presence of 20mM creatine as a control given they are not regulated directly by ADP. Complex III-supported mH_2O_2 was unchanged in Heart, Diaphragm and Quad muscle and significantly lower in D2.*mdx* WG relative to WT (-37% vs WT, $p<0.05$; **Supplemental Figure 1E**). PDC-supported mH_2O_2 emission was significantly lower in D2.*mdx* Heart (-26% vs WT, $p<0.05$), Diaphragm (-38% vs WT, $p<0.05$) and Quad (-52% vs WT, $p<0.05$) and unchanged in WG (**Supplemental Figure 1F**). These findings collectively suggest there is a creatine specific impairment in ADP's control of bioenergetics in aged D2.*mdx* muscle.

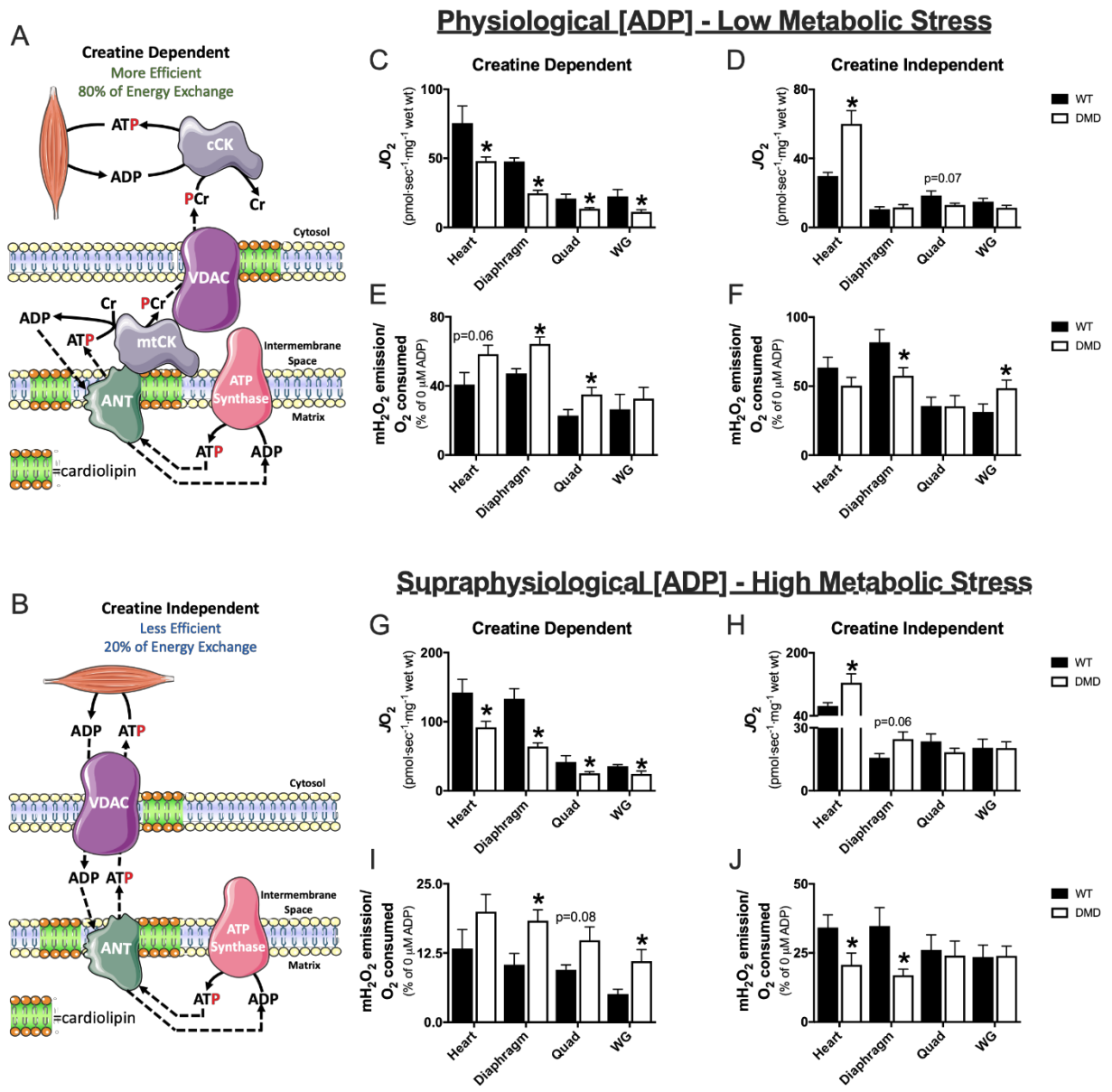

Figure 7-2: Complex I supported respiration and mH_2O_2 emission in aged D2.*mdx* mice. The leading model for energy exchange involves a (**A**) creatine-dependent and (**B**) creatine-independent pathway. ADP stimulated respiration and H_2O_2 emission, supported by Complex-I substrates pyruvate (5mM) and malate (2mM), was assessed in the presence (Creatine Dependent) and absence (Creatine Independent) of 20mM creatine. Assessments of bioenergetic function were completed in Heart, Diaphragm, Quad and WG muscles in the presence of physiological (25µM) [ADP] (**C-F**) and supraphysiological (500µM) [ADP] (**G-J**). Results represent means ± SEM; n=6-10; * compared to WT, $p<0.05$.

Muscle specific alterations in key regulators of energy exchange in dystrophic tissue

We next determined whether altered mitochondrial bioenergetics were related to changes in protein content of key regulators of energy exchange. In D2.*mdx* Heart and Quad muscle, protein content of ANT 1 (**Figure 3A**) and VDAC 2 (**Figure 3B**), situated in the inner and outer mitochondrial membranes respectively (**Figure 2A and B),** mtCK (**Figure 3C**), the primary driver of creatine-dependent energy exchange and the components of the electron transport chain **(Figure 3D and F**) were unchanged. In D2.*mdx* Diaphragm muscle, there was decreased protein content of all regulators of energy exchange (ANT 1: -33% vs WT, $p<0.05$; **Figure 3A**; VDAC 2: -33% vs WT, $p<0.05$; **Figure 3B;** MtCK: -28% vs WT, $p<0.05$; **Figure 3C**) and ETC components (Complex I: -16% vs WT, $p=0.07$; Complex II: -29% vs WT, $p<0.05$; Complex III: -25% vs WT, $p<0.05$; Complex IV: -28% vs WT, $p<0.05$; Complex V: -19% vs WT, $p<0.05$; Sum of Complexes: -25% vs WT, $p<0.05$; **Figure 3E**) suggesting an overall decrease in mitochondrial content in D2.*mdx* Diaphragm relative to WT.

On the contrary, in D2.*mdx* WG muscle, there were increased or tendencies for increased protein content of ANT 1 and VDAC 2 (ANT 1: +87% vs WT, $p=0.08$; **Figure** 3A; VDAC 2: +171% vs WT, $p<0.05$; **Figure 3B**) relative to WT but no differences in mtCK content. Additionally, there were increases in all complexes other than CIII of the ETC relative to WT (Complex I: +29% vs WT, $p<0.05$; Complex II: +122% vs WT, $p<0.05$; Complex IV: +113% vs WT, $p<0.05$; Complex V: +36% vs WT, $p=0.08$; Sum of Complexes: +46% vs WT, $p<0.05$; **Figure 3G**).

MtCK is oxidized in D2.mdx mice

Given that altered bioenergetics could not be explained by changes in protein content of key regulators of energy exchange, we next assessed the redox status of mtCK in Heart muscle of D2.*mdx* mice relative to WT controls. Heart was selected for analysis given it is established as the most creatine sensitive muscle [286]. IR-Dye 800CW-Maleimide binds to reduced thiols on

proteins. Whole Heart lysate from D2.*mdx* and WT animals was labeled with the IR-Dye and mtCK was immunoprecipitated from this lysate. Fluorescent maleimide labeling revealed mtCK is oxidized in D2.*mdx* Heart muscle as evidenced by a significant decrease in signal relative to WT controls (-57% vs WT, $p<0.05$; **Figure 3H**). Please see **Supplemental Figure 7-2** for specific details about the methodological approach for this assay.

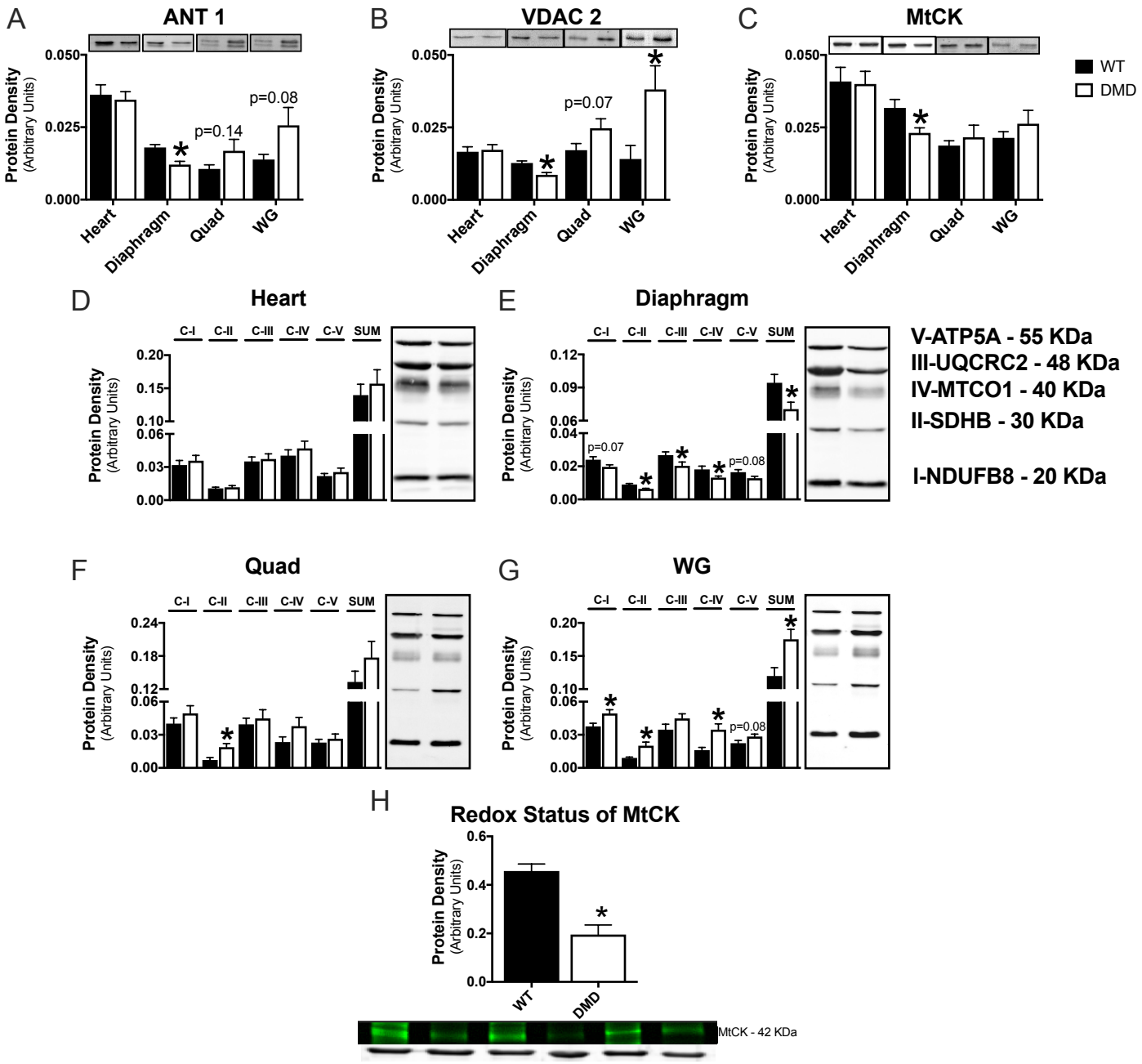

Figure 7-3: Muscle-specific changes in essential regulators of bioenergetics in DMD. Protein content of adenine nucleotide translocase 1 (ANT 1) on the inner mitochondrial membrane (**A**), voltage dependent anion carrier 2 (VDAC 2) on the outer mitochondrial membrane (**B**), and mitochondrial creatine kinase (mtCK) found in the inner membrane space (**C**) were quantified in Heart, Diaphragm, Quad and WG. Protein content of electron transport chain components were also quantified in Heart (**D**), Diaphragm (**E**), Quad (**F**) and WG (**G**). Results represent mean ± SEM; n=8; * $p<0.05$ compared to WT. Redox status of purified mtCK was evaluated in (**H**) Heart muscle. Results represent mean ± SEM; n=3; * $p<0.05$ compared to WT.

In vitro treatment with SBT-20 improves creatine-dependent oxidative phosphorylation and protects mtCK from oxidative modifications

Cardiolipin, which binds to mtCK, is the binding site of the mitochondrial targeted peptide SBT-20. Given the binding of cardiolipin to mtCK is known to affect mtCK function, we sought to determine if *in vitro* treatment with SBT-20 could improve creatine-dependent energy exchange through the stabilization of mtCK **(Figure 4E**). Complex I-supported state III respiration was stimulated with NADH generated by pyruvate (5mM) and malate (2mM) in the presence of physiological (25μM) supra-physiological (500μM) concentrations of ADP in Quad muscle (saline or SBT-20 treated) from 4-week old D2.*mdx* mice in the presence (+Cr) and absence (-Cr) 20mM creatine to drive energy transfer dependent (**Figure 2A)** or independent of mtCK (**Figure 2B**), respectively. Quad muscle was used given the established impairment in creatine sensitivity at this time point recently reported by our laboratory [156].

Following treatment with SBT-20, there were no differences in oxidative phosphorylation between any of the groups in the presence of a low metabolic stress (25μM ADP) (**Figure 4A**). However, in the presence of a high metabolic stress, SBT-20 increased creatine-dependent respiration relative to saline treated fibres (+35% vs +Cr-Saline, $p<0.05$). However, SBT-20 did not increase creatine-independent respiration relative to saline treated fibres indicating that SBT-20 improved oxidative phosphorylation in a creatine-dependent manner. Finally, there were no differences in +Cr-Saline respiration relative to –Cr-Saline, reproducing our finding of an impairment in creatine sensitivity in this muscle. SBT-20 increased creatine-dependent respiration such that it was higher than –Cr-saline (+73% vs –Cr-Saline, $p<0.05$) and –Cr-SBT-20 (+44% vs –Cr-SBT-20, $p<0.05$) rates, indicating that SBT-20 rescued the impairment in creatine sensitivity in D2.*mdx* Quad muscle (**Figure 4B**).

Following the induction of state III respiration, H_2O_2 was titrated into the chamber to assess the ability of SBT-20 to protect against oxidant-induced decreases in respiration, believed to occur through the oxidation of mtCK [309, 310]. Following the addition of both 100 μM and 250 μM H_2O_2, +Cr-saline fibres saw the greatest drop in respiration (100 μM: -45%; **Figure 4C;** 250 μM: -83%; **Figure 4D**) which was a significantly greater drop than –Cr-saline (100 μM: -34%, $p<0.05$; 250 μM: -65%, $p<0.05$) suggesting an oxidant-induced modification of mtCK activity. Furthermore, +Cr-SBT-20 respiration dropped to a similar degree as both –Cr-Saline and –Cr-SBT-20 indicating that SBT-20 protected against the inactivation of mtCK.

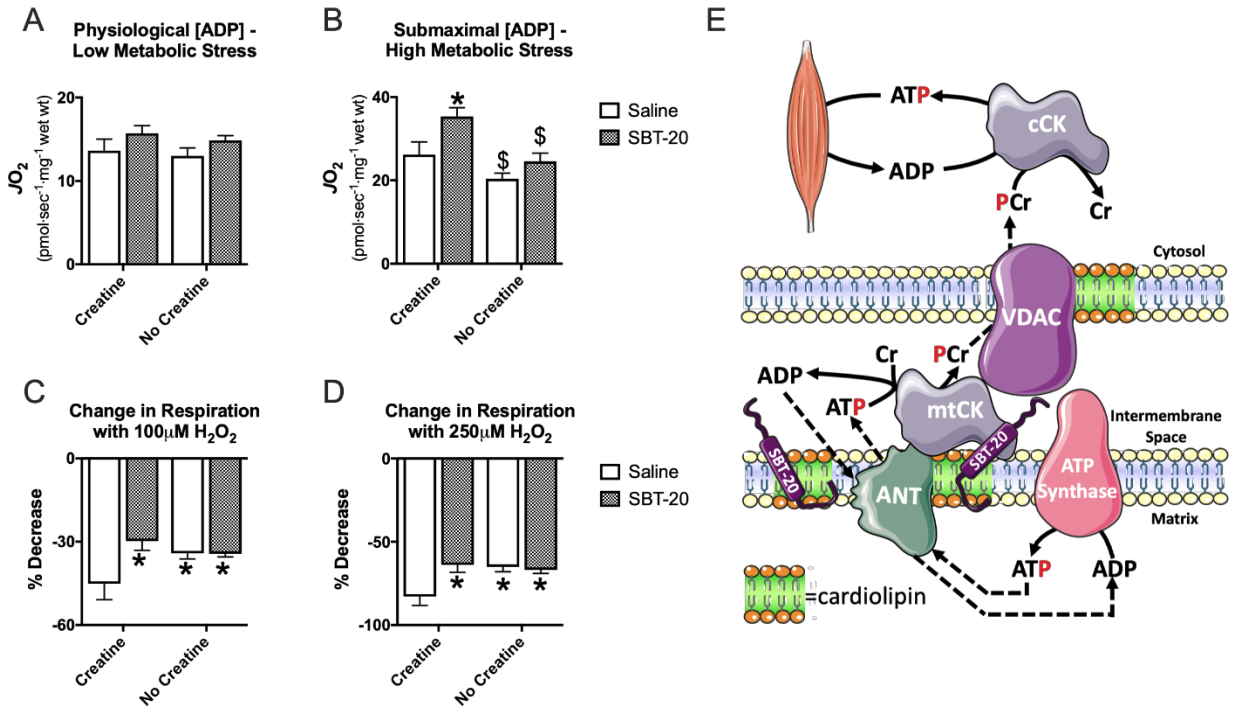

Figure 7-4: Oxidative phosphorylation following *in vitro* treatment with cardiolipin-binding peptide SBT-20. ADP stimulated respiration, supported by Complex-I substrates pyruvate (5mM) and malate (2mM), was assessed following the *in vitro* incubation of Quad muscle from D2.*mdx* mice with 1μM SBT-20 or volume equivalent saline in the presence (Creatine) or absence (No Creatine) of 20mM Creatine. Assessments of oxidative phosphorylation were made in the presence of physiological (25μM) [ADP] (**A**) and supraphysiological (500μM) [ADP] (**B**). Results represent means ± SEM; n=9-10; * $p<0.05$ compared to Creatine-Saline; $ $p<0.05$ compared to Creatine-SBT-20. (C) 100 μM and (**D**) 250 μM H_2O_2 were added to assess the oxidant-induced decrease in state III respiration. Results represent means ± SEM; n=6-8; * $p<0.05$ compared to Creatine-Saline. SBT-20 binds to cardiolipin (**E**) and is believed to play a role in the stabilization of mtCK functionality.

In vivo treatment with SBT-20 improves creatine-dependent mitochondrial bioenergetics

Following 12 weeks of treatment with SBT-20, Complex I-supported respiration and H_2O_2 emission during oxidative phosphorylation were stimulated in saline (SAL) and SBT-20 treated Heart, Diaphragm, Quad and WG muscle with NADH generated by pyruvate (5mM) and malate (2mM) in the presence of physiological (25μM) and supraphysiological (500μM) concentrations of ADP to mimic a low and high metabolic stress respectively. This titration was repeated with

(+Cr) and without (-Cr) 20mM creatine to drive energy transfer dependent (**Figure 2A)** or independent of mtCK (**Figure 2B**), respectively as well as a third condition of 13.9mM PCr and 9.1mM Cr (+PCr/Cr) which provides an equilibrium across mtCK as occurs in skeletal muscle at rest *in vivo* [247].

+Cr, SBT-20 treatment significantly increased oxidative phosphorylation in Heart muscle at both low (+33% vs SAL, $p<0.05$; **Figure 5A**) and high (+25% vs SAL, $p<0.05$; **Figure 5F**) ADP. Similarly, +Cr, SBT-20 lowered mH_2O_2 emission during oxidative phosphorylationin Heart muscle at low (-38% vs SAL, $p=0.09$; **Figure 5D**) and high (-49% vs SAL, $p<0.05$; **Figure 5I**) ADP relative to saline treated animals. However, SBT-20 treatment had no effect –Cr oxidative phosphorylation (**Figure 5C**) or mH_2O_2 emission (**Figure 5E**).

In Diaphragm muscle, SBT-20 improved +PCr/Cr respiration (25μM: +97% vs SAL, $p<0.05$; **Figure 5B**; 500μM: +58% vs SAL, $p=0.09$; **Figure 5G)** and lowered +Cr mH_2O_2 emission during oxidative phosphorylation (25μM: -28% vs SAL, $p=0.06$; **Figure** 5D; 500μM: -32% vs SAL, $p=0.11$; **Figure 5I**) but had no effect on –Cr respiration (**Figure 5C and H)** or mH_2O_2 emission (**Figure 5E and J**).

In Quad muscle, SBT-20 improved +PCr/Cr respiration (25μM: +53% vs SAL, $p<0.05$; **Figure 5B**; 500μM: +157% vs SAL, $p=0.09$; **Figure 5G)** and tended to lower +Cr mH_2O_2 emission during oxidative phosphorylation at high [ADP] only (500μM: -26% vs SAL, $p=0.08$; **Figure 5I**. Similar to both Heart and Diaphragm, SBT-20 had no effect on –Cr respiration (**Figure 5C and H**) or mH_2O_2 emission (**Figure 5E and J**).

WG muscle was used as a negative control given its established insensitivity to creatine due to the low degree of mtCK activity in this glycolytic tissue [286]. Indeed, SBT-20 treatment had no effect

on mitochondrial bioenergetics save for a decrease in +Cr respiration with 25μM ADP (-29% vs SAL, $p<0.05$; **Figure 5A**). Furthermore, Complex III and PDC-supported mH_2O_2 emission were also assessed in the presence of 20mM creatine as negative controls given they are not regulated directly by ADP. SBT-20 had no effect on Complex III or PDC supported mH_2O_2 emission in any muscle from D2.*mdx* mice **(Supplemental Figure 2A and B**). Overall, these results indicate that SBT-20 improves ADP's control of creatine-dependent bioenergetics in D2.*mdx* muscles that are sensitive to mtCK functionality.

The improvements in creatine-dependent mitochondrial bioenergetics were not associated with changes in muscle wasting or weakness following 12 weeks of treatment with SBT-20 (**Supplemental Figure 3)** apart from improved hind-limb torque for a given frequency relative to saline (main effect for group, $p<0.05$; **Supplemental Figure 3F**)**.**

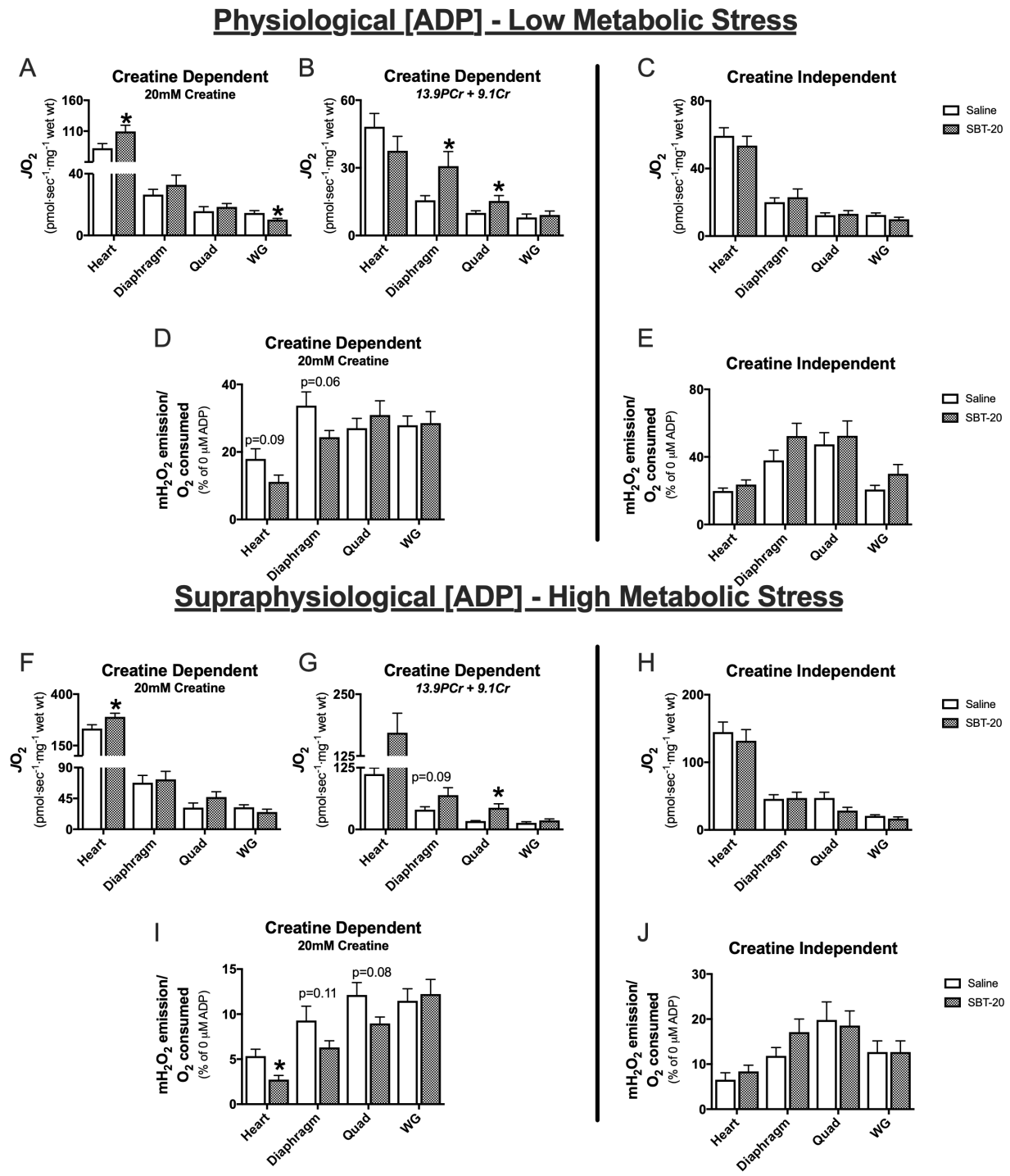

Figure 7-5: Mitochondrial bioenergetics following 12 weeks of treatment with mitochondrial-targeted peptide SBT-20. ADP-stimulated respiration and mH_2O_2 emission during oxidative phosphorylation, supported by Complex-I substrates pyruvate (5mM) and malate (2mM), was assessed in the presence of 20mM Creatine, 13.9PCr + 9.1 Cr or in the absence of creatine. Assessments of bioenergetic function were completed in Heart, Diaphragm, Quad and WG muscles in the presence of physiological (25μM) [ADP] (**A-E)** and supraphysiological **(**500μM) [ADP] (**F-J**). Results represent means ± SEM; n=10-12; * $p<0.05$ compared to Saline.

Discussion

Recent work from our laboratory has identified the mitochondrial as a source of ROS during impaired oxidative phosphorylation in cardiac, respiratory and skeletal muscles from D2.*mdx* mice [304, 156]. Pioneering work by Braun et al., identified an impairment in creatine sensitivity in oxidative muscle from 10-11 month old *mdx* mice [201], a finding that was replicated in young (4-week) D2.*mdx* mice [304, 156]. These findings highlight a potential underlying defect in mitochondrial creatine kinase (mtCK) in dystrophic tissue yet the specific alteration in mtCK functionality and its subsequent contribution to impaired mitochondrial bioenergetics in DMD remains unknown. The present study identified oxidized mtCK as a source of creatine-dependent impairments in mitochondrial bioenergetics in the late stages of disease progression in D2.*mdx* muscle. *In vitro and in vivo* treatment with the cardiolipin-binding peptide SBT-20 improved mitochondrial bioenergetics in a creatine-dependent manner and protected against oxidant-induced decreases in creatine-dependent oxidative phosphorylation, highlighting mtCK as a therapeutic target of SBT-20.

Impairments in mitochondrial bioenergetics are creatine and ADP-dependent in aged D2.mdx mice

At 4 weeks of age D2.*mdx* mice exhibit elevated mH_2O_2 emission during impaired oxidative phosphorylation in cardiac, respiratory and skeletal muscle [304, 156]. While this is accompanied by an impairment in creatine sensitivity in oxidative muscles, impairments in bioenergetics were evident regardless of the energy exchange pathway activated (Figure 2A and B). At late stages of disease progression, the same muscles from D2.*mdx* mice exhibit divergent alterations in mitochondrial bioenergetics such that creatine-dependent function is impaired in all muscles while creatine-independent function is either unchanged (Quad and WG) or exhibits compensatory improvements (Heart and Diaphragm). While the creatine-dependent impairments in Diaphragm

may be explained by a decrease in mtCK content, alternative mechanisms are likely in Heart, Quad and WG muscle. mtCK is highly susceptible to oxidative modifications, leading to enzymatic inactivation and octamer dissociation, as well as formation of crystalline mitochondrial inclusion bodies, all resulting in loss of enzyme functionality [153, 152]. Evaluation of redox status of purified mtCK revealed that mtCK is oxidized in D2.*mdx* cardiac muscle, identifying a mechanism of dysfunction in creatine-dependent bioenergetics. Furthermore, creatine-dependent impairments appear to be ADP-dependent. Complex III and PDC are two membrane potential independent sites of mitochondrial ROS production and therefore, production rates are not governed by ADP. In the presence of creatine, mH_2O_2 emission rates were either unchanged or significantly lower in D2.*mdx* muscle signifying that there is a specific impairment in ADP's control of bioenergetics. Given that mtCK facilitates ADP's role in lowering mitochondrial H_2O_2 emission while stimulating oxidative phosphorylation, these findings collectively highlight oxidized mtCK as the underlying cause of impaired mitochondrial bioenergetics in aged D2.*mdx* mice [205, 157].

Improvements in creatine-independent bioenergetics in Heart and Diaphragm muscle can also not be explained by altered protein content of key regulators of energy exchange (ANT 1 and VDAC 2) as protein content was unchanged in Heart and decreased in Diaphragm muscle. These findings suggest that post-translational regulation of these proteins may have been altered. Indeed, ANT and VDAC have known phosphorylation and acetylation sites [264, 265] although the physiological relevance of this regulatory paradigm remains unknown [200]. Furthermore, given the fact that these proteins are involved in both energy exchange pathways it is difficult to reconcile the divergent alterations in bioenergetics at the level of these regulators. It is possible that compensatory increases in ANT and VDAC permeability result in improvements in creatine-independent bioenergetics yet this improved functionality is masked in creatine-dependent energy

exchange due to the overarching dysfunction in mtCK. The mechanisms surrounding the improved creatine-independent bioenergetics in Heart and Diaphragm muscle remain unknown but warrants consideration of post–translational modifications in the future.

Targeting cardiolipin improves creatine and ADP-dependent bioenergetics in D2.mdx mice

Cardiolipin is a unique phospholipid found almost exclusively on the inner mitochondrial membrane (IMM) that has been shown to interact with a variety of proteins on the IMM [200]. Notably, cardiolipin binds both ANT and mtCK, forming a proteolipid complex with VDAC on the OMM. This complex creates stable contact sites between the IMM and OMM, and is shown to regulate energy exchange, reduce ROS formation and prevent permeability transition pore opening [200]. However, both mtCK and cardiolipin are highly susceptible to oxidative modifications and when oxidized, lose their binding affinity resulting in the dissociation of the proteolipid complex [305, 261].

SBT-20 is an aromatic–cationic peptide that bears alternating aromatic and basic amino acid residues targeting the mitochondria and binding specifically to cardiolipin [223]. *In vitro* treatment with this compound resulted in a significant increase in creatine-dependent oxidative phosphorylation while it had no effect on the creatine-independent dependent pathway. Similarly, *in vivo* treatment with SBT-20 improved creatine-dependent bioenergetics in oxidative muscle while it had no effect on the creatine-independent pathway. These findings suggest that SBT-20 is directly altering mtCK functionality, which was further supported by the lack of effect of SBT-20 in WG, a highly glycolytic muscle that is insensitive to creatine [286]. Furthermore, SBT-20 prevented an oxidant-induced decrease in creatine-dependent respiration, suggesting it protects mtCK from oxidative modifications. It is therefore likely that SBT-20 improves creatine-dependent energy exchange through the stabilization of the proteolipid complex by preventing the

oxidation of mtCK, cardiolipin or both. Future work should examine the redox status of mtCK and cardiolipin to fully elucidate the mechanism by which SBT-20 is improving creatine-dependent bioenergetics in DMD.

Creatine as a therapeutic strategy in DMD

Creatine supplementation in DMD has been explored extensively in both animal models and human clinical trials with reports of improved strength and histopathology following treatment [311, 312]. The use of creatine has been shown to increase muscle mass as well as improve energy metabolism through the creatine-dependent energy exchange pathway. Furthermore, because of this effect on energy exchange, creatine has been shown to decrease apoptotic and necrotic cell death through its ability to influence rates ROS production and oxidative phosphorylation within the mitochondria [313]. Indeed, creatine supplementation has been shown to improve mitochondrial respiration and decrease necrosis in the *mdx* mouse [268]. The findings from this study demonstrate a drastic impairment in the ability of dystrophic tissue to use creatine efficiently, a cellular defect that was improved following treatment with SBT-20. While improvements in strength and histopathology have been demonstrated previously, it is conceivable that the enhancement of creatine sensitivity within dystrophic muscle would augment the beneficial effects of creatine in DMD. As such, an attractive therapeutic approach would involve a cocktail therapy of SBT-20 and creatine for the treatment and prevention of disease progression in DMD.

D2.mdx mice exhibit compensation over lifespan

A side observation from the present investigation was the establishment of a timeline of muscle function dynamics in the D2.*mdx* mouse. The D2.*mdx* mouse model (D2.B10-DMD^{mdx}/2J) exhibits attenuated muscle regeneration arising from a natural mutation in TGF-β binding protein 4 in the background D2A strain. This mouse model has been shown to mimic human disease progression more closely than the classic *mdx* mouse (C57BL10/ScSn^{mdx}) and furthermore, has a

more severe phenotype than the *mdx* mouse at any given stage of disease progression [60, 59]. However, minimal work to date has been done in this model of DMD. As such, we evaluated body composition and whole body functional parameters at various time points from 4 to 52 weeks of age to assess the degree of pathology from early to late stages of disease progression relative to WT controls (Figure 1). While muscle wasting was robust at 4 weeks of age, and in a fashion similar to the *mdx* mouse, D2.*mdx* animals recovered following this period of extensive degeneration [52]. A decrement in muscle volume was once again evident at 24 weeks of age and remained apparent at all remaining time points. While *in vivo* muscle function was impaired relative to WT controls at all time points, qualitatively an interesting pattern developed and is worth noting. From weeks 4 – 16, markers of muscle function improved in DMD animals relative to the previous time point yet by 24 weeks, the point at which muscle wasting is re-established, muscle function declined relative to 16 weeks and continued to decline across remaining time points. Evidently, while D2.*mdx* mice demonstrate impaired muscle function relative to WT controls throughout disease progression, muscle wasting and weakness is not a linear progression in this mouse model.

This period of compensation may also contribute to the lack of functional benefit following *in vivo* treatment with SBT-20. 12 weeks of age falls directly in the period of peak muscle function in D2.*mdx* mice and as such, any improvements in muscle function resulting from drug treatment may be masked by the compensation occurring at this time. In order to truly elucidate the functional benefit of improved mitochondrial bioenergetics and mtCK functionality following SBT-20 treatment, a time point outside of the compensation window should be evaluated.

Conclusions

In summary, oxidized mtCK contributes to impaired mitochondrial bioenergetics in the late stages of disease progression in D2.*mdx* mice. *In vitro* and *in vivo* treatment with the cardiolipin-binding peptide SBT-20 improves mitochondrial bioenergetics in a creatine-dependent manner and protects dystrophic muscle from oxidant-induced decreases in creatine-dependent oxidative phosphorylation. Collectively, these findings underscore mtCK as an underlying cause of dysfunction in dystrophic muscle and highlight a potential therapeutic target for the treatment and prevention of disease progression in DMD.

Conflicts of interest: none

Funding: Funding was provided to C.G.R.P. by the National Science and Engineering Research Council (NSERC #436138-2013) and Stealth Biotherapeutics with infrastructure supported by Canada Foundation for Innovation, the Ontario Research Fund, NSERC Research Tools and Instruments, and the James H. Cummings Foundation. J.A.S. is a new investigator with Heart and Stroke Foundation of Canada and the Heart and Stroke Foundation of Canada (HSFC; S13 SI 0592). P.B. was supported by Canadian Institutes of Health Research, Project Grant (PJT 153159) and a Canada Research Chair in Cardiovascular Biology. M.C.H. and P.C.T. were supported by a NSERC CGS-PhD scholarship. S.V.R. was supported by an Ontario Graduate Scholarship.

Acknowledgements: none

Author Contributions: MCH and CGRP contributed to the rationale and study design. All authors conducted experiments and/or analysed all data. CGRP and MCH wrote the manuscript. All authors contributed to the interpretation of the data.. All persons designated as authors qualify for authorship, and all those who qualify for authorship are listed.

Supplemental Figures – Included in Manuscript

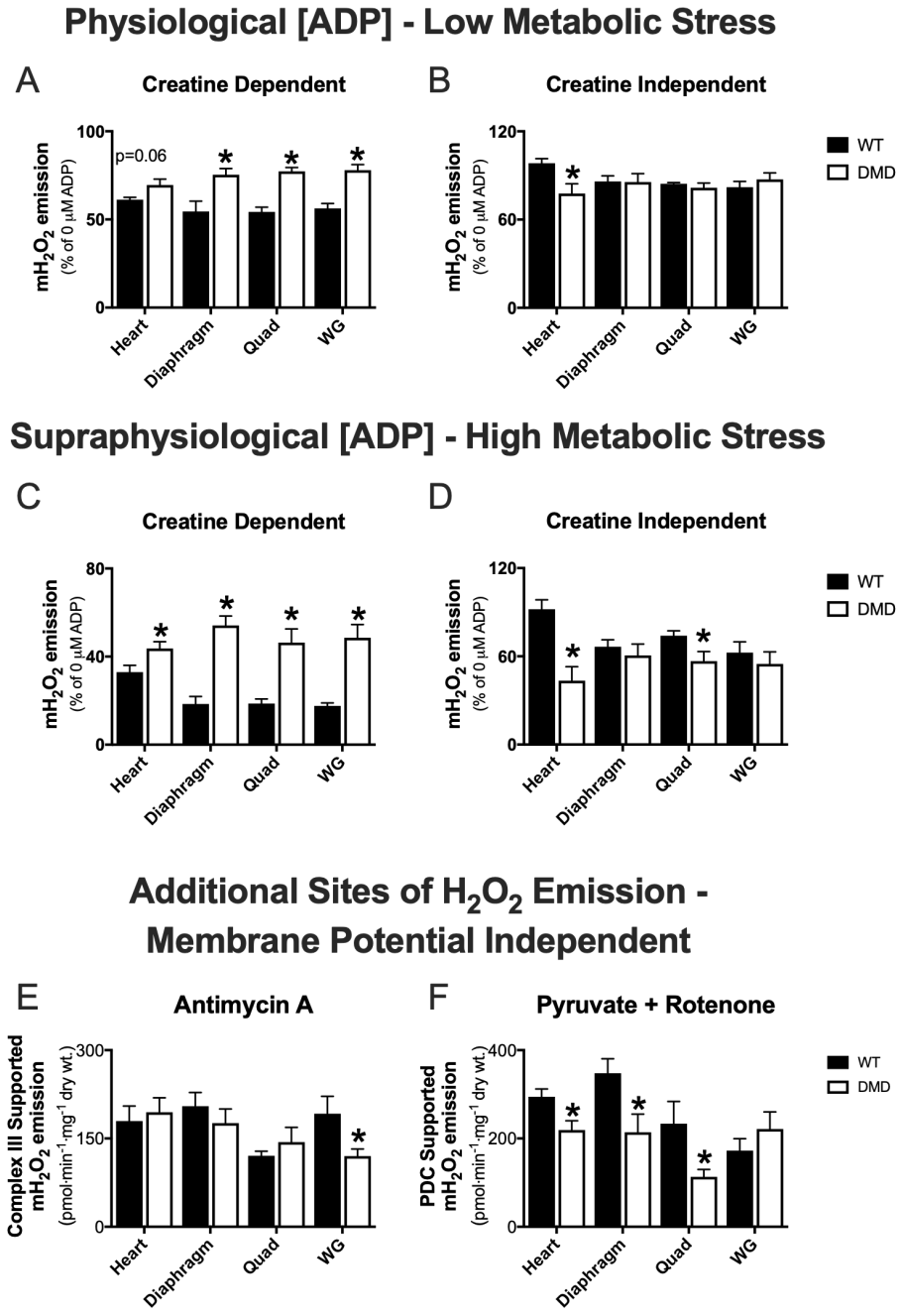

Supplemental Figure 7-1: Complex II, Complex III and Pyruvate Dehydrogenase Complex supported mH_2O_2 emission in D2.*mdx* mice. Complex II (10mM Succinate)- supported mH_2O_2 emission was evaluated in the presence of physiological (25μM) (**A+B**) and supraphysilogical (500μM) (**C+D**) ADP in aged D2.*mdx* mice. In the absence of ADP, complex III-supported mH_2O_2 was assessed using Complex-III inhibitor antimycin A (2.5μM) (**E**) while Pyruvate dehydrogenase complex (PDC)-supported mH_2O_2 was assessed using pyruvate (10mM) and Complex-I inhibitor rotenone (0.5μM) (**F**). Results represent means ± SEM; n=6-10; * $p<0.05$ compared to WT.

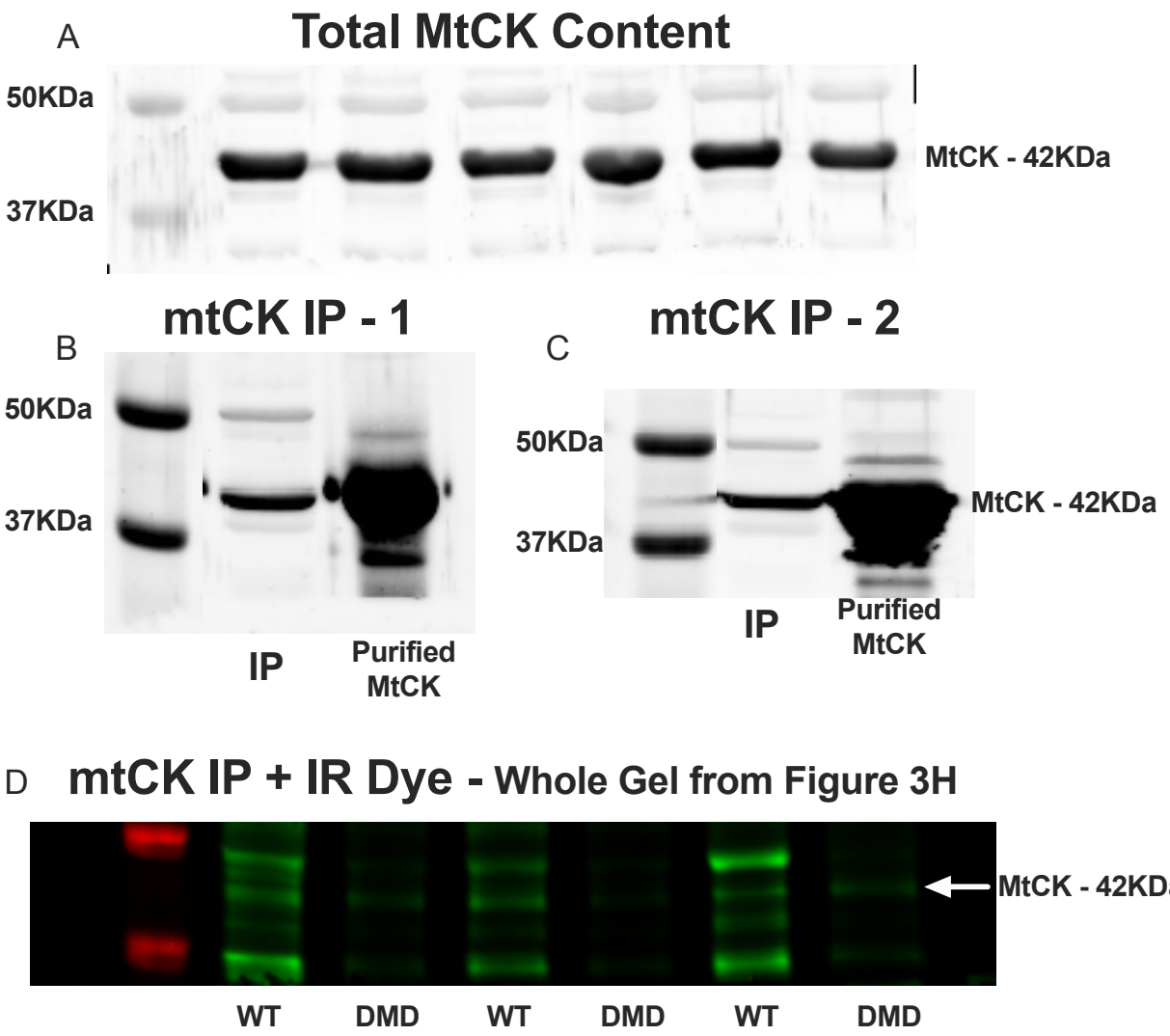

Supplemental Figure 7-2: Representative images from mtCK immunoprecipitation and IR Dye methods development. Total mtCK content as measured by western blotting (**A)**. Replicate examples of immunoprecipitated mtCK next to purified heart mtCK (**B + C**). Whole gel image of immunoprecipitated mtCK conjugated to the IR Dye Maelmide 800 CW (**D**). Limitations with this method are discussed in greater detail in Section 8.2 Limitations.

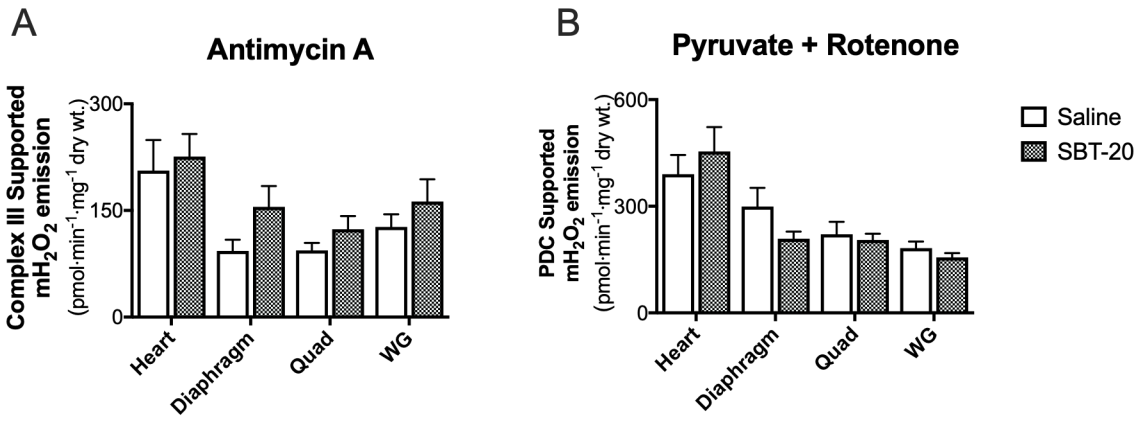

Supplemental Figure 7-3: Complex III and Pyruvate Dehydrogenase Complex supported H_2O_2 emission in D2.*mdx* mice following treatment with SBT-20. In the absence of ADP, complex III-supported mH_2O_2 was assessed using Complex-III inhibitor antimycin A (2.5μM) (**A**) while Pyruvate dehydrogenase complex (PDC)-supported mH_2O_2 was assessed using pyruvate (10mM) and Complex-I inhibitor rotenone (0.5μM) (**B**). Results represent means ± SEM; n=10-12; * $p<0.05$ compared to Saline.

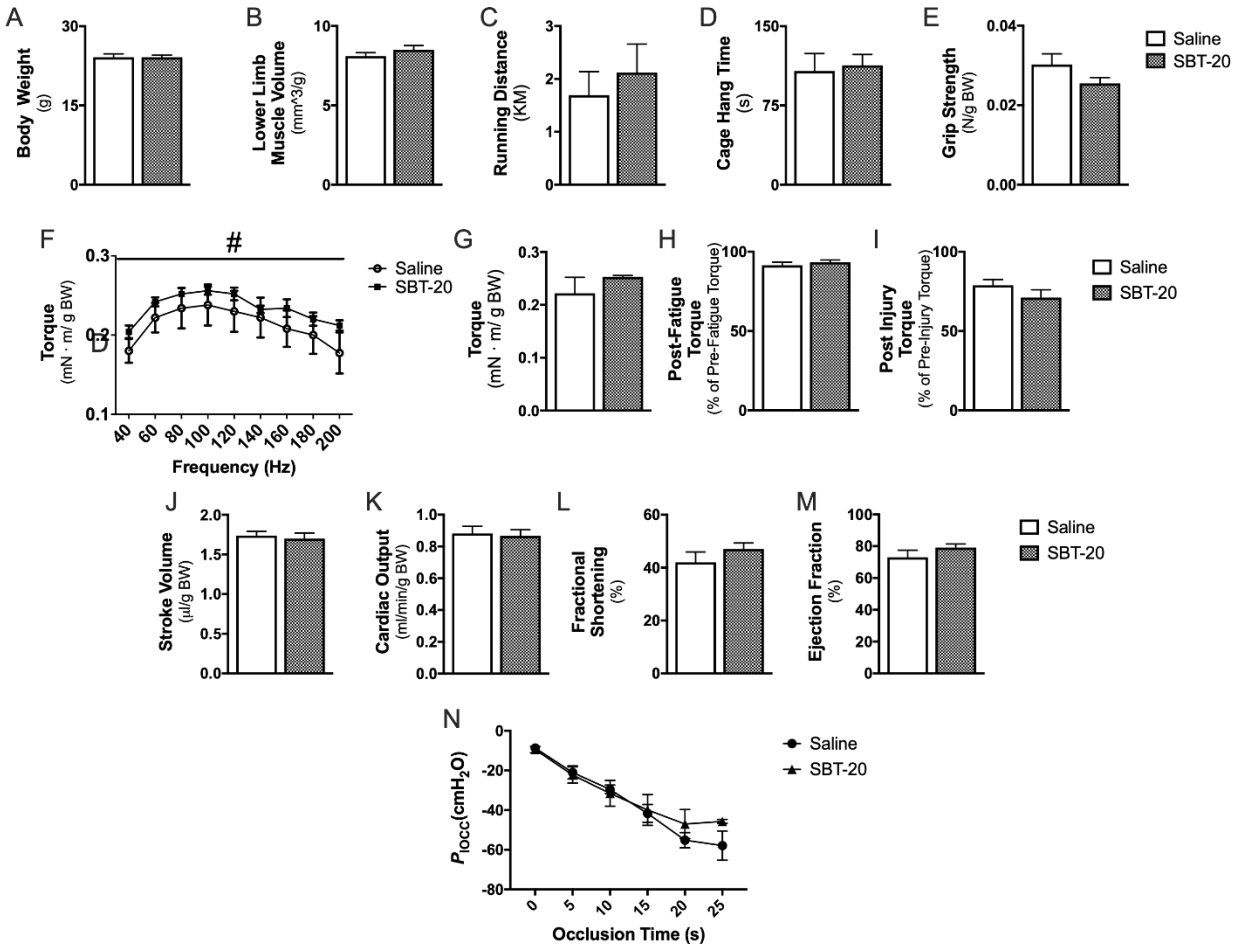

Supplemental Figure 7-4: Evaluation of muscle wasting and weakness in DMD following treatment with SBT-20. Body weight (**A**, n=12) and microCT analysis of lower limb muscle volume (**B**, n=12) were used to assess body composition. Indices of muscle function were assessed by 24-hour voluntary wheel running (**C**, n=12), cage hang time (**F**, n=12) and forelimb grip strength (**G**, n=12). Lower hindlimb force production was assessed *in vivo* using through torque-frequency relationship (**F**) followed by a max-torque challenge **(G**, n=5). Recovery from fatigue (**H**, n=5) and recovery following eccentric contraction-induced injury (**I**, n=5) were evaluated. Cardiac function was evaluated through echocardiography including stroke volume (**J,** n=5), cardiac output (**K,** n=5), fractional shortening (**L**, n=5) and ejection fraction (**M**, n=5). Respiratory function in vivo was assessed through esophageal pressure transduction to determine maximal inspiratory pressure (P_{Iocc}) (**N**, n=4-5). Results represent mean ± SEM; # $p<0.05$ main effect compared to WT; * $p<0.05$ compared to WT.

Supplemental Data – Not Included in Manuscript

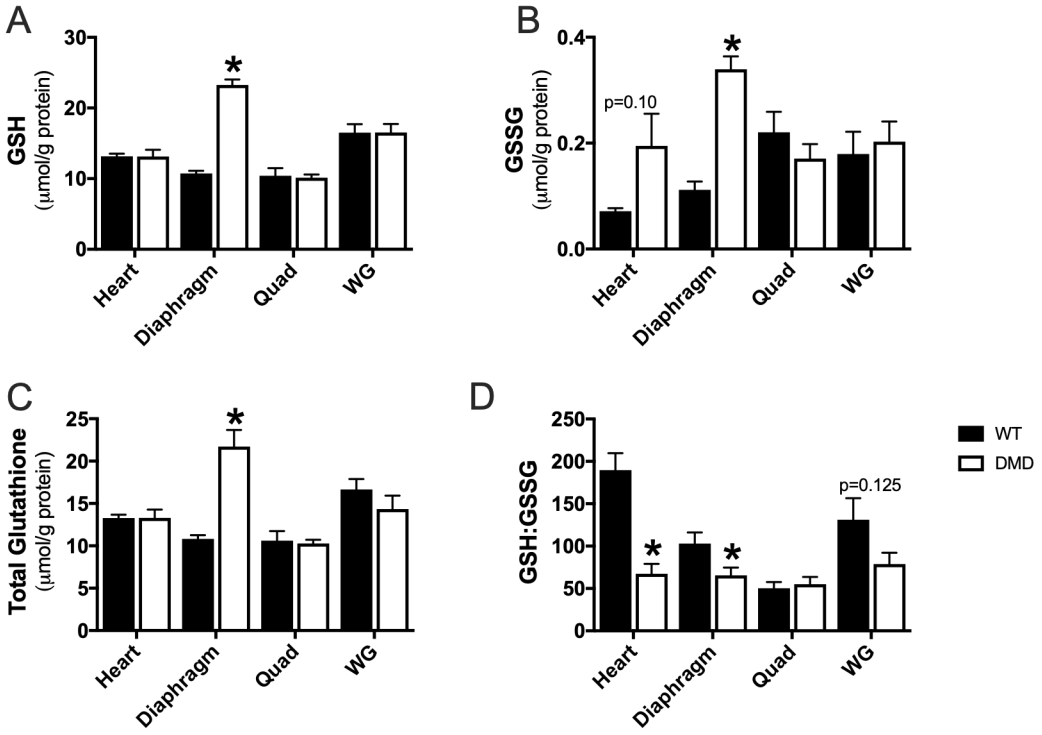

Supplemental Figure 7-5: Evaluation of glutathione levels in aged D2.*mdx* muscle. Glutathione was measured in muscle homogenate using HPLC-UV for the detection of GSH (**A**) and HPLC-Fluorescence for the detection of GSSG (**B**). The GSH:GSSG ratio (**C**) and total glutathione (**D**) were calculated from GSH and GSSG measurements. Results represent mean ± SEM; n=4-8; * p<0.05 compared to WT.

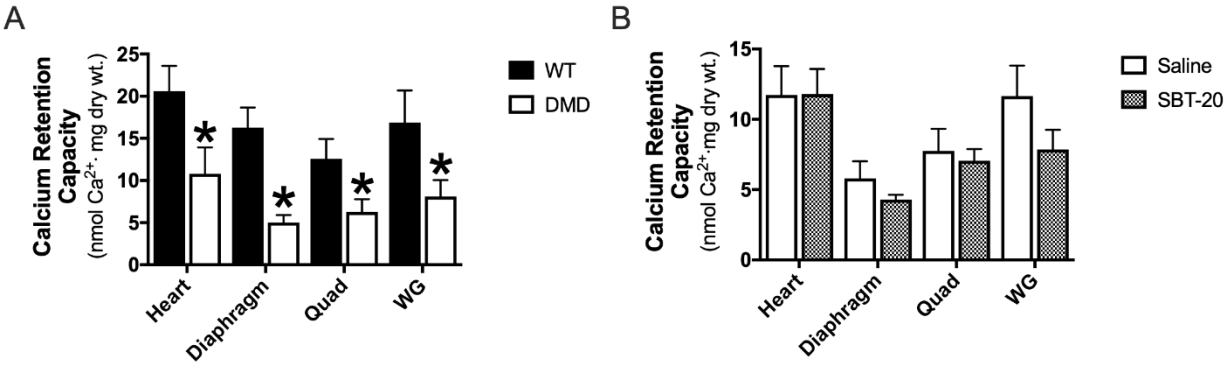

Supplemental Figure 7-6: Susceptibility to permeability transition pore opening in D2.*mdx* mice. Calcium retention capacity, an index of susceptibility to permeability transition pore opening, was assessed in (**A**) aged D2.*mdx* muscle and (**B**) following 12 weeks of treatment with SBT-20. Results represent mean ± SEM; n=7-12; * p<0.05 compared to WT.

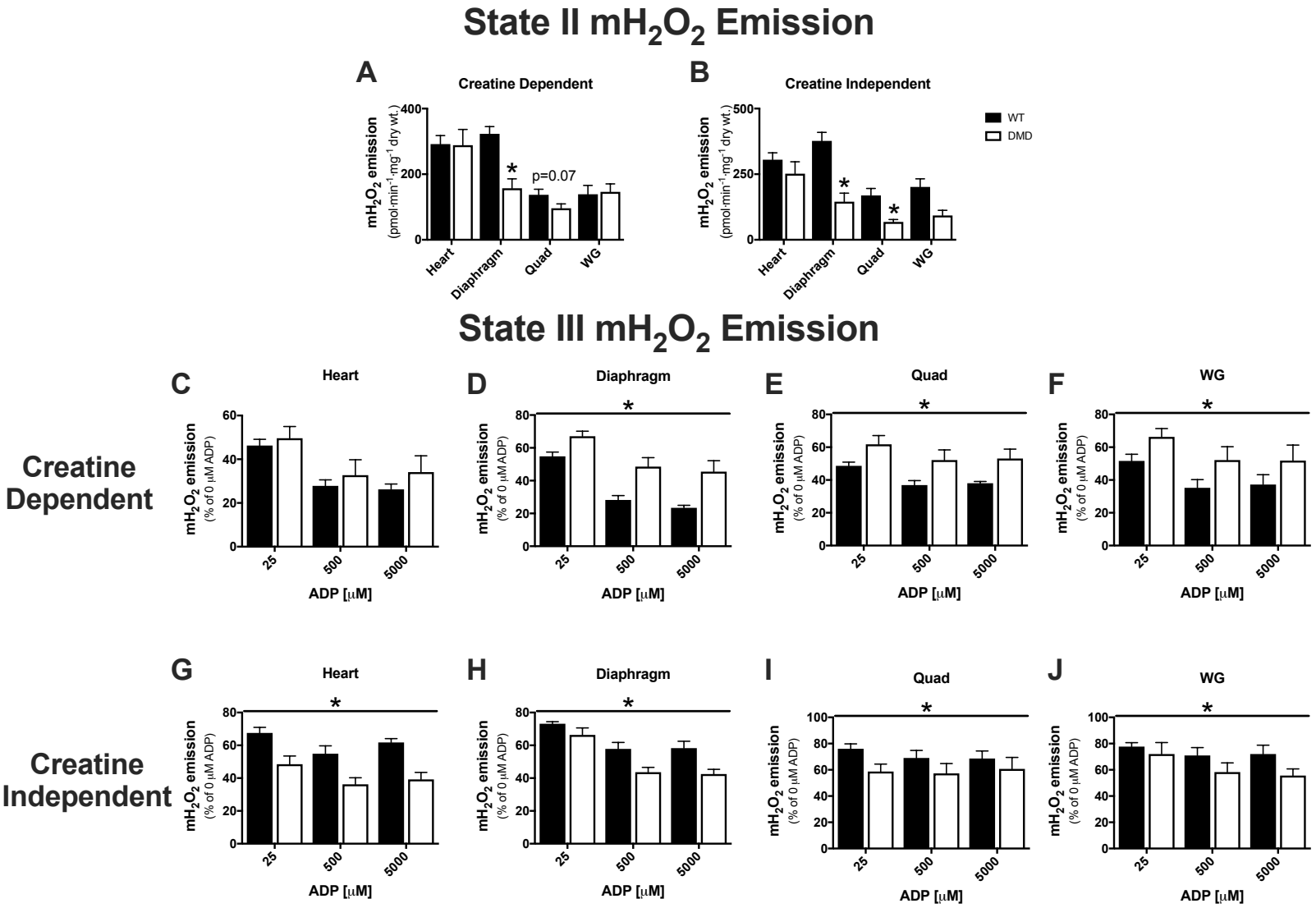

Supplemental Figure 7-7: Absolute complex-I supported mH_2O_2 emission. State II mH_2O_2 was supported by Complex-I substrates Pyruvate (5mM) and Malate (2mM) in the **A.** presence (Creatine Dependent) and **B**. absence (Creatine Independent) of 20mM creatine. ADP's attenuation of maximal mH_2O_2 emission (state III) was evaluated in the same creatine dependent (**C-F**) and independent conditions (**G-J**). Results represent mean ± SEM; n=7-10; * $p<0.05$ compared to WT.

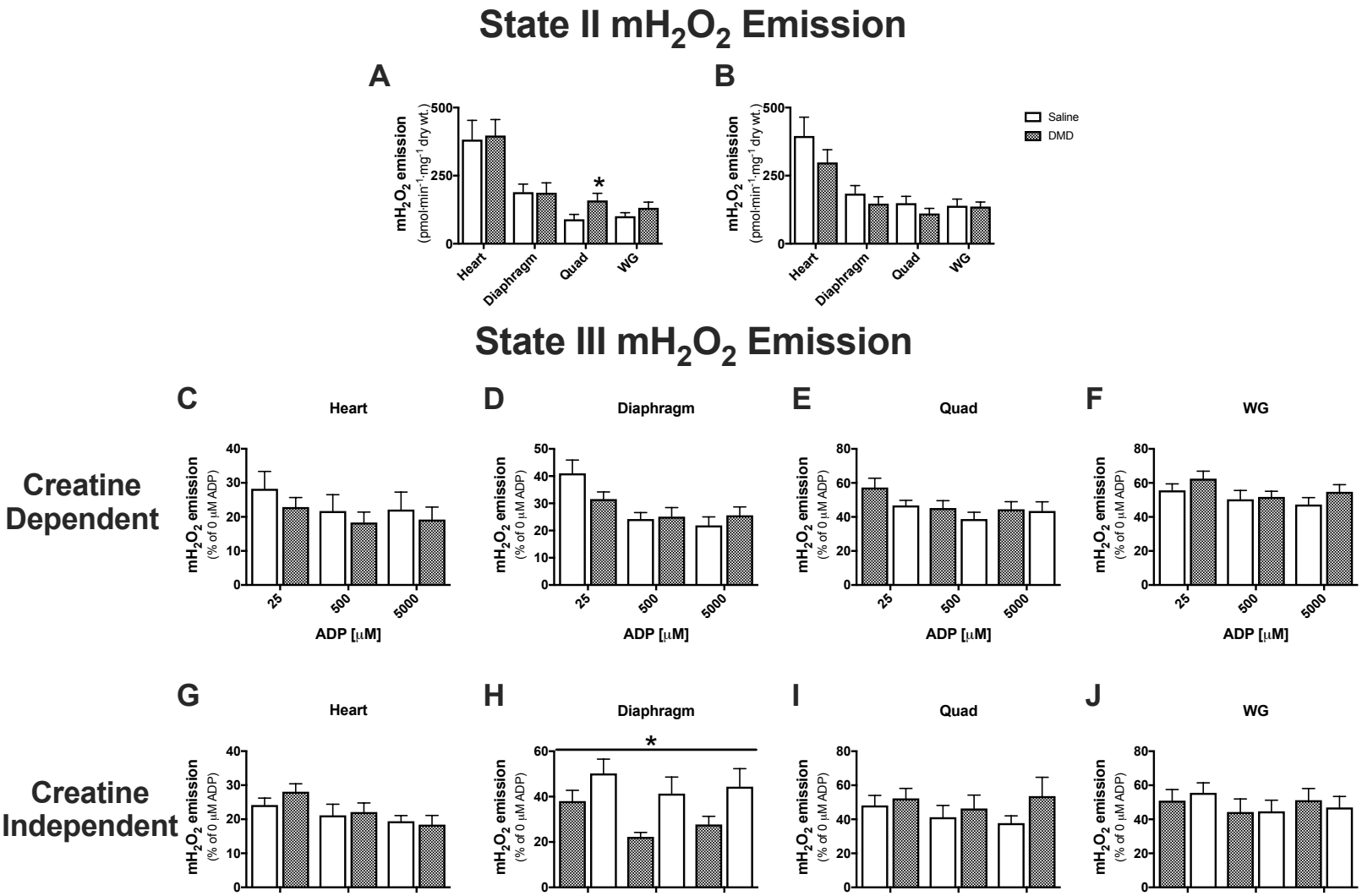

Supplemental Figure 7-8: Absolute complex-I supported mH_2O_2 emission. State II mH_2O_2 was supported by Complex-I substrates Pyruvate (5mM) and Malate (2mM) in the **A.** presence (Creatine Dependent) and **B**. absence (Creatine Independent) of 20mM creatine. ADP's attenuation of maximal mH_2O_2 emission (state III) was evaluated in the same creatine dependent (**C-F)** and independent conditions (**G-J**). Results represent mean ± SEM; n=7-10; * $p<0.05$ compared to Saline

8 Summary of Findings

8.1 General Discussion and Future Directions

DMD is an X-linked muscle wasting disease resulting from a mutation in the gene encoding for the structural protein dystrophin. This debilitating disease targets limb muscles first, leading to loss of ambulation followed by premature death due to cardiac/respiratory failure [2]. Affecting 1 in 3500 boys, there is currently no cure DMD. Given that gene based therapies have had minimal success to date and current standard of care involves the use of glucocorticoids, which have a several negative side effects associated with long-term treatment, extensive research has focused on identifying other therapeutics for the treatment and prevention of DMD [46]. The present thesis sought to first comprehensively evaluate the mitochondria across a spectrum of cardiac, respiratory and skeletal muscles to determine the precise mechanism and degree of mitochondrial dysfunction that occurs in DMD (Chapter 4 and 5). Based on these findings we then assessed the efficacy of the mitochondrial-targeted peptide SBT-20 in improving 1) the pathophysiology of DMD through the alteration of mitochondrial bioenergetics (Chapter 6) and 2) mitochondrial creatine kinase functionality in DMD, our proposed underlying mechanism of mitochondrial dysfunction (Chapter 7). The findings from this thesis identify the mitochondria as a source of ROS during impaired oxidative phosphorylation in DMD and more specifically, that mtCK may be the underlying cause of mitochondrial dysfunction in oxidative muscle. Subsequently, the mitochondrial-targeted peptide SBT-20 presents promising therapeutic potential for the treatment of DMD myopathy, a direct result of its ability to improve mitochondrial bioenergetics in dystrophic muscle.

Modeling in vivo conditions during in vitro assays reveals divergent alterations in mitochondrial bioenergetics in DMD

A consistent and major finding across the four projects of this thesis was the importance of designing *in vitro* protocols to mimic *in vivo* conditions in order to comprehensively evaluate mitochondrial bioenergetics. Firstly, in the absence of ADP, Complex-I stimulated mH_2O_2 emission reveals the maximal capacity of oxidant generation by complex-I but does not reflect *in vivo* conditions whereby ROS production is a by-product of oxidative phosphorylation and is dependent on ADP's ability to govern membrane potential through the stimulation of ATP synthesis [200]. Indeed, our conclusions surrounding mitochondrial mH_2O_2 emission in DMD would be entirely different had we just evaluated maximal capacity in the absence of ADP, particularly when considering the efficacy of SBT-20, which appears to be ADP-dependent in nature.

Secondly, the opening of the mitochondrial permeability transition pore (PTP) is a membrane potential-dependent process and therefore, is also regulated by ADP [314]. Given our identification of specific impairments in ADP's ability to govern bioenergetics in DMD, the design of our calcium retention capacity (CRC) assay warrants further discussion. In Chapter 4, Quad muscle from D2.*mdx* mice exhibit the suspected decrease in the $[Ca^{2+}]$ required to stimulate PTP opening. However, this assay was performed in the absence of ADP and as such, the effectiveness of ADP in lowering membrane potential is unidentified. Based on our findings from Chapter 4 and 5, when evaluating CRC in Chapter 6, ADP was added to the assay media. We were surprised to find that CRC was actually elevated in D2.*mdx* Quad muscle, suggesting a decreased susceptibility to PTP opening but importantly, an entirely different conclusion in the presence of ADP. While the explanation of this seemingly counterintuitive result is somewhat speculative at this point, this suggests an impairment in the ability of dystrophic mitochondria to induce programmed cell death, likely due to limited ATP supply[184], a notion supported by the decrease in CRC following SBT-

20 treatment. Nevertheless, the divergent findings from Chapter 4 and 6 further highlight the necessity of modelling *in vivo* conditions in *in vitro* assays.

Thirdly, and perhaps most strikingly, were the divergent responses in ADP-supported bioenergetics when modelling different pathways of energy-exchange. Leading models of energy exchange suggest that ADP and ATP can be cycled in and out of the mitochondria through a creatine-dependent pathway, whereby mtCK facilitates the transfer of high energy phosphate groups allowing for the efficient cycling of ADP/ATP or through a creatine-independent pathway whereby ADP and ATP bypass mtCK and rely solely on diffusion (Figure 2-6) [200]. The creatine-dependent pathway is believed to make up about 80% of energy exchange in cardiac muscle and is heavily relied on by all other oxidative muscles as it is considerably more efficient. However, in the majority of literature to date, the role of creatine-dependent phosphate shuttling through mtCK was not assessed which means conclusions are limited to alterations in ATP/ADP diffusion, save for one study that reported an impairment in creatine sensitivity in oxidative muscles [201].

Our findings from Chapter 7 highlight the potential discrepancy in findings that would be reported if bioenergetics were assessed in the absence of *in vivo* conditions. Specifically, in late stages of disease progression, there are severe impairments in creatine-dependent oxidative phosphorylation and ADP's suppression of mH_2O_2 emission. However, there are also compensatory improvements in creatine-independent energy exchange, masking impairments in bioenergetics at this time point. If our assay conditions had followed experimental procedure from literature to date, we would have concluded that mitochondrial bioenergetics are improved in D2.*mdx* mice in the late stages of disease progression. Indeed, a recently published paper by Gaglianone et al., reported no impairments in mitochondrial respiration in *mdx* soleus muscle, a highly oxidative muscle, yet their assay conditions were devoid of creatine [315]. Additionally, SBT-20's effects appear to not

only be ADP-dependent, but creatine-dependent in nature as well. We hypothesize this is through the protection again oxidant-induced damage of mtCK. Importantly, modeling creatine-dependent energy exchange *in vitro* allowed us to uncover this beneficial effect, a finding that would have been missed if the assays focused solely on creatine-independent pathways.

Periods of compensation in the D2.mdx mouse may affect therapeutic windows

The four projects in this thesis also implemented a relatively new and unstudied mouse model of DMD. The majority of work in rodent models of DMD to date has been done in the C57bl/10-*mdx*, a naturally occurring mouse model with a mutation in exon 23, resulting in the dystrophic phenotype [51]. Unfortunately, the *mdx* mouse represents a poor model relative to human disease progression given its highly compensatory nature [52]. We therefore employed a relatively new mouse model, the D2.B10-DMD^{mdx}/2J (D2.*mdx*), which exhibits attenuated muscle regeneration arising from a natural mutation in TGF-β binding protein 4 in the background D2A strain [60, 59]. D2.*mdx* mice have a more severe phenotype relative to *mdx* mice and have demonstrated pathology relative to WT mice at all time points [59, 58]. However, a time course evaluation of D2.*mdx* mice reveal qualitative compensation within this strain as well.

At 4 weeks of age, in a similar fashion to *mdx* mice, D2.*mdx* mice exhibit muscle wasting and weakness relative to WT controls. In *mdx* mice, this period of peak degeneration is followed by robust regeneration and compensation that results in a relatively mild dystrophic phenotype until 15 months of age [51]. Based on our findings, D2.*mdx* mice also undergo a period of compensation, albeit less robust and lasting only until 24 weeks at which point the phenotype progressively worsens (Supplemental Figure 7-3). We believe that this compensatory window may help to guide therapeutic timelines in this animal model.

Firstly, work by Chang and colleagues demonstrated that the *mdx* mouse has lengthened telomeres which promote their regenerative capabilities [203]. Patients with DMD are identified as having shortened telomeres which limit the stem cell pool and ultimately inhibit the regeneration of damaged muscle, leading to muscle wasting. Through the shortening of *mdx* telomeres, not only were previously unidentified cellular impairments now evident, a more severe cardiomyopathy was apparent, highlighting the fact that heightened regeneration may be masking dysfunction in rodent models of DMD [203, 204]. This in turn may partially explain why we revealed bioenergetic dysfunctions in the D2.*mdx* mice at 4 weeks of age that were previously unidentified in *mdx* counterparts, but also identifies the need to evaluate therapeutics during periods of disease progression that are not underscored with heightened regeneration. It is possible that our time-point dependent effects of SBT-20 on force production were due to the severity of the disease. At 4 weeks of age, when SBT-20 was effective at improving muscle function, muscle wasting and weakness was also heightened. In contrast, at 12 weeks of age, when SBT-20 had no beneficial effects on muscle function, the animals were in a period of compensation. Future work should extend treatment past the compensatory window into the second phase of severe myopathy. Specifically, evaluating the ability of this compound to extend lifespan would provide great insight into potential clinical benefits, regardless of force production outcomes.

Comparison of methods to measure muscle function in rodent models of DMD

A third point of consideration that was an underlying topic throughout this thesis was the design of protocols to analyze muscle function. We employed both *in vivo* whole-body muscle function tests as well as *in vitro* isolated muscle function tests within Chapters 4,6 and 7 in order to comprehensively evaluate both clinical markers of myopathy as well as muscle specific force production. The findings from these evaluations led to divergent conclusions. All *in vivo* tests at 4-weeks of age showed minimal effect of SBT-20, save for an increase in forelimb grip strength.

We speculate that this may be due to the voluntary nature of these experiments. While SBT-20 is beneficial to dystrophic muscle at a cellular level and improves specific force of individual muscles, this treatment is by no means a cure and it begs to question what impact this drug had on energy levels and perception of strength in these animals. For example, 24 hours of voluntary wheel running involves a 24-hour acclimation period with a locked running wheel followed by 24 hours of recorded running distance. If the animals, despite having improvements at the cellular level, do not feel better overall, they are unlikely to choose to partake in voluntary exercise. On the contrary, when a strip of diaphragm muscle is evaluated *in vitro*, there is no neurological component to this assay, removing this confounding variable that exists in *in vivo* assessments.

Similarly, in addition to the previously discussed compensation that occurs at 12 weeks of age, the neural component of muscle function may also partially explain the lack of effect of SBT-20 in the diaphragm, that was previously evident at 4 weeks of age. Specifically, following 12 weeks of treatment with SBT-20, diaphragm force production was evaluated using an *in vivo* assessment of esophageal pressure transduction. While mice were anesthetized, respiratory drive was still a confounding factor affecting the partial pressures produced in these animals and given that neural drive to breath is believed to be altered in patients with DMD [316, 294], this approach for the assessment of respiratory function may have masked the potential beneficial effects of SBT-20 that would have been elucidated with an *in vitro* model. While *in vivo* measures of function are considered to be more clinically relevant, generalized interpretations about muscle strength should be made with caution given the neural component of these evaluations cannot be controlled for.

Future Directions

In Chapter 5, analysis of mitochondrial bioenergetics was limited to the left ventricle (LV) from heart tissue. Initially, this chamber was selected given that cardiomyopathy usually manifests in

the LV and furthermore, that echocardiographic measures were performed on LV. Through histochemical analysis, a high degree of fibrosis was evident in the right ventricle (RV) at 4 weeks of age, a surprising finding we did not anticipate. Therefore, our conclusions regarding impaired mitochondrial bioenergetics preceding the onset of cardiac dysfunction and remodeling are limited specifically to the LV and it remains possible that evaluation of the RV would have revealed dysfunction and remodelling at this early age. An intriguing possibility for future investigation is to determine whether the well-characterized diaphragm weakness in this disease drives right ventricular failure through decreased pulmonary perfusion, and whether this contributes to a joint RV and LV mechanism for the progression of cardiomyopathy. Furthermore, to fully and comprehensively evaluate cardiac function, invasive hemodynamic measurements would have been required. Considered the gold standard for evaluating cardiac function in heart failure, using invasive hemodynamic techniques would have presented us with both systolic and diastolic functional data as well as right side function allowing for more in-depth conclusions about the development of cardiomyopathy at the time point in question.

Secondly, while we identified the mitochondria as a source of oxidative stress in DMD in Chapters 4 and 5, we did not identify alterations in the overall redox status of the cell when measured through markers of reversible oxidative stress (lipid peroxidation, protein carbonylation). However, the use of these markers do not rule out H_2O_2 acting as a reversible redox signal within the cell, as evidenced by the oxidized status of mtCK presented in Chapter 7. Future work should consider the redox status of ANT, VDAC and mtCK collectively to further understand the mechanistic causes of impaired mitochondrial bioenergetics in DMD.

The collective findings from this thesis also suggest that a cocktail therapy may provide a more potent treatment option for the attenuation of disease progression in DMD. The first, and likely

most viable option, as was discussed in Chapter 7, is a combination therapy with creatine. Creatine supplementation in both animal models and human clinical trials has proven highly beneficial, particularly in the context of improved muscle strength [311, 312]. The use of creatine has been shown to increase muscle mass as well as improve energy metabolism through its effect on creatine dependent energy exchange. This involves decreasing apoptotic and necrotic cell death through creatine's ability to influence the rates ROS production and oxidative phosphorylation within the mitochondria [313]. A key finding from this thesis was the underlying impairment in creatine dependent energy exchange in dystrophic muscle, specifically due to the oxidation of mtCK. Given that the DMD phenotype involves a shift from type II to type I fibres throughout lifespan and that mtCK activity is predominant in oxidative tissue, it stands to believe that the enhancement of creatine sensitivity within dystrophic muscle following SBT-20 would augment the beneficial effects of creatine in DMD. Secondly, SBT-20, aside from its evident benefits in DMD as a stand-alone therapeutic, is also attractive because of its unique mitochondrial-targeting abilities. Unlike the majority of widely used mitochondrial-targeted antioxidants, SBT-20 is not membrane potential dependent [228]. This is an important distinction in diseases of impaired ADP governance, like DMD. Idebenone, a synthetic analog to coenzyme Q_{10}, has provided positive results in clinical trials of DMD, specifically in its ability to improve cardiac and respiratory function [208, 209, 76, 210, 287]. However, there are concerns surrounding idebenone's bioavailability. Conjugating idebenone to SBT-20 would increase the uptake of idebenone by the mitochondria and would conceivably heighten its benefits in dystrophic muscle. Indeed, using SBT-20 as a vehicle to target the mitochondria presents a promising and unexplored avenue for therapy development to date.

8.2 Limitations

Although every effort was made in the design and execution of the studies in this dissertation to control for variables, it must be acknowledged that limitations do exist. Firstly, in Chapter 4, due to tissue limitations, TEM analysis was done in the plantaris as opposed to the Quad muscle. While plantaris and the vastus intermedius (the portion of the Quad used for bioenergetic assays) exhibit similar fibre type compositions [236], given the heterogeneity of disease progression across muscles in DMD, our conclusions about mitochondrial morphology in the Quad must remain speculative given we did not assess this marker in this specific muscle.

In Chapter 6 there are two important limitations to discuss. Firstly, SBT-20 treatment was initiated at 4 days of age and continued for 28 days, taking animals at the age of sacrifice to 32 days at the youngest. While we controlled for age as best as possible, given the size of some litters and the fact that due to tissue viability and technical limitations, only one mouse could be sacrificed each day, animals ranged from 32-36 days at the time of sacrifice. While the groups all had an average age of sacrifice of 34 days, this brings animals closer to five weeks of age than four. Given that compensation occurs within this model sometime between 4 and 8 weeks of age, it is possible that the phenotype of these animals is less severe than animals that are sacrificed at 28 days, the time point used in Chapter 4. Therefore, comparisons between the two studies (Chapter 4 and 6) proved difficult as the underlying effect of compensation was unknown at the second-time point and may explain some divergent findings. In hindsight, a shorter treatment window and subsequent younger age of sacrifice may have decreased variability. However, this may not be feasible given the time requirements for the breadth of measures performed in this study.

In Chapter 7, the *in vivo* SBT-20 study is lacking a WT control group. While our initial study design was more mechanistic in nature with a specific interest in looking at the impact of SBT-20

on mtCK function, a lack of WT control makes it hard to determine the overall efficacy of SBT-20. Indeed, while our comparison to a saline group allows for the determination of SBT-20's efficacy in DMD, we cannot determine the degree to which SBT-20 rescued myopathy in relation to WT. Additionally, a critical finding from this study was the presence of oxidized mtCK in DMD muscle relative to WT. Additional time is required to resolve technical issues with the method (**Supplemental Figure 7.2**) which limit the strength of conclusions at this time. The antibody being used for mtCK immunoprecipitation (IP) is a polyclonal serum based antibody and as such, has non-specific biding that is evident on a standard western blot (Supplemental Figure 7-2A) and becomes particularly evident when the contrast is increased on an image. While a regular IP of mtCK reveals high specificity for mtCK (Supplemental Figure 7-2B and C), the IR Dye appears to be much more sensitive and brings out several non-specific bands (Supplemental Figure 7-2D). Additionally, due to the oxidized state of mtCK in the DMD samples, the contrast must be increased significantly in order to bring out bands in the DMD lanes. This also brightens the WT lane causing an overabundance of bands around 42KDa. While we are comfortable in our conclusion that mtCK is oxidized given the conclusion is identical regardless of the band you quantify, samples will be re-run in the near future to try and decrease the non-specific binging that is evident when using the IR Dye

A final limitation in Chapter 7, which has been touched on briefly through the discussion, is the choice of functional tests used following 12 weeks of treatment with SBT-20. Firstly, skeletal muscle function was evaluated through force production of the hind-limb plantarflexors (soleus and gastrocnemius). Given that SBT-20 provided no therapeutic benefit to the WG at the mitochondrial level, in hindsight it was not surprisingly that treatment elicited no functional benefit on this muscle. Unfortunately, force production assessments are done prior to bioenergetic assays

and as such, the lack of treatment effect in the WG was unknown at the time of measure. Furthermore, echocardiography was our only method of cardiac function and therefore, it remains to be seen if improvements in function would have been revealed through invasive hemodynamics. Based on literature in the D2.*mdx* mouse, cardiomyopathy does not manifest until approximately 28 weeks of age so we did not expect to see functional deficits or subsequent drug-induced improvements at this time. Cardiac muscle was evaluated on a mechanistic level based on its known sensitivity to creatine [286].

8.3 Conclusions

The findings from this thesis highlight the mitochondria as a source of ROS during impaired oxidative phosphorylation in DMD and that mechanistically, mtCK underlies these bioenergetic impairments. Subsequently, impaired mitochondrial bioenergetics do indeed contribute to DMD pathophysiology, an influence that can be attenuated through the use of the mitochondrial-targeted peptide SBT-20, likely through its protection of mtCK from oxidant-induced dysfunction (**Figure 8-1**). Overall, SBT-20 may be a promising therapeutic candidate for the improvement of DMD pathophysiology and should be considered further in both lifespan studies as well as a component in cocktail therapy approaches for the treatment and prevention of DMD myopathy.

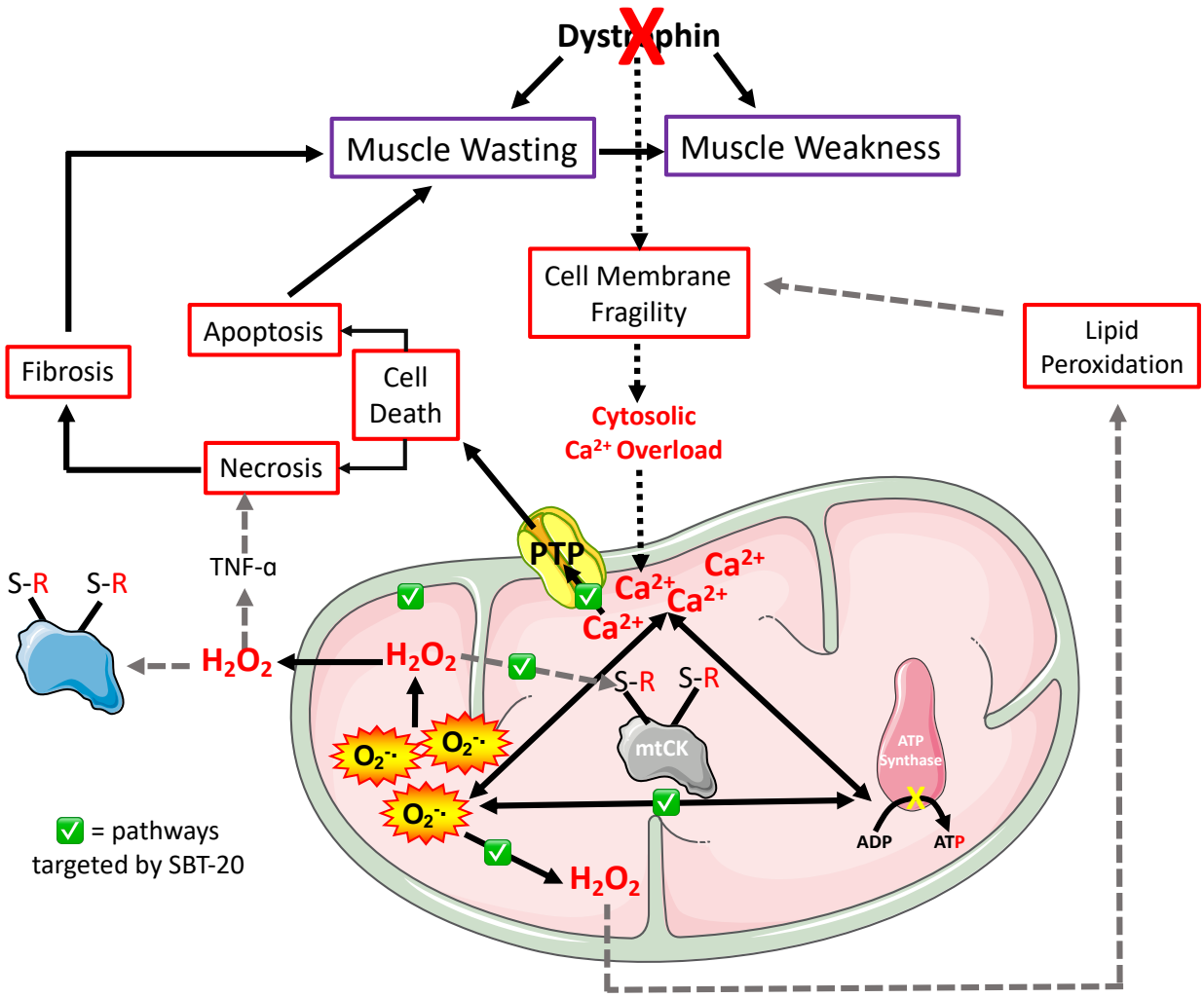

Figure 8-1: Summary of the mechanisms of mitochondrial dysfunction in dystrophic muscle and the role of SBT-20 in attenuating their effect on DMD pathophysiology. A lack of dystrophin results in cell membrane fragility and contraction-induced tearing. This causes an influx of calcium (Ca^{2+}) into the cytosol. The mitochondria uptake this Ca^{2+} causing Ca^{2+} overload within the mitochondria. Mitochondria exhibit impaired oxidative phosphorylation and elevated ROS emission during this impaired oxidative phosphorylation. Elevated Ca^{2+}, impaired ATP production and elevated ROS form a pathological triad within the mitochondria leading to 1. H_2O_2-induced oxidative modifications on mitochondrial proteins (mitochondrial creatine kinase, mtCK) through the oxidation of exposed cysteines (SH→S-→S-R), 2. H_2O_2 leaving the mitochondria and acting as a redox signal (oxidative modifications, S-R and macromolecular damage, lipid peroxidation) 3. Permeability transition pore opening and the activation of mitochondrial-derived cell death pathways. Mitochondrial derived cell death can induce muscle wasting through apoptosis or necrosis and subsequent fibrosis. Muscle wasting causes muscle weakness in dystrophic muscle. Solid black arrows represent pathways directly assessed within this thesis. Dashed black arrows represent well characterized aspects of the DMD phenotype not directly measured in this thesis. Grey dashed arrows represent proposed cellular influences of elevated mitochondrial H_2O_2 emission.

References

1. Hoffman EP, Brown RH, Kunkel LM. Dystrophin: The protein product of the duchenne muscular dystrophy locus. Cell. 1987;51(6):919-28. doi:http://dx.doi.org/10.1016/0092-8674(87)90579-4.

2. Cohn RD, Campbell KP. Molecular basis of muscular dystrophies. Muscle Nerve. 2000;23(10):1456-71.

3. Worton RG, Thompson MW. GENETICS OF DUCHENNE MUSCULAR DYSTROPHY. Annual Review of Genetics. 1988;22(1):601-29. doi:10.1146/annurev.ge.22.120188.003125.

4. Judge DP, Kass DA, Thompson WR, Wagner KR. Pathophysiology and Therapy of Cardiac Dysfunction in Duchenne Muscular Dystrophy. American Journal of Cardiovascular Drugs. 2011;11(5):287-94. doi:10.2165/11594070-000000000-00000.

5. Lofaso F, Orlikowski D, Raphael JC. Ventilatory assistance in patients with Duchenne muscular dystrophy. European Respiratory Journal. 2006;28(3):468.

6. Rando TA. The dystrophin–glycoprotein complex, cellular signaling, and the regulation of cell survival in the muscular dystrophies. Muscle & Nerve. 2001;24(12):1575-94. doi:10.1002/mus.1192.

7. Matthews E, Brassington R, Kuntzer T, Jichi F, Manzur AY. Corticosteroids for the treatment of Duchenne muscular dystrophy. Cochrane Database of Systematic Reviews. 2016(5). doi:10.1002/14651858.CD003725.pub4.

8. Shimizu-Motohashi Y, Komaki H, Motohashi N, Takeda Si, Yokota T, Aoki Y. Restoring Dystrophin Expression in Duchenne Muscular Dystrophy: Current Status of Therapeutic Approaches. Journal of Personalized Medicine. 2019;9(1). doi:10.3390/jpm9010001.

9. Monaco AP, Neve RL, Colletti-Feener C, Bertelson CJ, Kurnit DM, Kunkel LM. Isolation of candidate cDNAs for portions of the Duchenne muscular dystrophy gene. Nature. 1986;323(6089):646-50. doi:10.1038/323646a0.

10. Duncan C. Role of intracellular calcium in promoting muscle damage: A strategy for controlling the dystrophic condition. Experientia. 1978;34(12):1531-5. doi:10.1007/BF02034655.

11. Ohlendieck K. The pathophysiological role of impaired calcium handling in muscular dystrophy. 2006. p. 183-92.

12. Mendell JR, Engel WK, Derrer EC. Duchenne muscular dystrophy: functional ischemia reproduces its characteristic lesions. Science. 1971;172(3988):1143-5.

13. Binder HJ, Herting DC, Hurst V, Finch SC, Spiro HM. Tocopherol deficiency in man. N Engl J Med. 1965;273(24):1289-97. doi:10.1056/NEJM196512092732401.

14. Kar NC, Pearson CM. Catalase, superoxide dismutase, glutathione reductase and thiobarbituric acid-reactive products in normal and dystrophic human muscle. Clinica Chimica Acta. 1979;94(3):277-80. doi:10.1016/0009-8981(79)90076-7.

15. Ragusa RJ, Chow CK, Porter JD. Oxidative stress as a potential pathogenic mechanism in an animal model of Duchenne muscular dystrophy. Neuromuscular Disorders. 1997;7(6-7):379-86. doi:10.1016/S0960-8966(97)00096-5.

16. Disatnik MH, Dhawan J, Yu Y, Beal MF, Whirl MM, Franco AA et al. Evidence of oxidative stress in mdx mouse muscle: studies of the pre-necrotic state. Journal of the neurological sciences. 1998;161(1):77-84.

17. Murphy ME, Kehrer JP. Oxidation state of tissue thiol groups and content of protein carbonyl groups in chickens with inherited muscular dystrophy. Biochemical Journal. 1989;260(2):359-64.

18. Haycock JW, MacNeil S, Jones P, Harris JB, Mantle D. Oxidative damage to muscle protein in Duchenne muscular dystrophy. Neuroreport. 1996;8(1):357-61.

19. Burr IM, Asayama K, Fenichel GM. Superoxide dismutases, Glutathione peroxidase, And catalase in neuromuscular Disease. Muscle & Nerve. 1987;10(2):150-4. doi:10.1002/mus.880100208.

20. Austin L, de Niese M, McGregor A, Arthur H, Gurusinghe A, Gould MK. Potential oxyradical damage and energy status in individual muscle fibres from degenerating muscle diseases. Neuromuscular Disorders. 1992;2(1):27-33. doi:10.1016/0960-8966(92)90023-Y.

21. Dudley RW, Khairallah M, Mohammed S, Lands L, Des Rosiers C, Petrof BJ. Dynamic responses of the glutathione system to acute oxidative stress in dystrophic mouse (mdx) muscles. Am J Physiol Regul Integr Comp Physiol. 2006;291(3):R704-10. doi:10.1152/ajpregu.00031.2006.

22. Cole MA, Rafael JA, Taylor DJ, Lodi R, Davies KE, Styles P. A quantitative study of bioenergetics in skeletal muscle lacking utrophin and dystrophin. Neuromuscular Disorders. 2002;12(3):247-57. doi:http://dx.doi.org/10.1016/S0960-8966(01)00278-4.

23. Percival JM, Siegel MP, Knowels G, Marcinek DJ. Defects in mitochondrial localization and ATP synthesis in the mdx mouse model of Duchenne muscular dystrophy are not alleviated by PDE5 inhibition. Human Molecular Genetics. 2013;22(1):153-67.

24. Shuttlewood RJ, Griffiths JR. The Purine Nucleotide Profile in Mouse, Chicken and Human Dystrophic Muscle: An Abnormal Ratio of Inosine plus Adenine Nucleotides to Guanine Nucleotides. Clinical Science. 1982;62(1):113.

25. Scarpa A, Azzone GF. The Mechanism of Ion Translocation in Mitochondria. European Journal of Biochemistry. 1970;12(2):328-35. doi:10.1111/j.1432-1033.1970.tb00854.x.

26. Zulian A, Schiavone M, Giorgio V, Bernardi P. Forty years later: Mitochondria as therapeutic targets in muscle diseases. Pharmacological Research. 2016;113:563-73. doi:https://doi.org/10.1016/j.phrs.2016.09.043.

27. Nikoletopoulou V, Markaki M, Palikaras K, Tavernarakis N. Crosstalk between apoptosis, necrosis and autophagy. Biochimica et Biophysica Acta (BBA) - Molecular Cell Research. 2013;1833(12):3448-59. doi:https://doi.org/10.1016/j.bbamcr.2013.06.001.

28. Bhattacharya SK, Johnson PL, Thakar JH. Reversal of impaired oxidative phosphorylation and calcium overloading in the in vitro cardiac mitochondria of CHF-146 dystrophic hamsters with hereditary muscular dystrophy. Journal of the neurological sciences. 1993;120(2):180-6. doi:10.1016/0022-510X(93)90271-Y.

29. Sperl W, Skladal D, Gnaiger E, Wyss M, Mayr U, Hager J et al. High resolution respirometry of permeabilized skeletal muscle fibers in the diagnosis of neuromuscular disorders. Mol Cell Biochem. 1997;174(1-2):71-8.

30. Kuznetsov AV, Winkler K, Wiedemann F, von Bossanyi P, Dietzmann K, Kunz WS. Impaired mitochondrial oxidative phosphorylation in skeletal muscle of the dystrophin-deficient mdx mouse. Mol Cell Biochem. 1998;183(1):87-96. doi:10.1023/A:1006868130002.

31. Onopiuk M, Brutkowski W, Wierzbicka K, Wojciechowska S, Szczepanowska J, Fronk J et al. Mutation in dystrophin-encoding gene affects energy metabolism in mouse myoblasts. Biochemical and Biophysical Research Communications. 2009;386(3):463-6. doi:https://doi.org/10.1016/j.bbrc.2009.06.053.

32. Burelle Y, Khairallah M, Ascah A, Allen BG, Deschepper CF, Petrof BJ et al. Alterations in mitochondrial function as a harbinger of cardiomyopathy: lessons from the dystrophic heart. J Mol Cell Cardiol. 2010;48(2):310-21. doi:10.1016/j.yjmcc.2009.09.004.

33. Godin R, Daussin F, Matecki S, Li T, Petrof BJ, Burelle Y. Peroxisome proliferator-activated receptor γ coactivator 1-α gene transfer restores mitochondrial biomass and improves mitochondrial calcium handling in post-necrotic mdx mouse skeletal muscle. The Journal of Physiology. 2012;590(Pt 21):5487-502. doi:10.1113/jphysiol.2012.240390.

34. Rybalka E, Timpani CA, Cooke MB, Williams AD, Hayes A. Defects in Mitochondrial ATP Synthesis in Dystrophin-Deficient Mdx Skeletal Muscles May Be Caused by Complex I Insufficiency. PLoS ONE. 2014;9(12):e115763. doi:10.1371/journal.pone.0115763.

35. Pauly M, Daussin F, Burelle Y, Li T, Godin R, Fauconnier J et al. AMPK activation stimulates autophagy and ameliorates muscular dystrophy in the mdx mouse diaphragm. Am J Pathol. 2012;181(2):583-92. doi:10.1016/j.ajpath.2012.04.004.

36. Millay DP, Sargent MA, Osinska H, Baines CP, Barton ER, Vuagniaux G et al. Genetic and pharmacologic inhibition of mitochondrial-dependent necrosis attenuates muscular dystrophy. Nat Med. 2008;14(4):442-7. doi:http://www.nature.com/nm/journal/v14/n4/suppinfo/nm1736_S1.html.

37. Nigro G, Comi LI, Limongelli FM, Giugliano MAM, Politano L, Petretta V et al. Prospective study of X-linked progressive muscular dystrophy in campania. Muscle & Nerve. 1983;6(4):253-62. doi:10.1002/mus.880060403.

38. Tuffery-Giraud S, Béroud C, Leturcq F, Yaou RB, Hamroun D, Michel-Calemard L et al. Genotype–phenotype analysis in 2,405 patients with a dystrophinopathy using the UMD–DMD database: a model of nationwide knowledgebase. Human Mutation. 2009;30(6):934-45. doi:10.1002/humu.20976.

39. Ahn AH, Kunkel LM. The structural and functional diversity of dystrophin. Nature Genetics. 1993;3(4):283-91. doi:10.1038/ng0493-283.

40. Takeshima Y, Yagi M, Okizuka Y, Awano H, Zhang Z, Yamauchi Y et al. Mutation spectrum of the dystrophin gene in 442 Duchenne/Becker muscular dystrophy cases from one Japanese referral center. Journal Of Human Genetics. 2010;55:379. doi:10.1038/jhg.2010.49.

41. Mah JK, Selby K, Campbell C, Nadeau A, Tarnopolsky M, McCormick A et al. A Population-Based Study of Dystrophin Mutations in Canada. Canadian Journal of Neurological Sciences / Journal Canadien des Sciences Neurologiques. 2014;38(3):465-74. doi:10.1017/S0317167100011896.

42. Okubo M, Minami N, Goto K, Goto Y, Noguchi S, Mitsuhashi S et al. Genetic diagnosis of Duchenne/Becker muscular dystrophy using next-generation sequencing: validation analysis of DMD mutations. Journal Of Human Genetics. 2016;61:483. doi:10.1038/jhg.2016.7 https://www.nature.com/articles/jhg20167 - supplementary-information.

43. Nigro G, Comi LI, Politano L, Bain RJI. The incidence and evolution of cardiomyopathy in Duchenne muscular dystrophy. International Journal of Cardiology. 1990;26(3):271-7. doi:https://doi.org/10.1016/0167-5273(90)90082-G.

44. Boland BJ, Silbert PL, Groover RV, Wollan PC, Silverstein MD. Skeletal, cardiac, and smooth muscle failure in Duchenne muscular dystrophy. Pediatric Neurology. 1996;14(1):7-12. doi:https://doi.org/10.1016/0887-8994(95)00251-0.

45. Emery AE. Duchenne muscular dystrophy--Meryon's disease. Neuromuscul Disord. 1993;3(4):263-6.

46. Guiraud S, Davies KE. Pharmacological advances for treatment in Duchenne muscular dystrophy. Current Opinion in Pharmacology. 2017;34:36-48. doi:https://doi.org/10.1016/j.coph.2017.04.002.

47. Aartsma-Rus A, Straub V, Hemmings R, Haas M, Schlosser-Weber G, Stoyanova-Beninska V et al. Development of Exon Skipping Therapies for Duchenne Muscular Dystrophy: A Critical Review and a Perspective on the Outstanding Issues. Nucleic acid therapeutics. 2017;27(5):251-9. doi:10.1089/nat.2017.0682.

48. McDonald CM, Henricson EK, Abresch RT, Duong T, Joyce NC, Hu F et al. Long-term effects of glucocorticoids on function, quality of life, and survival in patients with Duchenne

muscular dystrophy: a prospective cohort study. The Lancet. 2018;391(10119):451-61. doi:https://doi.org/10.1016/S0140-6736(17)32160-8.

49. Mendell JR, Moxley RT, Griggs RC, Brooke MH, Fenichel GM, Miller JP et al. Randomized, Double-Blind Six-Month Trial of Prednisone in Duchenne's Muscular Dystrophy. New England Journal of Medicine. 1989;320(24):1592-7. doi:10.1056/NEJM198906153202405.

50. Griggs RC, Herr BE, Reha A, Elfring G, Atkinson L, Cwik V et al. Corticosteroids in Duchenne muscular dystrophy: Major variations in practice. Muscle & Nerve. 2013;48(1):27-31. doi:10.1002/mus.23831.

51. Bulfield G, Siller WG, Wight PA, Moore KJ. X chromosome-linked muscular dystrophy (mdx) in the mouse. Proceedings of the National Academy of Sciences of the United States of America. 1984;81(4):1189-92.

52. McGreevy JW, Hakim CH, McIntosh MA, Duan D. Animal models of Duchenne muscular dystrophy: from basic mechanisms to gene therapy. Disease Models & Mechanisms. 2015;8(3):195-213. doi:10.1242/dmm.018424.

53. Stedman HH, Sweeney HL, Shrager JB, Maguire HC, Panettieri RA, Petrof B et al. The mdx mouse diaphragm reproduces the degenerative changes of Duchenne muscular dystrophy. Nature. 1991;352(6335):536-9. doi:10.1038/352536a0.

54. Deconinck N, Dan B. Pathophysiology of Duchenne Muscular Dystrophy: Current Hypotheses. Pediatric Neurology. 2007;36(1):1-7. doi:https://doi.org/10.1016/j.pediatrneurol.2006.09.016.

55. Straub V, Rafael JA, Chamberlain JS, Campbell KP. Animal Models for Muscular Dystrophy Show Different Patterns of Sarcolemmal Disruption. The Journal of Cell Biology. 1997;139(2):375-85.

56. Matsumura K, Ervasti JM, Ohlendieck K, Kahl SD, Campbell KP. Association of dystrophin-related protein with dystrophin-associated proteins in mdx mouse muscle. Nature. 1992;360(6404):588-91. doi:10.1038/360588a0.

57. Willmann R, Possekel S, Dubach-Powell J, Meier T, Ruegg MA. Mammalian animal models for Duchenne muscular dystrophy. Neuromuscular Disorders. 2009;19(4):241-9. doi:https://doi.org/10.1016/j.nmd.2008.11.015.

58. Roblin D, Kay DE. The potential of utrophin modulators for the treatment of Duchenne muscular dystrophy AU - Guiraud, Simon. Expert Opinion on Orphan Drugs. 2018;6(3):179-92. doi:10.1080/21678707.2018.1438261.

59. Coley WD, Bogdanik L, Vila MC, Yu Q, Van Der Meulen JH, Rayavarapu S et al. Effect of genetic background on the dystrophic phenotype in mdx mice. Hum Mol Genet. 2016;25(1):130-45. doi:10.1093/hmg/ddv460.

60. Fukada S-i, Morikawa D, Yamamoto Y, Yoshida T, Sumie N, Yamaguchi M et al. Genetic Background Affects Properties of Satellite Cells and mdx Phenotypes. The American Journal of Pathology. 2010;176(5):2414-24. doi:10.2353/ajpath.2010.090887.

61. Valentine BA, Cooper BJ, de Lahunta A, O'Quinn R, Blue JT. Canine X-linked muscular dystrophy: An animal model of Duchenne muscular dystrophy: Clinical studies. Journal of the neurological sciences. 1988;88(1):69-81. doi:https://doi.org/10.1016/0022-510X(88)90206-7.

62. Yucel N, Chang AC, Day JW, Rosenthal N, Blau HM. Humanizing the mdx mouse model of DMD: the long and the short of it. npj Regenerative Medicine. 2018;3(1):4. doi:10.1038/s41536-018-0045-4.

63. Webster C, Silberstein L, Hays AP, Blau HM. Fast muscle fibers are preferentially affected in Duchenne muscular dystrophy. Cell. 1988;52(4):503-13. doi:https://doi.org/10.1016/0092-8674(88)90463-1.

64. Minetti C, Ricci E Fau - Bonilla E, Bonilla E. Progressive depletion of fast alpha-actinin-positive muscle fibers in Duchenne muscular dystrophy. Neurology. 1991(0028-3878 (Print)).

65. Kaminski HJ, Al-Hakim M, Leigh RJ, Bashar MK, Ruff RL. Extraocular muscles are spared in advanced duchenne dystrophy. Annals of Neurology. 1992;32(4):586-8. doi:10.1002/ana.410320418.

66. Karpati G, Carpenter S, Prescott S. Small-caliber skeletal muscle fibers do not suffer necrosis in mdx mouse dystrophy. Muscle & Nerve. 1988;11(8):795-803. doi:10.1002/mus.880110802.

67. Cros D, Harnden P, Pellissier JF, Serratrice G. Muscle hypertrophy in Duchenne muscular dystrophy. Journal of Neurology. 1989;236(1):43-7. doi:10.1007/BF00314217.

68. Bernat JL, Ochoa JL. Muscle hypertrophy after partial denervation: a human case. Journal of Neurology, Neurosurgery & Psychiatry. 1978;41(8):719. doi:10.1136/jnnp.41.8.719.

69. Smith PEM, Calverley PMA, Edwards RHT, Evans GA, Campbell EJM. Practical Problems in the Respiratory Care of Patients with Muscular Dystrophy. New England Journal of Medicine. 1987;316(19):1197-205. doi:10.1056/NEJM198705073161906.

70. LoMauro A, D'Angelo MG, Aliverti A. Assessment and management of respiratory function in patients with Duchenne muscular dystrophy: current and emerging options. Therapeutics and Clinical Risk Management. 2015;11:1475-88. doi:10.2147/TCRM.S55889.

71. Eagle M, Baudouin SV, Chandler C, Giddings DR, Bullock R, Bushby K. Survival in Duchenne muscular dystrophy: improvements in life expectancy since 1967 and the impact of home nocturnal ventilation. Neuromuscular Disorders. 2002;12(10):926-9. doi:https://doi.org/10.1016/S0960-8966(02)00140-2.

72. Mayer OH, Finkel RS, Rummey C, Benton MJ, Glanzman AM, Flickinger J et al. Characterization of pulmonary function in Duchenne Muscular Dystrophy. Pediatric Pulmonology. 2015;50(5):487-94. doi:10.1002/ppul.23172.

73. Roberto R, Fritz A Fau - Hagar Y, Hagar Y Fau - Boice B, Boice B Fau - Skalsky A, Skalsky A Fau - Hwang H, Hwang H Fau - Beckett L et al. The natural history of cardiac and pulmonary function decline in patients with duchenne muscular dystrophy. Spine. 2011(1528-1159 (Electronic)).

74. Machado DL, Silva EC, Resende MBD, Carvalho CRF, Zanoteli E, Reed UC. Lung function monitoring in patients with duchenne muscular dystrophy on steroid therapy. BMC Research Notes. 2012;5(1):435. doi:10.1186/1756-0500-5-435.

75. Biggar WD, Harris VA, Eliasoph L, Alman B. Long-term benefits of deflazacort treatment for boys with Duchenne muscular dystrophy in their second decade. Neuromuscular Disorders. 2006;16(4):249-55. doi:https://doi.org/10.1016/j.nmd.2006.01.010.

76. Buyse GM, Goemans N, van den Hauwe M, Meier T. Effects of glucocorticoids and idebenone on respiratory function in patients with duchenne muscular dystrophy. Pediatr Pulmonol. 2013;48(9):912-20. doi:10.1002/ppul.22688.

77. Verhaert D, Richards K, Rafael-Fortney JA, Raman SV. Cardiac Involvement in Patients With Muscular Dystrophies. Circulation: Cardiovascular Imaging. 2011;4(1):67.

78. D'Amario D, Amodeo A, Adorisio R, Tiziano FD, Leone AM, Perri G et al. A current approach to heart failure in Duchenne muscular dystrophy. Heart. 2017;103(22):1770. doi:10.1136/heartjnl-2017-311269.

79. Alderton JM, Steinhardt RA. How Calcium Influx through Calcium Leak Channels Is Responsible for the Elevated Levels of Calcium-dependent Proteolysis in Dystrophic Myotubes. Trends in Cardiovascular Medicine. 2000;10(6):268-72. doi:https://doi.org/10.1016/S1050-1738(00)00075-X.

80. Turner PR, Fong PY, Denetclaw WF, Steinhardt RA. Increased calcium influx in dystrophic muscle. The Journal of cell biology. 1991;115(6):1701-12.

81. MacLennan PA, McArdle A, Edwards RH. Effects of calcium on protein turnover of incubated muscles from mdx mice. American Journal of Physiology-Endocrinology and Metabolism. 1991;260(4):E594-E8. doi:10.1152/ajpendo.1991.260.4.E594.

82. Whitehead NP, Yeung EW, Allen DG. Muscle damage in mdx (dystrophic) mice: role of calcium and reactive oxygen species. Clin Exp Pharmacol Physiol. 2006;33(7):657-62. doi:10.1111/j.1440-1681.2006.04394.x.

83. Ruegg UT, Nicolas-Métral V, Challet C, Bernard-Hélary K, Dorchies OM, Wagner S et al. Pharmacological control of cellular calcium handling in dystrophic skeletal muscle. Neuromuscular Disorders. 2002;12:S155-S61. doi:https://doi.org/10.1016/S0960-8966(02)00095-0.

84. Divet A, Huchet-Cadiou C. Sarcoplasmic reticulum function in slow- and fast-twitch skeletal muscles from mdx mice. Pflügers Archiv. 2002;444(5):634-43. doi:10.1007/s00424-002-0854-5.

85. Divet A, Lompré AM, Huchet-Cadiou C. Effect of cyclopiazonic acid, an inhibitor of the sarcoplasmic reticulum Ca-ATPase, on skeletal muscles from normal and mdx mice. Acta Physiologica Scandinavica. 2005;184(3):173-86. doi:10.1111/j.1365-201X.2005.01450.x.

86. Kargacin ME, Kargacin GJ. The sarcoplasmic reticulum calcium pump is functionally altered in dystrophic muscle. Biochimica et Biophysica Acta (BBA) - General Subjects. 1996;1290(1):4-8. doi:https://doi.org/10.1016/0304-4165(95)00180-8.

87. Periasamy M, Kalyanasundaram A. SERCA pump isoforms: Their role in calcium transport and disease. Muscle & Nerve. 2007;35(4):430-42. doi:10.1002/mus.20745.

88. Schneider JS, Shanmugam M, Gonzalez JP, Lopez H, Gordan R, Fraidenraich D et al. Increased sarcolipin expression and decreased sarco(endo)plasmic reticulum Ca2+ uptake in skeletal muscles of mouse models of Duchenne muscular dystrophy. J Muscle Res Cell Motil. 2013;34(5-6):349-56. doi:10.1007/s10974-013-9350-0.

89. Culligan K, Ohlendieck K. Diversity of the Brain Dystrophin-Glycoprotein Complex. Journal of Biomedicine and Biotechnology. 2002;2(1). doi:10.1155/s1110724302000347.

90. Voit A, Patel V, Pachon R, Shah V, Bakhutma M, Kohlbrenner E et al. Reducing sarcolipin expression mitigates Duchenne muscular dystrophy and associated cardiomyopathy in mice. Nat Commun. 2017;8(1):1068. doi:10.1038/s41467-017-01146-7.

91. Morine KJ, Sleeper MM, Barton ER, Sweeney HL. Overexpression of SERCA1a in the mdx Diaphragm Reduces Susceptibility to Contraction-Induced Damage. Human Gene Therapy. 2010;21(12):1735-9. doi:10.1089/hum.2010.077.

92. Goonasekera SA, Lam CK, Millay DP, Sargent MA, Hajjar RJ, Kranias EG et al. Mitigation of muscular dystrophy in mice by SERCA overexpression in skeletal muscle. The Journal of Clinical Investigation. 2011;121(3):1044-52. doi:10.1172/JCI43844.

93. Allen DG, Whitehead NP, Froehner SC. Absence of Dystrophin Disrupts Skeletal Muscle Signaling: Roles of Ca2+, Reactive Oxygen Species, and Nitric Oxide in the Development of Muscular Dystrophy. Physiol Rev. 2016;96(1):253-305. doi:10.1152/physrev.00007.2015.

94. Görlach A, Bertram K, Hudecova S, Krizanova O. Calcium and ROS: A mutual interplay. Redox Biology. 2015;6:260-71. doi:https://doi.org/10.1016/j.redox.2015.08.010.

95. Jones DP. Radical-free biology of oxidative stress. American journal of physiology Cell physiology. 2008;295(4):C849-C68. doi:10.1152/ajpcell.00283.2008.

96. Rando TA. Oxidative stress and the pathogenesis of muscular dystrophies. Am J Phys Med Rehabil. 2002;81(11 Suppl):S175-86. doi:10.1097/01.PHM.0000029774.56528.A6.

97. Powers SK, Ji LL, Kavazis AN, Jackson MJ. Reactive oxygen species: impact on skeletal muscle. Comprehensive Physiology. 2011;1(2):941-69. doi:10.1002/cphy.c100054.

98. Hurd TR, Murphy MP. Biological Systems Relevant for Redox Signaling and Control. In: Jacob C, Winyard PG, editors. Redox Signaling and Regulation in Biology and Medicine: Wiley-VCH Verlag GmbH & Co. KGaA; 2009. p. 13-43.

99. Grosso S, Perrone S, Longini M, Bruno C, Minetti C, Gazzolo D et al. Isoprostanes in dystrophinopathy: Evidence of increased oxidative stress. Brain Dev. 2008;30(6):391-5. doi:10.1016/j.braindev.2007.11.005.

100. Rando TA, Disatnik MH, Yu Y, Franco A. Muscle cells from mdx mice have an increased susceptibility to oxidative stress. Neuromuscul Disord. 1998;8(1):14-21.

101. Ragusa RJ, Chow CK, St Clair DK, Porter JD. Extraocular, limb and diaphragm muscle group-specific antioxidant enzyme activity patterns in control and mdx mice. Journal of the neurological sciences. 1996;139(2):180-6.

102. Chou T, Hill EJ, Bartle E, Woolley K, LeQuire V, Olson W et al. Beneficial effects of penicillamine treatment on hereditary avian muscular dystrophy. The Journal of Clinical Investigation. 1975;56(4):842-9. doi:10.1172/JCI108163.

103. Serafin WE, Dement SH, Brandon S, Hill EJ, Park CR, Park JH. Interactions of vitamin E and penicillamine in the treatment of hereditary avian muscular dystrophy. Muscle & Nerve. 1987;10(8):685-97. doi:10.1002/mus.880100804.

104. Bornman L, Rossouw H, Gericke GS, Polla BS. Effects of iron deprivation on the pathology and stress protein expression in murine X-linked muscular dystrophy. Biochemical Pharmacology. 1998;56(6):751-7. doi:https://doi.org/10.1016/S0006-2952(98)00055-0.

105. Mâncio RD, Hermes TdA, Macedo AB, Mizobuti DS, Rupcic IF, Minatel E. Dystrophic phenotype improvement in the diaphragm muscle of mdx mice by diacerhein. PLOS ONE. 2017;12(8):e0182449. doi:10.1371/journal.pone.0182449.

106. Mâncio RD, Hermes TdA, Macedo AB, Mizobuti DS, Valduga AH, Rupcic IF et al. Vitamin E treatment decreases muscle injury in mdx mice. Nutrition. 2017;43-44:39-46. doi:https://doi.org/10.1016/j.nut.2017.07.003.

107. Messina S, Altavilla D, Aguennouz M, Seminara P, Minutoli L, Monici MC et al. Lipid peroxidation inhibition blunts nuclear factor-kappaB activation, reduces skeletal muscle degeneration, and enhances muscle function in mdx mice. Am J Pathol. 2006;168(3):918-26.

108. Nakae Y, Hirasaka K, Goto J, Nikawa T, Shono M, Yoshida M et al. Subcutaneous injection, from birth, of epigallocatechin-3-gallate, a component of green tea, limits the onset of muscular dystrophy in mdx mice: a quantitative histological, immunohistochemical and electrophysiological study. Histochemistry and Cell Biology. 2008;129(4):489-501. doi:10.1007/s00418-008-0390-2.

109. Dorchies OM, Wagner S, Vuadens O, Waldhauser K, Buetler TM, Kucera P et al. Green tea extract and its major polyphenol (−)-epigallocatechin gallate improve muscle function in a

mouse model for Duchenne muscular dystrophy. American Journal of Physiology-Cell Physiology. 2006;290(2):C616-C25. doi:10.1152/ajpcell.00425.2005.

110. Hnia K, Gayraud J, Hugon G, Ramonatxo M, De La Porte S, Matecki S et al. l-Arginine Decreases Inflammation and Modulates the Nuclear Factor-κB/Matrix Metalloproteinase Cascade in Mdx Muscle Fibers. The American Journal of Pathology. 2008;172(6):1509-19. doi:https://doi.org/10.2353/ajpath.2008.071009.

111. Whitehead NP, Pham C, Gervasio OL, Allen DG. N-Acetylcysteine ameliorates skeletal muscle pathophysiology in mdx mice. J Physiol. 2008;586(7):2003-14. doi:10.1113/jphysiol.2007.148338.

112. Williams IA, Allen DG. The role of reactive oxygen species in the hearts of dystrophin-deficient mdx mice. Am J Physiol Heart Circ Physiol. 2007;293(3):H1969-77. doi:10.1152/ajpheart.00489.2007.

113. Terrill JR, Radley-Crabb HG, Grounds MD, Arthur PG. N-Acetylcysteine treatment of dystrophic mdx mice results in protein thiol modifications and inhibition of exercise induced myofibre necrosis. Neuromuscular Disorders. 2012;22(5):427-34. doi:10.1016/j.nmd.2011.11.007.

114. de Senzi Moraes Pinto R, Ferretti R, Moraes LHR, Neto HS, Marques MJ, Minatel E. N-Acetylcysteine treatment reduces TNF-alpha levels and myonecrosis in diaphragm muscle of mdx mice. Clinical Nutrition. 2013;32(3):472-5. doi:10.1016/j.clnu.2012.06.001.

115. Pinniger GJ, Terrill JR, Assan EB, Grounds MD, Arthur PG. Pre-clinical evaluation of N-acetylcysteine reveals side effects in the mdx mouse model of Duchenne muscular dystrophy. The Journal of Physiology. 2017;595(23):7093-107. doi:10.1113/JP274229.

116. Stern LZ, Ringel SP, Ziter FA, Menander-Huber KB, Ionasescu V, Pellegrino RJ et al. Drug Trial of Superoxide Dismutase in Duchenne's Muscular Dystrophy. Archives of Neurology. 1982;39(6):342-6. doi:10.1001/archneur.1982.00510180020004.

117. Roelofs RI, de Arango GS, Law PK, Kinsman D, Buchanan DC, Park JH. Treatment of Duchenne's Muscular Dystrophy With Penicillamine: Results of a Double-Blind Trial. Archives of Neurology. 1979;36(5):266-8. doi:10.1001/archneur.1979.00500410044005.

118. Bäckman E, Nylander E, Johansson I, Henriksson KG, Tagesson C. Selenium and vitamin E treatment of Duchenne muscular dystrophy: no effect on muscle function. Acta Neurologica Scandinavica. 1988;78(5):429-35. doi:10.1111/j.1600-0404.1988.tb03681.x.

119. Fenichel GM, Brooke MH, Griggs RC, Mendell JR, Miller JP, Moxley Iii RT et al. Clinical investigation in Duchenne muscular dystrophy: Penicillamine and vitamin E. Muscle & Nerve. 1988;11(11):1164-8. doi:10.1002/mus.880111110.

120. Walton Jn Fau - Nattrass FJ, Nattrass FJ. On the classification, natural history and treatment of the myopathies. Brain and Behavior. 1954(0006-8950 (Print)). doi:D - CLML: 5527:1656:300 OTO - NLM.

121. Whitehead NP, Yeung EW, Froehner SC, Allen DG. Skeletal muscle NADPH oxidase is increased and triggers stretch-induced damage in the mdx mouse. PloS one. 2010;5(12):e15354-e. doi:10.1371/journal.pone.0015354.

122. Kim JH, Kwak HB, Thompson LV, Lawler JM. Contribution of oxidative stress to pathology in diaphragm and limb muscles with Duchenne muscular dystrophy. J Muscle Res Cell Motil. 2013;34(1):1-13. doi:10.1007/s10974-012-9330-9.

123. Tonon E, Ferretti R, Shiratori JH, Santo Neto H, Marques MJ, Minatel E. Ascorbic acid protects the diaphragm muscle against myonecrosis in mdx mice. Nutrition. 2012;28(6):686-90. doi:https://doi.org/10.1016/j.nut.2011.09.013.

124. Gervásio OL, Whitehead NP, Yeung EW, Phillips WD, Allen DG. TRPC1 binds to caveolin-3 and is regulated by Src kinase – role in Duchenne muscular dystrophy. Journal of Cell Science. 2008;121(13):2246. doi:10.1242/jcs.032003.

125. Shkryl VM, Martins AS, Ullrich ND, Nowycky MC, Niggli E, Shirokova N. Reciprocal amplification of ROS and Ca(2+) signals in stressed mdx dystrophic skeletal muscle fibers. Pflugers Archiv : European journal of physiology. 2009;458(5):915-28. doi:10.1007/s00424-009-0670-2.

126. Javesghani D, Magder SA, Barreiro E, Quinn MT, Hussain SNA. Molecular Characterization of a Superoxide-Generating NAD(P)H Oxidase in the Ventilatory Muscles. American Journal of Respiratory and Critical Care Medicine. 2002;165(3):412-8. doi:10.1164/ajrccm.165.3.2103028.

127. Spurney CF, Knoblach S, Pistilli EE, Nagaraju K, Martin GR, Hoffman EP. Dystrophin-deficient cardiomyopathy in mouse: Expression of Nox4 and Lox are associated with fibrosis and altered functional parameters in the heart. Neuromuscular Disorders. 2008;18(5):371-81. doi:10.1016/j.nmd.2008.03.008.

128. Tseng BS, Zhao P, Pattison JS, Gordon SE, Granchelli JA, Madsen RW et al. Regenerated mdx mouse skeletal muscle shows differential mRNA expression. Journal of Applied Physiology. 2002;93(2):537-45. doi:10.1152/japplphysiol.00202.2002.

129. Jung C, Martins AS, Niggli E, Shirokova N. Dystrophic cardiomyopathy: amplification of cellular damage by Ca2+ signalling and reactive oxygen species-generating pathways. Cardiovascular Research. 2008;77(4):766-73. doi:10.1093/cvr/cvm089.

130. Khairallah RJ, Shi G, Sbrana F, Prosser BL, Borroto C, Mazaitis MJ et al. Microtubules Underlie Dysfunction in Duchenne Muscular Dystrophy. Science signaling. 2012;5(236):10.1126/scisignal.2002829. doi:10.1126/scisignal.2002829.

131. Spencer MJ, Tidball JG. Do immune cells promote the pathology of dystrophin-deficient myopathies? Neuromuscular Disorders. 2001;11(6):556-64. doi:https://doi.org/10.1016/S0960-8966(01)00198-5.

132. Spencer MJ, Walsh CM, Dorshkind KA, Rodriguez EM, Tidball JG. Myonuclear apoptosis in dystrophic mdx muscle occurs by perforin-mediated cytotoxicity. The Journal of clinical investigation. 1997;99(11):2745-51. doi:10.1172/JCI119464.

133. Morrison J, Lu QL, Pastoret C, Partridge T, Bou-Gharios G. T-Cell-Dependent Fibrosis in the mdx Dystrophic Mouse. Laboratory Investigation. 2000;80:881. doi:10.1038/labinvest.3780092.

134. Wehling-Henricks M, Sokolow S, Tidball JG, Villalta SA, Lee JJ, Myung KH. Major basic protein-1 promotes fibrosis of dystrophic muscle and attenuates the cellular immune response in muscular dystrophy. Human Molecular Genetics. 2008;17(15):2280-92. doi:10.1093/hmg/ddn129.

135. Spencer MJ, Montecino-Rodriguez E, Dorshkind K, Tidball JG. Helper (CD4+) and Cytotoxic (CD8+) T Cells Promote the Pathology of Dystrophin-Deficient Muscle. Clinical Immunology. 2001;98(2):235-43. doi:https://doi.org/10.1006/clim.2000.4966.

136. Mann DL. The emerging role of innate immunity in the heart and vascular system: for whom the cell tolls. Circ Res. 2011;108(9):1133-45. doi:10.1161/CIRCRESAHA.110.226936.

137. Kumar A, Boriek AM. Mechanical stress activates the nuclear factor-kappaB pathway in skeletal muscle fibers: a possible role in Duchenne muscular dystrophy. The FASEB Journal. 2003;17(3):386-96. doi:10.1096/fj.02-0542com.

138. Acharyya S, Villalta SA, Bakkar N, Bupha-Intr T, Janssen PML, Carathers M et al. Interplay of IKK/NF-κB signaling in macrophages and myofibers promotes muscle degeneration in Duchenne muscular dystrophy. The Journal of Clinical Investigation. 2007;117(4):889-901. doi:10.1172/JCI30556.

139. Carlson CG, Samadi A, Siegel A. Chronic treatment with agents that stabilize cytosolic IκB-α enhances survival and improves resting membrane potential in MDX muscle fibers subjected to chronic passive stretch. Neurobiology of Disease. 2005;20(3):719-30. doi:https://doi.org/10.1016/j.nbd.2005.05.003.

140. Reid MB, Li YP. Cytokines and oxidative signalling in skeletal muscle. Acta Physiologica Scandinavica. 2001;171(3):225-32. doi:10.1046/j.1365-201x.2001.00824.x.

141. Grounds MD, Torrisi JO. Anti-TNFα (Remicade®) therapy protects dystrophic skeletal muscle from necrosis. The FASEB Journal. 2004;18(6):676-82. doi:10.1096/fj.03-1024com.

142. Nicholls DG, Ferguson SJ. 5 - Respiratory chains. In: Ferguson DGNJ, editor. Bioenergetics (Third Edition). London: Academic Press; 2003. p. 89-XIII.

143. Mitchell P. Coupling of Phosphorylation to Electron and Hydrogen Transfer by a Chemi-Osmotic type of Mechanism. Nature. 1961;191(4784):144-8.

144. Nicholls DG, Ferguson SJ. 4 - The chemiosmotic proton circuit. In: Ferguson DGNJ, editor. Bioenergetics (Third Edition). London: Academic Press; 2003. p. 57-88.

145. Wallimann T, Wyss M, Brdiczka D, Nicolay K, Eppenberger HM. Intracellular compartmentation, structure and function of creatine kinase isoenzymes in tissues with high and fluctuating energy demands: the 'phosphocreatine circuit' for cellular energy homeostasis. Biochemical Journal. 1992;281(Pt 1):21-40.

146. Aliev M, Guzun R, Karu-Varikmaa M, Kaambre T, Wallimann T, Saks V. Molecular System Bioenergics of the Heart: Experimental Studies of Metabolic Compartmentation and Energy Fluxes versus Computer Modeling. International Journal of Molecular Sciences. 2011;12(12):9296-331. doi:10.3390/ijms12129296.

147. Wallimann T, Tokarska-Schlattner M, Schlattner U. The creatine kinase system and pleiotropic effects of creatine. Amino Acids. 2011;40(5):1271-96. doi:10.1007/s00726-011-0877-3.

148. Ventura-Clapier R, Kuznetsov A, Veksler V, Boehm E, Anflous K. Functional coupling of creatine kinases in muscles: Species and tissue specificity. Mol Cell Biochem.184(1-2):231-47.

149. Saks VA, Khuchua ZA, Vasilyeva EV, Belikova OY, Kuznetsov AV. Metabolic compartmentation and substrate channelling in muscle cells. Mol Cell Biochem. 1994;133-134(1):155-92. doi:10.1007/BF01267954.

150. Guzun R, Gonzalez-Granillo M, Karu-Varikmaa M, Grichine A, Usson Y, Kaambre T et al. Regulation of respiration in muscle cells in vivo by VDAC through interaction with the cytoskeleton and MtCK within Mitochondrial Interactosome. Biochimica et Biophysica Acta (BBA) - Biomembranes. 2012;1818(6):1545-54. doi:http://dx.doi.org/10.1016/j.bbamem.2011.12.034.

151. Schlattner U, Dolder M, Wallimann T, Tokarska-Schlattner M. Mitochondrial creatine kinase and mitochondrial outer membrane porin show a direct interaction that is modulated by calcium. Journal of Biological Chemistry. 2001. doi:10.1074/jbc.M106524200.

152. Schlattner U, Tokarska-Schlattner M, Wallimann T. Mitochondrial creatine kinase in human health and disease. Biochimica et Biophysica Acta (BBA) - Molecular Basis of Disease. 2006;1762(2):164-80. doi:http://dx.doi.org/10.1016/j.bbadis.2005.09.004.

153. Schlattner U, Wallimann T. Octamers of Mitochondrial Creatine Kinase Isoenzymes Differ in Stability and Membrane Binding. Journal of Biological Chemistry. 2000;275(23):17314-20.

154. Wyss M, Smeitink J, Wevers RA, Wallimann T. Mitochondrial creatine kinase: a key enzyme of aerobic energy metabolism. Biochimica et Biophysica Acta (BBA) - Bioenergetics. 1992;1102(2):119-66. doi:http://dx.doi.org/10.1016/0005-2728(92)90096-K.

155. Wallimann T, Moser H, Zurbriggen B, Wegmann G, Eppenberger H. Creatine kinase isoenzymes in spermatozoa. Journal of Muscle Research & Cell Motility. 1986;7(1):25-34. doi:10.1007/BF01756199.

156. Hughes MC, Ramos SV, Turnbull PC, Rebalka IA, Cao A, Monaco CMF et al. Early myopathy in Duchenne muscular dystrophy is associated with elevated mitochondrial H_2O_2

emission during impaired oxidative phosphorylation. Journal of Cachexia, Sarcopenia and Muscle. In Press. doi:10.1002/jcsm.12405.

157. Meyer RA, Sweeney HL, Kushmerick MJ. A simple analysis of the "phosphocreatine shuttle". American Journal of Physiology - Cell Physiology. 1984;246(5):C365-C77.

158. Brand MD. Mitochondrial generation of superoxide and hydrogen peroxide as the source of mitochondrial redox signaling. Free Radical Biology and Medicine. 2016;100:14-31. doi:https://doi.org/10.1016/j.freeradbiomed.2016.04.001.

159. Korshunov SS, Skulachev VP, Starkov AA. High protonic potential actuates a mechanism of production of reactive oxygen species in mitochondria. FEBS Letters. 1997;416(1):15-8. doi:10.1016/S0014-5793(97)01159-9.

160. Lambert AJ, Brand MD. Superoxide production by NADH:ubiquinone oxidoreductase (complex I) depends on the pH gradient across the mitochondrial inner membrane. The Biochemical journal. 2004;382(Pt 2):511-7. doi:10.1042/BJ20040485.

161. Maggiorani D, Manzella N, Edmondson DE, Mattevi A, Parini A, Binda C et al. Monoamine Oxidases, Oxidative Stress, and Altered Mitochondrial Dynamics in Cardiac Ageing. Oxidative medicine and cellular longevity. 2017;2017:3017947-. doi:10.1155/2017/3017947.

162. Wong HS, Dighe PA, Mezera V, Monternier PA, Brand MD. Production of superoxide and hydrogen peroxide from specific mitochondrial sites under different bioenergetic conditions. The Journal of biological chemistry. 2017;292(41):16804-9. doi:10.1074/jbc.R117.789271.

163. Weisiger RA, Fridovich I. Superoxide Dismutase: ORGANELLE SPECIFICITY. Journal of Biological Chemistry. 1973;248(10):3582-92.

164. Turrens JF. Mitochondrial formation of reactive oxygen species. The Journal of physiology. 2003;552(Pt 2):335-44. doi:10.1113/jphysiol.2003.049478.

165. Murphy MP. How mitochondria produce reactive oxygen species. The Biochemical journal. 2009;417(1):1-13. doi:10.1042/BJ20081386.

166. Lu J, Holmgren A. The thioredoxin antioxidant system. Free Radical Biology and Medicine. 2014;66:75-87. doi:https://doi.org/10.1016/j.freeradbiomed.2013.07.036.

167. Chernyak BV, Bernardi P. The Mitochondrial Permeability Transition Pore is Modulated by Oxidative Agents Through Both Pyridine Nucleotides and Glutathione at Two Separate Sites. European Journal of Biochemistry. 1996;238(3):623-30. doi:10.1111/j.1432-1033.1996.0623w.x.

168. Pozzan T, Bragadin M, Azzone GF, Veronese P. Disequilibrium between steady-state Ca2+ ion accumulation ratio and membrane potential in mitochondria. Pathway and role of Ca2+ ion efflux. Biochemistry. 1977;16(25):5618-25. doi:10.1021/bi00644a036.

169. Haworth RA, Hunter DR. The Ca2+-induced membrane transition in mitochondria: II. Nature of the Ca2+ trigger site. Archives of Biochemistry and Biophysics. 1979;195(2):460-7. doi:https://doi.org/10.1016/0003-9861(79)90372-2.

170. Hunter DR, Haworth RA. The Ca2+-induced membrane transition in mitochondria: I. The protective mechanisms. Archives of Biochemistry and Biophysics. 1979;195(2):453-9. doi:https://doi.org/10.1016/0003-9861(79)90371-0.

171. Hunter DR, Haworth RA. The Ca2+-induced membrane transition in mitochondria: III. Transitional Ca2+ release. Archives of Biochemistry and Biophysics. 1979;195(2):468-77. doi:https://doi.org/10.1016/0003-9861(79)90373-4.

172. Halestrap AP, Clarke SJ, Javadov SA. Mitochondrial permeability transition pore opening during myocardial reperfusion—a target for cardioprotection. Cardiovascular Research. 2004;61(3):372-85. doi:10.1016/S0008-6363(03)00533-9.

173. Halestrap AP, Pasdois P. The role of the mitochondrial permeability transition pore in heart disease. Biochimica et Biophysica Acta (BBA) - Bioenergetics. 2009;1787(11):1402-15. doi:https://doi.org/10.1016/j.bbabio.2008.12.017.

174. Wrogemann K, Pena SDJ. MITOCHONDRIAL CALCIUM OVERLOAD: A GENERAL MECHANISM FOR CELL-NECROSIS IN MUSCLE DISEASES. The Lancet. 1976;307(7961):672-4. doi:https://doi.org/10.1016/S0140-6736(76)92781-1.

175. Bernardi P, Rasola A, Forte M, Lippe G. The Mitochondrial Permeability Transition Pore: Channel Formation by F-ATP Synthase, Integration in Signal Transduction, and Role in Pathophysiology. Physiological Reviews. 2015;95(4):1111-55. doi:10.1152/physrev.00001.2015.

176. Giorgio V, Burchell V, Schiavone M, Bassot C, Minervini G, Petronilli V et al. Ca2+ binding to F-ATP synthase β subunit triggers the mitochondrial permeability transition. EMBO reports. 2017;18(7):1065. doi:10.15252/embr.201643354.

177. Neginskaya MA, Solesio ME, Berezhnaya EV, Amodeo GF, Mnatsakanyan N, Jonas EA et al. ATP Synthase C-Subunit-Deficient Mitochondria Have a Small Cyclosporine A-Sensitive Channel, but Lack the Permeability Transition Pore. Cell Reports. 2019;26(1):11-7.e2. doi:https://doi.org/10.1016/j.celrep.2018.12.033.

178. Amodeo GF, Solesio ME, Pavlov EV. From ATP synthase dimers to C-ring conformational changes: unified model of the mitochondrial permeability transition pore. Cell death & disease. 2017;8(12):1-. doi:10.1038/s41419-017-0042-3.

179. Fontaine E, Eriksson O, Ichas F, Bernardi P. Regulation of the Permeability Transition Pore in Skeletal Muscle Mitochondria: MODULATION BY ELECTRON FLOW THROUGH THE RESPIRATORY CHAIN COMPLEX I. Journal of Biological Chemistry. 1998;273(20):12662-8.

180. Kerr JF, Wyllie AH, Currie AR. Apoptosis: a basic biological phenomenon with wide-ranging implications in tissue kinetics. British journal of cancer. 1972;26(4):239-57.

181. Festjens N, Vanden Berghe T, Vandenabeele P. Necrosis, a well-orchestrated form of cell demise: Signalling cascades, important mediators and concomitant immune response. Biochimica et Biophysica Acta (BBA) - Bioenergetics. 2006;1757(9):1371-87. doi:https://doi.org/10.1016/j.bbabio.2006.06.014.

182. Salvesen GS, Dixit VM. Caspases: Intracellular Signaling by Proteolysis. Cell. 1997;91(4):443-6. doi:10.1016/S0092-8674(00)80430-4.

183. Li P, Nijhawan D, Budihardjo I, Srinivasula SM, Ahmad M, Alnemri ES et al. Cytochrome c and dATP-Dependent Formation of Apaf-1/Caspase-9 Complex Initiates an Apoptotic Protease Cascade. Cell. 1997;91(4):479-89. doi:https://doi.org/10.1016/S0092-8674(00)80434-1.

184. Eguchi Y, Shimizu S, Tsujimoto Y. Intracellular ATP Levels Determine Cell Death Fate by Apoptosis or Necrosis. Cancer Research. 1997;57(10):1835.

185. McConkey DJ. Biochemical determinants of apoptosis and necrosis. Toxicology Letters. 1998;99(3):157-68. doi:https://doi.org/10.1016/S0378-4274(98)00155-6.

186. Li YP, Atkins CM, Sweatt JD, Reid MB. Mitochondria mediate tumor necrosis factor-alpha/NF-kappaB signaling in skeletal muscle myotubes. Antioxid Redox Signal. 1999;1(1):97-104. doi:10.1089/ars.1999.1.1-97.

187. Trump BE, Berezesky IK, Chang SH, Phelps PC. The Pathways of Cell Death: Oncosis, Apoptosis, and Necrosis. Toxicologic Pathology. 1997;25(1):82-8. doi:10.1177/019262339702500116.

188. Majno G, Joris I. Apoptosis, oncosis, and necrosis. An overview of cell death. The American journal of pathology. 1995;146(1):3-15.

189. Lemasters JJ, Qian T, Bradham CA, Brenner DA, Cascio WE, Trost LC et al. Mitochondrial Dysfunction in the Pathogenesis of Necrotic and Apoptotic Cell Death. Journal of Bioenergetics and Biomembranes. 1999;31(4):305-19. doi:10.1023/A:1005419617371.

190. Dreyfus J-C, Schapira G, Schapira F. BIOCHEMICAL STUDY OF MUSCLE IN PROGRESSIVE MUSCULAR DYSTROPHY. The Journal of Clinical Investigation. 1954;33(5):794-7. doi:10.1172/JCI102950.

191. Di Mauro S, Angelini C, Catani C. Enzymes of the glycogen cycle and glycolysis in various human neuromuscular disorders. Journal of Neurology, Neurosurgery & Psychiatry. 1967;30(5):411. doi:10.1136/jnnp.30.5.411.

192. Chi MMY, Hintz CS, McKee D, Felder S, Grant N, Kaiser KK et al. Effect of Duchenne muscular dystrophy on enzymes of energy metabolism in individual muscle fibers. Metabolism. 1987;36(8):761-7. doi:http://dx.doi.org/10.1016/0026-0495(87)90113-2.

193. Chinet AE, Even PC, Decrouy A. Dystrophin-dependent efficiency of metabolic pathways in mouse skeletal muscles. Experientia. 1994;50(6):602-5. doi:10.1007/BF01921731.

194. Glesby MJ, Rosenmann E, Nylen EG, Wrogemann K. Serum CK, calcium, magnesium, and oxidative phosphorylation in mdx mouse muscular dystrophy. Muscle & Nerve. 1988;11(8):852-6. doi:10.1002/mus.880110809.

195. Timpani CA, Hayes A, Rybalka E. Revisiting the dystrophin-ATP connection: How half a century of research still implicates mitochondrial dysfunction in Duchenne Muscular Dystrophy aetiology. Medical Hypotheses. 2015;85(6):1021-33. doi:http://dx.doi.org/10.1016/j.mehy.2015.08.015.

196. Chen Y-W, Zhao P, Borup R, Hoffman EP. Expression Profiling in the Muscular Dystrophies. The Journal of Cell Biology. 2000;151(6):1321. doi:10.1083/jcb.151.6.1321.

197. Matsumura CY, Menezes de Oliveira B, Durbeej M, Marques MJ. Isobaric Tagging-Based Quantification for Proteomic Analysis: A Comparative Study of Spared and Affected Muscles from mdx Mice at the Early Phase of Dystrophy. PLOS ONE. 2013;8(6):e65831. doi:10.1371/journal.pone.0065831.

198. Even PC, Decrouy A, Chinet A. Defective regulation of energy metabolism in mdx-mouse skeletal muscles. Biochemical Journal. 1994;304(Pt 2):649-54.

199. Ascah A, Khairallah M, Daussin F, Bourcier-Lucas C, Godin R, Allen BG et al. Stress-induced opening of the permeability transition pore in the dystrophin-deficient heart is attenuated by acute treatment with sildenafil. American Journal of Physiology-Heart and Circulatory Physiology. 2010;300(1):H144-H53. doi:10.1152/ajpheart.00522.2010.

200. Schlattner U, Kay L, Tokarska-Schlattner M. Mitochondrial Proteolipid Complexes of Creatine Kinase. In: Harris JR, Boekema EJ, editors. Membrane Protein Complexes: Structure and Function. Singapore: Springer Singapore; 2018. p. 365-408.

201. Braun U, Paju K, Eimre M, Seppet E, Orlova E, Kadaja L et al. Lack of dystrophin is associated with altered integration of the mitochondria and ATPases in slow-twitch muscle cells of MDX mice. Biochim Biophys Acta. 2001;1505(2-3):258-70.

202. Tanabe Y, Esaki K, Nomura T. Skeletal muscle pathology in X chromosome-linked muscular dystrophy (mdx) mouse. Acta Neuropathologica. 1986;69(1):91-5. doi:10.1007/BF00687043.

203. Chang ACY, Ong S-G, LaGory EL, Kraft PE, Giaccia AJ, Wu JC et al. Telomere shortening and metabolic compromise underlie dystrophic cardiomyopathy. Proceedings of the National Academy of Sciences of the United States of America. 2016;113(46):13120-5. doi:10.1073/pnas.1615340113.

204. Mourkioti F, Kustan J, Kraft P, Day JW, Zhao MM, Kost-Alimova M et al. Role of telomere dysfunction in cardiac failure in Duchenne muscular dystrophy. Nat Cell Biol. 2013;15(8):895-904. doi:10.1038/ncb2790.

205. Meyer LE, Machado LB, Santiago APSA, da-Silva WS, De Felice FG, Holub O et al. Mitochondrial Creatine Kinase Activity Prevents Reactive Oxygen Species Generation:

ANTIOXIDANT ROLE OF MITOCHONDRIAL KINASE-DEPENDENT ADP RE-CYCLING ACTIVITY. Journal of Biological Chemistry. 2006;281(49):37361-71.

206. Zs.-Nagy I. Chemistry, toxicology, pharmacology and pharmacokinetics of idebenone: a review. Archives of Gerontology and Geriatrics. 1990;11(3):177-86. doi:https://doi.org/10.1016/0167-4943(90)90063-C.

207. Gillis JC, Benfield P, McTavish D. Idebenone. Drugs & Aging. 1994;5(2):133-52. doi:10.2165/00002512-199405020-00007.

208. Buyse GM, Van der Mieren G, Erb M, D'Hooge J, Herijgers P, Verbeken E et al. Long-term blinded placebo-controlled study of SNT-MC17/idebenone in the dystrophin deficient mdx mouse: cardiac protection and improved exercise performance. Eur Heart J. 2009;30(1):116-24. doi:10.1093/eurheartj/ehn406.

209. Buyse GM, Goemans N, van den Hauwe M, Thijs D, de Groot IJ, Schara U et al. Idebenone as a novel, therapeutic approach for Duchenne muscular dystrophy: results from a 12 month, double-blind, randomized placebo-controlled trial. Neuromuscul Disord. 2011;21(6):396-405. doi:10.1016/j.nmd.2011.02.016.

210. Buyse GM, Voit T, Schara U, Straathof CS, D'Angelo MG, Bernert G et al. Efficacy of idebenone on respiratory function in patients with Duchenne muscular dystrophy not using glucocorticoids (DELOS): a double-blind randomised placebo-controlled phase 3 trial. Lancet. 2015;385(9979):1748-57. doi:10.1016/S0140-6736(15)60025-3.

211. Buyse GM, Voit T, Schara U, Straathof CS, D'Angelo MG, Bernert G et al. Treatment effect of idebenone on inspiratory function in patients with Duchenne muscular dystrophy. Pediatr Pulmonol. 2017;52(4):508-15. doi:10.1002/ppul.23547.

212. Agency EM. CHMP ASSESSMENT REPORT FOR Sovrima London2008 Nov. 20, 2008.

213. Watkins SC, Cullen MJ. A qualitative and quantitative study of the ultrastructure of regenerating muscle fibres in Duchenne muscular dystrophy and polymyositis. Journal of the neurological sciences. 1987;82(1):181-92. doi:https://doi.org/10.1016/0022-510X(87)90017-7.

214. Robert V, Massimino ML, Tosello V, Marsault R, Cantini M, Sorrentino V et al. Alteration in Calcium Handling at the Subcellular Level inmdx Myotubes. Journal of Biological Chemistry. 2001;276(7):4647-51.

215. Reutenauer J, Dorchies OM, Patthey-Vuadens O, Vuagniaux G, Ruegg UT. Investigation of Debio 025, a cyclophilin inhibitor, in the dystrophic mdx mouse, a model for Duchenne muscular dystrophy. British Journal of Pharmacology. 2008;155(4):574-84. doi:10.1038/bjp.2008.285.

216. Percival JM, Whitehead NP, Adams ME, Adamo CM, Beavo JA, Froehner SC. Sildenafil reduces respiratory muscle weakness and fibrosis in the mdx mouse model of Duchenne muscular dystrophy. The Journal of Pathology. 2012;228(1):77-87. doi:10.1002/path.4054.

217. Khairallah M, Khairallah RJ, Young ME, Allen BG, Gillis MA, Danialou G et al. Sildenafil and cardiomyocyte-specific cGMP signaling prevent cardiomyopathic changes associated with dystrophin deficiency. Proceedings of the National Academy of Sciences of the United States of America. 2008;105(19):7028-33. doi:10.1073/pnas.0710595105.

218. Adamo CM, Dai D-F, Percival JM, Minami E, Willis MS, Patrucco E et al. Sildenafil reverses cardiac dysfunction in the mdx mouse model of Duchenne muscular dystrophy. Proceedings of the National Academy of Sciences. 2010;107(44):19079. doi:10.1073/pnas.1013077107.

219. Leung DG, Herzka DA, Thompson WR, He B, Bibat G, Tennekoon G et al. Sildenafil does not improve cardiomyopathy in Duchenne/Becker muscular dystrophy. Annals of Neurology. 2014;76(4):541-9. doi:10.1002/ana.24214.

220. Sheu S-S, Nauduri D, Anders MW. Targeting antioxidants to mitochondria: A new therapeutic direction. Biochimica et Biophysica Acta (BBA) - Molecular Basis of Disease. 2006;1762(2):256-65. doi:https://doi.org/10.1016/j.bbadis.2005.10.007.

221. Murphy MP. Targeting lipophilic cations to mitochondria. Biochimica et Biophysica Acta (BBA) - Bioenergetics. 2008;1777(7):1028-31. doi:https://doi.org/10.1016/j.bbabio.2008.03.029.

222. Severin FF, Severina II, Antonenko YN, Rokitskaya TI, Cherepanov DA, Mokhova EN et al. Penetrating cation/fatty acid anion pair as a mitochondria-targeted protonophore. Proceedings of the National Academy of Sciences of the United States of America. 2010;107(2):663-8. doi:10.1073/pnas.0910216107.

223. Zhao K, Zhao G-M, Wu D, Soong Y, Birk AV, Schiller PW et al. Cell-permeable Peptide Antioxidants Targeted to Inner Mitochondrial Membrane inhibit Mitochondrial Swelling, Oxidative Cell Death, and Reperfusion Injury. Journal of Biological Chemistry. 2004;279(33):34682-90.

224. Dai W, Cheung E, Alleman RJ, Perry JB, Allen ME, Brown DA et al. Cardioprotective Effects of Mitochondria-Targeted Peptide SBT-20 in two Different Models of Rat Ischemia/Reperfusion. Cardiovasc Drugs Ther. 2016;30(6):559-66. doi:10.1007/s10557-016-6695-9.

225. Cho J, Won K, Wu D, Soong Y, Liu S, Szeto HH et al. Potent mitochondria-targeted peptides reduce myocardial infarction in rats. Coron Artery Dis. 2007;18(3):215-20. doi:10.1097/01.mca.0000236285.71683.b6.

226. Szeto HH. Mitochondria-targeted cytoprotective peptides for ischemia-reperfusion injury. Antioxid Redox Signal. 2008;10(3):601-19. doi:10.1089/ars.2007.1892.

227. Karaa A, Haas R, Goldstein A, Vockley J, Weaver WD, Cohen BH. Randomized dose-escalation trial of elamipretide in adults with primary mitochondrial myopathy. Neurology. 2018;90(14):e1212. doi:10.1212/WNL.0000000000005255.

228. El-Hattab AW, Zarante AM, Almannai M, Scaglia F. Therapies for mitochondrial diseases and current clinical trials. Molecular Genetics and Metabolism. 2017;122(3):1-9. doi:https://doi.org/10.1016/j.ymgme.2017.09.009.

229. Emery A. Genetic heterogeneity in Duchenne muscular dystrophy. Am J Med Genet. 1987;26(1):235-6. doi:10.1002/ajmg.1320260138.

230. Bridges LR. The association of cardiac muscle necrosis and inflammation with the degenerative and persistent myopathy of MDX mice. Journal of the neurological sciences. 1986;72(2-3):147-57.

231. Schuh RA, Jackson KC, Khairallah RJ, Ward CW, Spangenburg EE. Measuring mitochondrial respiration in intact single muscle fibers. Am J Physiol Regul Integr Comp Physiol. 2012;302(6):R712-9. doi:10.1152/ajpregu.00229.2011.

232. Nicholls DG, Ferguson SJ. Bioenergetics 4. Elsevier; 2013.

233. Aartsma-Rus A, van Putten M. Assessing Functional Performance in the Mdx Mouse Model. Journal of Visualized Experiments : JoVE. 2014(85):51303. doi:10.3791/51303.

234. Foster AJ, Platt MJ, Huber JS, Eadie AL, Arkell AM, Romanova N et al. Central-acting therapeutics alleviate respiratory weakness caused by heart failure–induced ventilatory overdrive. Science Translational Medicine. 2017;9(390).

235. Warren GL, Stallone JL, Allen MR, Bloomfield SA. Functional recovery of the plantarflexor muscle group after hindlimb unloading in the rat. European Journal of Applied Physiology. 2004;93(1):130-8. doi:10.1007/s00421-004-1185-3.

236. Bloemberg D, Quadrilatero J. Rapid Determination of Myosin Heavy Chain Expression in Rat, Mouse, and Human Skeletal Muscle Using Multicolor Immunofluorescence Analysis. PLoS ONE. 2012;7(4):e35273. doi:10.1371/journal.pone.0035273.

237. Tonkonogi M, Harris B, Sahlin K. Mitochondrial oxidative function in human saponin-skinned muscle fibres: effects of prolonged exercise. The Journal of Physiology. 1998;510(Pt 1):279-86. doi:10.1111/j.1469-7793.1998.279bz.x.

238. Kuznetsov AV, Tiivel T, Sikk P, Kaambre T, Kay L, Daneshrad Z et al. Striking Differences Between the Kinetics of Regulation of Respiration by ADP in Slow-Twitch and Fast-Twitch Muscles In Vivo. European Journal of Biochemistry. 1996;241(3):909-15. doi:10.1111/j.1432-1033.1996.00909.x.

239. Ydfors M, Hughes MC, Laham R, Schlattner U, Norrbom J, Perry CG. Modelling in vivo creatine/phosphocreatine in vitro reveals divergent adaptations in human muscle mitochondrial respiratory control by ADP after acute and chronic exercise. J Physiol. 2016;594(11):3127-40. doi:10.1113/JP271259.

240. Perry CGR, Kane DA, Lanza IR, Neufer PD. Methods for Assessing Mitochondrial Function in Diabetes. Diabetes. 2013;62(4):1041-53. doi:10.2337/db12-1219.

241. Zhang Y, Dong Y, Wu X, Lu Y, Xu Z, Knapp A et al. The mitochondrial pathway of anesthetic isoflurane-induced apoptosis. J Biol Chem. 2010;285(6):4025-37. doi:10.1074/jbc.M109.065664.

242. Fisher-Wellman KH, Gilliam LA, Lin CT, Cathey BL, Lark DS, Neufer PD. Mitochondrial glutathione depletion reveals a novel role for the pyruvate dehydrogenase complex as a key H2O2-emitting source under conditions of nutrient overload. Free Radic Biol Med. 2013;65:1201-8. doi:10.1016/j.freeradbiomed.2013.09.008.

243. Perry CGR, Kane DA, Lin C-T, Kozy R, Cathey BL, Lark DS et al. Inhibiting Myosin-ATPase Reveals Dynamic Range of Mitochondrial Respiratory Control in Skeletal Muscle. The Biochemical journal. 2011;437(2):10.1042/BJ20110366. doi:10.1042/BJ20110366.

244. Hughes MC, Ramos SV, Turnbull PC, Nejatbakhsh A, Baechler BL, Tahmasebi H et al. Mitochondrial bioenergetics and fibre type assessments in microbiopsy vs Bergstrom percutaneous sampling of human skeletal muscle. Frontiers in Physiology. 2015;6. doi:10.3389/fphys.2015.00360.

245. Pesta D, Gnaiger E. High-Resolution Respirometry: OXPHOS Protocols for Human Cells and Permeabilized Fibers from Small Biopsies of Human Muscle. In: Palmeira CM, Moreno AJ, editors. Mitochondrial Bioenergetics: Methods and Protocols. Totowa, NJ: Humana Press; 2012. p. 25-58.

246. Walsh B, Tonkonogi M, Söderlund K, Hultman E, Saks V, Sahlin K. The role of phosphorylcreatine and creatine in the regulation of mitochondrial respiration in human skeletal muscle. The Journal of Physiology. 2001;537(Pt 3):971-8. doi:10.1111/j.1469-7793.2001.00971.x.

247. Perry CGR, Heigenhauser GJF, Bonen A, Spriet LL. High-intensity aerobic interval training increases fat and carbohydrate metabolic capacities in human skeletal muscle. Applied Physiology, Nutrition, and Metabolism. 2008;33(6):1112-23. doi:10.1139/H08-097.

248. Perry CGR, Kane DA, Herbst EAF, Mukai K, Lark DS, Wright DC et al. Mitochondrial creatine kinase activity and phosphate shuttling are acutely regulated by exercise in human skeletal muscle. The Journal of Physiology. 2012;590(Pt 21):5475-86. doi:10.1113/jphysiol.2012.234682.

249. Fisher-Wellman KH, Mattox TA, Thayne K, Katunga LA, La Favor JD, Neufer PD et al. Novel role for thioredoxin reductase-2 in mitochondrial redox adaptations to obesogenic diet and exercise in heart and skeletal muscle. J Physiol. 2013;591(14):3471-86. doi:10.1113/jphysiol.2013.254193.

250. Tsien RY. Fluorescent indicators of ion concentrations. Methods Cell Biol. 1989;30:127-56.

251. Campbell TL, Mitchell AS, McMillan EM, Bloemberg D, Pavlov D, Messa I et al. High-fat feeding does not induce an autophagic or apoptotic phenotype in female rat skeletal muscle. Exp Biol Med (Maywood). 2015;240(5):657-68. doi:10.1177/1535370214557223.

252. Dam AD, Mitchell AS, Rush JW, Quadrilatero J. Elevated skeletal muscle apoptotic signaling following glutathione depletion. Apoptosis. 2012;17(1):48-60. doi:10.1007/s10495-011-0654-5.

253. Nilsson MI, MacNeil LG, Kitaoka Y, Suri R, Young SP, Kaczor JJ et al. Combined aerobic exercise and enzyme replacement therapy rejuvenates the mitochondrial–lysosomal axis and alleviates autophagic blockage in Pompe disease. Free Radical Biology and Medicine. 2015;87(Supplement C):98-112. doi:https://doi.org/10.1016/j.freeradbiomed.2015.05.019.

254. Tarnopolsky MA, Rennie CD, Robertshaw HA, Fedak-Tarnopolsky SN, Devries MC, Hamadeh MJ. Influence of endurance exercise training and sex on intramyocellular lipid and mitochondrial ultrastructure, substrate use, and mitochondrial enzyme activity. American Journal of Physiology-Regulatory, Integrative and Comparative Physiology. 2007;292(3):R1271-R8. doi:10.1152/ajpregu.00472.2006.

255. Mandel ER, Dunford EC, Abdifarkosh G, Turnbull PC, Perry CGR, Riddell MC et al. The superoxide dismutase mimetic tempol does not alleviate glucocorticoid-mediated rarefaction of rat skeletal muscle capillaries. Physiol Rep. 2017;5(10). doi:10.14814/phy2.13243.

256. Schlattner U, Mockli N, Speer O, Werner S, Wallimann T. Creatine Kinase and Creatine Transporter in Normal, Wounded, and Diseased Skin. J Investig Dermatol. 2002;118(3):416-23. doi:10.1046/j.0022-202x.2001.01697.x.

257. Larsen S, Nielsen J, Hansen CN, Nielsen LB, Wibrand F, Stride N et al. Biomarkers of mitochondrial content in skeletal muscle of healthy young human subjects. J Physiol. 2012;590(14):3349-60. doi:10.1113/jphysiol.2012.230185.

258. Brown DA, Perry JB, Allen ME, Sabbah HN, Stauffer BL, Shaikh SR et al. Mitochondrial function as a therapeutic target in heart failure. Nature Reviews Cardiology. 2016;14:238. doi:10.1038/nrcardio.2016.203.

259. Hurd TR, Prime TA, Harbour ME, Lilley KS, Murphy MP. Detection of Reactive Oxygen Species-sensitive Thiol Proteins by Redox Difference Gel Electrophoresis: IMPLICATIONS FOR MITOCHONDRIAL REDOX SIGNALING. Journal of Biological Chemistry. 2007;282(30):22040-51.

260. Barker RG, Wyckelsma VL, Xu H, Murphy RM. Mitochondrial content is preserved throughout disease progression in the mdx mouse model of Duchenne muscular dystrophy, regardless of taurine supplementation. American Journal of Physiology-Cell Physiology. 2017;314(4):C483-C91. doi:10.1152/ajpcell.00046.2017.

261. Koufen P, Rück A, Brdiczka D, Wendt S, Wallimann T, Stark G. Free radical-induced inactivation of creatine kinase: influence on the octameric and dimeric states of the mitochondrial enzyme (Mib-CK). Biochemical Journal. 1999;344(Pt 2):413-7.

262. Lemasters JJ, Holmuhamedov E. Voltage-dependent anion channel (VDAC) as mitochondrial governator—Thinking outside the box. Biochimica et Biophysica Acta (BBA) -

Molecular Basis of Disease. 2006;1762(2):181-90. doi:http://dx.doi.org/10.1016/j.bbadis.2005.10.006.

263. O-Uchi J, Ryu S-Y, Jhun BS, Hurst S, Sheu S-S. Mitochondrial Ion Channels/Transporters as Sensors and Regulators of Cellular Redox Signaling. Antioxidants & Redox Signaling. 2014;21(6):987-1006. doi:10.1089/ars.2013.5681.

264. Kerner J, Lee K, Tandler B, Hoppel CL. VDAC proteomics: post-translation modifications. Biochimica et biophysica acta. 2012;1818(6):1520-5. doi:10.1016/j.bbamem.2011.11.013.

265. Feng J, Lucchinetti E, Enkavi G, Wang Y, Gehrig P, Roschitzki B et al. Tyrosine phosphorylation by Src within the cavity of the adenine nucleotide translocase 1 regulates ADP/ATP exchange in mitochondria. American Journal of Physiology - Cell Physiology. 2010;298(3):C740-C8.

266. Brand MD. The sites and topology of mitochondrial superoxide production. Experimental Gerontology. 2010;45(7–8):466-72. doi:http://dx.doi.org/10.1016/j.exger.2010.01.003.

267. Menazza S, Blaauw B, Tiepolo T, Toniolo L, Braghetta P, Spolaore B et al. Oxidative stress by monoamine oxidases is causally involved in myofiber damage in muscular dystrophy. Hum Mol Genet. 2010;19(21):4207-15. doi:10.1093/hmg/ddq339.

268. Passaquin A-C, Renard M, Kay L, Challet C, Mokhtarian A, Wallimann T et al. Creatine supplementation reduces skeletal muscle degeneration and enhances mitochondrial function in mdx mice. Neuromuscular Disorders. 2002;12(2):174-82. doi:http://dx.doi.org/10.1016/S0960-8966(01)00273-5.

269. Min K, Smuder AJ, Kwon OS, Kavazis AN, Szeto HH, Powers SK. Mitochondrial-targeted antioxidants protect skeletal muscle against immobilization-induced muscle atrophy. J Appl Physiol (1985). 2011;111(5):1459-66. doi:10.1152/japplphysiol.00591.2011.

270. Powers SK, Hudson MB, Nelson WB, Talbert EE, Min K, Szeto HH et al. Mitochondria-targeted antioxidants protect against mechanical ventilation-induced diaphragm weakness. Crit Care Med. 2011;39(7):1749-59. doi:10.1097/CCM.0b013e3182190b62.

271. Adlam VJ, Harrison JC, Porteous CM, James AM, Smith RA, Murphy MP et al. Targeting an antioxidant to mitochondria decreases cardiac ischemia-reperfusion injury. FASEB J. 2005;19(9):1088-95. doi:10.1096/fj.05-3718com.

272. Singh K, Hood DA. Effect of denervation-induced muscle disuse on mitochondrial protein import. American journal of physiology Cell physiology. 2011;300(1):C138-45. doi:10.1152/ajpcell.00181.2010.

273. Pollock N, Staunton CA, Vasilaki A, McArdle A, Jackson MJ. Denervated muscle fibers induce mitochondrial peroxide generation in neighboring innervated fibers: Role in muscle aging. Free Radic Biol Med. 2017;112:84-92. doi:10.1016/j.freeradbiomed.2017.07.017.

274. Bernardi P, von Stockum S. The permeability transition pore as a Ca(2+) release channel: New answers to an old question. Cell Calcium. 2012;52(1):22-7. doi:10.1016/j.ceca.2012.03.004.

275. Giacomotto J, Brouilly N, Walter L, Mariol M-C, Berger J, Ségalat L et al. Chemical genetics unveils a key role of mitochondrial dynamics, cytochrome c release and IP3R activity in muscular dystrophy. Human Molecular Genetics. 2013;22(22):4562-78. doi:10.1093/hmg/ddt302.

276. Cai J, Yang J, Jones D. Mitochondrial control of apoptosis: the role of cytochrome c. Biochimica et Biophysica Acta (BBA) - Bioenergetics. 1998;1366(1):139-49. doi:https://doi.org/10.1016/S0005-2728(98)00109-1.

277. Schulze-Osthoff K, Bakker AC, Vanhaesebroeck B, Beyaert R, Jacob WA, Fiers W. Cytotoxic activity of tumor necrosis factor is mediated by early damage of mitochondrial functions. Evidence for the involvement of mitochondrial radical generation. Journal of Biological Chemistry. 1992;267(8):5317-23.

278. Buck M, Chojkier M. Muscle wasting and dedifferentiation induced by oxidative stress in a murine model of cachexia is prevented by inhibitors of nitric oxide synthesis and antioxidants. The EMBO Journal. 1996;15(8):1753-65.

279. Dudley RW, Danialou G, Govindaraju K, Lands L, Eidelman DE, Petrof BJ. Sarcolemmal damage in dystrophin deficiency is modulated by synergistic interactions between mechanical and oxidative/nitrosative stresses. Am J Pathol. 2006;168(4):1276-87; quiz 404-5. doi:10.2353/ajpath.2006.050683.

280. Khairallah M, Khairallah R, Young ME, Dyck JRB, Petrof BJ, Des Rosiers C. Metabolic and signaling alterations in dystrophin-deficient hearts precede overt cardiomyopathy. Journal of Molecular and Cellular Cardiology. 2007;43(2):119-29. doi:10.1016/j.yjmcc.2007.05.015.

281. Baines CP. The mitochondrial permeability transition pore and ischemia-reperfusion injury. Basic research in cardiology. 2009;104(2):181-8. doi:10.1007/s00395-009-0004-8.

282. Ong S-B, Samangouei P, Kalkhoran SB, Hausenloy DJ. The mitochondrial permeability transition pore and its role in myocardial ischemia reperfusion injury. Journal of Molecular and Cellular Cardiology. 2015;78:23-34. doi:10.1016/j.yjmcc.2014.11.005.

283. Anderson EJ, Yamazaki H, Neufer PD. Induction of Endogenous Uncoupling Protein 3 Suppresses Mitochondrial Oxidant Emission during Fatty Acid-supported Respiration. Journal of Biological Chemistry. 2007;282(43):31257-66.

284. Jegier W, Sekelj P, Auld PAM, Simpson R, McGregor M. THE RELATION BETWEEN CARDIAC OUTPUT AND BODY SIZE. British Heart Journal. 1963;25(4):425-30.

285. Willis WT, Miranda-Grandjean D, Hudgens J, Willis EA, Finlayson J, De Filippis EA et al. Dominant and sensitive control of oxidative flux by the ATP-ADP carrier in human skeletal muscle mitochondria: Effect of lysine acetylation. Arch Biochem Biophys. 2018;647:93-103. doi:10.1016/j.abb.2018.04.006.

286. Ventura-Clapier R, Kuznetsov A, Veksler V, Boehm E, Anflous K. Functional coupling of creatine kinases in muscles: Species and tissue specificity. Mol Cell Biochem. 1998;184(1-2):231-47.

287. McDonald CM, Meier T, Voit T, Schara U, Straathof CS, D'Angelo MG et al. Idebenone reduces respiratory complications in patients with Duchenne muscular dystrophy. Neuromuscul Disord. 2016;26(8):473-80. doi:10.1016/j.nmd.2016.05.008.

288. Wissing ER, Millay DP, Vuagniaux G, Molkentin JD. Debio-025 is more effective than prednisone in reducing muscular pathology in mdx mice. Neuromuscular disorders : NMD. 2010;20(11):753-60. doi:10.1016/j.nmd.2010.06.016.

289. Kirschner J, Schessl J, Schara U, Reitter B, Stettner GM, Hobbiebrunken E et al. Treatment of Duchenne muscular dystrophy with ciclosporin A: a randomised, double-blind, placebo-controlled multicentre trial. The Lancet Neurology. 2010;9(11):1053-9. doi:https://doi.org/10.1016/S1474-4422(10)70196-4.

290. Fajardo VA, Smith IC, Bombardier E, Chambers PJ, Quadrilatero J, Tupling AR. Diaphragm assessment in mice overexpressing phospholamban in slow-twitch type I muscle fibers. Brain and Behavior. 2016;6(6):e00470. doi:10.1002/brb3.470.

291. Gregorevic P, Plant DR, Leeding KS, Bach LA, Lynch GS. Improved Contractile Function of the mdx Dystrophic Mouse Diaphragm Muscle after Insulin-Like Growth Factor-I Administration. The American Journal of Pathology. 2002;161(6):2263-72.

292. Bombardier E, Smith IC, Vigna C, Fajardo VA, Tupling AR. Ablation of sarcolipin decreases the energy requirements for Ca2+ transport by sarco(endo)plasmic reticulum Ca2+-ATPases in resting skeletal muscle. FEBS Letters. 2013;587(11):1687-92. doi:10.1016/j.febslet.2013.04.019.

293. Lo Mauro A, Aliverti A. Physiology of respiratory disturbances in muscular dystrophies. Breathe (Sheff). 2016;12(4):318-27. doi:10.1183/20734735.012716.

294. Burns DP, Murphy KH, Lucking EF, O'Halloran KD. Inspiratory pressure-generating capacity is preserved during ventilatory and non-ventilatory behaviours in young dystrophic mdx mice despite profound diaphragm muscle weakness. The Journal of Physiology. 2019;597(3):831-48. doi:10.1113/JP277443.

295. Khawli FA, Reid MB. N-acetylcysteine depresses contractile function and inhibits fatigue of diaphragm in vitro. Journal of Applied Physiology. 1994;77(1):317-24. doi:10.1152/jappl.1994.77.1.317.

296. Diaz PT, Brownstein E, Clanton TL. Effects of N-acetylcysteine on in vitro diaphragm function are temperature dependent. Journal of Applied Physiology. 1994;77(5):2434-9. doi:10.1152/jappl.1994.77.5.2434.

297. Shindoh C, DiMarco A, Thomas A, Manubay P, Supinski G. Effect of N-acetylcysteine on diaphragm fatigue. Journal of Applied Physiology. 1990;68(5):2107-13. doi:10.1152/jappl.1990.68.5.2107.

298. Reid MB, Stokić DS, Koch SM, Khawli FA, Leis AA. N-acetylcysteine inhibits muscle fatigue in humans. The Journal of Clinical Investigation. 1994;94(6):2468-74. doi:10.1172/JCI117615.

299. Medved I, Brown MJ, Bjorksten AR, Murphy KT, Petersen AC, Sostaric S et al. N-acetylcysteine enhances muscle cysteine and glutathione availability and attenuates fatigue during prolonged exercise in endurance-trained individuals. Journal of Applied Physiology. 2004;97(4):1477-85. doi:10.1152/japplphysiol.00371.2004.

300. Anzueto A, Andrade FH, Maxwell LC, Levine SM, Lawrence RA, Gibbons WJ et al. Resistive breathing activates the glutathione redox cycle and impairs performance of rat diaphragm. Journal of Applied Physiology. 1992;72(2):529-34. doi:10.1152/jappl.1992.72.2.529.

301. Supinski GS, Stofan D, Ciufo R, Dimarco A. N-acetylcysteine administration alters the response to inspiratory loading in oxygen-supplemented rats. Journal of Applied Physiology. 1997;82(4):1119-25. doi:10.1152/jappl.1997.82.4.1119.

302. Renjini R, Gayathri N, Nalini A, Srinivas Bharath MM. Oxidative damage in muscular dystrophy correlates with the severity of the pathology: role of glutathione metabolism. Neurochem Res. 2012;37(4):885-98. doi:10.1007/s11064-011-0683-z.

303. Tidball JG, Albrecht DE, Lokensgard BE, Spencer MJ. Apoptosis precedes necrosis of dystrophin-deficient muscle. Journal of Cell Science. 1995;108(6):2197.

304. Hughes MC, Ramos SV, Turnbull PC, Edgett BA, Huber JS, Polidovitch N et al. Impairments in left ventricular mitochondrial bioenergetics precede overt cardiac dysfunction and remodelling in Duchenne muscular dystrophy. The Journal of Physiology. 2019;0(ja). doi:10.1113/JP277306.

305. Dolder M, Wendt S, Wallimann T. Mitochondrial Creatine Kinase in Contact Sites: Interaction with Porin and Adenine Nucleotide Translocase, Role in Permeability Transition and Sensitivity to Oxidative Damage. Neurosignals. 2001;10(1-2):93-111.

306. Mailloux RJ, McBride SL, Harper M-E. Unearthing the secrets of mitochondrial ROS and glutathione in bioenergetics. Trends in Biochemical Sciences. 2013;38(12):592-602. doi:https://doi.org/10.1016/j.tibs.2013.09.001.

307. Sloan RC, Moukdar F, Frasier CR, Patel HD, Bostian PA, Lust RM et al. Mitochondrial permeability transition in the diabetic heart: Contributions of thiol redox state and mitochondrial calcium to augmented reperfusion injury. Journal of Molecular and Cellular Cardiology. 2012;52(5):1009-18. doi:https://doi.org/10.1016/j.yjmcc.2012.02.009.

308. Frasier CR, Moukdar F, Patel HD, Stewart LM, Alleman RJ, Brown DA et al. Redox-dependent increases in glutathione reductase and exercise preconditioning: role of NADPH oxidase and mitochondria. Cardiovascular Research. 2013;98(1):47-55. doi:10.1093/cvr/cvt009.

309. Stachowiak O, Dolder M, Wallimann T, Richter C. Mitochondrial Creatine Kinase Is a Prime Target of Peroxynitrite-induced Modification and Inactivation. Journal of Biological Chemistry. 1998;273(27):16694-9.

310. Yuan G, Kaneko M, Masuda H, Hon RB, Kobayashi A, Yamazaki N. Decrease in heart mitochondrial creatine kinase activity due to oxygen free radicals. Biochimica et Biophysica Acta (BBA) - Bioenergetics. 1992;1140(1):78-84. doi:https://doi.org/10.1016/0005-2728(92)90022-T.

311. Kley RA, Tarnopolsky MA, Vorgerd M. Creatine for treating muscle disorders. Cochrane Database of Systematic Reviews. 2013(6). doi:10.1002/14651858.CD004760.pub4.

312. Tarnopolsky MA. Creatine as a therapeutic strategy for myopathies. Amino Acids. 2011;40(5):1397-407. doi:10.1007/s00726-011-0876-4.

313. Gualano B, Artioli GG, Poortmans JR, Lancha Junior AH. Exploring the therapeutic role of creatine supplementation. Amino Acids. 2010;38(1):31-44. doi:10.1007/s00726-009-0263-6.

314. Brookes PS, Yoon Y, Robotham JL, Anders MW, Sheu SS. Calcium, ATP, and ROS: a mitochondrial love-hate triangle. American journal of physiology Cell physiology. 2004;287(4):C817-33. doi:10.1152/ajpcell.00139.2004.

315. Gaglianone RB, Santos AT, Bloise FF, Ortiga-Carvalho TM, Costa ML, Quirico-Santos T et al. Reduced mitochondrial respiration and increased calcium deposits in the EDL muscle, but not in soleus, from 12-week-old dystrophic mdx mice. Scientific Reports. 2019;9(1):1986. doi:10.1038/s41598-019-38609-4.

316. Beck J, Weinberg J, Hamnegård C-H, Spahija J, Olofson J, Grimby G et al. Diaphragmatic function in advanced Duchenne muscular dystrophy. Neuromuscular Disorders. 2006;16(3):161-7. doi:https://doi.org/10.1016/j.nmd.2006.01.003.

Appendix A - Detailed Experimental Methods

A.1 - SkyScan 1278 – Scanning an Animal

1. Open Skyscan 1278
2. Click X-Ray button – if this is the first time the machine has been used in a while, it can take up to 10 minutes for the x-ray to warm up
3. With nothing in the machine, you must update the bright and dark flat field
    a. Option: Update flat field for current mode
    b. Want background of mouse to be grey colour not white – want average to be 90% not 100%, 100% is saturated
4. Set your parameters
    a. Resolution (# of pixels): 50, 100 or 200 microns
    b. Filter (energy, controls x-ray voltage): 0, 0.5mm, 1mm aluminum or low dose
5. Load mouse, make sure mouse is centered and arms and legs are taped down
6. Click the TV screen icon to turn on x-ray and bring up live image of mouse
7. Right click to bring up transmission values
    a. Want a minimum value of 20-30%, if this is too high, lower the filter in the bottom right corner
    b. If you change any parameter values, you must update the flat field
8. Click the green arrow to bring up scanning parameters
    a. For 50 + 100 microns – use step and shoot
    b. For 200 microns – use continuous acquisition
    c. For a mouse, use 180°. For a rat, use 360°

** Make sure the parameters used are the same for entire study

9. Click scan

A.2 - SkyScan 1278 μCT - % Body Fat

Step 1) Open the reconstructed images made in NRecon software. They are saved in the folder containing the original scans. Click on the firs image and press open.

Step 2) Click on the icon of square with magnifying glass. This opens the profile tab (sometimes the profile tab do not fully open and gets hidden on top of palette tab. You can open the profile tab by double clicking on it). Click on the icon of black square with snowflake on it (it is called maximum intensity projection). This opens the maximum intensity projection tab. Click on Ok button. This will generate a coronal view of the animal so that you can navigate better. Click on the icon of magnifying glass with the arrow next to it (called send image into projection window) and then click on the icon on the right (called close window).

Step 3) This step is called "thresholding". Click on the icon of black and white cactus (called binary selection preview) on the top. This will open the binary selection tab (next to raw images tab) in the top, and the histogram tab in the bottom. When you perform these steps, the transverse view of the animal turns into a black and white (binary) preview. This view is hard to highlight fat. Click on the colored cactus image with a red dot in background (called toggle half tone view) in the histogram tab. This will bring back the original transverse preview of the animal under a green filter. Open "from dataset" tab in the histogram tab. On the binary view, scroll down to the very bottom slice (or any slice that shows fat clearly). Highlight fat accurately using the selectors on top and bottom of the histogram (the highlighted area will be red in the transverse view).
Sometimes, a part of the lung will stay in slices after reconstruction. To check for that, scroll to the top slices in binary selection. The lung usually appears in the top few slices. They have to be removed because they get highlighted as fat. To do so, find the first slice from the top in the binary selection that does not contain the lungs. Left click on that slice and select "set the top of the selection". This will eliminate the slices that contain lungs. Then click on the icon of histogram with an arrow on top (called automatic thresholding). This will highlight the entire animal together with isoflurane tube and the mouse housing.

Step 4) In this step, we separate the isoflurane tube and the housing from the animal. To do so, we need to create a region in space that **only** contains the animal called region of interest (ROI). Click on the hexagonal colored cactus icon (called regions of interest preview). This will open the regions of interest tab next to raw images tab. In this step, the transverse view is colored red. This makes it hard to visualize the animal. From the palette tab, select the filter that works best for you (from experience, "color" shows the fat better, but "color 2" shows the edges better than the "greyscale").

Step 5) In this step we create the ROI. To create the ROI we draw shapes around the mouse every few slides from bottom to top. Software will generate a 3D space by connecting these shapes along the longitudinal axis of the animal. This space separates the animal from the housing and the isoflurane tube.
Shapes are drawn manually by mouse. You need to hold the right click while drawing the shapes. When drawing the shapes, make sure to avoid the tube and the housing. If you need to remove a

shape, click on the scissors icon (called cut ROI) on the top. Go up and down inslices to make sure ROI contains **all** of the animal and **non** of the tube and the housing.

Step 6) Click on the icon of the face on the top (called custom processing preview). This will open the custom processing tab, next to binary selection tab, and the plug-ins tab on the bottom. Go to the internal tab in the plug-ins tab. Click on the thresholding section. This will open threshold tab. Leave the setting as global and check the default box. Then click ok.
To run every step in internal tab, you need to press play and then press continue.
This will highlight everything that you selected in the thresholding step and turn it into binary.

Step 7) In this step, we remove the isoflurane tube and the housing from the animal. The internal tab has 4 views. You can navigate them using 4 icons on the right. These views, from left to right, are "Image", "Image inside ROI", "ROI", and "Clipboard".
From the internal tab, click on the "Bitwise operations". The way that bitwise operations works is similar to Venn diagrams with the same logical rules of "and", "or", "not" etc. Bitwise operations allow you to modify the "Image" using the shapes in other views. When you click on the bitwise operations, it will open bitwise operation tab. Put the settings in the following way: Image = Image AND Region of Interest.
This will remove the isoflurane tube and housing.

Step 8) In this step, you need to modify the image. Parts of the housing or the tube might still stay in the image that must be removed. Click on "Despeckle". Select the settings according to the image (in the remove section, the largest object is the highlighted animal). Click on the play icon to run the despeckle.
Some parts of the tube or the housing may still be attached to the animal. To remove them click on the "Morphological operations". Select the settings according to the image and press ok.
Always despckle after any morphological operation to remove any speckles that might be created.
You need to save the image after the modifications. Software allows you to save the image only in the clipboard view. To do so, click on the "bitwise operations". Set the setting as follow: Clipboard = Image AND Image.

Step 9) In this step, we turn the image into a solid region. To do that, click on the "ROI shrink-wrap". Make sure that it is applied to 2D space. The default should be to keep "stretch over the holes" unchecked. But, if there are dips in the image you need to check that box. You also need to assign a diameter measured in pixels. The diameter should be set as the lowest number possible because this will increase the ROI volume. The right diameter is found through trial and error. Start with a high diameter (20 pixels) and work your way down. When you click on OK, a solid shape that has all the holes filled will be created in the ROI view in the internal tab. If the dip is covered, click on the bitwise operations and put the settings as follow: Image = clipboard AND clipboard. This will load the image again. Go back the "ROI shrink-wrap and put a lower diameter. Repeat these steps until you reach the lowest diameter that covers all the dips.
Until now, we have created a space in ROI that consist of the entire mouse. This space will be the total volume which is the denominator in the percent body fat formula. Now we need to select the fat.

Step 10) Click on the bitwise operation and put the setting as follow: Image = region of interest AND region of interest. Then click OK.

Step 11) In this step, we threshold the fat. Go back to the binary selection tab. Scroll down to the very bottom slice (or any slice that shows fat accurately). Use the selectors on top and bottom of the histogram and highlight fat (it should be the same thresholding values as you found in step 3).

Step 12) Go back to the custom processing tab. Click on the internal tab. Click on the "Reload". This will open the reload tab. Set apply to "Image" and then click OK. This will load the original image in the transverse view (make sure you are in the image view of the internal tab).
Click on thresholding and then click OK. This will highlight the parts of the animal (fat) that was selected in step 11 and turn the entire image into binary.
Click on the bitwise operations and put the settings as follow: Image = Image AND Region of Interest. This will remove the isoflurane tube and the housing from the selected area of the animal.

Step 13) Click on the "3D Analysis" in the internal tab. This will open 3D analysis tab. Leave the settings as it is and click on OK.
This step will perform the 3D calculations to measure the percent body fat.
To see the results, go to the Output/Report tab and click on the first Open from the top. This will open a text file containing the results. Scroll down to the very bottom and you can find the results. Measurements are made in mm^3. Total VOI volume is the volume of ROI. It is the total volume of the animal that was selected which is the denominator of the percent body fat formula. Object volume is the volume of fat, the numerator of the percent body fat formula. Percent object volume is the percent body fat which is calculated by dividing object volume by total VOI volume.

A.3 - SkyScan 1278 μCT - Analyzing Hind-Limb Muscle Volume

Step 1) Open the reconstructed images made in NRecon software. They are saved in the folder containing the original scans. Click on the firs image and press open.

Step 2) Click on the icon of square with magnifying glass. This opens the profile tab (sometimes the profile tab do not fully open and gets hidden on top of palette tab. You can open the profile tab by double clicking on it). Click on the icon of black square with snowflake on it (it is called maximum intensity projection). This opens the maximum intensity projection tab. Click on Ok button. This will generate a coronal view of the animal so that you can navigate better. Click on the icon of magnifying glass with the arrow next to it (called send image into projection window) and then click on the icon on the right (called close window).

Step 3) Click on the image of black and white cactus (called binary selection preview). Click on the "from dataset" tab in histogram tab. Go to the top slices in the binary tab. Scroll up and down until you find the knee joint. In the transverse view (superior part of the tibia has a curved shape in coronal view; therefore, it will be shown like two parallel ovals in transverse view). Left click on the slice that it the top of the tibia and select "set the top of selection". This will eliminate the higher slices from the selection.
Use the selectors on top and bottom of the histogram to select muscle. Muscle is usually the second spike after on the right of the spike for fat. Use the top slices to highlight muscle.

Step 4) In this step, we separate the isoflurane tube and the housing from the animal's leg. To do so, we need to create a region in space that **only** contains the animal called region of interest (ROI). Click on the hexagonal colored cactus icon (called regions of interest preview). This will open the regions of interest tab next to raw images tab. In this step, the transverse view is colored red. This makes it hard to visualize the animal. From the palette tab, select the filter that works best for you (from experience, "color" shows the fat better, but "color 2" shows the edges better than the "greyscale").

Step 5) In this step we create the ROI. To create the ROI we draw shapes around the leg every few slides from bottom to top. Software will generate a 3D space by connecting these shapes along the longitudinal axis of the animal. This space separates the animal's leg from the housing and the isoflurane tube.
Shapes are drawn manually by mouse. You need to hold the right click while drawing the shapes. When drawing the shapes, make sure to avoid the tube and the housing. If you need to remove a shape, click on the scissors icon (called cut ROI) on the top. Go up and down in slices to make sure ROI contains **all** of the animal's leg and **non** of the tube and the housing.

Step 6) Click on the icon of the face on the top (called custom processing preview). This will open the custom processing tab, next to binary selection tab, and the plug-ins tab on the bottom. Go to the internal tab in the plug-ins tab. Click on the thresholding section. This will open threshold tab. Leave the setting as global and check the default box. Then click ok.
To run every step in internal tab, you need to press play and then press continue.

This will highlight everything that you selected in the thresholding step and turn it into binary.

Step 7) In this step, we remove the isoflurane tube and the housing from the animal's leg. The internal tab has 4 views. You can navigate them using 4 icons on the right. These views, from left to right, are "Image", "Image inside ROI", "ROI", and "Clipboard".
From the internal tab, click on the "Bitwise operations". The way that bitwise operations works is similar to Venn diagrams with the same logical rules of "and", "or", "not" etc. Bitwise operations allow you to modify the "Image" using the shapes in other views. When you click on the bitwise operations, it will open bitwise operation tab. Put the settings in the following way: Image = Image AND Region of Interest.

Step 8) Click on the "3D Analysis" in the internal tab. This will open 3D analysis tab. Leave the settings as it is and click on OK.
To see the results, go to the Output/Report tab and click on the first Open from the top. This will open a text file containing the results. Scroll down to the very bottom and you can find the results. Measurements are made in mm^3. Object Volume is the hind limb muscle volume.

A.4 - *In Vivo* Hind-limb Plantarflexor Force Production

See attached video for step up procedure (1).

In Vivo force is measuring Torque production (mN/m)

BEFORE STARTING ENSURE UNITS ARE CORRECT, IF NOT:
SETUP:CHANNEL SETUP:FORCE IN DEVICE – select mN/m

Protocol

1. Create a folder to save files for each animal - Setup:Autosave Folder, open folder you created; click "current folder"
2. Setup:Instant Stim
    a. Pulse Frequency: 1Hz
    b. Pulse Width: 0.2ms
    c. Number of Pulses: 1
    d. Train Frequency: 0.1Hz
    e. Run Time: 1 second
3. Open Live Data monitor and set time to 10 minutes
4. Optimize Current
    a. Range:100mA
    b. Run instant stim
    c. Adjust range to ensure all muscle fibres are being recruited – obtain 3 twitches in a row where force does not increase (run instant stim and increase current between twitches (wait about 30 seconds in between twitches)
    d. Set supramaximal current by increasing current by 15%
5. Optimize Resting Length
    a. Increase/decrease length of quad until maximal twitch force is achieved, wait about 30 seconds in between twitches to avoid fatigue

Once optimal current and length have been set, protocol is ready to begin

6. Load **"In Vitro Torque Frequency"** sequence
    a. Frequencies of 40Hz, 60Hz, 80Hz, 100Hz, 120Hz, 140Hz, 160Hz, 180 Hz, 200Hz
        i. Initial Delay: 200ms
        ii. Pulse Frequency: ____Hz
        iii. Pulse Width: 0.2ms
        iv. Duration: 300ms
    b. 30 seconds in between
7. Allow 5 minutes of recovery
8. Load the tetanic protocol at the frequency that produced the highest torque during step 6
9. Perform Max Force Test – make sure to save this file!
10. Allow 2 minutes recovery
11. Load "**In Vitro Fatigue"** sequence
    a. 60 Hz, stim every second for 120 seconds
    b. 300ms stimulation, 700ms rest
    c. 119 repeats (total of 2 minutes)
12. Allow 10 minute recovery from fatigue
13. Perform a second max torque test at the same frequency used in step 8 – this assesses recovery from fatigue

14. Wait 5 minutes

15. Load "**Eccentric Contraction – Injury"** protocol
    a. Set offset on main DMC screen to -19, this allows for full range of motor of the foot plate
    b. 30° translation of the footplate at a velocity of 40mm/s after the first 200ms of the isometric contraction
    c. 20 times, 45 seconds in between
    d. Allow 10 minute recovery from injury
    e. Perform a third max torque test at the same frequency used in step 8 – this assesses recovery from injury

A.5 - *In Situ* Quadriceps Force Production

See attached paper for step up procedure with videos (1).
In Situ force is measuring force production (mN)
BEFORE STARTING ENSURE UNITS ARE CORRECT, IF NOT:
SETUP:CHANNEL SETUP:FORCE IN DEVICE – select mN

Protocol

1. Create a folder to save files for each animal - Setup:Autosave Folder, open folder you created; click "current folder"
2. Setup:Instant Stim
    a. Pulse Frequency: 1Hz
    b. Pulse Width: 0.2ms
    c. Number of Pulses: 1
    d. Train Frequency: 0.1Hz
    e. Run Time: 1 second
3. Open Live Data monitor and set time to 10 minutes
4. Optimize Current
    a. Range:100mA
    b. Run instant stim
    c. Adjust range to ensure all muscle fibres are being recruited – obtain 3 twitches in a row where force does not increase (run instant stim and increase current between twitches (wait about 30 seconds in between twitches)
    d. Set supramaximal current by increasing current by 15%
5. Optimize Resting Length
    a. Increase/decrease length of quad until maximal twitch force is achieved, wait about 30 seconds in between twitches to avoid fatigue

Once optimal current and length have been set, protocol is ready to begin

6. Load **"Quad In Situ Force Frequency"** sequence
    a. Frequencies of 40Hz, 60Hz, 80Hz, 100Hz, 120Hz, 140Hz, 160Hz
        i. Initial Delay: 0.2ms
        ii. Pulse Frequency: ____Hz
        iii. Pulse Width: 0.2ms
        iv. Duration: 300ms
    b. 45 seconds in between
7. Allow 5 minutes of recovery
8. Load the tetanic protocol at the frequency that produced the highest force during step 6
9. Perform Max Force Test – make sure to save this file!
10. Allow 2 minutes recovery
11. Load "**Quad In Situ Fatigue"** sequence
    a. 60 Hz, stim every second for 120 seconds
12. Allow 10 minute recovery from fatigue
13. Perform a second max force test at the same frequency used in step 8 – this assesses recovery from fatigue
14. Harvest muscle and before freezing **MAKE SURE TO RECORD MUSCLE WEIGHT**

***Data will be normalized to muscle mass*

A.6 - *In vitro* Diaphragm Strip Force Production

See attached paper for protocol (1) and step up procedure with videos (2).

In Vitro force is measuring force production (mN)

BEFORE STARTING ENSURE UNITS ARE CORRECT, IF NOT:
SETUP:CHANNEL SETUP:FORCE IN DEVICE – select mN

Protocol

1. Create a folder to save files for each animal - Setup:Autosave Folder, open folder you created; click "current folder"
2. Setup:Instant Stim
    a. Pulse Frequency: 1Hz
    b. Pulse Width: 0.2ms
    c. Number of Pulses: 1
    d. Train Frequency: 0.1Hz
    e. Run Time: 1 second
3. Open Live Data monitor and set time to 10 minutes
4. Optimize Current
    a. Range:100mA
    b. Run instant stim
    c. Adjust range to ensure all muscle fibres are being recruited – obtain 3 twitches in a row where force does not increase (run instant stim and increase current between twitches (wait about 30 seconds in between twitches)
    d. Set supramaximal current by increasing current by 15%
5. Optimize Resting Length
    a. Increase/decrease length of diaphragm until maximal twitch force is achieved, wait about 30 seconds in between twitches to avoid fatigue
6. Measure the length of the diaphragm and record, this is L_O and can be input on the main DMC screen and will be used for analysis
    a. Setup:Normalization – enter reference length in mm

Once optimal current and length have been set, protocol is ready to begin

7. Load **"Diaphragm In Vitro Force Frequency"** sequence
    a. Frequencies of 1Hz, 10Hz, 20Hz, 40Hz, 60Hz, 80Hz, 100Hz, 120Hz, 140Hz
        i. Initial Delay: 0.2ms
        ii. Pulse Frequency: ____Hz
        iii. Pulse Width: 0.2ms
        iv. Duration: 400ms
    b. 60 seconds in between
8. Allow 5 minutes recovery
9. Load the tetanic protocol at the frequency that produced the highest force during step 7
10. Perform Max Force Test – make sure to save this file!
11. Allow 2 minutes recovery
12. Load "**Diaphragm In Vitro Fatigue"** sequence
    a. 70 Hz (350ms stim, 0.2ms pulse width) every 2 second for 5 minutes
13. Allow 10 minute recovery from fatigue

14. Perform a second max force test at the same frequency used in step 8 – this assesses recovery from fatigue
15. Harvest muscle and before freezing **MAKE SURE TO RECORD MUSCLE LENGTH AND MUSCLE WEIGHT (remove muscle from ribs/central tendon before weighing)**

***Data will be normalized to muscle cross sectional area: mass x length x density*

- *Mammalian skeletal muscle density = 1.06 g/cm^3 (Mendez and Keys, 1960)*

Rodent Ringer's Solution – Bombardier et al 2013

Chemical	Molecular Weight	Weight (g) for 1L	Final Concentration (mM)
$NaCl_2$	58.4	7.07	121
KCl	74.6	0.373	5
$NaHCO_3$	84.0	2.016	24
$CaCl_2$	147.02	0.26	1.8
NaH_2PO_4	119.98	0.05	0.4
Glucose	180.16	0.99	5.5
EDTA	292.24	0.029	0.1
$MgCl_2$	203.3	0.10	0.5
pH to 7.3			

A.7 - Serum Creatine Kinase

Assay is done using Pointe Scientific Serum CK Kit (**C7522**)

1. Set Excitation to 340 and Emission to 450
2. Each sample will be run in duplicates and therefore requires 500ul of assay buffer
    a. # of samples x 2 x 250ul = total buffer volume
    b. Mix Buffer 1 and Buffer 2 in a 4:1 ratio to get the total buffer volume required
3. Load 250ul of assay buffer into small cuvette and let background run for 3 minutes – this allows buffer to settle at 37 degrees
4. Add 1ul of serum into buffer
5. Record fluorescence for 5 more minutes
6. Repeat once more with same sample (if duplicates appear variable, a 3rd assay can be run but the duplicates are usually very consistent)

Standard Curve

1. Make up a stock of 1.12mM NADPH (1mg in 1mL water)
2. Load 250ul assay buffer into cuvette and obtain background for 3 minutes
3. Follow the following step wise titration waiting 2 minutes between additions:

Stock (mM)	Volume (ul) Added to Cuvette	Final [NADPH] in Cuvette (uM) (after dilution)
1.12	2.22	9.858
1.12	3.33	14.594
1.12	5.56	23.849
1.12	11.11	45.710

A.8 Measuring Mitochondrial Respiration

BIOPS Buffer

Chemical	Stock Solution	Molecular Weight	Final Concentration	Addition to *2 Litre* final volume
CaK_2EGTA*	100mM		2.77mM	55.4mL
K_2EGTA*	100mM		7.23mM	144.6mL
Na_2ATP		555.1	5.77mM	6.28g
$MgCl_2 \bullet 6H_2O$		203.3	6.56mM	2.67g
Taurine		125.1	20mM	5.02g
Na_2Phosphocreatine		327.14	15mM	9.81g
Imidazole		68.1	20mM	2.72g
Dithiothreitol (DTT)		154.2	0.5mM	0.154g
MES Hydrate		195.2	50mM	19.52g

** prepare stock solutions (see instructions below)*

BIOPS contains the following ion concentrations:	
Ca^{2+} Free	0.1 uM
Mg^{2+} Free	1mM
MgATP	5mM
Ionic Strength	160mM

CaK_2EGTA: Dissolve 2.002g $CaCO_3$ in 100mM hot (80°C) solution of EGTA (7.608g of EGTA in 200mL ddH_2O). Add 2.3g of KOH and adjust pH to 7.0 using KOH. Freeze unused portions

K_2EGTA: dissolve 7.608g EGTA and 2.3g KOH into 200mL ddH_2O. Adjust pH to 7.0 using KOH. Freeze unused portions

To make BIOPS:

1. Add approximately 1500mL of ddH_2O to 2000mL beaker
2. While constantly stirring add stock solutions of CaK_2EGTA and K_2EGTA
3. Weigh and add all powder chemicals
4. Adjust pH to 7.1 using KOH pellets
5. Using graduated cylinder, bring total volume to 2000mL
6. Filter and then aliquot into 50mL falcon tubes
7. Freeze falcon tubes

MiRO Buffer

Chemical	Stock Solution	Molecular Weight	Final Concentration	Addition to *2 Litre* final volume
EGTA		380.4	0.5mM	0.38g
$MgCl_2 \bullet 6H_2O$		203.3	3mM	1.22g
K-Lactobionate*	0.5M	358.3 free acid	60mM	240mL
Taurine		125.1	20mM	5.02g
KH_2PO_4		136.1	10mM	2.72g
HEPES		238.3	20mM	9.54g
Sucrose		342.3	110mM	75.3g
BSA		154.2	1g/L	2g

** prepare stock solution (see instructions below)*

MiRO contains the following ion concentrations:	
Ca^{2+} Free	0.0 uM
Mg^{2+} Free	2.1mM
K^+	90mM
Na^+	0
EGTA free	0.46mM
Osmolarity	330 mOsm
Ionic Strength	95mM

K-Lactobionate: Dissolve 71.6g lactobionic acid in 300mL ddH_2O, adjust pH to 7.0, adjust final volume to 400mL with ddH_2O

To make MiRO:

1. Add approximately 1500mL of ddH_2O to 2000mL beaker
8. While constantly stirring add stock solution of K-Lactobionate
9. Weigh and add all powder chemicals
10. Adjust pH to 7.1 using KOH pellets
11. Using graduated cylinder, bring total volume to 2000mL
12. Filter and then aliquot into 50mL falcon tubes
13. Freeze falcon tubes

Chemical Bank

Chemical	Stock Concentration	Dissolved in:	Storage after Removal
Glutamate	500mM, 1M, 2M	Water	Fridge
Malate	1M	Water	Fridge
Succinate	500mM, 1M, 2M	Water	Fridge
ADP	5mM, 50mM, 500mM	Water	Fridge

Oligomyocin	4mg/mL	Ethanol	Freezer
FCCP	1mM	Ethanol	Freezer
Rotenone	1mM	Ethanol	Freezer
BLEB	10mM	DMSO	Fridge
Cytochrome C	4mM	Water	Fridge
P.Carn	10mM	Water	Fridge
PCoA	10mM	Water	Fridge
L-Carnitine	200mM	Water	Fridge
Antimycin A	5mM	Ethanol	Freezer

Permeabilized Fibre Preparation

Pre-surgery

1. For every fibre bundle you are going to make you will need one 0.5mL tube for wet weights one 1.5mL eppendorf tube for permeabilization and one 1.5mL tube for wash

* Keep all tubes and buffers on ice

2. In a 5mL tube, make 10mg/mL Saponin solution by dissolving a small amount of saponin in distilled water
    a. Vortex gently and place on rocker until ready for use
3. Fill all permeabilization tubes with 1.5mL of freshly thawed BIOPS (or BIOPS from fridge with fresh EGTA…see "Other Things to Consider") and *40ug/mL saponin (6uL in 1.5mL BIOPS).
    a. * different saponin concentrations may be used depending on species/tissue type but 40ug/mL is standard for rodent
4. Fill all wash tubes with 1.5mL freshly thawed MiRO (or from fridge…same as above)
5. Fill all 0.5mL tubes with 500uL of BIOPS
6. Using a 50mL falcon tube, weigh out ~ 0.05g of creatine (this number will change based on the number of chambers you need with creatine), add the correct amount of MiRO to make a 20mM Creatine MiRO Solution
    a. Place on rocker as creatine takes some time to dissolve
7. Label and fill a 5mL tube with 3.5mL BIOPS for every muscle that will be harvested during surgery
8. Proceed to "O2k Setup" Section, after O2k's are setup you are ready for surgery

Post-Surgery

1. Separate fibres in BIOPS as quickly and carefully as possible
    a. Remember to change ice block/ice pack frequently as buffer should never be allowed to warm up
2. Place separated fibres in corresponding 0.5mL tube with BIOPS and proceed to wet weight procedure

Bundle Wet Weights

1. Fill a 1.5mL tube with BIOPS until a dome of liquid covers the top
2. Place tube in holder on scale and tare the scale

3. With fine forceps remove first bundle from eppendorf and using a kim wipe, blot the bundle to remove excess liquid
    a. Try to blot no more than 3 times and try to turn the bundle the same way each time to get consistent blotting
4. Very carefully place bundle in liquid on scale, making sure the forceps to not draw up any liquid
5. Wait for scale to stabilize and record weight
6. Until accuracy is proven, do duplicates of each weight and take average if within 0.2mg, repeat weighing if weights are more variable
7. When done weighing, place back in 0.5mL eppendorf tube until all bundles have been weighed

Permeabilization

1. Once all bundles are weighed, switch bundles to permeabilization tubes (the ones that have saponin) using forceps or a gel loading pipette tip
2. Place on nutator in the fridge for 30 minutes
    a. Make sure all eppendorfs have the liquid mixing by ensuring that the air bubble is moving
    b. If air bubble appears stuck, invert eppendorf 1-2 times to allow for movement and place back on nutator
3. After 30 minutes, transfer bundles to corresponding wash tubes using gel loading pipette tip
4. Place bundles in wash back on nutator in the fridge for 15 minutes
    a. Permeabilized bundles can remain in fridge in wash for up to 2 hours but will start to lose viability after that point so use bundles ASAP
5. After 15 minute wash proceed to "Running an Experiment"

<u>Using the O2k</u>

O2k Setup

1. Using the switch on the back of the machine, turn machine on
2. Open up DatLab and a connection box should pop up
    a. For O2k 1 and O2k 2
        i. O2k 1 – USB: E-0085
        ii. O2k 2 – Com 3: C-0024
    b. When connection box pops up ensure the top blue bar says E-0.0085
    c. If it does not, click the configuration tab, click "select communication port" and select USB
    d. Click the control tab and click "Connect to Oxygraph-2k"
    e. A screen will pop up asking you to change the file name, save file in location of choice
    f. An "Edit Experiment" screen will appear, click "Save"
    g. After O2k 1 is connected, open DatLab again and an error screen will appear, change the serial port to "Com 3" and click ok
    h. Follow steps d-f for O2k 2
    i. For O2k 3 and O2k 4
        i. O2k 3 – Com 3: D-0008

ii. O2k 4 – Com 4: D-0098

j. Follow steps b-g for O2k 3 and O2k 4

3. Remove stoppers and place with top down on top of the O2k
4. Turn on the aspirator and remove ethanol from chambers…keep aspirator AWAY from membrane inside the chamber
    a. the best way to ensure this is to only touch the bottom of the chamber on the wide opposite the membrane to avoid contact
5. Fill chambers with water and aspirate out water
    a. When cleaning chambers be sure to not let chambers stay dry for very long, always replace liquid immediately
6. Repeat rinse with ethanol
7. Finish with 3 rounds of water rinses and leave spinning in water until ready to load buffers
   * If this is the first experiment of the day do Volume Calibration before loading buffers
8. Load chambers with 2.1mL Creatine MiRO (or just regular MiRO if no creatine is wanted)
9. Push stoppers down and adjust height with the plastic wrench so both stoppers are at the same height
10. Wait for both O_2 Concentration and O_2 Slope to reach steady state and then proceed with "Air Calibration"

Volume Calibration

1. Volume calibrate chambers at the start of each day but it is not necessary to do in-between rounds of experiments
2. Add 2.1mL of water to each chamber
3. Using the allen wrench found in the O2k Accessory kit loosen the collar on the stopper and push it all the way to the top
4. Slowly lower stopper into chamber until the first bit of liquid comes out the top of the capillary in the stopper
5. Push the collar all the way to the bottom and tighten with allen wrench

Air Calibration

1. When a steady state has been achieved, click on the blue Y_1 box in the top right corner of chamber A
2. Holding down the shift button, use your mouse, click down and drag across the steady O_2 concentration line to create a "mark"
3. Click "F5"
4. Select 01 in the "Select Mark" box for the "Air Calibration" line

If the sensors are working properly, your [O_2] should be somewhere between 180 and 200 units during air phase. If this value is too high or too low:

1. Confirm that O_2 solubility is set to 0.92 for MiRO (F5 screen)
2. Wash out chamber very well and re-do air phase – if this doesn't fix the values, membrane likely needs to be changed and the sensor needs to be cleaned

<u>Running an Experiment</u>

1. When fibres are done washing and chambers have been air phased, remove stoppers and place on top of O2k
2. Add 5uM BLEB and stop the stir bar pressing F11 for Chamber A and F12 for Chamber B

3. Add fibre and loosely place stopper in chamber (do not push down at all)
4. Turn stir bar back on by clicking F11 and F12
5. Add a very small amount of O_2 with syringe through capillary in stopper
6. Wait until O_2 concentration reaches ~350 and remove stopper, O_2 concentration will continue to rise, when the levels begin to fall push stopper in all the way so there is a tight seal between the chamber and stopper
7. Ensure there is no air bubble in the chamber
8. If no air bubble, press F10 to shut off lights
9. If there is an air bubble, remove stopper, add more buffer and repeat steps 5-8
10. Wait for background to reach a steady state…this usually takes 10+ minutes (see "Important Considerations, proceed with following protocol (remember to always achieve a steady state after the addition of a substrate)
    a. See "Important Considerations" for important tips on setting up syringes/beakers and substrates
11. In order to record when you add each substrate, by clicking "Control" and Left Clicking your mouse on the spot on the graph that you added a substrate you can make an event
    a. A screen will pop up allowing you to name your event and you can pick whether it is for Chamber A, Chamber B or both
    b. Do this after the addition of each substrate
12. At the end of the experiment, turn lights on clicking F10 and stop stir bars
13. Remove tissue if being saved and place in labeled eppendorf
14. Turn stir bars back on and proceed with cleaning
    a. 2 water washes
    b. 2 ethanol washes
    c. 1 water wash
    d. Add 70% ethanol and leave in chamber
    e. Rinse stoppers in sink with water and ethanol
    f. Place stoppers loosely in chamber with caps on and turn off machine

Analyzing Data

1. Open file you wish to analyze and click "F3"
2. In the box labeled "background correction" click "Copy from File"
3. Select the O2k file that contains your most recent background curve for that machine (See "Background Curve" section)
    a. Note you can also manually enter the slope and y-intercepts from your background curve in each file
4. Click save
5. In the top right corner of Chamber A, click on Y_2 so the red box is highlighted
6. Using the technique to "make a mark" like you did for air calibration, make marks for each of your steady states following a substrate addition as well as your background steady state
    a. If you make a mark and wish to delete it, hold shift and right click your mouse and drag over the mark you wish to delete, then let go and the mark will disappear
7. Once all marks are made, click "layout" at the top of the screen and select "05 Flux per Volume Corrected"
    a. Your data is not corrected using the background curve you imported
8. Click F2 and select copy to clipboard, your data can now be pasted into excel

9. Repeat steps 5-8 for Chamber B
    a. Note that while clicking F2 and pasting will export both Chamber A and Chamber B data…the data is not accurate unless you see the "X" beside that chamber in the pasted data (glitch in the system)

POS Service and Membrane Mounting

** Membranes should be changed and electrode should be cleaned when data appears excessively noisy or air calibration curves have dropped below normal**

** See O2k Manual for detailed instructions and pictures

POS Service

1. IMORTANT: make sure to touch somewhere on the sides of the O2K to de-static yourself before removing the sensors
2. Pull back the blue sheath and slowly remove sensor from inside the system
3. Unplug the wire from the port on the O2K (should be plugged in to the port labeled O_2)
4. Remove the black cap from the sensor and keep in safe place as this may be reused
5. Using the black "membrane mounting tool" use the open end of the smaller piece to squeeze and remove the membrane ring off the sensor head
6. Using clean forceps remove the membrane from the top of the sensor and discard
7. Using distilled water, rinse sensor 1-2 times with water but covering sensor until dome of water appears and then dump water off
8. If gold cathode looks dirty (not shiny, dark grey colour) it must be cleaned with extreme care
    a. Using the "O2K Polishing Cloth" that is in the O2K accessory kit, add a small amount of "polishing powder" to the top of the cloth and wet with distilled water
    b. Place the top of the centre face down on the cloth and very gently make small circles using the cloth and powder to clean the cathode, continue until cathode appears gold and shiny again
9. Rinse sensor with distilled water 1-2 times
10. The anode also becomes oxidized over time changing it from a cream colour to a dark grey colour, when this happens it must be cleaned with 25% ammonia
11. Under fume hood, cover sensor with 25% ammonia until a dome appears, leave for 10 minutes
12. Repeat 1-2 times until grey colour disappears, if anode is very dark it may require overnight treatment with ammonia and/or a higher percentage solution of ammonia
13. If leaving overnight in ammonia seal ammonia in with membrane (see below) and make sure sensor is protected from light
14. After cleaning, rinse 1-2 times with water to make sure all traces of ammonia are removed

Membrane Mounting

1. If this is the first time mounting a membrane, fill "electrolyte solution" up to the 10mL mark with distilled water
    a. This is simply 1M KCl (you can also dissolve 1.49g KCl in 20mL water)
2. Cover sensor with electrolyte until dome appears
3. With forceps, remove a membrane from the membrane box avoiding contact with skin and making sure to remove the paper on either side of the membrane

4. Using the wider piece of "membrane mounting tool", place membrane flat on the ledge inside the tool
5. Pull down sheath on blue POS connector and place membrane mounting tool on top of sensor, letting go of sheath so it locks in place with the membrane lying flat on top of the electrolyte solution
6. Place membrane ring around circle on the end of the smaller piece of the membrane mounting tool
7. Using a good amount of force, going straight up and down push the smaller piece of the membrane mounting tool straight down on top of the membrane so the membrane ring locks in place
8. Remove both pieces of the membrane mounting tool (pull back sheath to remove bigger piece)
9. Check for air bubbles under the membrane, if there are considerable air bubbles you must restart at step 2 with a new membrane
10. Once membrane is mounted with no air bubbles, cover the sensor with the black rubber cap and make sure the entire gold cathode is visible
11. Plug connector wire into O_2 port, pull back sheath on POS and place sensor back in place in the O2k
12. Let Datlab run with the machine on for 24 hours to allow new membrane to equilibrate
    a. File will start off very noisy but by the end of 24 hours it should be a flat line, if file is still noisy, remove sensor and check membrane

* over time the black caps get looser, if you notice the chamber leaking after replacing the membrane, replace the black cap so there is a tighter seal

Background Curves

1. Set up O2k as you would for normal experiment (see "O2k Setup") loading chambers with 2.1mL of MiRO Buffer
2. When a steady state is achieved for the air phase, complete air calibration (see "Air Calibration")
3. Add O_2 to chambers until O_2 levels reach ~350, remove stoppers to ensure no air is trapped in stoppers
4. When O_2 levels start to drop, push stoppers in all the way and make sure there is no air bubble within the chamber
5. Allow for a background steady state to be achieved
6. Using the "zeroing powder" (dithionite) in the O2k accessory kit, mix a few grains of dithionite with distilled water and vortex
7. Add 1uL of dithionite solution to each chamber once a steady state is achieved
    a. It is impossible to know how much dithionite to add, you want the oxygen concentration to drop 30-40 units with each addition so with your first addition add 1uL, see how much it drops and add more if necessary
    b. Dithionite degrades over the course of the experiment so towards the end of the titration you will need a larger volume to get the same decrease in oxygen
8. after each addition wait for a steady state to be achieved, continue with dithionite additions until O_2 concentration reaches ~0. When O_2 looks to be reaching zero add a large amount of dithionite (~20uL) to ensure O_2 levels are at 0.

9. Once O_2 has reached zero, create a mark measuring O_2 concentration at the zero level in the same way you would make your air calibration mark
10. Click F5 and insert "02" in the zero calibration "select mark" box
    a. Note, "01" should already be inserted in the "air calibration" select mark box"
11. Click "Calibrate and Copy to Clipboard"
12. Click on the red Y_2 box in the upper right corner of each chamber to switch to "respiration mode", using the method for making marks (see "Air Calibration"), make marks for each steady state that occurs after a dithionite addition (including the background steady state)
13. With Chamber A highlighted (click anywhere on the chamber A box), select "F2" and then select "copy to clipboard"
14. In excel paste the data you have just copied from DatLab
15. Using the "O_2 Concentration (A)" and "O_2 Slope uncorr. (A)" data, create a graph with concentration on the y-axis and slope on the x-axis
    a. By having 7-10 points to use, you can drop outliers that do not fit the straight line model
16. Repeat steps 13-15 for chamber B
17. Record the slope and y intercept for each chamber
18. Back in your DatLab file click "F3" In the section that says "background correction" insert your y intercept for each chamber in the a° boxes and the slopes in the b° boxes and click save

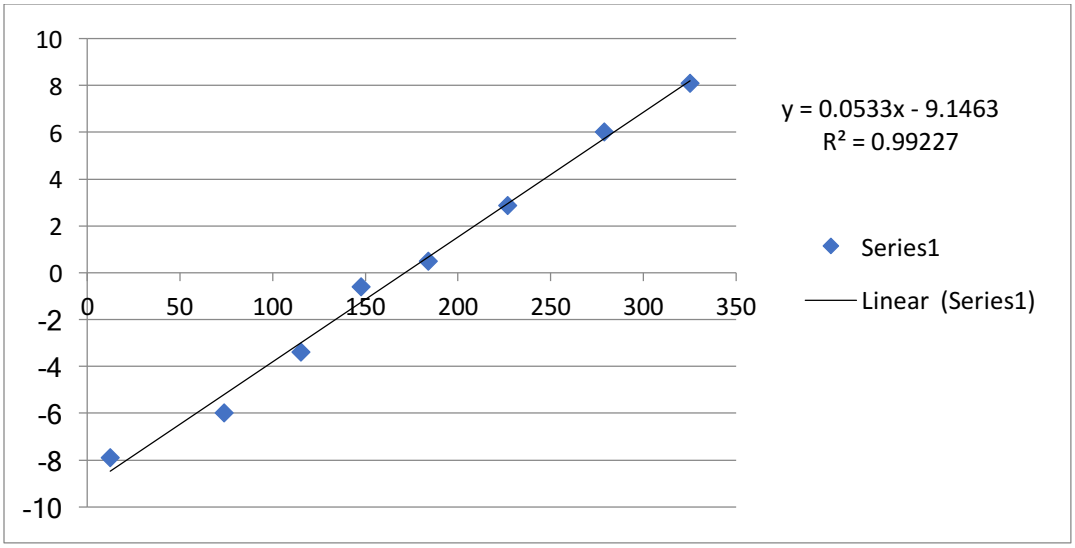

Important Considerations

Buffers

Buffers must be thawed fresh each day for actual data collection. When thawed, write the date of thawing on the tube and place any left over in the fridge. For practice, buffers in the fridge can be reused…if it was thawed <2 days prior, it is fine to use as is. If it was thawed 3 days prior or more (up to 1 week….throw out buffers that are more than a week old) it must be topped up with EGTA. To do this, pour buffer into graduated cylinder to get accurate volume. Thaw a 0.5M EGTA from the freezer and add corresponding volume to get the following final concentrations:

BIOPS: 10mM

MiRO: 0.5mM

Buffer Z: 1mM

Substrates

When making substrates, pH to 7.1 and aliquot into small volumes, enough for 6 chambers for 1 protocol. When running experiments, thawed substrates cannot be put back in the freezer, they must be placed in fridge and can be used for up to 1 week after thawing (except for FCCP, Oligomyocin and Rotenone, see below).

** ADP must be thawed fresh each day, do not reuse for actual data collection (ok for practice)

Pyruvate must be made fresh each day, make 2M solution in a 1.5mL eppendorf by combining power and water, throw out pyruvate at the end of each day.

Syringes and Beakers

Each protocol being followed should have it's own separate syringe and beaker filled with water. Syringes should be rinsed with water prior to use and should be wiped with a kim wipe after being put in the chamber to remove residual buffer. When switching substrates, syringes should be rinsed thoroughly with water.

IMPORTANT: FCCP, Oligomyocin and Rotenone have THEIR OWN SYRINGES AND BEAKERS. Beakers should be filled with ethanol and these inhibitors should never be near other syringes. Only use these labeled syringes for their specific chemical and keep beakers labeled and separate from other beakers being used. Additionally, these inhibitors can be placed back in the freezer after use as they are dissolved in Ethanol

Rotenone/Oligomyocin

Rotenone and Oligomyocin stick to the chambers even after multiple water/ethanol washes. It is necessary to use yeast to remove all residual chemicals. After your experiment, rinse chambers with 2 water washes and 2 99% ethanol washes. Then add a small scoop of yeast to each chamber and fill chamber with water. Allow yeast to spin for 10 minutes. Aspirate out yeast solution using aspirator (if yeast clumps in tip use pipette tip to loosen). Repeat yeast wash 2 more times for a total of 30 minutes in yeast. Rinse chambers with water 2-3 times or until there is no residual yeast left. Complete 2 more 99% ethanol washes and leave in 70% ethanol over night.

Steady States

It is very important to make sure a steady state is achieved before each addition in order to get accurate data. When waiting for background steady state (after adding fibre but before adding any substrates) wait until respiration has leveled out ABOVE zero. If the background is below zero respiration will be a negative and all data will be corrected for a negative rate. This may take 10+ minutes to achieve proper steady state.

After adding Glutamate/Pyruvate/Malate respiration often tends to slowly increase, again, make sure you have an accurate steady state so you do not end up over estimating this rate and getting a lower rate with your first substrate addition (may need to way 5+ minutes).

If data is very noisy, make a large mark over steady state as opposed to trying to find a small flat line. Taking a larger area average will give a more accurate reading.

Oxygen Levels

Do not let oxygen levels drop below 150. If oxygen is below 200, make next addition and wait for steady state, once respiration has achieved steady state, loosen stopper and re-oxygenate up to 350. Push stopper back in and wait for steady state. Often when reoxygenating, respiration rates steady state higher than before reoxygenation, if this happens, take an average of the rate before reoxygenation and after reoxygenation and then proceed with adding next addition.

A.9 Measuring Mitochondrial H_2O_2 Emission

Buffer Z

Chemical	Molecular Weight	Final Concentration	Addition to *500mL* final volume
K-MES	233.33	105mM	12.26g
KCl	74.55	30mM	1.12g
KH_2PO_4	136.08	10mM	0.7g
$MgCl_2 \bullet 6H_2O$	203.3	5mM	0.51g
EGTA	380.35	1mM	0.19g
BSA		5mg/ml	2.5g

To make Buffer Z:

14. Add approximately 400mL of ddH_2O to 1000mL beaker
15. Weigh and add all powder chemicals
16. Adjust pH to 7.4 using KOH pellets
17. Using graduated cylinder, bring total volume to 500mL
18. Filter and then aliquot into 50mL falcon tubes
19. Freeze falcon tubes

Amplex Ultra Red – Preparation

Total volume per experiment: 1000ul
Total volume per black tube: 1050ul

Stock A and B ingredients required:

Amplex Ultra-Red (Invitrogen A36006)
5000 IU/ml Cu/Zn Superoxide dismutase (SOD1; Sigma S9697)
10mM Blebbistatin (BLEB; Cayman)
DMSO
Buffer Z (5mg/ml BSA)
0.5M EGTA (aliquots in freezer)

Stock B additional ingredients:

20mM Creatine hydrate

Final concentrations for both AUR Stock A and AUR Stock B:

10uM AUR
5uM BLEB
25U/ml Cu/Zn SOD1
2mM EGTA

Work fairly quickly given AUR and BLEB should not be stored on ice. Best to prepare with lights out in lab as AUR and BLEB are light sensitive.

Preparation of AUR Stock A (No Creatine):

Step 1: Prepare 5mM AUR. Add 666.6ul of DMSO to 1mg AUR. Vortex gently. Prepare in black tube but do not place on ice (DMSO will freeze).

Step 2: Prepare 10mM BLEB. Add 1.71 ml DMSO to 5mg bottle of BLEB. Prepare in black tube but do not place on ice.

Step 3: Prepare 10uM AUR stock. Mix the following:

- 160.6 ml of Buffer Z (5mg/ml BSA). Note: sucrose buffers lower oxidant emission.
- 325ul of 5mM AUR
- 812.5ul of 5000 IU/ml SOD1
- 80.3ul of 10mM BLEB
- 325ul of 0.5M EGTA

Aliquot 1.050 ul in black tubes. Store @ -20°C.

Preparation of AUR Stock B (20mM Creatine):

Prepare 10uM AUR stock as in Stock A but with 20mM creatine monohydrate. Mix the following:

- 160.6 ml of Buffer Z (5mg/ml BSA)
- 484.74 mg creatine monohydrate
- 325ul of 5mM AUR
- 812.5ul of 5000 IU/ml SOD1
- 80.3ul of 10mM BLEB
- 325ul of 0.5M EGTA

Aliquot 1.050 ul in black tubes. Store @ -20°C.
(recommend 1050ul next time)

H_2O_2 Protocols

Treatment in Saponin Solution	In Cuvette Prior to Experiment	Volume to Add	Substrate added to induce H_2O_2	Volume to add
NONE	Amplex Red 1U/mL HRP	1mL 2uL of 500U/ml	10mM Succinate	5uL of 2M
35uM CDNB	Amplex Red	1mL	10mM Pyruvate 2mM Malate	5uL of 2M 2uL of 1M

(5uL of 10.5mM Stock)	1U/mL HRP	2uL of 500U/ml		
35uM CDNB (5uL of 10.5mM Stock)	Amplex Red 1U/mL HRP	1mL 2uL of 500U/ml	20mM Glycerol-3-Phosphate	20uL of 1M
35uM CDNB (5uL of 10.5mM Stock)	Amplex Red 1U/mL HRP **0.5uM Rotenone****	1mL 2uL of 500U/ml **2uL of 250uM**	10mM Pyruvate	5uL of 2M
NONE	Amplex Red 1U/mL HRP	1mL 2uL of 500U/ml	2.5uM Antimycin A	5uL of 0.5mM
NONE	Amplex Red 1U/mL HRP	1mL 2uL of 500U/ml	250uM Tyramine	5uL of 50mM

****Use Green Tape Cuvettes for Rotenone as it sticks to glass**

ADP Titration for:

1. Succinate
2. Pyruvate + Malate
3. G3P

Addition 1: 25uM ADP – 5uL of 5mM
* Open lid prior to addition, wait 2 minutes before next addition

Addition 2: 500uM ADP – 9.5uL of 50mM
* Open lid prior to addition, wait 2 minutes before next addition

Addition 3: 5mM ADP – 10uL of 500mM
* Open lid prior to addition, wait 2 minutes before next addition

CDNB for H_2O_2

CDNB – Sigma 237329-10G
** use gloves when handling…very toxic!

Make a 1M Stock of CDNB – dissolve in 100% ethanol

- will need to heat at 95°
- needs to be made fresh daily

If working with **RATS**:
Dilute 1M stock to make 20mM working solution
- add 7.5 µL to your saponin tubes for a final concentration of **100 µM**

If working with **MICE**:
Dilute 1M stock to make 10.5mM working solution
- add 5 µL to your saponin tubes for a final concentration of **35 µM**

Use CDNB in your saponin tubes for the following H_2O_2 Protocols:
1. 10mM Pyruvate + 2mM Malate
2. 10mM Pyruvate + 0.5µM Rotenone
3. 20mM Glycerol-3-Phosphate

H_2O_2 Standard curve for Amplex Ultra Red

1. H_2O_2 dilution (serial dilution)
   - H_2O_2 is light sensitive. Keep in dark when possible.
   - Use H_2O_2 purchased within last 6 months (stored in fridge, wrapped in foil).
   - One standard curve per batch is acceptable, but re-make curve if batch approaches 6 months of age. Discard if curve no longer consistent with original curve.
   - Good in -20C freezer up to 6 months or so.
   - Use stock 3% w/w H_2O_2 : 3 g H_2O_2 / 100 mL solution (1 mol H_2O_2 / 34.01 g) = 0.0882 mol H2O2 / .100 L = .882 mol H_2O_2 / 1 L = 0.882 M H_2O_2
     (1) 4310ul ddH2O + 100ul 3% w/w H_2O_2 >>>> 20mM H_2O_2. Use in dilution step 2.
     (2) 3980ul ddH2O + 20ul of 20mM H_2O_2 >>>>>> 100uM H_2O_2. Use in dilution step 3 for 20uM.
     (3) 3200ul ddH2O + 800ul 100uM H_2O_2 >>>>> 20uM H_2O_2. Use in table below.
     (4) 2000ul ddH2O + 2000ul 20uM H_2O_2 >>>>>> 10uM H_2O_2. Use in table below.
     (5) 2000ul ddH2O + 2000ul 10uM H_2O_2 >>>>>> 5uM H_2O_2. Use in table below.

   NOTE:
   - H_2O_2 is light sensitive.
   - Prepare large volumes to minimize pipetting/dilution errors.
   - Do not vortex - $H_2O_2$is unstable and dismutates spontaneouslyover time. Agitation may worsen. Flip tube in hand several times.

2. Add your Amplex UltraRed, HRP, (oligomycin) and other substrates (G/M/S/G-3-P……) into the cuvette as per your protocol.
   NOTE:
   - Each component of the protocol may affect background fluorescence so it is important to complete the standard curve in the conditions you will use in your experiments. The only exception is the absence of sample: while fibres/isolated mitochondria/cells could affect background fluorescence AND 'scavenge' H2O2 via cysteine/histidine reactions, it is difficult to include tissue in standard curves without a source of oxidants.
   - Another limitation is that we are not obtaining a separate standard curve in the presence of each substrate. Ie. H_2O_2 titrations with pyruvate alone, or pyrumate/malate, or

pyruvate/malate/ADP. In theory, this would be ideal to isolate the effect of each addition and apply a unique standard curve to each component of your experimental protocol. This is not feasible. Moreover, each substrate has negligible effect on fluorescence for amplex ultra red. The compromise is to simply add all components of a protocol during the H_2O_2 standard curve titration.

3. H_2O_2 titration. NOTE: [final H_2O_2] depends on the final volume in the cuvette, which will vary depending on your protocol.

   Make sure to clean the pipette tip by pipetting up and down in a beaker of ddH2O after each addition, and wipe pipette tip with kim wipe. This avoids excess additions of H2O2 as you progress.

If for 1000 ul Titrate very fast, 45-60 sec		**If for 600ul** Titrate very fast, 45-60 sec	
[H2O2] (µM)	Add (µl))	[H2O2] (µM)	Add (µl))
5	3.33	5	2.0
5	3.33	5	2.0
10	3.33	10	2.0
10	5	10	3
20	5	20	3
20	5	20	3
20	10	20	6

4. Repeat 3 times. Average all 3 standard curves to make one equation for analyses in excel. See next page…

   NOTE: Prepare a standard curve for each protocol. For example, you may have a H2O2 standard curve for PM-D-G-CytC-S protocols, and another for ROT-ADP-SUC protocols, etc.

Generate Considerations:

- You will have 7 points in the Standard Curve. Consult experienced personnel on judgement for quantifying steady state fluorescence. In general, make an addition ever 3 minutes. The key is to have at least 2 minutes of approximate steady state fluorescence (following <1 min equilibration of signal). Do not wait longer than 5 minutes as there is a positive drift over time that will inflate your standard curve.
- During analyses, it is common to drop the 6^{th} or 7^{th} point given the relationship begins to form a curvilinear response. Check curve closely following analyses. Aim for at least 4 data points in the final curve.
- Finally, the accuracy of dilutions as an enormous effect on the lowest H2O2 points of the standard curve. It is not uncommon for new trainees to see scattered points at the low end. The stocks must be re-made with new curves prepared if this is the case.

A.10 Measuring Calcium Retention Capacity

Buffers:

1. **BIOPS**

Chemical	Stock Solution	Molecular Weight	Final Concentration	Addition to *2 Litre* final volume
CaK_2EGTA*	100mM		2.77mM	55.4mL
K_2EGTA*	100mM		7.23mM	144.6mL
Na_2ATP		555.1	5.77mM	6.28g
$MgCl_2 \bullet 6H_2O$		203.3	6.56mM	2.67g
Taurine		125.1	20mM	5.02g
Na_2Phosphocreatine		327.14	15mM	9.81g
Imidazole		68.1	20mM	2.72g
Dithiothreitol (DTT)		154.2	0.5mM	0.154g
MES Hydrate		195.2	50mM	19.52g

** prepare stock solutions (see full BIOPS recipe)*

2. **Buffer Y – pH 7.1**

Chemical	Final Concentration	Addition to *500mL* final volume
Sucrose	250mM	42.78g
Tris-HCl	10mM	0.788g
Tris Base	20mM	1.21g
KH_2PO_4	10mM	0.68g
BSA	0.5mg/mL	0.25g

- *store in fridge at 4 C*
- *may require heat to dissolve everything*

3. **CRC Assay Buffer – 600uL aliquots**

Chemical	Final Concentration	Addition to *120mL* final volume
Buffer Y (freshly made)		120mL
Creatine	20mM	0.358g
EGTA	40uM	9.6uL of 0.5M
2-Deoxyglucose	5mM	0.0984g
Hexokinase	2U/mL	160uL of 1500U/mL
BLEB	5uM	60uL of 10mM
Calcium Green*	1uM	400uL of 0.3mM
Tharpsigargin**	2uM	160uL of 1.5mM

* Dissolve 0.5mg CG5N in 1.398mL water

** 1mg vial, make 1mL, aliquot into 165uL stocks and freeze

4. Create a stock of 50mM $CaCl_2$ dissolved in water and store in 50uL aliquots in freezer

Procedure

* place cuvettes on stir plate and fill with ddH_2O and 10uL EGTA (0.5M stock)

1. Harvest muscle and place in ice cold **BIOPS**
2. Separate fibres into bundles (very small and overly separated).
3. Permeabilize for 30 minutes in BIOPS with 40ug/mL saponin
4. WASH 1: 10 minutes in 1.5mL Buffer Y + 1mM EGTA (3uL of 0.5M)
5. Turn on fluorometer to allow lamp to heat up
6. WASH 2: 10 minutes in 1.5mL Buffer Y + 5uM BLEB (0.75uL of 10mM BLEB)
7. Aspirate out water from cuvette but DO NOT RINSE (keep cuvette lined with EGTA)
8. Select Calcium Uptake Assay Protocol on PTI Software. Make sure the following parameters are set:
    a. Excitation: 506
    b. Emission: 532
    c. Duration – 3000 seconds
    d. Slit Widths: Excitation 3nM
       Emission 3nM
    e. x-axis window: 2000 seconds
    f. y axis max and min: 500 000 and 800 000

Substrate	Stock Concentration	Addition to cuvette	Final Concentration in Cuvette
CRC Assay Buffer		300uL	
Glutamate	2M	1.5uL	10mM
Malate	1M	1.5uL	5mM
ADP	500mM	3uL	5mM
Fibre ** make sure fibre is at the bottom of cuvette attached to stir bar**			
Collect 400 second background to establish "F-Min"			
$CaCl_2$	5mM	2.5uL	8nmol
Wait 5 minutes or until steady state			
$CaCl_2$	5mM	1.25uL	12nmol (4nmol pulse)
Wait 5 minutes in between pulses and continue pulsing until pore opens			
$CaCl_2$	50mM	3uL	0.5mM Pulse (F-Max)
Wait 3 minutes before final addition, this should establish F-Max but last addition is to make sure			
$CaCl_2$	50mM	3uL	0.5mM Pulse (F-Max)

* for each additions remove cuvette from holder and ensure fibre has not been disrupted

**Make sure y axis is no more than 300 000 units or you will miss opening

9. Remove bundle and save for freeze drying (if applicable)

A.11 Caspase Activity Assay

Chemicals
Homogenisation buffer: 500 ml

Chemical	Molecular Weight	Concentration	Amount added
Sucrose	342.3	250 mM	42.8g
Tris	121.14	50 mM	3.03g
DTT	154.25	1 mM	0.077g
EDTA	372.24	1 mM	0.186g
$MgCl_2$	203.3	5 mM	0.51g
Glycerol		10%	50mL

pH 7.5
Incubation buffer: 100 ml

Chemical	Molecular Weight	Concentration	Amount added
HEPES	283.3	100 mM	2.38g
Sucrose		10%	10g
DTT	154.25	1 mM	0.015g

pH 7.5

Fluorescent substrates for Caspase activities:

Caspase 3: AC-DEVD-AMC (Enzo - **ALX-260-031-M001)**
1mg into 1.48 mL DMSO for 1mM Stock

Caspase 3 Inhibitor: AC-DEVD-CHO (Enzo - **ALX-260-030-M001)**
1mg into 2mL DMSO for 1mM Stock

Caspase 8: AC-IETD-AMC (Enzo - **ALX-260-042-M001)**
1mg into 1.48 mL DMSO for 1mM Stock

Caspase 8 Inhibitor: AC-IETD-CHO (Enzo - **ALX-260-043-M001)**
1mg into 2mL DMSO for 1mM Stock

Caspase 9: AC-LEHD-AMC (Enzo - **ALX-260-080-M001)**
1mg into 1.45 mL DMSO for 1mM Stock **different MW from 3 and 8

Caspase 9 Inhibitor: AC-LEHD-CHO (Enzo - **ALX-260-079-M001)**
1mg into 1.86mL DMSO for 1mM Stock

** Aliquot Substrates into 300uL, Aliquot inhibitors into 10uL. Store in black tubes at -20

Experimental procedures

Preparation of lysosome and proteasome fractions:

Homogenise muscle biopsy using tapered pestle with a muscle:homogenate ratio of 10mg:100uL.

Centrifugation steps: (P = pellet; S = supernatant)

700×g 10 min at 4 degrees **P1** (nuclei, myofibrils)

S1 ↓

16,300×g 20 min at 4 degrees **P2** (lysosomes, mitochondria)

S2 (bound and free proteasomes)

S2: divide into 100 µl portions to be used for **CASPASE AND CALPAIN ASSAYS**

Freeze all fractions at -80ºC

Protein determination:

Protein determination is done with the Bradford method **USING THE REDUCING AGENT COMPATIABLE KIT.**

Caspase Activity:

1. Dilute 1mM stock of each substrate into 100µM using incubation buffer – make up total volume needed for all samples plus 200µL extra (see loading table in excel)
2. Add 10uL of protein from S2 into the wells (total of 3 wells for each sample, unless running an inhibitor test)
3. Add 100 uL of diluted caspase 3 substrate to 1 well of sample
4. Repeat step 3 using Caspase 8 and Caspase 9 substrate
5. Add 3uL of Caspase 3 inhibitor to well if required
6. Repeat step 5 for Caspase 8 and 9 inhibitor
7. Read every 2 minutes for 1 hour

**Do not need to run inhibitor well for every sample, just use as a check

Fluorescence measurements (using Haas fluorescent plate reader in LSB:

Prepare the plate reader settings before adding standards, muscle extracts and substrates into the micro plates.
Temperature 37ºC; Excitation filter 360 nm; Emission filter 460 nm
Gain 80 % of max value
Read every 2 min for 1 hour

A.12 Western Blotting

WESTERN BLOTTING – PREPARATION OF BUFFERS

	Stacking	Running				
		5%	6%	8%	10%	12%
dH_2O	6.8 ml	11.4	10.6 ml	9.4 ml	8 ml	6.7 ml
1.5M Tris-Base, pH 8.8	***	5 ml	5 ml	5 ml	5 ml	5 ml
1M Tris-Base, pH 6.8	1.25 ml	***	***	***	***	***
30 % Acrylamide	1.70 ml	3.4 ml	4 ml	5.3 ml	6.7 ml	8 ml
10 % SDS	100 µl	200 µl	200 µl	200 µl	200 µl	200 µl
10 % APS	100 µl	200 µl	200 µl	200 µl	200 µl	200 µl
Temed	20 µl	20 µl	20 µl	20 µl	20 µl	20 µl

10 X Running Buffer:

	500 ml	1 L	2 L
Tris	15 g	30 g	60 g
Glycine	72 g	144 g	288 g
SDS	5 g	10 g	20 g

1 X Running Buffer: 10 X Running buffer 100 ml
dH_2O 900 ml

---

10 X TBS (Tris Buffered Saline):

	500 ml	1 L
Tris	12.1 g	24.2 g
NaCl	40 g	80 g
Adjust to pH 7.6 with HCl		

1 X TBST:

	1 L	2 L
10 X TBS	100 ml	200 ml
dH_2O	900 ml	1800 ml
Tween 20	1 ml	2 ml

Note: Ensure solution is stirring when adding Tween

Primary Antibody
- Blocking Buffer
- .1% Tween
- .01% SDS

Secondary Antibody
- Blocking Buffer
- .1% Tween
- .01% SDS

CHAPS Buffer

For 200mL solution at pH 7.5

Amount	Reagent	Concentration	Molecular Weight
1.906g	HEPES pH 7.5	40mM	238.3
1.403g	NaCl	120mM	58.44
74.4mg	EDTA Na2	1mM	372.2
892mg	NaHP2O7.10H2O pyrophosphate	10mM	446.1
432mg	B-glycerophosphate	10mM	216.04
420mg	NaF	50mM	41.99
0.6g	CHAPS	0.30%	

Muscle Homogenization

** Turn on centrifuge and cool to 4°C

1. Place frozen muscle in corresponding eppendorf tube with Buffer/Inhibitors
    i. 10mg muscle = 100uL CHAPS Buffer
    ii. Fridge Protease Inhibitors = 1:100
    iii. Freezer Phosphatase Inhibitor = 1:200
2. On ice, use small scissors to mince tissue until it is broken up into small pieces
3. Rinse pestol with 70% ethanol followed by water, wipe pestol with kim wipe
4. Place eppendorf with minced tissue in beaker of ice
5. Push pestol to bottom of eppendorf
6. Turn on homogenizer and allow to run for 10 seconds while pushing pestol against eppendorf
7. Turn off for 10 seconds and scrape any muscle off of pestol
8. Repeat step 6 and 7 two more time (total of 3x10 seconds homogenizing)
9. Place sample back in ice box and repeat steps 1-9 for next sample

10. Once all samples are homogenized, place in centrifuge and spin for 10min: 800g at 4 degrees
11. Pipette off supernatant and place in new labeled tube
12. Throw out remaining pellet
13. Proceed with Bradford Protein Assay

Protein Assay – BCA

1. Create standards by diluting BSA in homogenization buffer
    Standards (BSA):
    0 mg/mL (buffer)
    0.0625 mg/mL
    0.125 mg/mL
    0.25 mg/mL
    0.50 mg/mL
    0.75mg/mL
    1.00 mg/mL
2. Dilute 5 µL of each sample in 45 µL of homogenization buffer
3. Using a 96 well plate load in triplicates each standard and each sample
4. Add 190uL of mixed solution (50:1 Solution A:SolutionB) into each well of sample

* Amount needed: (# of standards + # of unknowns) x (3 replicates) x (200uL)

5. Heat in over for 30 minutes at 37°C

Running a Western

1. In 50mL falcon tubes make running gel and stacking gel (1 column makes 2 gels) ***DO NOT ADD TEMED UNTIL READY TO LOAD***
2. Take 1 short plate and one spacer plate and clean both sides of glass with methanol and kimwipe
3. Place clean short plate on top of spacer place and place both in mounting apparatus, ensuring the edge of the plates are lined up against the bench top
4. Place plates in apparatus on foam piece in gel stand
5. Place 3 transfer pipettes and falcon tube with methanol close to gel stand
6. Add TEMED to running gel and invert falcon tube 1-2 times
7. Using transfer pipette, fill space between glass plates with running gel until solution reaches the top of the green doors
1. Using new transfer pipette add methanol to top of plate to create an even line along the top of the gel removing any bubbles
2. Let sit until remaining running gel has hardened in the falcon tube
3. Once gel has set, invert gel to remove any excess methanol
4. Add TEMED to stacking gel and invert 1-2 times
5. Using transfer pipette, add stacking gel to top of glass plates, use methanol transfer pipette to remove any bubbles
6. Add comb to top of gel and allow to set

7. Prepare diluted samples by combining sample, water and Laemmeli's buffer + 2-mercaptoehtanol (100 µl 2-mer: 900 µl Lam)

a. **Example of dilution to load 50µg protein at a concentration of 1µg/ µl**

Sample	Corr Prot (ug/ul)	Aliquot (ug)	Sample (ul)	H20	4X Laem (1:9 2-Mercap)	Vol for 1 Well
C7.5-A	4.599	50	10.9	26.6	12.5	50

8. Boil samples at 95 °C for 5 minutes
9. Spin down samples for 5 seconds
10. Make 1X running buffer in 1000mL graduated cylinder
11. Remove combs from gels and place gels in gasket
12. Place gasket with gels in tank and add 1X running buffer until it fills the top of gasket and tank
13. Load wells with desired concentration of samples
14. Run for desired time (40-75 minutes) at 160mV (or desired voltage)

15. Fill 2 plastic "biorad" dishes, one with methanol and one with transfer buffer
16. Place 2 transfer packs in dish of transfer buffer and place membrane in dish of methanol
17. After 2-3 minutes place first transfer pack on bottom of transfer case
18. Place membrane in transfer buffer for 10-15 seconds

19. Place membrane on top of transfer pack ensuring no air bubbles
20. Remove short plate from gel and place gel face down on membrane
21. Place second transfer pack on top of membrane
22. Using roller, roll from one side of transfer pack to the other to remove air bubbles
23. Hold firmly down in the middle of the transfer pack and remove excess liquid
24. Put lid on transfer case and run transfer (standard setting is 1.5mm gel for 10 minutes)

25. Following transfer remove membrane and place in dish with blocking buffer (50% Odyssey Blocking Buffer, 50% TBS) for 1 hour, rocking at room temperature
26. After 1 hour pour blocking buffer back into falcon tube (it can be resused) and add primary antibody
27. Place membrane in primary in fridge overnight, rocking
28. In the morning remove primary and pour back into falcon tube (can be resued)
29. Add TBST to dish and complete 3x5 minute TBST washes rocking at room temperature.
30. Add secondary antibody and leave rocking at room temperature for 1 hour
31. Remove secondary and place back in falcon tube (can be resused)
32. Complete 3 more 3x5 minute TBST washes
33. Detect using LiCOR Infrared Imager

Antibody Optimization

Antibody	Company	Concentration	Animal	Gel%	Molecular Weight	[Protein]
ANT 1	Abcam – 180715	1-1000	Rabbit	12%	33 Cut gel at 25 and 37 (right at 37 to get rid of thick band above 37)	Heart: 50 Diaphragm: 40 Quad: 30 WG: 50
VDAC 2	Sigma – SAB2501096	1ug/ml	Goat	12%	32	50
OXPHOS	Abcam	1:250 (6ug/mL)	Mouse	12%	20-50 Cut gel at 15 and 75	Heart: 30 Diaphragm: 40 Quad: 15 WG: 15
MiCK -	Uwe	1-1000	Rabbit	10%	42	15
4-HNE	Abcam – 46545	1-1000	Rabbit	12%	<75 kda	50
Oxyblot	Millipore Sigma – S7150	1-150	Rabbit	12%	Above 100, Below 20	Heart: 15 Diaphragm: 15 Quad: 40 WG: 40
PDH E1alpha	Abcam - ab110330	1-1000	Mouse	10%	43	50

A.13 Evaluating Redox Status of Specific Protein

Optimized for IP of MtCK

Lysis Buffer: Chaps

For 200mL solution at pH 7.5

Amount	Reagent	Concentration	Molecular Weight
1.906g	HEPES pH 7.5	40mM	238.3
1.403g	NaCl	120mM	58.44
74.4mg	EDTA Na2	1mM	372.2
892mg	NaHP2O7.10H2O pyrophosphate	10mM	446.1
432mg	B-glycerophosphate	10mM	216.04
420mg	NaF	50mM	41.99
0.6g	CHAPS	0.30%	

Stock solutions

	Catalog number	Molecular Weight (g/mole)	Amount (g)	Volume of Solvent
IR Dye – 8.4mM Licor, 929-80020	1191 0.5mg	DMSO	50ul	*5ul aliquots
	Dilute to 60uM Stock – freeze 60uM stock, can be reused several times 1uL of 8.4mM Dye into 140uL DMSO			
H_2O_2 – 0.1M Fresh	Sigma, 95321-100ml	34.01	113ul (of 3%)	WATER 887ul
NaI – 100% Fresh	Sigma 217301-100G	185.92	0.1g	WATER 100ul
TCEP – 0.1M Fresh	Fisher - 20490	286.65	1mg	WATER 34.9ul

Tissue Homogenization

N.B: The IRDye-Maleimide should be protected from light at all time

Day 1

1. Weigh **2x 60 mg** of left ventricular tissue (one will be labeled and the other one will be used for controls)
2. Place 60mg of tissue into 0.6 ml ice cold CHAPS buffer + protease inhibitors (standard homogenization protocol) and homogenize for 3x10seconds
3. Spin at 800g for 10 minutes (4°C)
4. Transfer supernatant to new tube
5. Determine protein concentration using standard BCA protein assay kit

6. Determine exact volume of lysate and calculate total protein in sample **Use prepared excel sheet*
7. Add 100nM dye/200ug protein (60uM stock)
8. Mix gently on nutator overnight at 4°C

Day 2

9. Remove excess Dye by passing the lysate over 2 successive 2ml desalting Zeba columns. Use the same column twice.
    a. Remove bottom closure and place column in 15ml Eppendorf tube
    b. Unscrew red cap
    c. Spin down for 2 minutes at 1000g to remove storage
    d. Mark with sharpie the side of the column that has resin slanted upwards – always place this side facing outwards in the centrifuge
    e. Add 1ml of water to column and spin down again for 2min at 1000g
    f. Place zeba column in new 15ml Eppendorf
    g. Slowly load up to 700ul of sample onto filter bed
    h. Spin down for 2 minutes at 1000g

10. Collect the cleaned sample
11. Determine protein concentration using BCA
12. Proceed to the IP

Immunoprecipitation Protocol – *based on BioRad SureBeads Protocol*

1. Vortex SureBeads in their solution and transfer 100ul (1mg of beads) of SureBeads to 1.5ml tubes – 1 tube/sample
2. Magnetize beads and aspirate off supernatant using pipette (aspirator is too aggressive and sucks up beads)
3. Wash with 1ml PBS-T (PBS + 0.1% Tween 20)
    a. Add PBS to Eppendorf running liquid overtop of beads
    b. Rotate Eppendorf 180 degrees, let bead sit, rotate another 180 degrees and allow bead to gather
4. Magnetize beads and aspirate off supernatant (always using pipette)
5. Repeat steps 3 and 4 three times
6. Remove tubes from magnet (should have no liquid) and add 200-volume of antibody ul of PBS-T over beads
7. Add desired concentration of antibody (usually between 1 and 10ug) and vortex well
    a. Total volume in tube should be 200ul
8. Rotate for 10 minutes at room temperature
9. Spin down to remove liquid from the cap
10. Wash with 1ml PBS-T (PBS + 0.1% Tween 20)
    a. Add PBS to Eppendorf running liquid overtop of beads
    b. Rotate Eppendorf 180 degrees, let bead sit, rotate another 180 degrees and allow bead to gather
11. Magnetize beads and aspirate off supernatant
12. Repeat steps 10 and 11 three times
13. Remove tube from magnet (beads should have no liquid in tube)
14. Add desired volume/concentration of lysate

15. Rotate for 1 hour at room temperature
16. Spin down to remove liquid from lid
17. Magnetize beads and discard supernatant
18. Wash with 1ml PBS-T (PBS + 0.1% Tween 20)
    a. Add PBS to Eppendorf running liquid overtop of beads
    b. Rotate Eppendorf 180 degrees, let bead sit, rotate another 180 degrees and allow bead to gather
19. Magnetize beads and aspirate off supernatant
20. Repeat steps 18 and 19 three times
    a. Before last magnetization, transfer the re-suspended beads to a new tube
21. Spin down tube for several seconds
22. Magnetize beads and aspirate residual buffer from the tubes

Elution:

1. Add 20mM Glycine (pH 2.0) – 20ul and incubate for 5 minutes at room temperature
2. Magnetize beads and move eluent to a new vial
3. Neutralize eluent with 2ul (10% of total volume) with 1M PBS, pH 7.4

** This elution strategy is used for IR Dye to avoid boiling and subsequent denaturing of proteins. If not using IR dye, standard Laemmli buffer plus boiling can be used to elute protein of interest

4. Proceed to Western Blot Sample Preparation – do not boil
    a. 22ul total sample +
    b. 10ul of 4x Sample Buffer (1/10 2-Mercap, 9/10 4x Laemellis) +
    c. 8ul of H2O
5. Spin samples down to remove bubbles
6. Load 35ul of sample into lane

Controls

Day 1

1. Homogenize in CHAPS buffer as above for samples.
2. Run samples through zeba desalting column twice to remove any glutathione
    a. Use 0.5ml zeba column to reduce protein loss that occurs when sample is spun through the large 2ml column
    b. Remove bottom closure and place column in 1.5ml Eppendorf tube
    c. Unscrew red cap
    d. Spin down for 1 minute at 1500g to remove storage
    e. Mark with sharpie the side of the column that has resin slanted upwards – always place this side facing outwards in the centrifuge
    f. Place zeba column in new 1.5ml Eppendorf
    g. Slowly load up to 130ul of sample onto filter bed
    h. Spin down for 2 minutes at 1500g

3. After spin, run protein assay with standard BCA kit
4. Divide sample into 3 aliquots of 4.167ug/ul diluted in CHAPS (total volume 200ul)
    a. Use prepared excel sheet for calculations
5. Add 5mM H_2O_2 + 0.5% NaI to oxidized sample – **this sample should turn yellow! Make sure you added H2O2 and NaI at the same time!**
    a. 5mM H_2O_2 = 10ul of 0.1M

b. 0.5% NaI = 1ul of 100%

6. Add 1mM TCEP to control sample
    a. 1mM TCEP = 2ul of 0.1M
7. Incubate at room temperature on nutator for 5 minutes along with non-treated control
8. Spin all samples through zeba column to remove excess reagent - twice
9. Run Protein Assay using reducing agent compatible BCA kit
10. Determine volume of remaining lysates – calculate total protein in sample
11. Add 100nM/200ug protein dye (60uM Stock)
12. Mix gently on nutator overnight at 4°C

Day 2

13. Remove excess Dye by passing the sample over 2 consecutive desalting Zeba columns (0.5mL columns). Use same column twice.
14. Collect the cleaned sample
15. Determine protein content using Reducing Agent Compatible BCA protein assay kit
16. Prepare samples for western blot – will need 2.5ug Protein

Western Sample Preparation

** Do not boil

**1/10 2-Mercaptoethanol; 9/10 4x Laemellis Buffer

A.14 Evan's Blue Dye

Evans Blue Dye Stock – 1% (0.01g/mL)
Inject IP - 50µl/10g BW of mouse
Wait 16-18 hours and harvest muscle

Procedure

1. 0.9% Saline
    a. 0.45g NaCl in 50mL ddH_2O
2. Dissolve EBD in Saline
    a. 0.1g in 10mL 0.9% Saline
    b. Run through sterile filter syringe
    c. Store in Fridge
3. Inject mouse IP with 50µl/10g BW
4. Wait 16-18 hours
5. Harvest Tissue and weigh individual muscles – take photos for representative images
6. Place in 1ml of **formamide** and incubate over night at 56 degrees on heat block
7. Day 2: remove the tissues from the formamide and keep the "blue" solution
8. Load 200µl from each tissue into a 96 well plate
9. Load standard curve (see below)
10. Read using spectophotometer set to $\mathbf{A_{620}}$

Standard Curve

a. Dissolve the 1% Evans Blue Solution 3:1000= 30mg/ml
    i. 3ul 1% EB in 1000ul formamide
b. 12.9µg/ml: 430µl of 30mg/ml in 570ul formamaide
c. 6.45µg/ml: 500ul of 12.9µg/ml in 500µl of formamide
d. 3.225 µg/ml: 500ul of 6.45/ml in 500µl of formamide
e. 1.6125 µg/ml: 500ul of 3.224/ml in 500µl of formamide
f. 0.806 µg/ml: 500ul of 1.6125/ml in 500µl of formamide
g. 0.403 µg/ml: 500ul of 0.806/ml in 500µl of formamide
h. 0.2015 µg/ml: 500ul of 0.403/ml in 500µl of formamide
i. 0.1 µg/ml: 500ul of 0.2015/ml in 500µl of formamide
j. load 200ul per well, can do duplicates

11. Convert amount of Evans blue to ng/mg of tissue

A.15 Glutathione

Buffer

- **TRIS-BSA:** homogenization buffer with Trizma Base + Boric Acid/Serine/Acivicin to inhibit γ-glutamyltranspeptidase from metabolizing GSH/GSSG.
    - 200mL HPLC grade water
    - 50mM Trizma Base: 1.212g -- (MW=121.14g)
    - 20mM Boric Acid: 0.248g – (MW=61.83g)
    - 2mM L-serine: 0.042g – (MW=105.69g)
    - 20uM Acivicin: (MW=178.57)
    - Acivicin inhibits y-glutamyltranspeptidase, a protein bound to the cell membrane which catabolizes glutathione upon contact
    - pH to 8 with HCL
- DAY OF:
    - Add 25ul 0.2M NEM for every 1ml TRIS-BSA fresh day of use (some suggest NEM is light sensitive, freeze sensitive, not sure if this is true or not, but adding it same day allows for to decide whether you would want to or not add NEM, only time you wouldn't add NEM is if you wanted to measure total glutathione)
    - NEM irreversibly binds to GSH creating a GS-NEM conjugate and inhibits glutathione reductase preventing the auto-oxidation GSH to GSSG

Making Mobile phase solvents

GSH mobile phase

- Solvent A: 0.25% Glacial Acetic Acid in HPLC grade water
    - 2.5mL glacial acetic acid into 997.5mL water
        - Or 1.25ml glacial acetic acid into 498.75mL water
    - pH to 3.1 by adding in a couple drops of 2M NaOH to bring pH up or glacial acetic acid to bring pH down
    - **Prepare fresh every day**
- Solvent B: 100% Acetonitrile

GSSG mobile phase

- Solvent A: 25mM Na_2HPO_4 in HPLC grade water
    - Make 425ml
        - pH to 6.0 using phosphoric acid
    - Add 75ml MeOH to get final 15% methanol mobile phase

Sample preparation:

- Make up 6 tubes:
    - Tube1 for homogenate/lysis
    - Tube2 for protein assay
        - 5ul homogenate into 45ul buffer/RIPA buffer for cells
        - Poke hole in top of tube
    - Tube3 with TCA
        - 7ul TCA into tube
    - Tube4 PCA
        - 70ul PCA into tube
    - Tube5 labeled GSH
        - Poke hole in top of tube

    - Tube6 labeled GSSG
        - 500ul 0.5M NaOH

For muscle:

- Homogenize tissue in TRIS-BSAN at a 1mg-10ul ratio, leave on ice until all samples (I usually do about 10 samples at a time, do samples in random order).
    - Try and get at least 145ul final volume, otherwise need to adjust volumes of TCA and PCA
- Spin samples at 800g for 10 minutes at 4 degrees
- Add supernatant to tube 1

- Now have cells or muscle homogenate in tube 1
- Take from tube 1:
    - 5ul tube 1 -> tube 2 (protein tube)
        - Freeze in liquid nitrogen
    - 70ul tube 1 -> tube 3 (TCA tube, for GSH)
        - Put onto rocker
    - 70ul tube 1 -> tube 4 (PCA tube, for GSSG)
        - Put onto rocker
    - Vortex tubes 3 and 4
- Spin TCA and PCA tubes at 20,000g for 5minutes at 4^{o}C
- Carefully take tubes out of centrifuge, be careful not to dislodge pellet
- From tube 3: Take off supernatant, and transfer to tube 5 (GSH tube)
- From tube 4: take 100ul of tube 4 -> tube 6 (GSSG tube)
- Freeze

Determine protein from samples using tube 2 (protein tube)

GSH determination (UV)

- GSH flow rate at 1.25 ml/min (new HPLC down to 1.05ml/min)
- Sample detected using VWD (UV detector) detector (on HPLC stack) at 265nm
- 94% Mobile phase A, 6% acetonitrile
    - Protocol name on HPLC is TurnbullGSH
- Take GSH tube, transfer total volume into HPLC vial.
- Have machine insert 10ul of sample into machine
    - GSH elutes as two peaks right before NEM spike
        - No idea why is elutes as two peaks, cant find answer (yet) but is reported as common – I think it is likely due to some of the amino acid residues being chimeric (maybe?)
        - Found answer: it is because the configuration of GSH (3 amino acids) can be built in two ways depending on the specific amino acid configuration, I always use 2nd peak because 1st peak is sometimes influenced by other compounds depending on the tissue being analyzed

GSH Standard

- Every day, run a 4 point standard
- 250uM GSH, 62.5uM GSH, 31.25uM GSH, 15.6uM GSH
- Step 1: Make 50mM GSH in TRIS-BSAN
- Step 2: Dilute 50mM GSH -> 5mM GSH in TRIS-BSAN

- Step 3: Dilute 5mM GSH -> 0.5mM GSH in TRIS-BSAN
- Step 4: Do serial dilutions from 0.5mM (500uM GSH)
  - 500uM GSH -> 250uM GSH -> 125uM GSH -> 62.5uM GSH -> 31.25uM GSH -> 15.6uM GSH
- Take 70ul of 250uM GSH, 62.5uM GSH, 31.25uM GSH, 15.6uM GSH tubes, and transfer to new tubes with 7ul TCA
- Transfer GSH-TCA tube to HPLC vial, ready to load

GSSG determination (fluorescent)

- Excitation/Emission 350/420nm
- Flow rate at 0.5 ml/min
- Sample elutes as a single peak
- Injection volume: 50ul
- Protocol is set up as TurnbullGSSG
- Take tube 6 out of freezer
- When thawed, add in 37.5ul of 0.1% OPA (our fluorophore, which is stored in -20^{o}C freezer)
- Incubate samples in the dark for at least 15 minutes
- After incubation, transfer to HPLC vial, ready for run.

GSSG Standard

- Every day, run a 4 point standard
- 10uM GSH, 2.5uM GSH, 1.25uM GSH, 0.625uM GSH
- Step 1: Make up 20mM GSSG in TRIS-BSAN
- Step 2: Dilute 20mM GSSG -> 2mM GSSG in TRIS-BSAN
- Step 3: Dilute 2mM GSSG -> 0.2mM GSSG in TRIS-BSAN
- Step 4: Dilute 0.2mM GSSG -> 20uM GSSG in TRIS-BSAN
- Step 5: Do serial dilutions starting from 20uM GSSG
  - 20uM GSSG -> 10uM GSSG -> 5uM GSSG -> 2.5uM GSSG -> 1.25uM GSSG -> 0.625uM GSSG.
- Step 6: Take 70ul of GSSG standard and mix with 70ul PCA
- Take 100uL from GSSG standards and transfer to new tube with 500ul 0.5M NaOH
- Add in 37.5ul of 0.1% OPA-MeOH (our fluorophore, which is stored in -20^{o}C freezer)
- Incubate standards in the dark for at least 15 minutes
- After incubation, transfer to HPLC vial, ready for run.